DETECTION OF ROLLING ELEMENT BEARING FAULTS VIA VIBRATION ANALYSIS

A Thesis Submitted to the
Graduate School of Natural and Applied Sciences of Dokuz Eylül University
In Partial Fulfillment of the Requirements for the Degree of Master of Science
in Mechanical Engineering, Machine Theory and Dynamics Program

by

Ahmet YİĞİT

August, 2008

İZMİR

M.Sc THESIS EXAMINATION RESULT FORM

We have read the thesis entitled **"DETECTION OF ROLLING ELEMENT BEARING FAULTS VIA VIBRATION ANALYSIS"** completed by **AHMET YİĞİT** under supervision of **ASSISTANT PROFESSOR ZEKİ KIRAL** and we certify that in our opinion it is fully adequate, in scope and in quality, as a thesis for the degree of Master of Science.

Assistant Professor Zeki KIRAL

Supervisor

(Jury Member)   (Jury Member)

Prof. Dr. Cahit HELVACI

Director

Graduate School of Natural and Applied Sciences

ACKNOWLEDGMENTS

DETECTION OF ROLLING ELEMENT BEARING FAULTS VIA VIBRATION ANALYSIS

ABSTRACT

Rolling element bearings are the main components in rotary machines due to their advantageous friction characteristics. It is very important to keep the rolling element bearings in good condition in terms of general machine health. In this study, the condition of deep groove rolling element bearings is monitored by means of vibration measurement. Experimental vibration signals are collected from a test rig, including two rolling element bearings, which carry a shaft having an unbalanced mass on it. A local defect on the inner or outer race of one of the rolling element bearings is introduced artificially and vibration measurements are performed using a portable vibration analyzer in terms of displacement, velocity and acceleration. Some statistical indices such as rms, peak to peak and kurtosis values of the vibration signals are calculated for healthy and faulty cases, in order to obtain the change in the time domain parameters due to bearing deterioration. The vibration measurements are performed for a broad range of shaft speed. Signs of the bearing deterioration are also investigated in frequency domain by the Fast Fourier Transform (FFT) and Short Time Fourier Transform (STFT). As the main part of this study, a nonlinear time domain transform, named as Curve Length Transform (CLT) is applied to the vibration signals for diagnostic purposes. The statistical indices of the CLT signals for healthy and faulty cases are calculated and compared, to make a decision about the condition of the rolling element bearing. The statistical indices of the CLT signals are also compared with the statistical indices calculated for raw vibration signals, in order to show the efficiency of the Curve Length Transform. The experimental results show that the CLT can be used successfully to enrich some time domain parameters, which give useful information in capturing the local bearing failures.

Keywords: Rolling element bearing, fault detection, vibration measurement, curve length transform, time domain parameters.

RULMANLI YATAK ARIZALARININ TİTREŞİM ANALİZİ İLE BELİRLENMESİ

ÖZ

Yuvarlanma elemanlı yataklar (rulmanlar) avantajlı sürtünme karakteristiklerinden dolayı dönel makinelerde temel elemanlardır. Rulmanlı yatakların iyi durumda tutulması genel makine sağlığı açısından çok önemlidir. Bu çalışmada, küresel bilyalı yatakların durumları titreşim ölçümü ile izlenir. Deneysel titreşim sinyalleri, iki adet rulmanlı yatak tarafından taşınan ve üzerinde dengelenmemiş kütle bulunduran bir mil içeren deney düzeneği üzerinden alınır. Rulmanlı yataklardan birinin iç veya dış bileziği üzerinde yapay olarak bir bölgesel hata oluşturulur ve titreşim ölçümleri taşınabilir bir titreşim analizatörü ile yer değiştirme, hız ve ivme cinsinden gerçekleştirilir. Rms (kare ortalamalarının karekökü), tepe tepe ve kurtosis değerleri gibi bazı istatistiksel göstergeler sağlıklı ve hatalı durumlar için zaman ortamı parametrelerinde rulman bozulmasından kaynaklanan değişimleri elde etmek için hesaplanır. Titreşim ölçümleri geniş bir mil hızı aralığı için gerçekleştirilir. Rulman bozulmasına ait göstergeler frekans ortamında da hızlı Fourier dönüşümü ve kısa zamanlı Fourier dönüşümü ile incelenmiştir. Bu çalışmanın ana kısmı olarak, Eğri Uzunluğu Dönüşümü olarak adlandırılan lineer olmayan bir zaman ortamı dönüşümü, arıza teşhisi amacı için titreşim sinyallerine uygulanır. Sağlıklı ve hatalı durumlardaki eğri uzunluğu dönüşüm sinyallerine ait istatistiksel göstergeler hesaplanır ve rulman durumu hakkında karar vermek için karşılaştırılırlar. Eğri uzunluğu dönüşümü sinyallerine ait istatistiksel göstergeler, eğri uzunluğu yönteminin etkinliğini göstermek için ham titreşim sinyalleri için hesaplanan istatistiki göstergeler ile de karşılaştırılır. Deneysel sonuçlar, eğri uzunluğu yönteminin, bölgesel rulman arızalarını yakalamada faydalı bilgiler veren bazı zaman ortamı parametrelerinin zenginleştirilmesinde başarılı olarak kullanılabileceğini gösterir.

Anahtar Kelimeler: Yuvarlanma elemanlı yatak, hata tespiti, titreşim ölçümü, eğri uzunluğu dönüşümü, zaman ortamı parametreleri.

CONTENTS   **Page**

CHAPTER ONE
INTRODUCTION

Rolling element bearings are inevitable mechanical components which permit the shafts to rotate with very low friction resulting low bearing detorioration. Thus, rolling element bearings are used in various industrial rotary machines. Due to environmental effects, like dirt or operation conditions such as sudden loads, different kind of defects may occur during operation. To detect and diagnose the defect in rolling element bearings, various condition monitoring tecniques have been developed. The condition monitoring methods can be classified as vibration analysis, acoustic emission measurement, shock pulse method (SPM), stator current measurement, adaptive filtering and temperature measurement. There are many studies in the literature related to the detection of the defects in rolling element bearings via these techniques.

Tandon & Choudhury (1999) presented a review of vibration and acoustic measurement methods for the detection of defects in rolling element bearings. In their study, vibration measurement in both time and frequency domains along with signal processing techniques such as the high-frequency resonance technique were covered. Acoustic measurement techniques such as sound pressure, sound intensity and acoustic emission were reviewed. Detection of both localized and distributed categories of defect were explained. They observed vibration in the time domain that can be measured through the parameters such as RMS level, crest factor, probability density and kurtosis. Kurtosis was mentioned as the most effective method. Vibration measurement in the frequency domain has the advantage that it can detect the location of the defect. But, the direct vibration spectrum from a defective bearing may not indicate the location of the defect especially at the initial stage. This problem has been overcomed by some signal processing techniques. The high-frequency resonance technique is the most popular among the other techniques. The sound intensity, which is one of the acoustic was reported techniques seemed to be better than sound pressure measurements for bearing diagnostics. They observed in the related studies, acoustic emission measurements have been better than vibration

measurements for detecting defects in rolling element bearings. In addition, acoustic emission signals can detect a defect even before it appears on the surface.

Kıral & Karagülle (2006) modelled the loading mechanism in a bearing structure which houses a deep groove ball bearing having different localised defects and carrying an unbalanced force rotating with the shaft. The finite element vibration analysis was employed to simulate the bearing vibration signals. They proposed the use of the finite element vibration analysis with the proper loading model which produces simulated vibration signals including the structural information in order to find the most efficient analysis method. The effects of different parameters such as the rotational speed, sensor location, angular position and number of the outer ring defects, defect type (inner ring defect and rolling element defect) on the vibration monitoring methods were examined by using the time and frequency domain parameters. They reported that the envelope method can be used efficiently in order to detect the outer and inner ring defects, but rolling element defects were not easy to detect via envelope and band energy ratio procedures.

Tandon, Ramakrishna, & Yadava (2007) presented a study which reports the effectiveness of vibration, stator current, AE signals and shock pulse value monitoring for the detection of contaminants in grease lubricated motor bearings. Brittle and ductile contaminant particles such as silica and ferric oxide were used. Different contaminant levels of constant particle size were prepared. Silica and ferric oxide particles are used as contaminant with varying particle size in the grease. Sufficient amount of grease was applied to the bearing. They observed that the vibration, stator current, acoustic emission and shock pulse measurements were appreciably increased as contaminant level and contaminant size increases. The increase in the contaminant level with constant size has shown less effect when compared to increase in particle size with constant contaminant level. Choudhury & Tandon (2000) investigated the changes in AE signal for different sizes of simulated defects on the inner race and a roller of radially loaded cylindrical roller bearings. The method of ringdown counts was found to be a very good parameter for the detection of defects in both the inner race and roller of the bearings tested. The

ringdown counts for the smallest defect size was a good parameter for incipient fault detection in bearings. But, AE counts were unable to provide any information about the progress of the defect for larger defect sizes. Distributions of events by ringdown counts and peak amplitudes were also found to be good indicators of bearing defect detection.

Khalid, Asok, K. P., D. K., & Steven (2007) investigated an alternative approach for detecting localized faults in the outer and inner races of a rolling element bearing using the envelope power spectrum of the Laplace Wavelet. The vibration model for a rolling element bearing with outer and inner race faults was given. The implemantation of a proposed approach for the detection of localized ball bearing defects for both simulated and actual bearing vibration signals was presented. The wavelet shape parameters (damping factor and the center frequency) were optimized by maximizing the kurtosis value for the wavelet transform coefficients vibration signal. The application of this technique for both of the simulated and real bearing vibration signals showed the effectiveness of the wavelet power spectrum in extraction of the bearing characteristic frequencies and its harmonics for outer and inner race defective bearings from noisy vibration signals.

Al-Ghamd & Mba (2006) investigated the relationship between AE RMS amplitude and kurtosis for a range of defect conditions. They processed, interpreted and classified the acquired data from experimental test rig. Then they compared results of vibration analysis and AE over a range of speed and load conditions. AE maximum amplitude and kurtosis has been observed to be more sensitive to the onset and growth of defects than vibration measurements.

Orhan, Aktürk, & Çelik (2006) investigated diagnosis techniques of the ball and cylindrical roller element bearing defects by vibration monitoring and spectral analysis. The vibration of a huge centrifugal pump with nine vanes was monitored. The experimental study had included three different cases. In case 1, the ball bearing has looseness on the housing. The vibration amplitudes were in low level at the initial stage. The vibration monitoring was continued and after a few weeks, they

reported the increase in vibration levels indicating development in the looseness. In case 2, inner bearing vibration of a fan motor, which is supported by cylindrical rolling element bearing was monitored. Existance of multipliers of outer race defect frequency in the spectrum was attributed to an outer race defect. In case 3, outer bearing vibration of the fan motor, which is supported by ball bearing was monitored. Vibration frequencies in the frequency spectrum are matched to the ball bearing outer race defect frequency and its harmonics. In the study, ball bearing looseness, a ball bearing outer race defect and a cylindrical bearing outer race defect were successfully diagnosed. They observed that ball and cylindrical rolling bearing defects were progressed in identical manner without depending on the type of the rolling element.

Tandon, Yadava, & Ramakrishna (2007) studied on the detection and diagnosis of rolling element bearing faults of an induction motor. Experimental investigation was conducted to study the changes in vibration, stator current, acoustic emission and shock pulse levels for bearings in good condition and with simulated varying defects in the outer race of the bearings of an induction motor. They reported that, AE monitoring has proved to be the best technique. AE peak amplitude and shock pulse maximum normalised value level increase much more than other techniques as defect size increases.

Mazanoğlu (2004) presented a study on the detection of a localized defect in a roller bearing using vibration analysis. The real roller bearing that was in both of healthy and faulty conditions was tested under different loads. The acquired vibration signals from experimental set was processed in time, frequency, and combined time and time- frequency domains. In conclusion, the presence of a fault was observed to reveal clearly by time and frequency analyses when severity of fault was large. Frequency peaks that were the results of application of envelope analysis were observed at characteristic frequency of fault component. When the application of combined time- frequency analysis, indications of fault were observed in the combined time- frequency maps as local increases in the energy levels of vibration only where components of bearing came into contact with defect.

Khemili & Chouchane (2005) presented a study on the application of adaptive filtering techniques for detection of rolling element faults. They constituted simulation and experimental test. For computer simulation tests, necessary signals were generated using a computer program written in MATLAB language. For the experimental tests, signals were acquired from two different accelerometers fixed on the defective bearing housing and several point of the mechanism. The adaptive noise cancellation algorithm (ANC) and the adaptive self tuning algorithm (AST) have been tested. They observed that the simulation tests showed the both algorithms were capable of a large reduction of noise. The experimental results showed that the AST filtering effect was more remarkable than that of the ANC filter, since a higher increase of the signal to noise ratio (SNR) have been observed for the AST filter than for the ANC filter. They concluded that, adaptive filtering is a very effective tool for noise reduction and signal to noise ratio amplification.

Sawalhi, Randall, & Endo (2007) presented an algorithm to enhance the surveillance and diagnostic capability of spectral kurtosis (SK) as an analysis tool for rolling element bearing, by combining it with the use of auto regressive (AR) based linear prediction filtering and minimum entropy deconvolution (MED). Signals taken from a high speed test rig were processed via these techniques. Results were given on graphs as raw signal, residual of the AR linear prediction filtered signal and MED filtered signal.

Liu, Ling, & Gribonval (2002) proposed matching pursuit that is a new approach for detection of localized defects of rolling element bearings. Matching pursuit is an adaptive approach of time-frequency analysis unlike short time Fourier transform and Wavelet transform. They used vibration signals which were collected from a test rig for different test configuration such as normal bearing, the bearing with an outer race defect, the bearing with an inner race defect. They processed vibration signals via matching pursuit approach. At the same time, they applied a typical traditional method, envelope detection to detect defects. They observed that matching pursuit approach was more sensitive than envelope detection.

Vyas & Satishkumar (2001) presented an algorithm for a neural network simulator for the prediction of faults in rotating machinery. Artificial neural networks simulate the biological process of human brain and nervous system. The training and test data were generated on an experimental rig for different cases; rotor with no fault, mass unbalance, bearing cap loose, misalignment, both mass unbalance and misalignment. The results reported show that the simulator was found suitable to identify an unknown fault to a good degree of accuracy.

Sawalhi & Randall (2008 Part1) presented a simulation model for a gearbox test rig, in which a range of bearing faults may be implemented. They (2008 Part 2) proposed a time-varying, non-linear stiffness bearing model in order to include into a previously presented gear model. They used spectral kurtosis and envelope analysis. They reported good agreement between the simulated and experimental acceleration signals.

The aim of this study is to detect the rolling element bearing faults via vibration analysis. For this aim, an experimental test rig is designed and produced including double rolling element bearings. Local defects are generated artificially on either inner race or outer race of ball bearings. Tests are performed for varying loads and shaft speeds. Vibration signals are measured by a piezoelectric accelerometer located on the bearing housing. This thesis is organized as fallows. In Section 2, geometry of rolling element bearings and types of the bearing faults are described. In Section 3, experimental setup and vibration measurements are introduced. In Section 4, the statistical indices used in this study are described. In Section 5, the results of the time domain vibration analyses are given. Results of the frequency domain analyses are given in Section 6. The formulation of the curve length transform, the results, the comparison between the statistical indices calculated for raw and transformed vibration signals are given in Section 7. Conclusions are given in Section 8.

CHAPTER TWO
ROLLING ELEMENT BEARINGS AND BEARING FAULTS

2.1 Brief History

Ancient man was forced to push or pull heavy objects long distances just to make basic improvements to his life (Figure 2.1). This effort to move objects was reduced considerably when he discovered simple forms of lubrication such as mud or water.

With the invention of the wheel it became obvious that rolling motion requires less effort and is less damaging to surfaces than sliding motion. It is not surprising therefore, that bearings, using only rolling motion, were eventually developed for use in machines, where metal sliding on metal causes considerable wear.

In fact, the first machine designs used journal (plain) bearings which consisted of steel shafts running in wooden blocks, impregnated with lubricant. Eventually as steel improved and manufacturing techniques improved, two steel rings with rolling elements between, replaced them. First precision stell rolling element was designed by Friedrick Fisher in 1883. This resulted in a bearing with greatly reduced friction and extended service life.
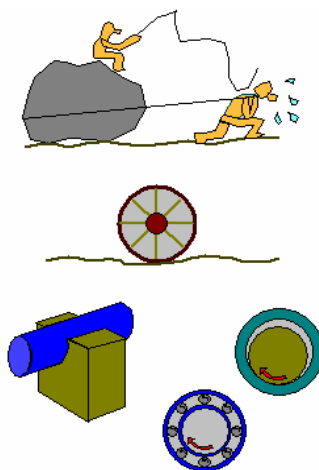
Figure 2.1 History of rolling element bearings (SKF, 1996).

2.2 Bearing Theory

Bearings can basically be categorized as two types, sliding bearings and rolling bearings. Sliding bearings includes linear bearings and journal bearings. Linear bearings are generally used for precise applications by precision engineering industries. Journal bearings can tolerate axial displacement of the shaft within certain limits.

All bearings that transfer loads via rolling elements are denoted rolling bearings. Depending on the type of rolling elements that are used rolling element bearings are divided into ball bearings and roller bearings. The balls in a ball bearing transfer the load over a very small surface point contact (Figure 2.2a) with the raceway. The load carrying capacity is therefore lower than for a roller bearing, where rollers transfer the load via line contact (Figure 2.2b) with the raceways.
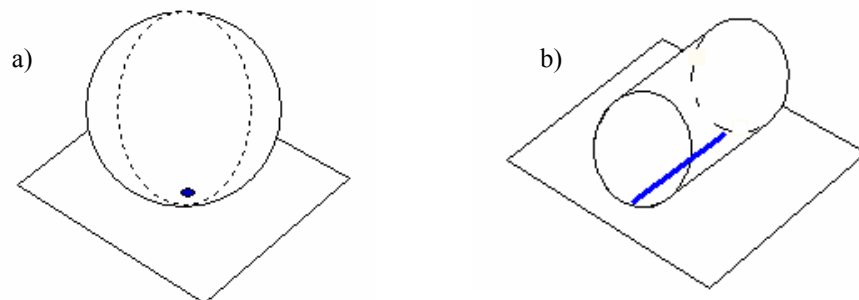
Figure 2.2 Type of contacts a) point contact b) line contact (SKF, 1996).

One of the factors which make the rolling element bearings so popular for most types of machinery is their very low friction. In a plain bearing, the shaft slides in a housing or bushing separated by more or less good lubrication film. In a rolling element bearing the, inner ring rolls via the rolling elements in the outer ring. Under the same load conditions the friction in a plain bearing is greater than that of a rolling bearing. Furthermore, the friction in a plain bearing varies with the rotational speed but is practically constant for a rolling bearing as shown in Figure 2.3.
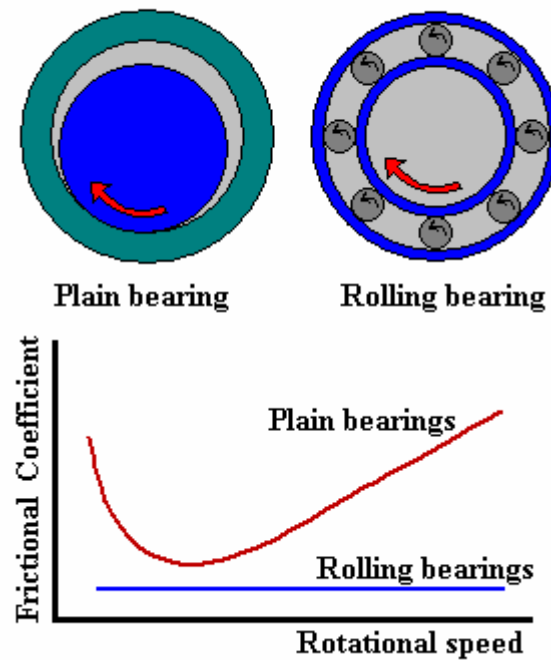
Figure 2.3 Frictional behaviour of plain and rolling
bearings (SKF, 1996).

There are two basic families, that is, ball and roller bearings, which are categorized according to the shape of the rolling elements. Each family includes a variety of bearing designs, depending on requirements such as available space for bearing, magnitude of load, direction of load (radial load, axial load, and combined load), misalignment, speed, precision, quiet running, stiffness, axial displacement, and so on. Ball bearings are usually used in light to moderately loaded applications and are suited for high-speed operations. Roller bearings are able to support heavier loads than ball bearings; therefore, heavy engineering industries use roller bearings. Rolling element bearings can also be classified into radial bearings and thrust bearings based on the direction of applied load. These types of direction-wise bearings are designed to transfer pure radial loads, pure thrust loads, or a combination of the radial and thrust loads. A radial bearing is designed primarily for carrying a radial load, which is a pressing force at right angle to the shaft axis. A thrust bearing is mainly intended to carry a thrust load (also called axial load) that is pushing force against the bearing parallel to the shaft axis. Since most rolling bearings, both radial and thrust bearing, can also carry some radial and axial load, there is no clear distinction between them. However, bearings with a contact angle $\alpha \leq 45°$ (shown in Figure 2.4) are considered radial bearings and their ratings are

given by radial load. Bearings with a contact angle $\alpha > 45°$ are considered thrust bearing and are rated by axial load.

D Outer diameter

d_m Pitch diameter

d Bore diameter

d_b Ball diameter
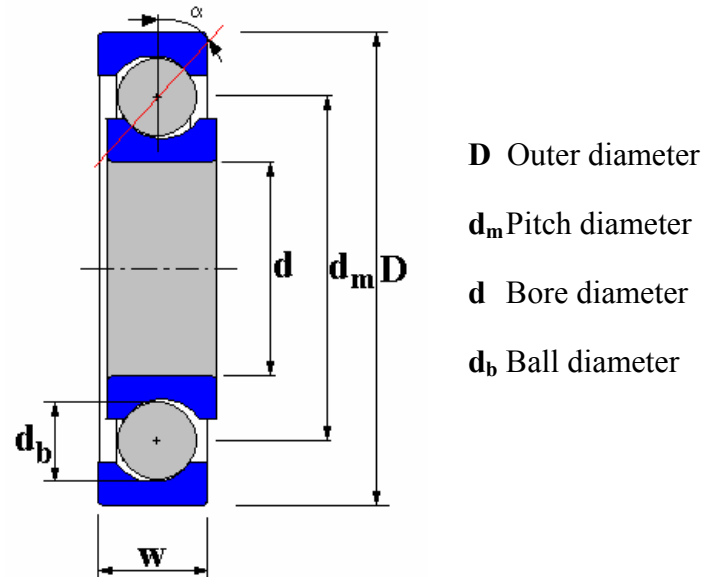
Figure 2.4 Bearing geometry.

2.3 Bearing Components

All rolling bearings are composed of four basic parts: inner ring, outer ring, rolling elements, and cage or separator as seen in Figure 2.5. Some bearings have additional components; the guide ring and seals are used only in some special bearings.
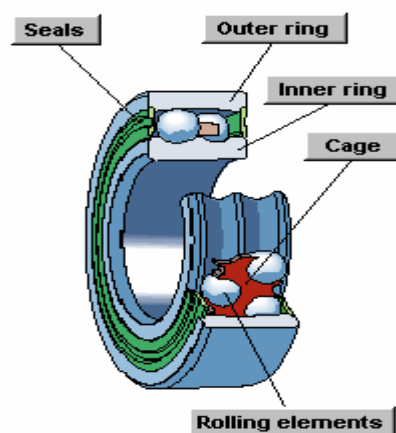
Figure 2.5 Components of the rolling

bearing (SKF, 1996).

2.3.1 Inner Ring

The inner ring is mounted on the shaft of the machine and is in most cases the rotating part. The bore can be cylindirical or tapered. The raceways against which the rolling elements run have different forms such as spherical, cylindirical or tapered, depending on the type of rolling elements.

2.3.2 Outer Ring

The outer ring is mounted in the housing of the machine and in most cases it does not rotate. The raceways against which the rolling elements run have different forms depending on the type of rolling elements. The forms of the raceways may be spherical, sylindirical or tapered.

2.3.3 Rolling Elements

The rolling elements may have different forms as shown in Figure 2.6. The forms of the rolling elements may be balls, cylindirical rollers, spherical rollers, tapered rollers or needle rollers. They rotate against the inner and outer ring raceways and transmit the load acting on the bearing via small surface contacts separated by a thin lubricating film. The rolling elements are made of carbon chromium steel, also called bearing steel.
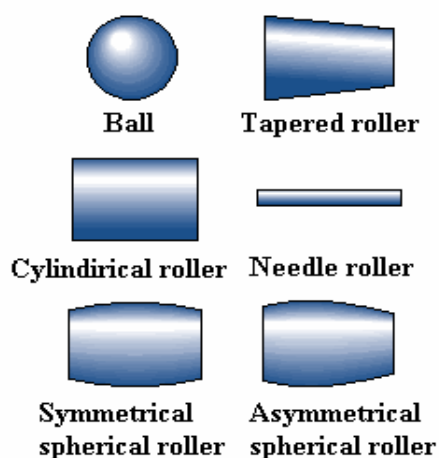
Figure 2.6 Types of rolling elements (SKF, 1996).

2.3.4 Cage

The cage separates the rolling elements to prevent metal-to-metal contact between them during operation that would cause poor lubrication conditions. With many bearing types the cage holds the bearing together during handling. Cages are made from cold rolled steel strip.

2.3.5 Seals

Seals are essential for a long and reliable life of the bearing. They protect the bearing from contamination and keep the lubricant inside the bearings.

2.3.6 Guide Ring

Guide rings are used in some spherical roller bearings that demand extremely high quality. The main function of the guide rings is to guide the rollers in the bearings so that they can rotate parallel to the shaft and distribute the load evenly to the raceways.

2.4 Types of the Bearing Failures and the Causes

Rolling element bearings are among the most important and popular components in the vast majority of machines. Additionally, the component most likely to cause machine downtime is the bearing, because all machine forces are transmitted through the bearings. Therefore, rolling element bearings have been the subject of extensive research over the years to improve their reliability. However, since a large number of bearings are associated with any critical process, system failure due to any individual bearing failing can occur in a short period of time. There are many reasons for early failure, such as heavy loading, inadequate lubrication, careless handling, ineffective sealing, or insufficient internal bearing clearance due to tight fits. Each of these factors results in its own particular type of damage and leaves its own special imprint on the bearing.

Rolling bearing damage may result in a complete failure of the rolling bearing at least, however, in a reduction in operating efficiency of the bearing arrangement. Only if operating and environmental conditions as well as the details of the bearing arrangement (bearing surrounding parts, lubrication, sealing) are completely in tune, can the bearing arrangement operate efficiently. Bearing damage does not always originate from the bearing alone. Damage due to bearing defects in material or workmanship are exceptional.

The types of mechanical bearing failure and their frequencies are categorized in Table 2.1. The most frequent bearing failure category is corrosion, which is lubrication related. Chemical reaction occurs between the oil and the surface of the bearing, generally from water or other corrosive materials present in the oil. Dimensional discrepancies of rolling element bearings are a consequence of damage prior to or during service. The causes of dimensional discrepancies could be manufacturing flaws, improper handling or installation, and severe overloading during service. Foreign objects, carried by contaminated lubricant, are trapped inside the bearing between the rolling element and the raceway, and are overloaded. Understanding the underlying reason for the defects and their consequences in terms of failures gives the diagnostic clues to detect early failures.

Table 2.1. The distribution of the bearing failure (Lee, 2000)

Reason	Failure percent
Corrosion	35 %
Dimensional Discrepancies	29 %
Foreign Objects	24 %
Other	10 %
Fatigue	2 %

Bearing failures that are not responsible for material fatigue are generally classified as premature. Typical reasons for rolling bearing damage (FAG, 1985):

Inexpert mounting:

- incorrect mounting method, wrong tools
- contamination
- too tight fit
- too loose fit
- misalignment

Abnormal conditions during operation:

- overload, absence of load
- vibrations
- excessive speeds

Unfavorable environmental influences:

- external heat
- dust, dirt
- passage of electric current
- humidity
- aggressive media

Inadequate lubrication:

- unsuitable lubricant
- lack of lubricant
- overlubrication

Each of the different causes of bearing failure generates its own characteristic damage. Such damage is also known as primary damage, which, in turn, creates

secondary, failure-inducing damages, such as spalling and cracks. Most failed bearings frequently display a combination of primary and secondary damage. The types of damage are summarized in Table 2.2 (Afshari, 1998).

Table 2.2 Types of bearing damages (Afshari, 1998).

| | | DAMAGE TYPE | |
	Primary Damages	Secondary Damages	Other Damages
DAMAGE CASES	Indentations	Spalling	Roll out
	Corrosion	Cracks	
	Wear	Cage damage	
	Electric current damage	Score marks	
	Surface distress		

2.4.1 Rolling Element Indentations

Raceways and rolling elements may became dented if the mounting pressure is applied to the wrong ring so that it passes through the rolling elements, or if the bearing is exposed to overloading while stationary. Foreign particles in the bearing also cause indentation.

Indentation caused by faulty mounting or overload is called as true brinelling. This defect is characterized by indentations at intervals corresponding to the roller spacing in the raceways of both the inner and outer rings as shown in Figure 2.7. These indentations in the raceways can increase bearing noise and vibration, leading to premature bearing failure. Common causes for this type of failure are mounting pressure applied to the wrong ring, excessively hard drive-up on tapered seating, and

overloading while stationary. It also occurs when a sharp impact is incorrectly applied to a bearing during mounting or dismounting.

Figure 2.7 Indentation of soft particles (FAG, 1985).

Indentation due to foreign particles is called contamination failure and is one of the leading causes of premature bearing failure. The signature for this defect is small indentations distributed around the rolling elements and the raceways of both the inner and outer rings. Foreign particles, such as airborne dust, dirt or any abrasive materials enter into the bearing and cause indentations when rolled into the raceways by the rolling elements. Indentation caused by larger metal chips or particles of dirt is identified as pitting and bruising. The depth and the number of the indentations caused by these larger particles determine whether the bearing must be replaced.

Figure 2.8 Indentation due to hard particles (FAG, 1985).

Figure 2.9 Indentation of brittle particles (FAG, 1985).

2.4.2 Corrosion Damage

2.4.2.1 Corrosion due to humidity (Rust)

Rust will form if water or corrosive materials enter into the bearing so that the lubricant cannot provide protection for the steel surfaces of the bearing elements. This process will soon lead to deep-seated rust. Corrosion generally results in increases in vibration, fallowed by wear, with subsequent increases in radial clearance or loss of preload.

2.4.2.2 Deep-seated rust

Water, moisture, or corrosive substances in the bearing over a long period of time cause deep-seated rust (Figure 2.10). Grayish black streaks across the raceways coinciding with the rolling element spacing appear. At a later stage, deep-seated rust of raceways and other surfaces of the bearing take place. The deep-seated rust is known as pits, and when the pits occur, the bearing should be discarded because the pitting is a serious defect and will develop into premature spalling.

Figure 2.10 Corrosion due to rust
(FAG, 1985).

2.4.2.3 Aggressive Media

Severe fissured surfaces are caused by the attack of aggressive media. The etching pits are generally of a black discoloration.
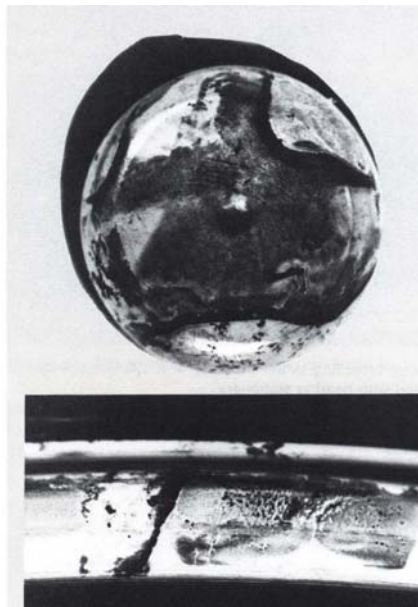
Figure 2.11 Corrosion due to
aggressive media (FAG, 1985).

2.4.2.4 Fretting Corrosion

Fretting corrosion is also called a loose fit failure, fretting corrosion takes place when there is relative movement between bearing ring and shaft or housing, due to loose fit (Figure 2.12). As a consequence of the fretting corrosion, the bearing rings may not be evenly supported and this produces an undesired effect on the load distribution in the bearings. With fretting corrosion, rust appears on the outside of the outer ring or in the bore of the inner ring. The raceway path pattern is heavily marked at corresponding positions.

Figure 2.12 Fretting corrosion (FAG, 1985).

2.4.3 Vibration with Bearing Stationary

This type of failure occurs because of the vibrations of stationary machines in the areas of the components in rolling contact. Compared with the marks caused by incorrect mounting there are no raised edges.
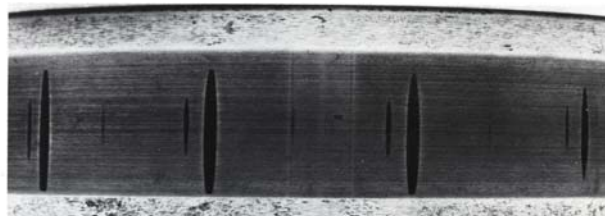
Figure 2.13 Vibration with bearing stationary (FAG, 1985).

2.4.4 Craters and Fluting due to Passage of Electric Current

When electric current passes from one ring to the other through the rolling elements in a rotating or non-rotating bearing, damage will occur. The process is similar to electric arc welding at the contact surfaces. This may cause a single burn or appear as a line of small burns, called fluting, along the line of contact between the rollers and the race (Figure 2.14 and Figure 2.15). Dark brown or grayish black fluting or craters appear in raceways and rollers, while localized burns appear in raceways and rolling elements. Balls have dark discoloration only. This type of damage is frequently seen in electric motors, but can be eliminated by ceramic coating on the outside surface of the outer ring.

Figure 2.14 Fluting in the outer ring raceway of a deep groove ball bearing (FAG, 1985).

Figure 2.15 Craters due to arching in a cylindrical roller bearing (FAG, 1985).

2.4.5 Wear Damage

In normal cases, there is no noticeable wear in rolling element bearings. However wear results when foreign objects enter into the bearing or when the lubrication is inadequate.

Foreign materials can enter the bearing during cleaning or through a damaged or worn seal. These result in premature wear of the bearing. If the wear is mild, involving only very light surface bruising or denting, the bearings may be reused after the housing and bearings thoroughly cleaned and properly adjusted. Bearings with excessive wear from foreign material should be replaced. Fine dust, metal particles, grinding dust, or normal airborne dirt that is common in a factory environment causes abrasive wear.

Inefficient load carrying lubricant film can also cause wear in rolling bearings. Lubricant that has gradually been used up or has lost its lubricating property causes this type of wear, overheating, and subsequent bearing failure. Generally, wear marks are first noticeable on the rolling element surfaces.
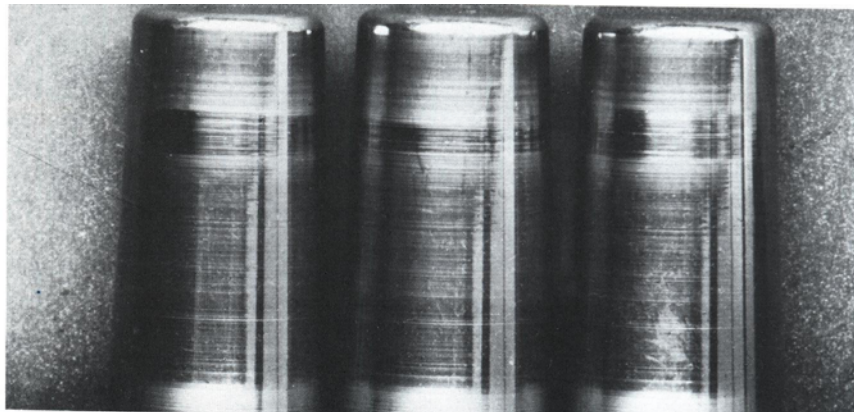
Figure 2.16 Wear damage (FAG, 1985).

2.4.6 Seizure under High Load

The components in rolling contact are welded, metal particles are torn away and applied to the apposite surface because of the insufficient lubrication and high loads. Too high preload of the bearing arrangement also causes the seizure as shown in Figure 2.17.
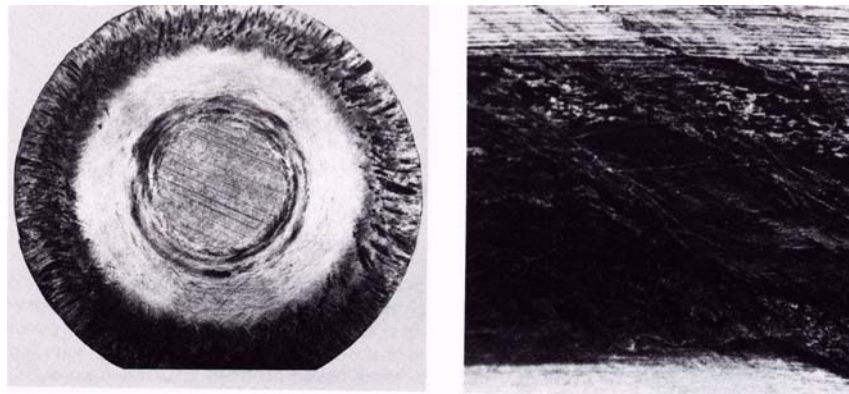
Figure 2.17 Seizure (FAG, 1985).

2.4.7 Skidding Damage

The rolling elements slide on the raceway in the case of low bearing loads and in the case of starved lubrication. Preloading and improvement of the lubrication can be a remedy for this case.

Figure 2.18 Skidding damage (FAG, 1985).

2.4.8 Fatigue Damage

Damage due to classical fatigue with cracks starting below the surface seldom occurs. In a much greater number of cases fatigue damage starts at the surface of the components in rolling contact due to inadequate lubrication or cleanliness deficiencies. In cases of advanced damage, the causes may no longer be recognizable.

2.4.8.1 Classical Fatigue

Dynamic stresses cause the fatigue in the rolling bearings. The existence of the non-load carrying film accelerates the fatigue. Classical fatigue can be recognized by pitting in the raceway of a deep grove ball bearing inner ring as shown in Figure 2.19. The bright, slightly shining track is an indication of a favourable separating lubricating film. Subsequent damage propagation results in material flaking occuring over the entire raceway.
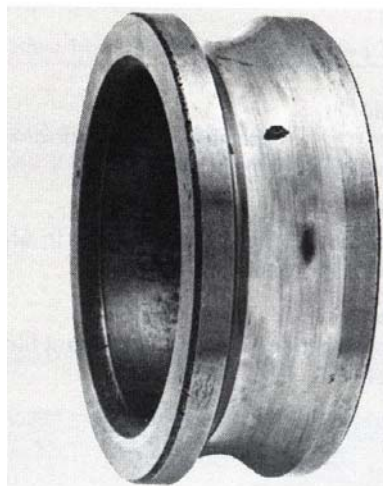
Figure 2.19 Classical fatigue (FAG, 1985).
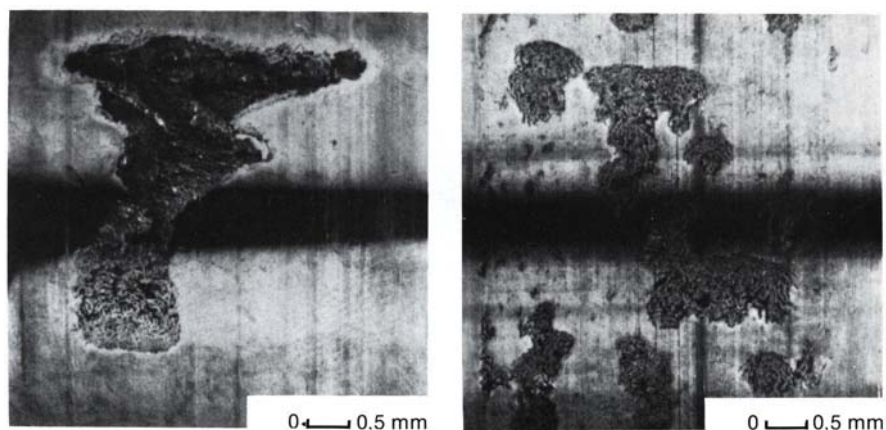
Figure 2.20 Large-area superficial flaking due to non load-carrying film (FAG, 1985).

If the lubricant film between raceways and rolling elements becomes too thin owing to inadequate or improper lubrication, the peaks of surface asperities will momentarily come into contact with each other. Small cracks then form in the surfaces and this is known as surface distress. Indentations of the hard particles also results in surface distress and consequently fatigue. Widening in the surface cracks occurs in the direction of cycling.
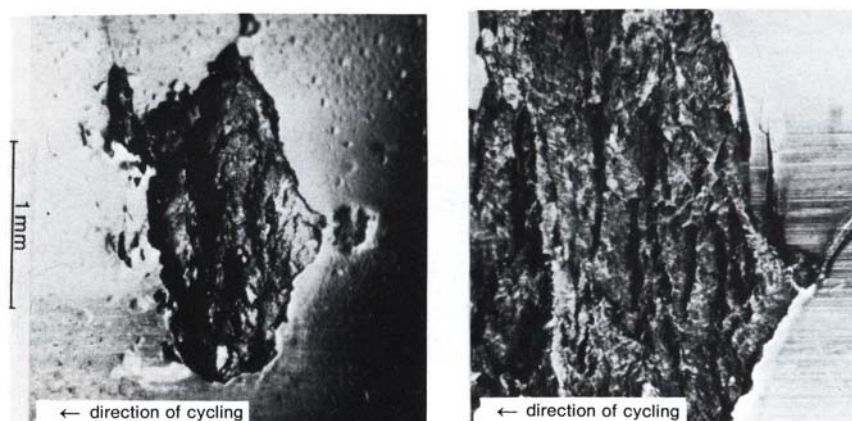
Figure 2.21 Fatigue damage due to particle indentation (FAG, 1985).

Another reason for fatigue is the local overloading. Contact ellipse "cut off" by the raceway boundary of a ball bearing shown in Figure 2.22 illustrates this situation.
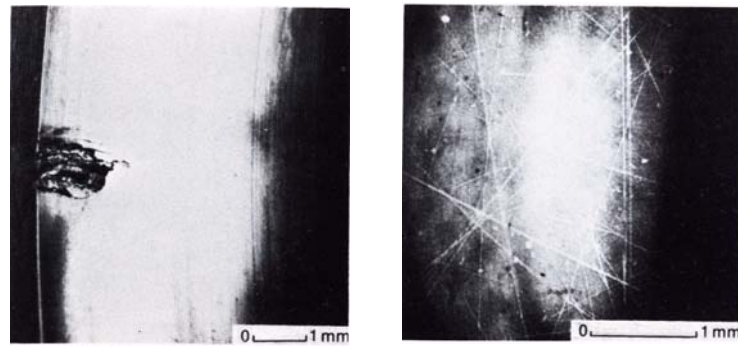
Figure 2.22 Fatigue at the track edge due to overloading (FAG, 1985).

Misalignment of the bearing rings in misaligned housing bores or at out-of-square abutment surfaces and excessive shaft deflections can also cause fatigue. If misaligned bearing is a ball bearing, the track of stationary ring is formed diagonally to the axial direction as shown in Figures 2.23c and 2.23d. On the other hand, tracks are more distinct on one edge of the raceway when cylindrical roller bearing is used as shown in Figures 2.23 (a and b). Misalignment is an inevitable result in bearing if a bended shaft or misaligned housing seat is used (Mazanoğlu, 2004).
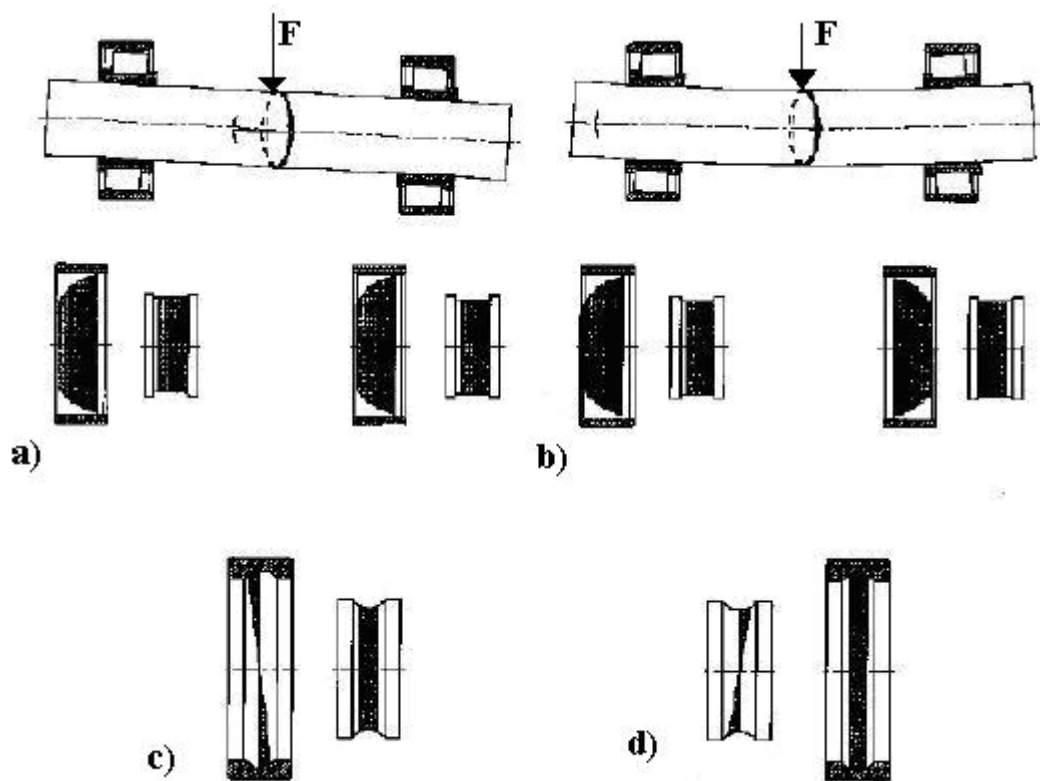
Figure 2.23 A bend shaft and misaligned housing seat and effects on rings are showed (Mazaoğlu, 2004).

2.4.9 Damage Due to Overheating

In case of insufficient clearance under operating conditions, especially of high speed bearings and overlubrication or starved lubrication the rollers leave deep impressions in the raceway due to overheat.
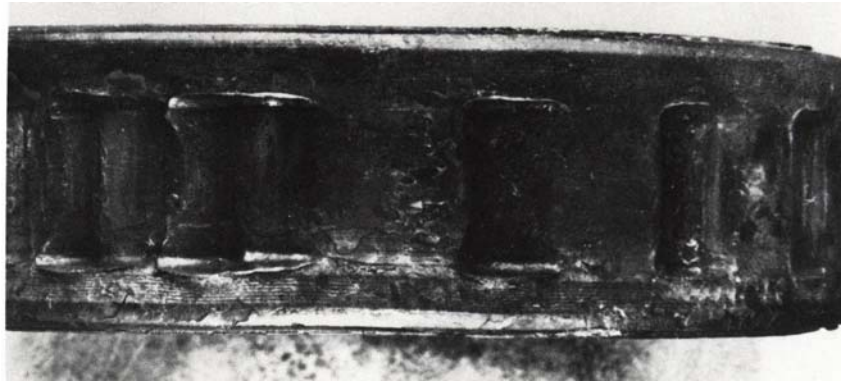
Figure 2.25 Damage due to overheating (FAG 1985).

2.4.10 Score Marks

Score marks on the raceway of a cylindrical roller bearing inner ring is caused by out-of-square insertion into rolling element set.

Figure 2.26 Score marks (FAG, 1985).

2.4.11 Cage Damage

Cage breakage does not happen often, but, when it does occur, it is often difficult to find the cause of the failure since other components of the bearing are damaged too. However, there are certain causes for cage failure, such as vibration, excessive speed, wear, misalignment and blockage.

When a bearing is exposed to vibration, the vibration forces cause fatigue cracks to form in the cage material. Sooner or later these cracks lead to cage fracture.

Figure 2.27 Cage fracture due to vibration (FAG, 1985).

Misalignment of the rings relative to each other leads to detrimentally high forces between balls and cage causing crosspiece fracture.

Figure 2.28 Cage fracture due to misalignment (FAG, 1985).

If the bearing is run at speed in excess of the cage specification, the cage is subjected to heavy inertial forces that may lead to fractures. The cage is always made

of softer material than the other components of the bearing and consequently it wears comparatively quickly because of the sliding in the contacts between the cage and the other components of the bearing. Fragments of flaked material or other hard particles may become wedged between the cage and a rolling element. When this happens, the rolling element is kept from rotating with respect to its own axis, leading to cage fracture.

2.4.12 Roll Out

Roll out is also called as sub-case yielding or case crushing. This type of damage exhibits circumferential cracks in the load zone. When a bearing is highly overloaded, the stress is exerted deep into the race. If the race has had hardened treatment, the stress may then exceed the strength of the relatively soft core. In this case, the core of the race will plastically deform in the axial direction since it is constrained in the radial direction by the housing. As the core expands axially, it carries the case with it causing the case to fracture circumferentially.

2.5 Types of Bearing Load

In the analysis of rolling element bearings, knowledge of the internal load distribution between the rolling elements can be essential. The sector of the raceway circumference of the stationary bearing ring which is loaded varies according to the direction of the loads acting on the bearing. This sector or circumferential contact area on the ring is called "load (or loaded) zone". Different external load conditions can give rise to loaded zones from 0 to 360 degrees. In deep grove ball bearings with pure radial load and a residual clearance in the bearing the load zone will be less than 180 degree (Figure 2.29a). If there is no internal clearance then one half of the circumference is loaded and there is a 180 degree loaded zone (Figure 2.29b). Under pure centrally acting axial load the whole circumference is equally loaded and the load zone extends over 360 degree (Figure 2.29c). Figures 2.29d and 2.29e illustrate the effect of the combined radial and axial loads.
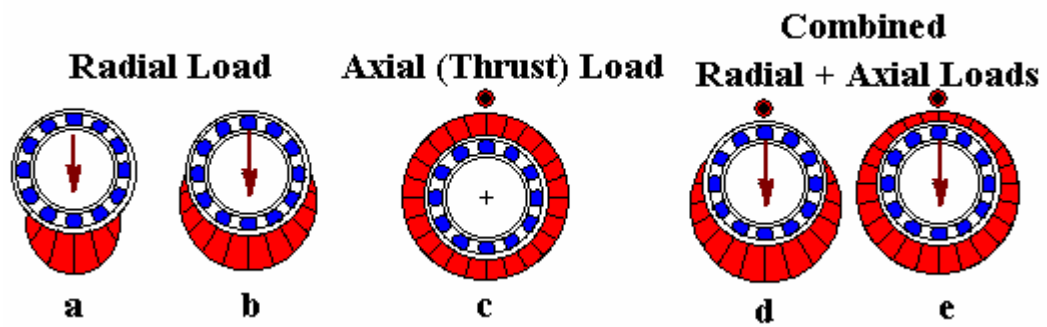
Figure 2.29 Types of the bearing load.

In the scope of this study, deep groove ball bearings having contact angle $\alpha=0°$ are considered and hence loading is assumed to be purely radial. The outer ring is assumed to be fixed in the housing and the inner ring mounted tightly on the shaft and rotates with the shaft frequency f_s. Generally, the form of the bearing load encountered in engineering applications can be:

a)   constant direction-constant magnitude
b)   varying direction-constant magnitude
c)   varying direction-varying magnitude

2.5.1 Constant Direction-Constant Magnitude Bearing Load

This type of bearing load is encountered in many applications such as transmission of the power via gear couples or belt-pulley systems as illustrated in Figure 2.30a. The direction of the bearing load is determined by the meshing position of the gear couples or configuration of the belt-pulley system. The magnitude of the bearing load is constant. Only a certain portion of the bearing structure is loaded and the radial load transmitted to the bearing structure through the rolling elements within the load zone. The loading of the rolling elements is periodic in nature.

2.5.2 Varying Direction-Constant Magnitude Bearing Load

This type of bearing loads is encountered in rotating shafts having an unbalanced mass on it as illustrated in Figure 2.30b. The direction of the bearing force changes as shaft rotates because the unbalanced mass rotates with shaft. The magnitude of the bearing force is proportional to the square of the angular speed of the shaft. Whole circumference of the bearing structure is loaded during operation because the radial load rotates with shaft. The rolling elements within the load zone transmit the load to the structure. A care must be paid to determine the rolling elements which play the role in force transmission because the position of the load zone varies. The loading of the rolling elements is non-periodic.

2.5.3 Varying Direction-Varying Magnitude Bearing Load

This type of bearing load is encountered in revolute joints of mechanisms as illustrated in Figure 2.30c. The direction and magnitude of the bearing force are determined by the dynamic considerations and vary as shaft rotates. The load zone is not attached to the shaft and has a slight or strong difference from the shaft rotation. The movement of the load zone may be an oscillation or may be a full rotation. A care must be paid because both the direction and the magnitude of the bearing force alter with per shaft rotation. The loading of the rolling elements is non-periodic.

The first type loading "constant direction-constant magnitude", which is the simplest form of the bearing loading, is considered in the studies related with the rolling element bearings (Kıral, 2002).
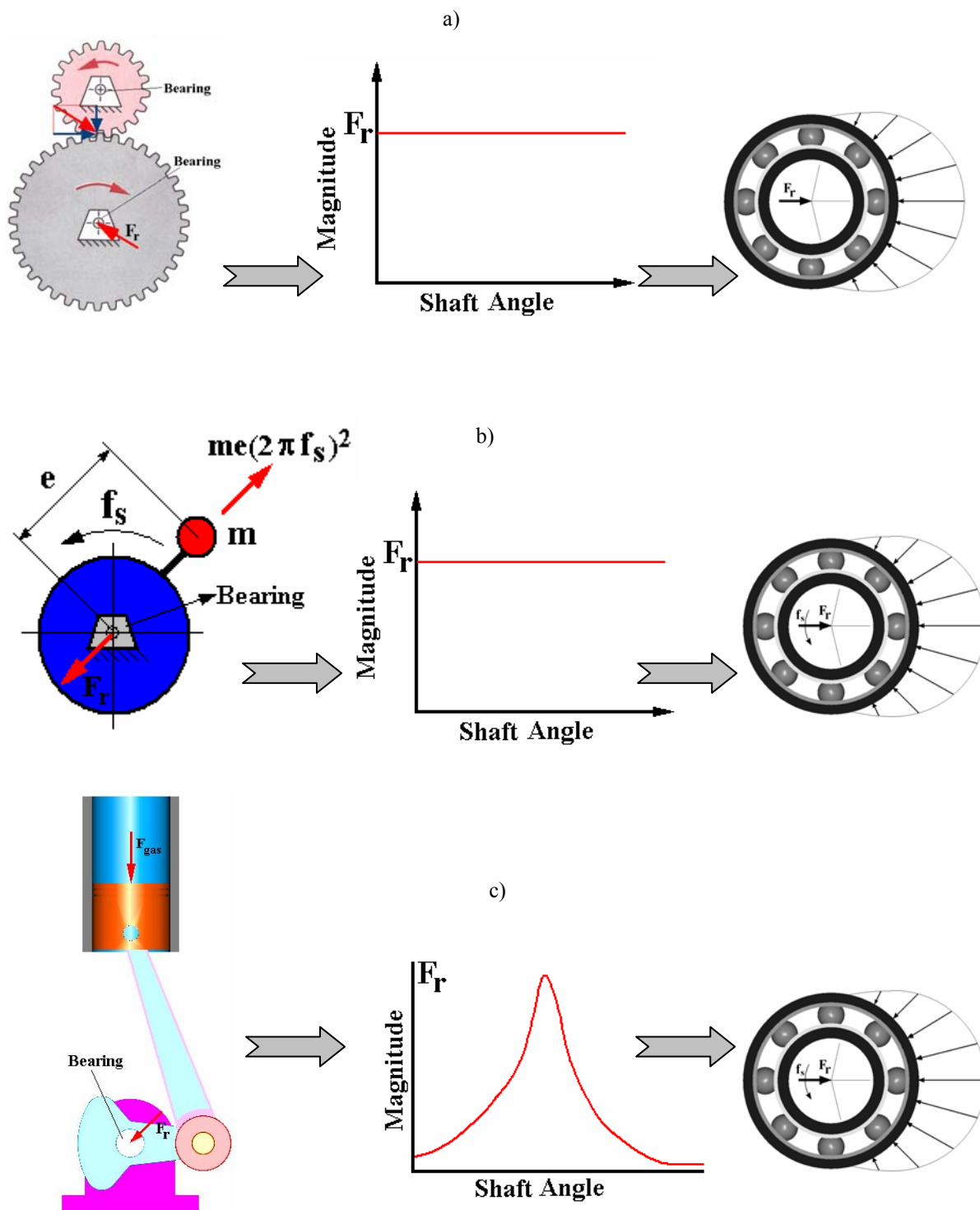
Figure 2.30 Types of bearing loads.

CHAPTER THREE
EXPERIMENTAL SETUP

3.1 Test Rig

The test rig used in the present research work is designed and manufactured as a double-bearing system. In this study, the test bearings are choosen as deep groove ball bearings of the type ORS 6205 (Orta Doğu Rulman Sanayi [ORS], 1995). Defects are introduced as simulated on either inner race or outer race of ball bearings. Disassembly and assembly of the bearing are accomplished with minimum distruption. Rolling element bearings are mounted on both side of the shaft. The faulty bearing is mounted at the front side while the healthy bearing is mounted on the rear side of the shaft. A closed enclosure was established by attaching cover plates to both sides and the top of the enclosure. The front side of the shaft at which the faulty bearing is mounted, is extended in order to attach a pulley for driving the shaft by an electrical motor with a V-shaped belt. The motor provided by AC power supply is monophase. Power of the motor is 0.55 kW. The speed of the motor is controlled by a speed controller. A piezoelectric type of accelerometer is mounted on the housing for vibration measurement. All of the components are put on a heavy plate. Rubber foots are mounted under the plate in order to reduce the vibration transmission from ground to test bearing. Two different unbalance masses are used to measure vibrations under different loading conditions. Schematic view of the experimental set-up is given in Figure 3.1. The real view of experimental set up is shown in Figure 3.2.

3.2 Instrumentation

In this thesis, vibration measurements are performed by a portable vibration meter, Sendig 911 (2007) as shown in Figure 3.2. The portable device has a piezoelectric accelerometer of the type L14A. The accelerometer sensitivity is 4.86 [pC/ms^{-2}] at 20 ^{0}C. The device can measure vibration signals in terms of acceleration, velocity and displacement and can save these signals into its memory. These signals can be fetched from the device memory to the computer by RS-232 connection.

Sendig 911 has its own data acquisition software which is called as MCME2.0H. A sample screen shot of the software is given in Figure 3.3. The vibration signals gathered via the vibration meter can be processed in both time and frequency domains. The sampling frequency of the vibration measurement is 2560 Hz and the total duration of measurement is 0.39 seconds.
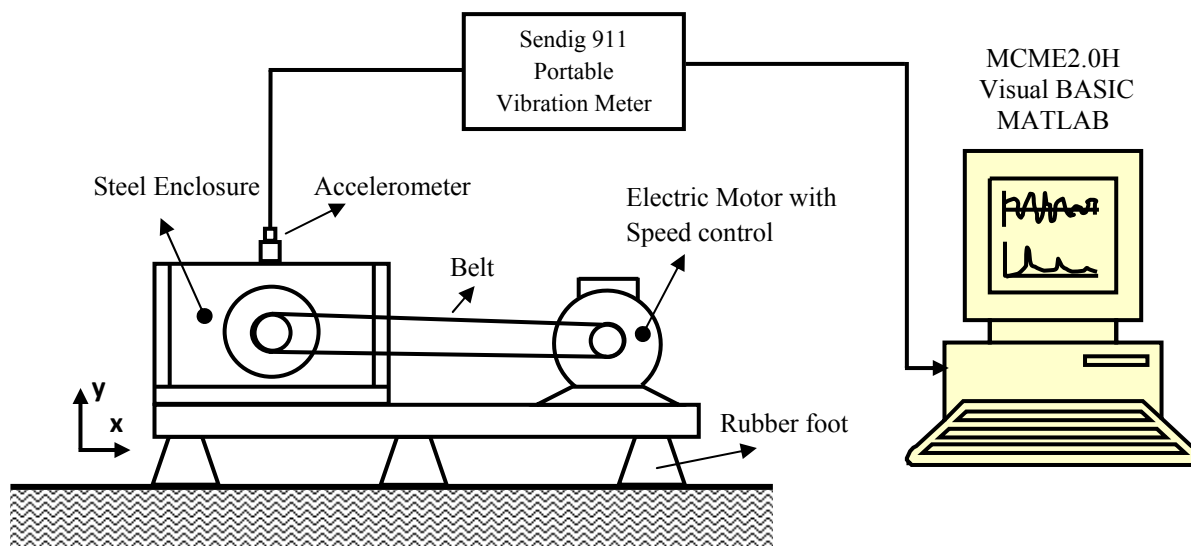
Figure 3.1 Schematic view of the experimental set-up.
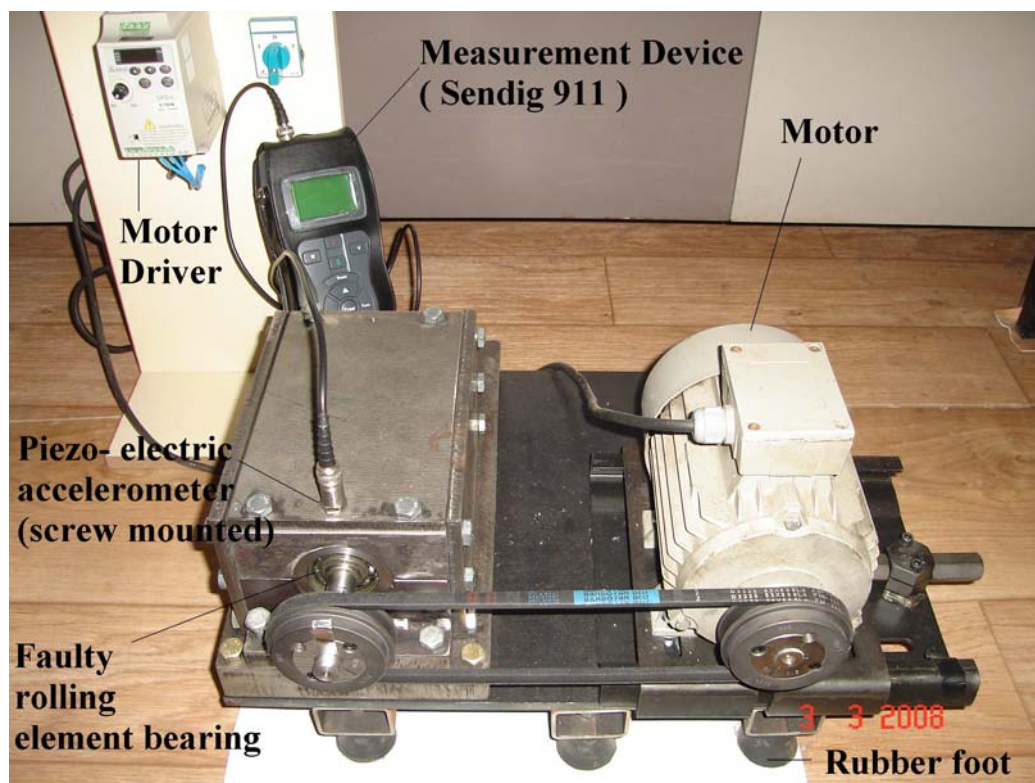
Figure 3.2 View of the experimental setup.
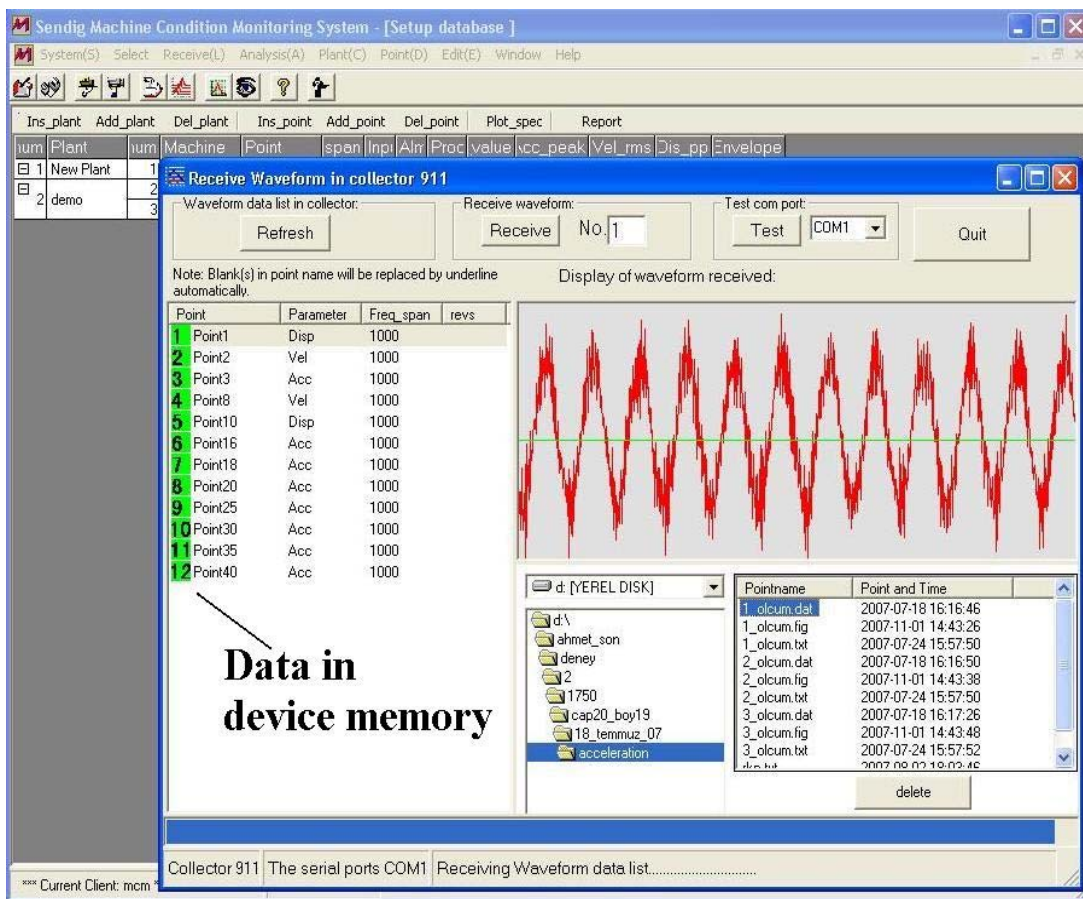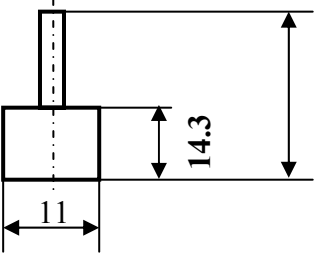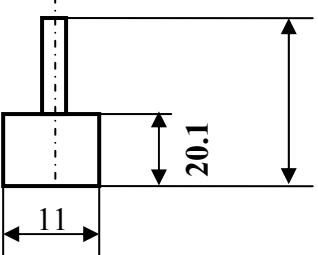
Figure 3.3 Screen shot of the software.

3.3 Measurement Conditions

Vibration signals are measured under various loading conditions: no load (no unbalance) and two different unbalance masses, 0 gram (L0), 16.52 gram (L1) and 20.90 gram (L2). The dimensions and weights of the unbalance masses are given in Table 3.1. The mass L2 is mounted to the beam is shown in Figure 3.4. The speed of the shaft is changed from 750 rpm to 2000 rpm by 250 rpm increment after each measurement. Outer or inner race defect is simulated as circular hole by means of a drilling machine. The view of the simulated defect is shown in Figure 3.5. One of the healthy rolling element bearing was disassembled and then assembled. Vibration signals taken from this bearing are used as reference while examining the signals obtained from faulty bearings.

Table 3.1 The dimensions and weights of the unbalance loads

Load	Dimensions (mm)	Weight (gram)
L1		**16.52**
L2		**20.90**
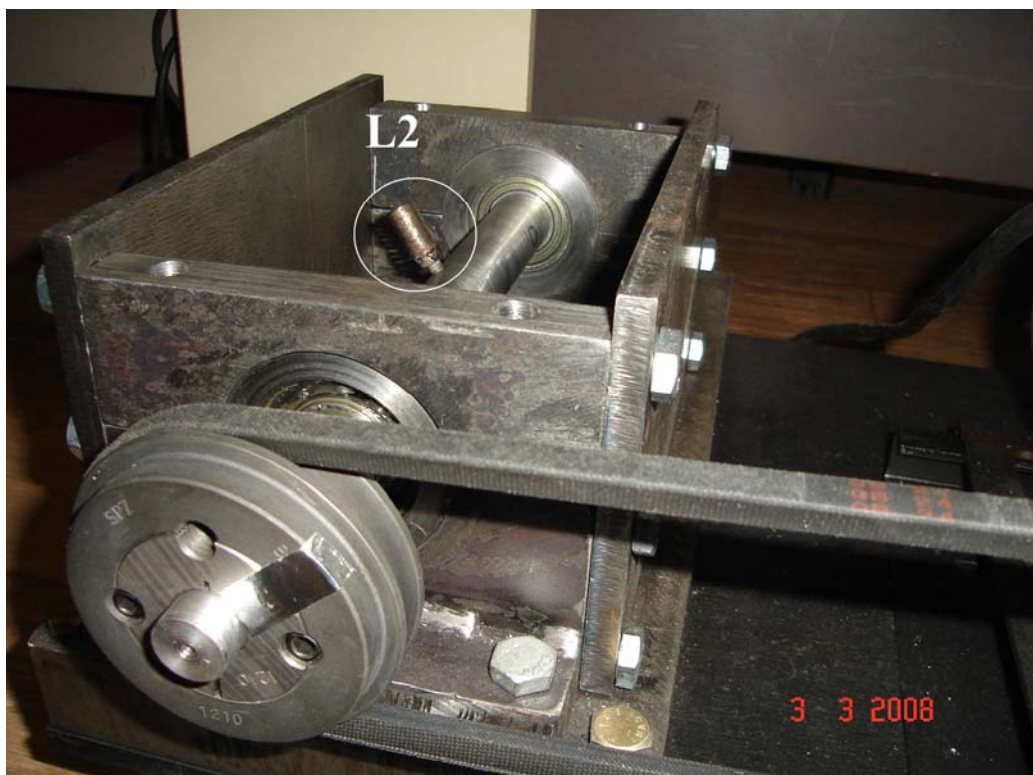
Figure 3.4 Unbalance mass L2 mounted on the shaft.
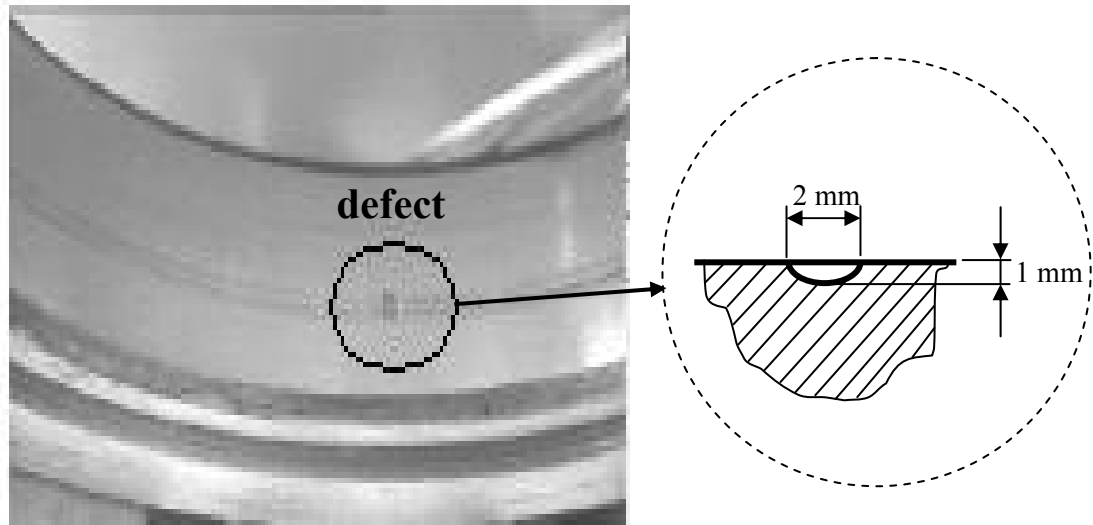
Figure 3.5. Simulated defect and its approximate dimensions.

CHAPTER FOUR
TIME DOMAIN PARAMETERS

In this study, different statistical indices derived from the experimental vibration signals are used to identify the condition of the rolling element bearing. Different moments of the vibration signals from faulty bearing are calculated and then compared with the reference values obtained for healthy bearing. The statistical indices used in the time domain analyses are described in this section.

4.1 Mean

The mean value is the arithmetic mean of the vibration signal. The mean value of a discrete time signal x having N samples is calculated (Neter, Wasserman, & Whitmore, 1988) as

$$\bar{x} = \frac{1}{N}\sum_{i=1}^{N} x_i \tag{4.1}$$

Generally, the mean value does not give useful knowledge about a widely distributed signal.

4.2 Standart Deviation (σ)

Standart deviation gives useful knowledge about a widely distributed signal. If the values of signal are close to the mean, standart deviation is low, otherwise standart deviation is high. It is equal to square root of variance (Heperkan, Kesgin, trans, 2002). The standart deviation of a signal x is calculated as,

$$\sigma = \sqrt{\frac{1}{N-1}\sum_{i=1}^{N}(\bar{x} - x_i)^2} \tag{4.2}$$

4.3 Peak to Peak (p2p)

Peak to peak is another statistical indices. Peak to peak is denoted as the difference between the maximum value and the minimum value of the signal. It is given as

$$p2p = x_{max} - x_{min} \tag{4.3}$$

4.4 Root Mean Square (rms)

The root mean square (rms) value of a vibration signal shows the energy content of the signal (Miettinen, Leinonen, 1999). For a vibration signal the rms value is calculated as

$$RMS = \sqrt{\frac{1}{N} \sum_{i=1}^{N} x_i^2} \tag{4.4}$$

4.5 Skewness

The 3rd standardized moment of the vibration signal is called as the skewness. Its value indicates the asymmetry of a distribution around its mean. Positive skewness denotes a distribution with an asymmetric tail extending toward more positive values. In consideration of negative skewness, a distribution with an asymmetric tail extending toward more negative values is observed. This situtation is shown in Figure 4.1. A symmetrical distribution is observed when skewness value is zero (Miettinen, Leinonen, 1999). The skewness value of a vibration signal is calculated as

$$skewness = \frac{1}{N\sigma^3} \sum_{i=1}^{N} (x_i - \bar{x})^3 \tag{4.5}$$

4.6 Kurtosis

The 4th standardized moment is named as kurtosis. Kurtosis indicates peakeness or flatness of a distribution compared with the normal distribution. Positive kurtosis denotes a relatively peaked distribution. Negative kurtosis denotes a relatively flat distribution. This situtation is illustrated in Figure 4.1. The kurtosis value of a vibration signal is calculated (Neter, Wasserman, & Whitmore, 1988) as

$$kurtosis = \frac{1}{N\sigma^4} \sum_{i=1}^{N} (x_i - \bar{x})^4 \tag{4.6}$$
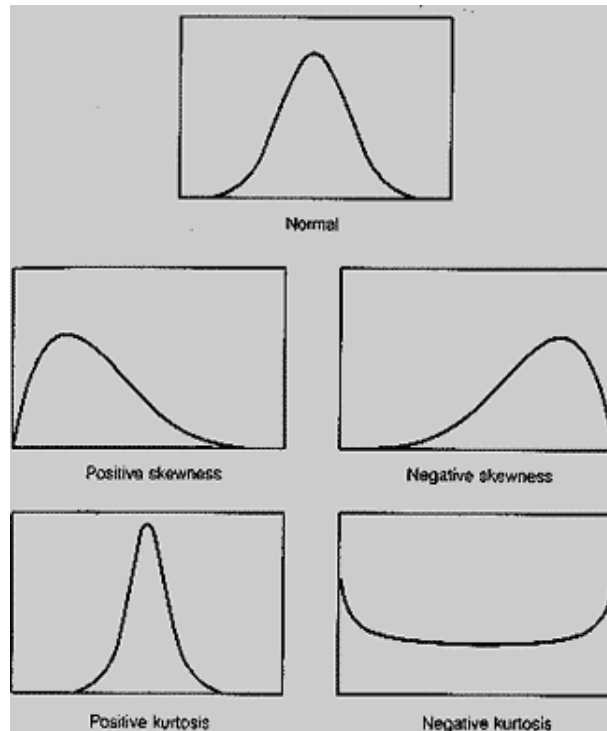
Figure 4.1   The shape of the skewness and kurtosis. (Normality, n.d.).

4.7 5ᵗʰ Standardized Moment

This statistical indice is calculated as

$$5^{\text{th}} \text{ moment} = \frac{1}{N\sigma^5} \sum_{i=1}^{N} (x_i - \bar{x})^5 \qquad (4.7)$$

4.8 Crest factor (cf)

The maximum peak amplitude of a vibration waveform divided by rms value determines the crest factor (Friedman, n.d.). Crest factor value is expected to be between 2 and 6 in healty situtation. This value increases when a fault appears (Lebold, McClintic, Campbell, Byington, & Maynard, 2000). Crest factor value is given by the following equation

$$cf = \frac{x_{max} - x_{min}}{rms(x)} \qquad (4.8)$$

CHAPTER FIVE

TIME DOMAIN ANALYSES

In this section rms, kurtosis and peak to peak (p2p) values of raw displacement, velocity and acceleration signals are examined under different load cases at various shaft speeds ranging from 750 rpm to 2000 rpm.

5.1 Sample Vibration Patterns

Vibration signals measured for healthy and faulty bearings at 1000 rpm under L0 and L2 load cases are given between Figure 5.1 and Figure 5.6 in order to show the sample vibration patterns collected from the test rig.

Comparison of Figure 5.1 and Figure 5.2 shows that the vibration levels increase in the case of L2 unbalance load. The increase in the vibration levels is the basic sign of unbalance. The sign of the unbalance in rotating shafts can also be seen in the frequency spectrum as increase in the spectrum amplitudes at shaft rotation frequency. This is discussed in the following section.

Figure 5.3 illustrates the vibration responses for inner race defect case at 1000 rpm under L0 load. Figure 5.4 shows the same responses under L2 load case. As seen from the figures that the vibration amplitudes increase in the case of bearing inner race defect as the unbalance increases. The vibration patterns also change considerably, but there is no distinct sign showing the inner race defect.

Figure 5.5 and Figure 5.6 show the vibration responses for outer race defect case at 1000 rpm under L0 and L2 loads, respectively. The vibration amplitudes increase by introducing unbalance, but it is not possible to see the outer race defect in the vibration time history at a first glance. Some statistical indices are used to derive useful information from the vibration responses to detect the bearing failures.
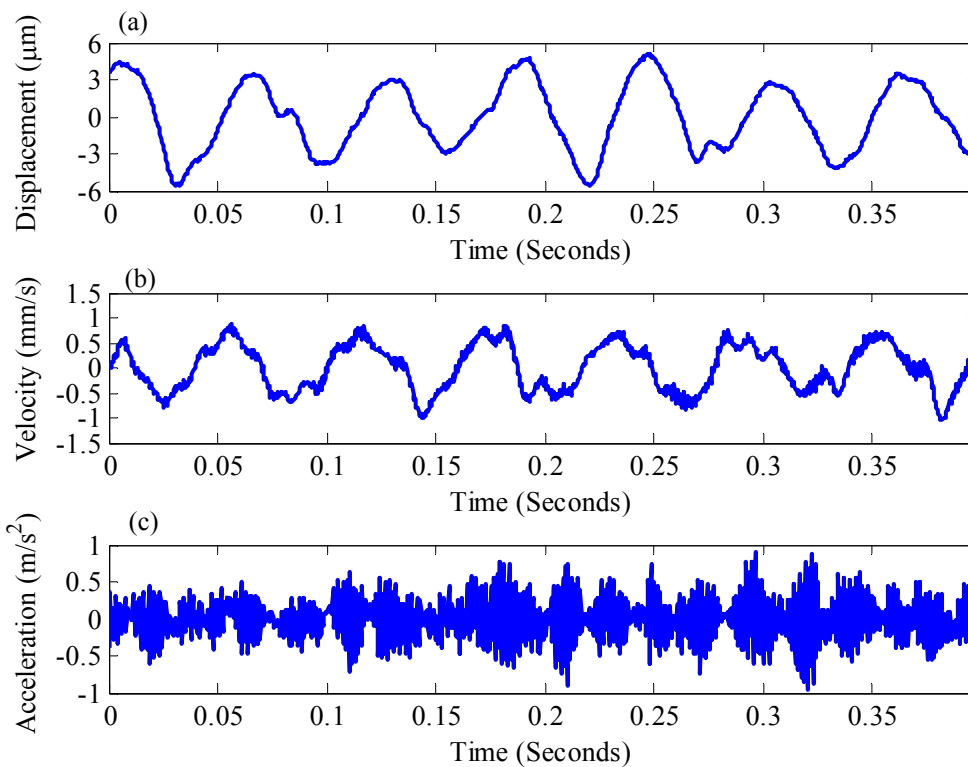
Figure 5.1 Vibration response in the case of healthy bearing at 1000 rpm under L0 load case
a) Displacement, b) Velocity, c) Acceleration.
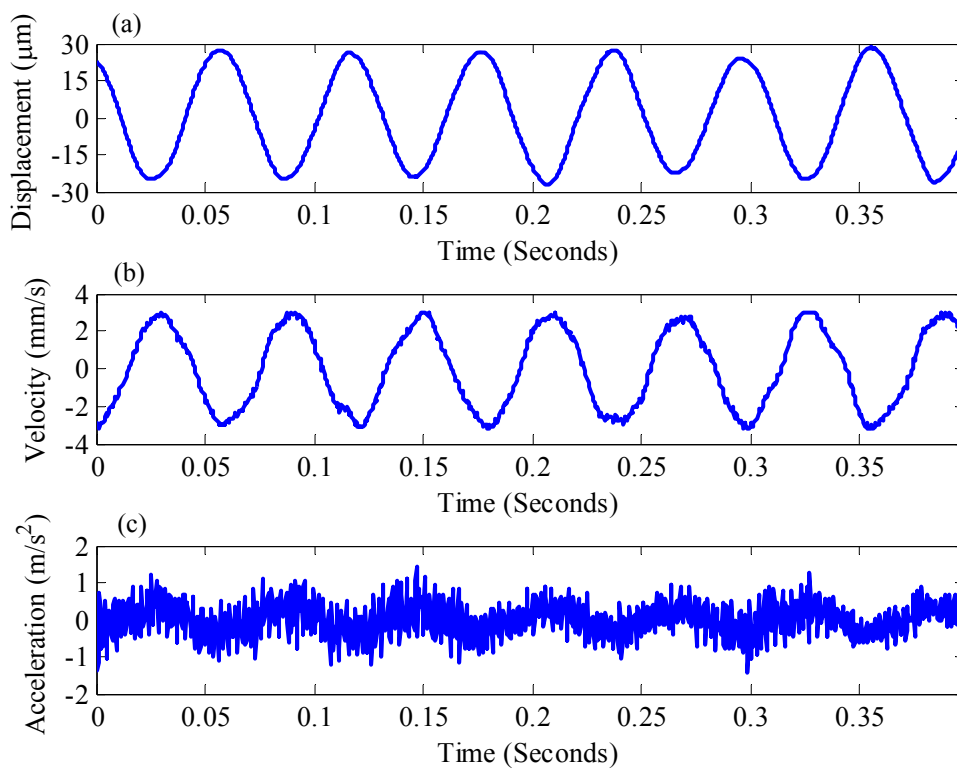
Figure 5.2 Vibration response in the case of healthy bearing at 1000 rpm under L2 load
case, a) Displacement, b) Velocity, c) Acceleration.
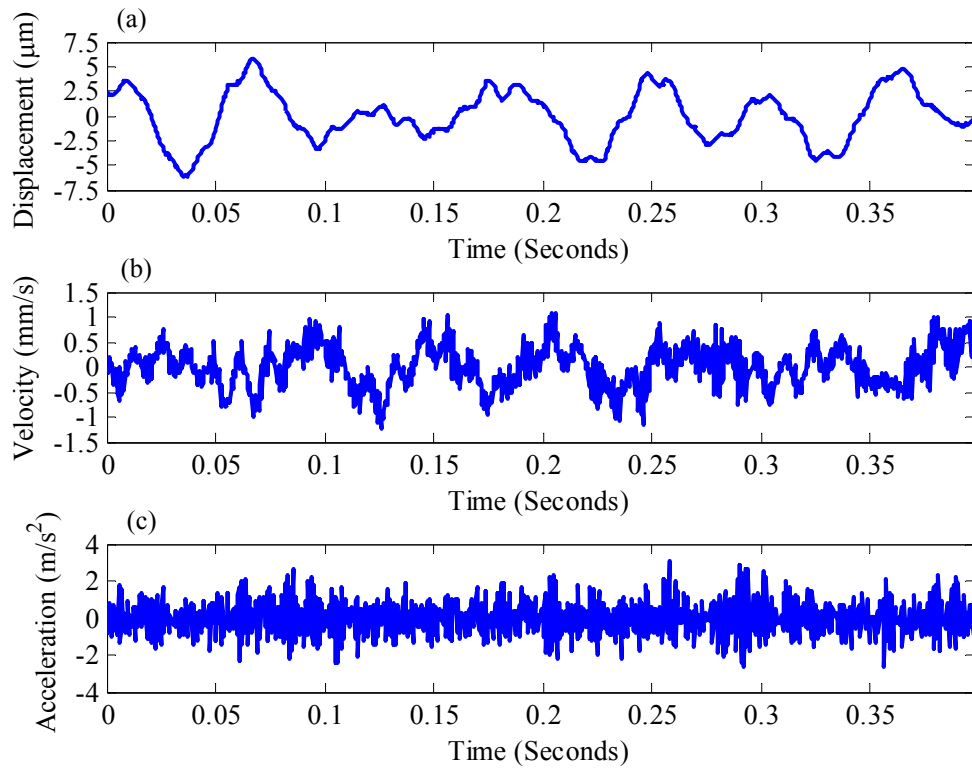
Figure 5.3 Vibration response in the case of inner race defect at 1000 rpm under L0 load case, a) Displacement, b) Velocity, c) Acceleration.
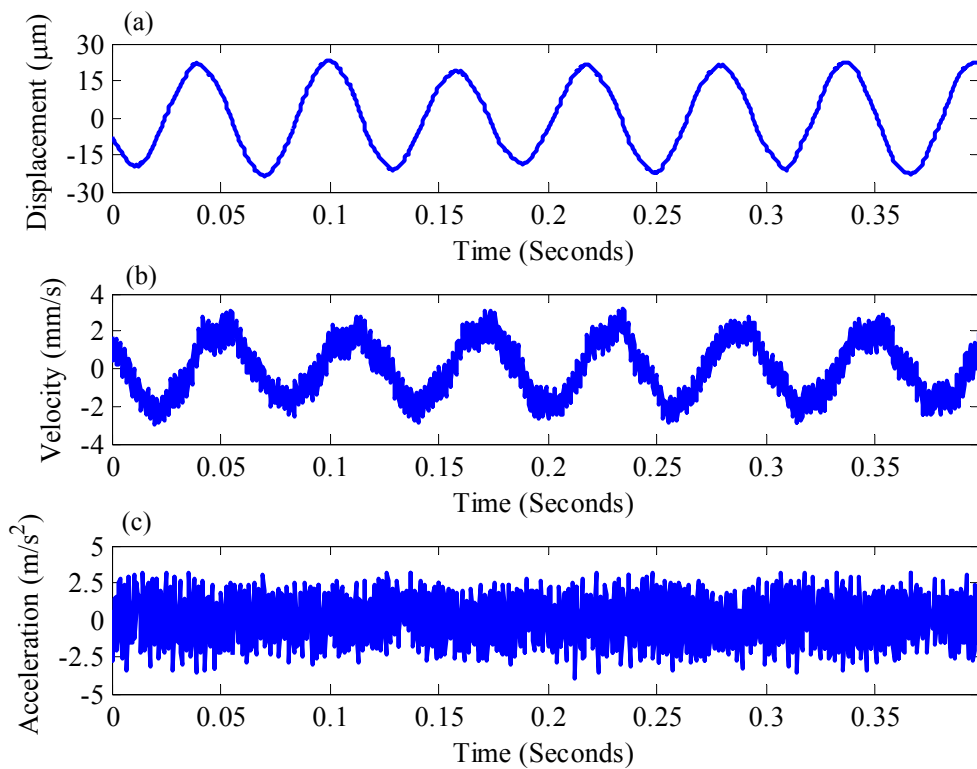
Figure 5.4 Vibration response in the case of inner race defect at 1000 rpm under L2 load case, a) Displacement, b) Velocity, c) Acceleration.
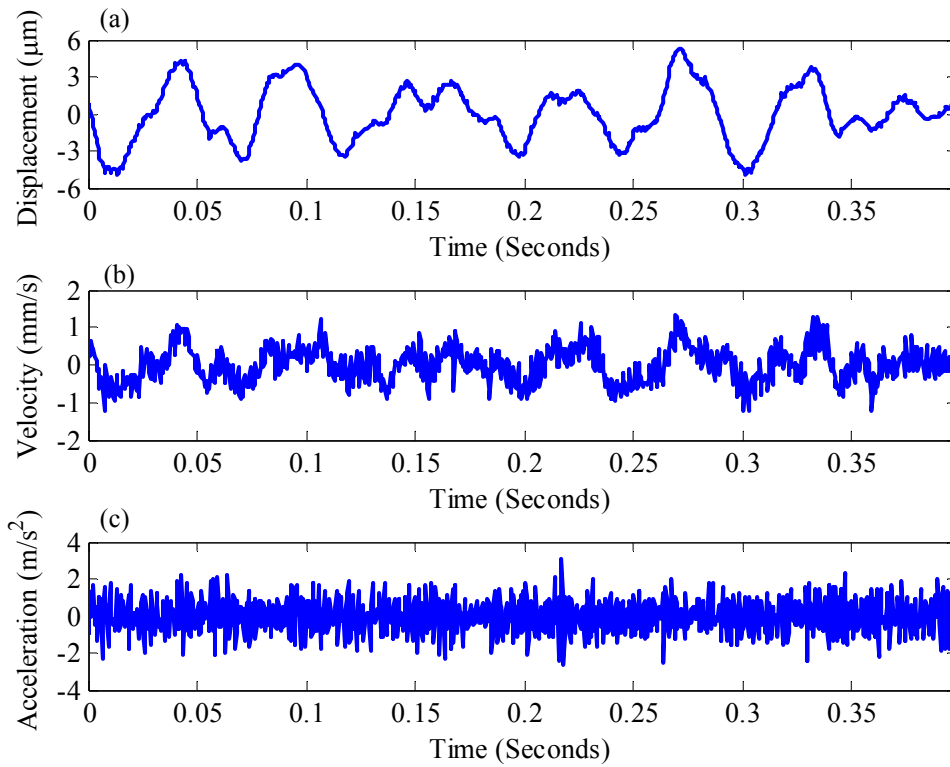
Figure 5.5 Vibration response in the case of outer race defect at 1000 rpm under L0 load case, a) Displacement, b) Velocity, c) Acceleration.
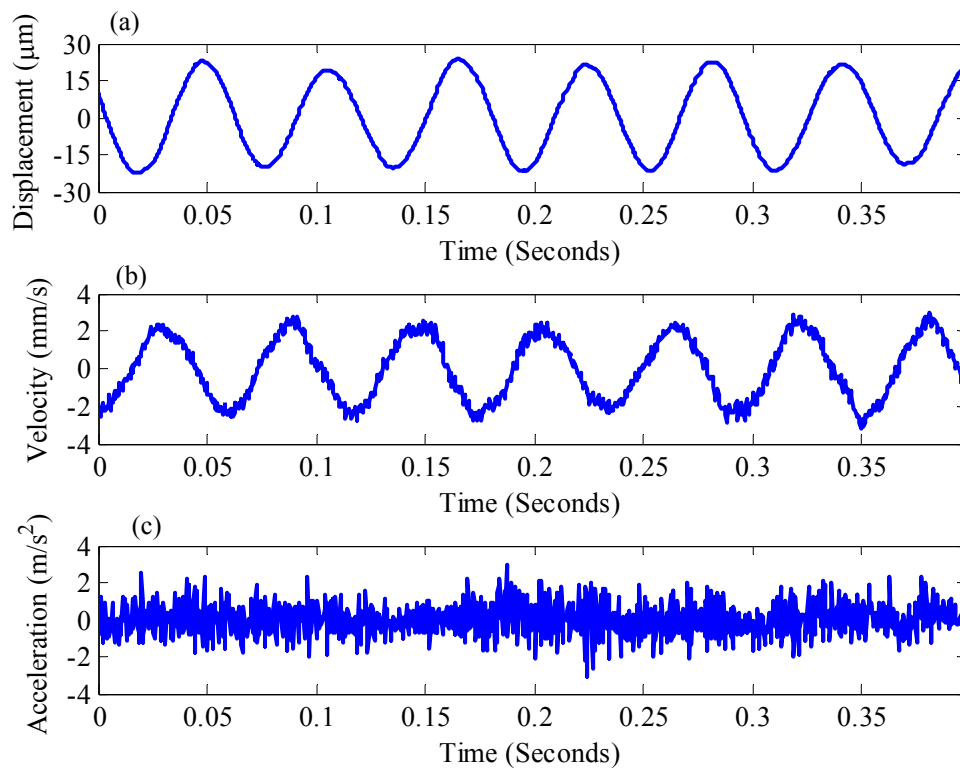
Figure 5.6 Vibration response in the case of outer race defect at 1000 rpm under L2 load case, a) Displacement, b) Velocity, c) Acceleration.

5.2 Analysis of Displacement Signals

5.2.1 Rms Values of Displacement Signals

Rms values of the raw displacement signals are given in Figure 5.7 for healthy bearing, inner race and outer race defected cases. The results show that, defect detection is possible only for outer race defect under L0 load case at the shaft speeds greater than 1000 rpm. The rms values for inner race defect are lower than those obtained for healthy bearing. Detecting the defects using displacement rms values is not possible for other load cases since the rms values of healthy or faulty bearings are very close.
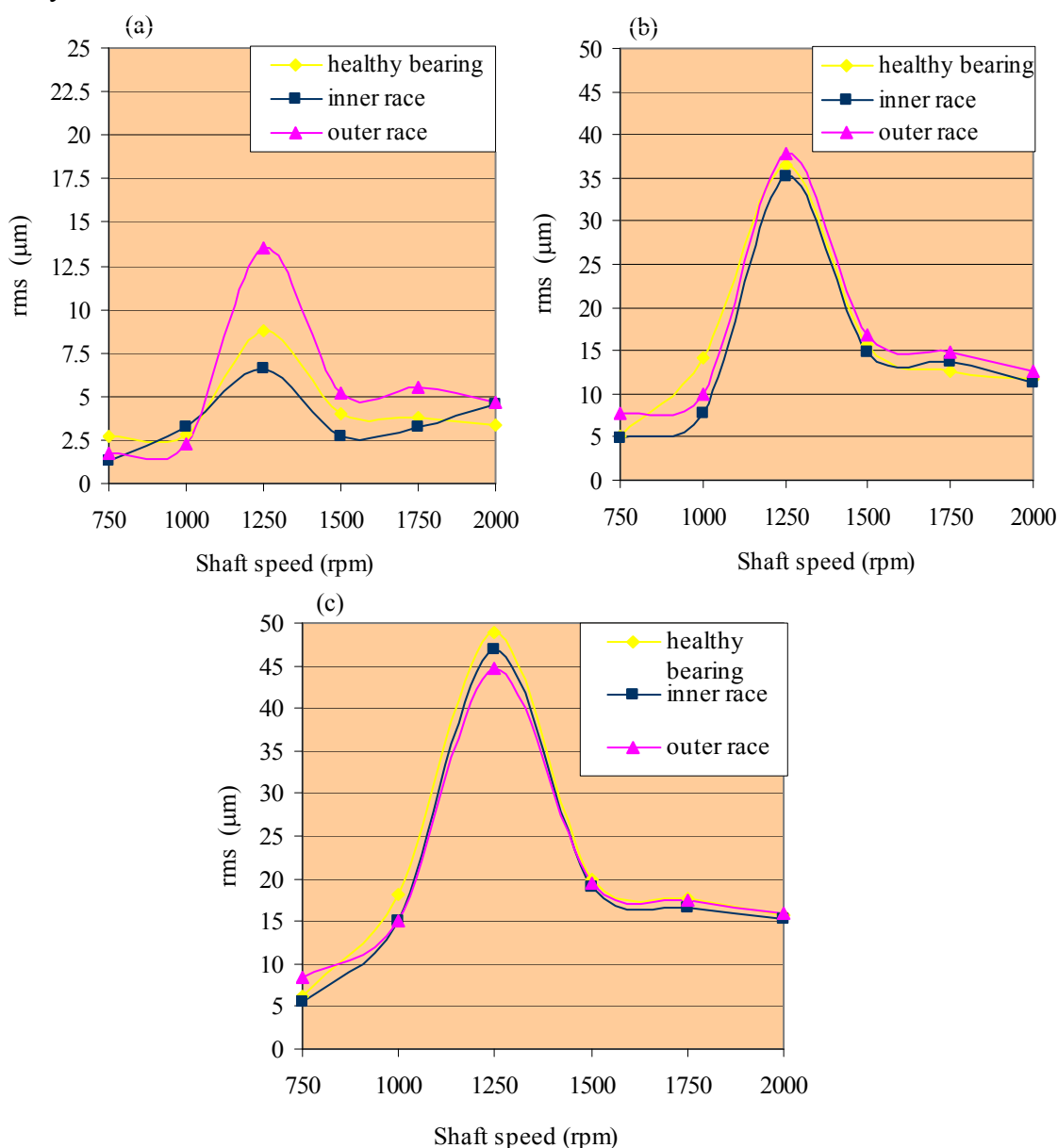
Figure 5.7 Rms values of displacement signals under a) L0, b) L1 and c) L2 load cases versus shaft speed.

5.2.2 Kurtosis Values of Displacement Signals

Kurtosis values of raw displacement signals are given in Figure 5.8 for different load cases and defect types. Kurtosis values of healthy bearing obtained for L0 load case are lower than those obtained for faulty cases except at 1500 rpm and 2000 rpm and can be used as a defect indicator. On the other hand, the kurtosis values of healthy and defected bearings for L1 and L2 load cases are very close and can not indicate the existence of a defect.
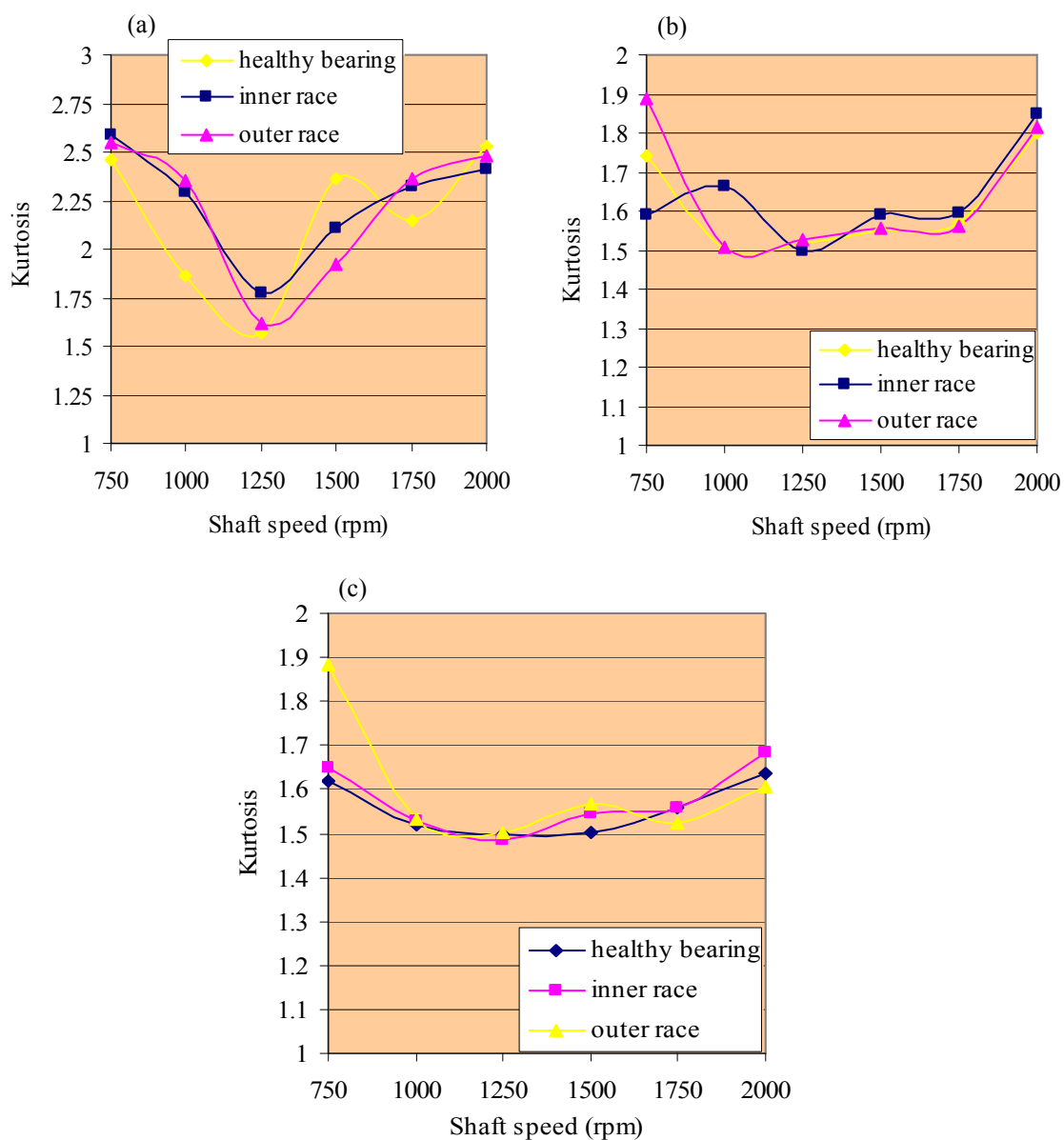
Figure 5.8 Kurtosis values of displacement signals under a) L0, b) L1 and c) L2 load cases versus shaft speed.

5.2.3 Peak to Peak Values of Displacement Signals

Peak to peak values of displacement signals for three load cases are given in Figure 5.9. As seen from the figure that the p2p values are very close for healthy and defected bearings and the peak to peak value has not any diagnostic information for displacement signals except some rotational speeds for L0 load case.
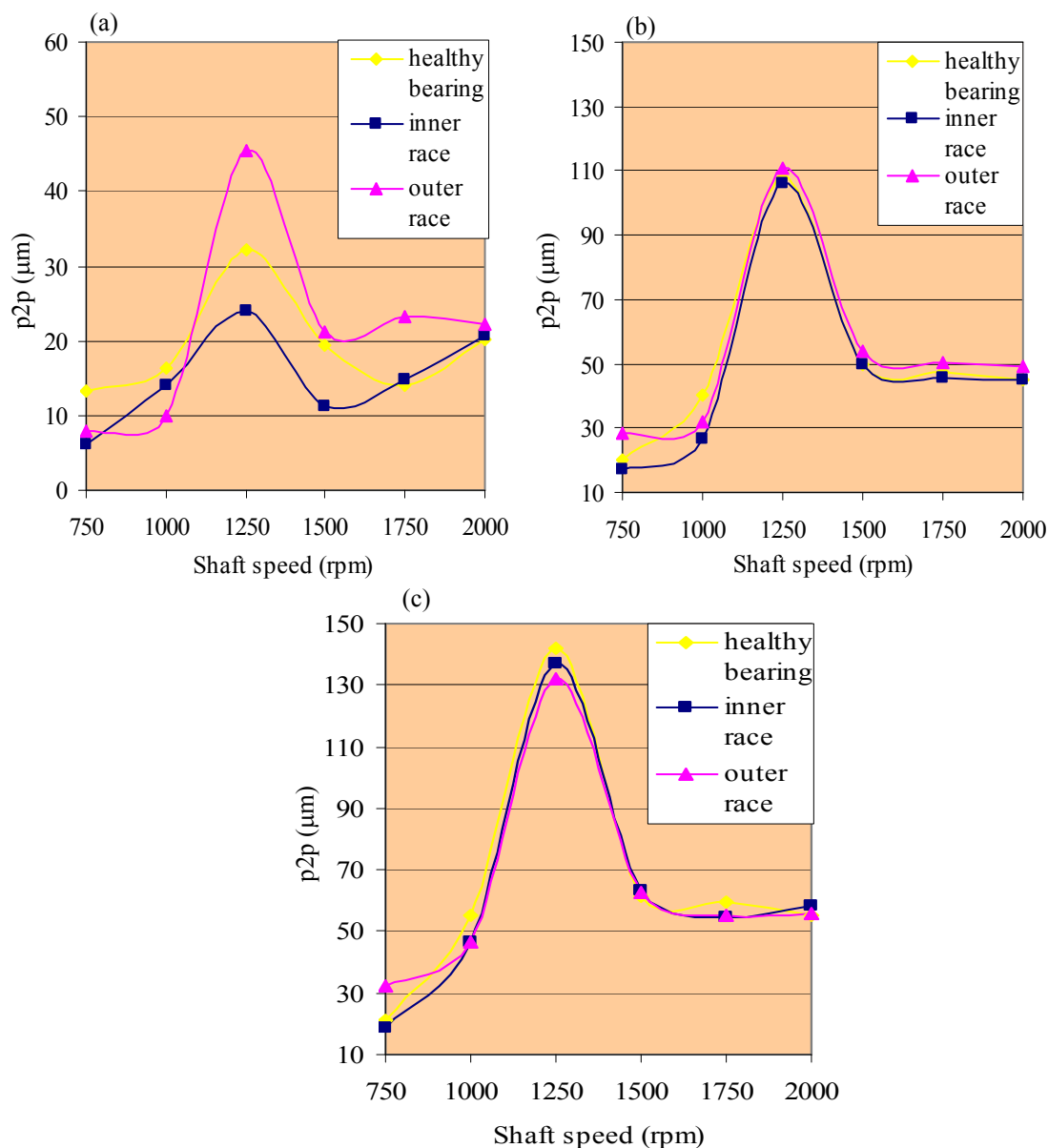
Figure 5.9 Peak to peak values of displacement signals under a) L0, b) L1 and c) L2 load cases versus shaft speed.

5.3 Analysis of Velocity Signals

5.3.1 Rms Values of Velocity Signals

Rms values of raw velocity signals derived for different load cases are given for a broad range of shaft speed in Figure 5.10. The velocity rms values for L0 load case can be used as a defect indicator at some speeds for outer race defect. But, generally the velocity rms values are not suitable defect indicator because there are no meaningful discrepancies between the healthy and defected cases.
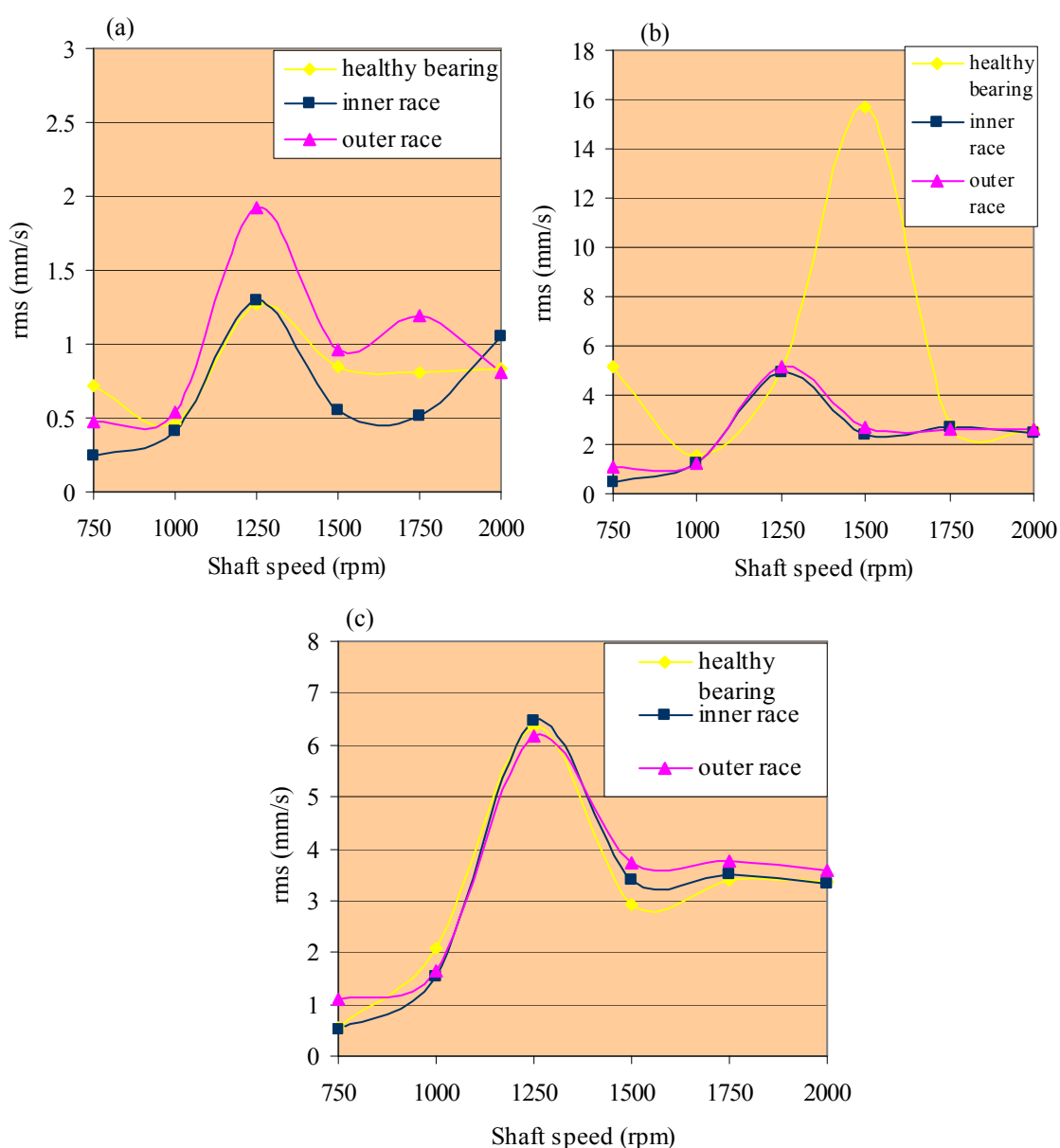
Figure 5.10 Rms values of velocity signals under a) L0, b) L1 and c) L2 load cases versus shaft speed.

5.3.2 Kurtosis Values of Velocity Signals

Kurtosis values of raw velocity signals are shown in Figure 5.11. The kurtosis values of defected cases for L0 load case differ considerably from the healthy bearing except at 2000 rpm. The same situation is not observed for L1 and L2 load cases but at low shaft speeds the kurtosis values of velocity signals can be used as the defect indicator for diagnostic purpose.
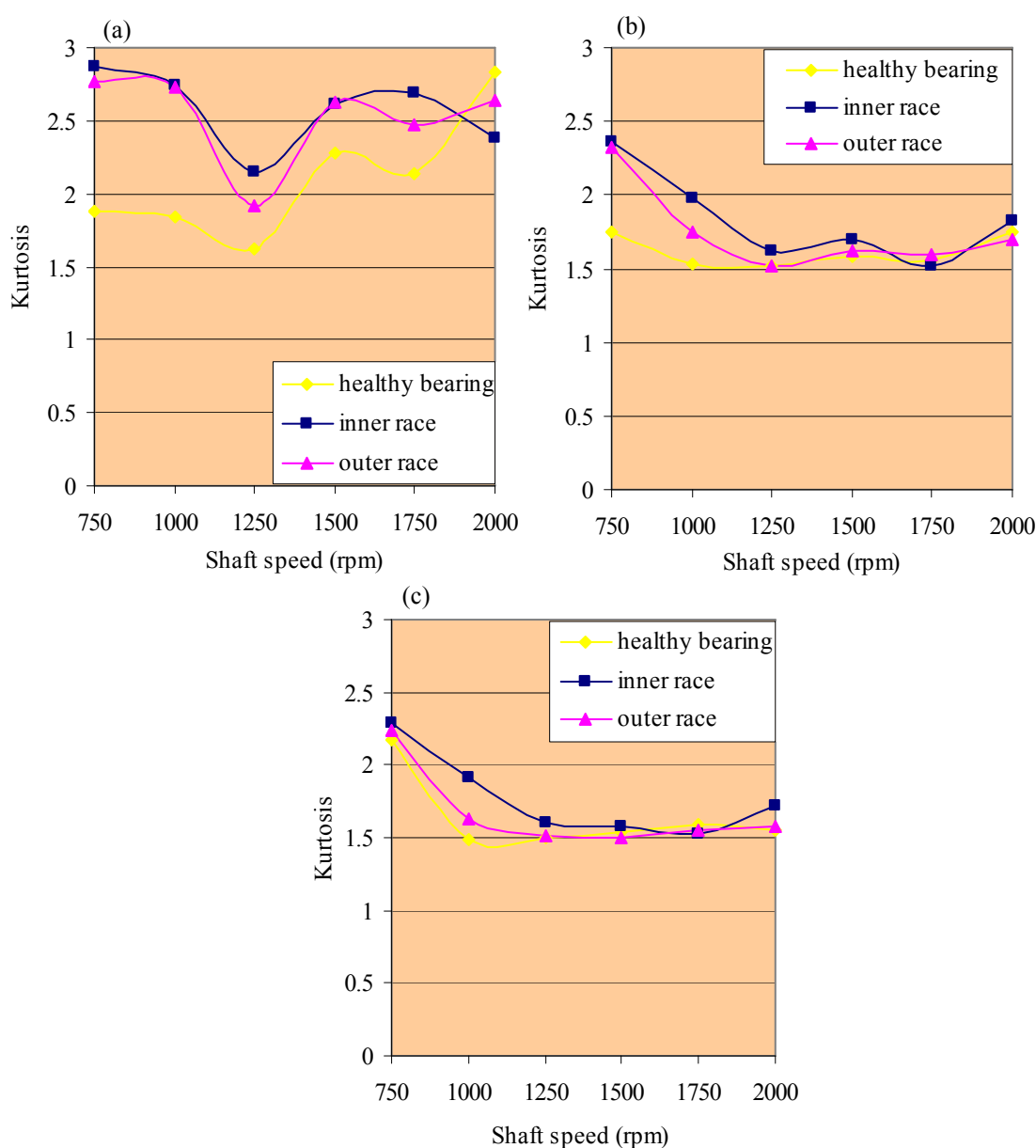
Figure 5.11 Kurtosis values of velocity signals under a) L0, b) L1 and c) L2 load cases versus shaft speed.

5.3.3 Peak to Peak Values of Velocity Signals

Peak to peak values of raw velocity signals are given in Figure 5.12. The p2p values of defected bearings are greater than those obtained for healthy bearing at some rotational speeds indicating the faulty bearing. Peak to peak values for L1 load case do not give useful information, but for L2 load case, the p2p values have slight differences than those obtained for healthy case. However, it is very difficult to interpret these slight differences as defect indicator.
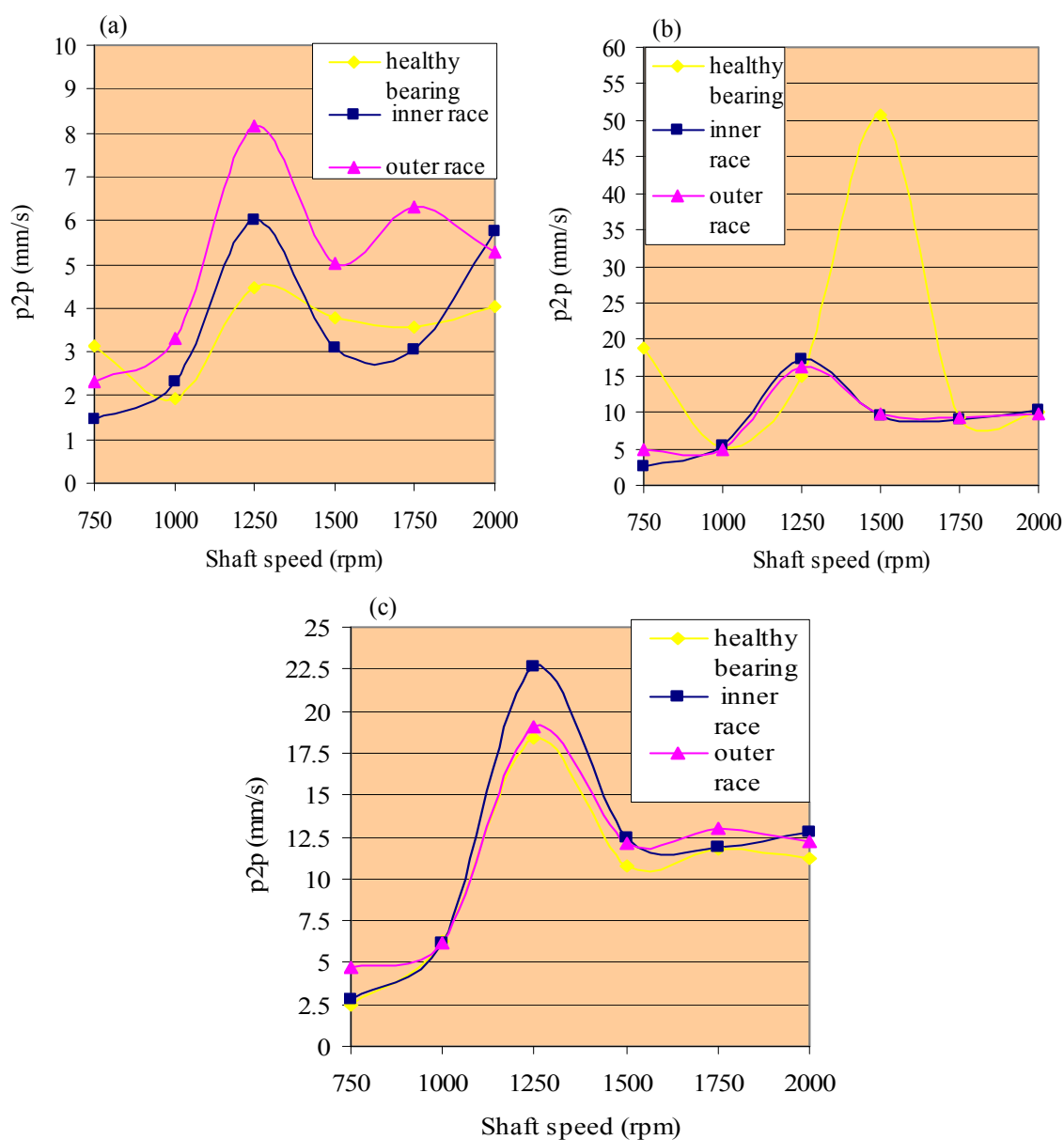
Figure 5.12 P2p values of velocity signals under a) L0, b) L1 and c) L2 load cases versus shaft speed.

5. 4 Analysis of Acceleration Signals

5.4.1 Rms Values of Acceleration Signals

Rms values of raw acceleration signals for different load cases versus different shaft speeds are given in Figure 5.13. The acceleration rms values can be used as defect indicator for all load values except at 2000 rpm. The rms ratios between the defected and healthy bearings are high indicating the existence of the bearing fault. The rms value indicates the bearing defect especially at low shaft speeds.
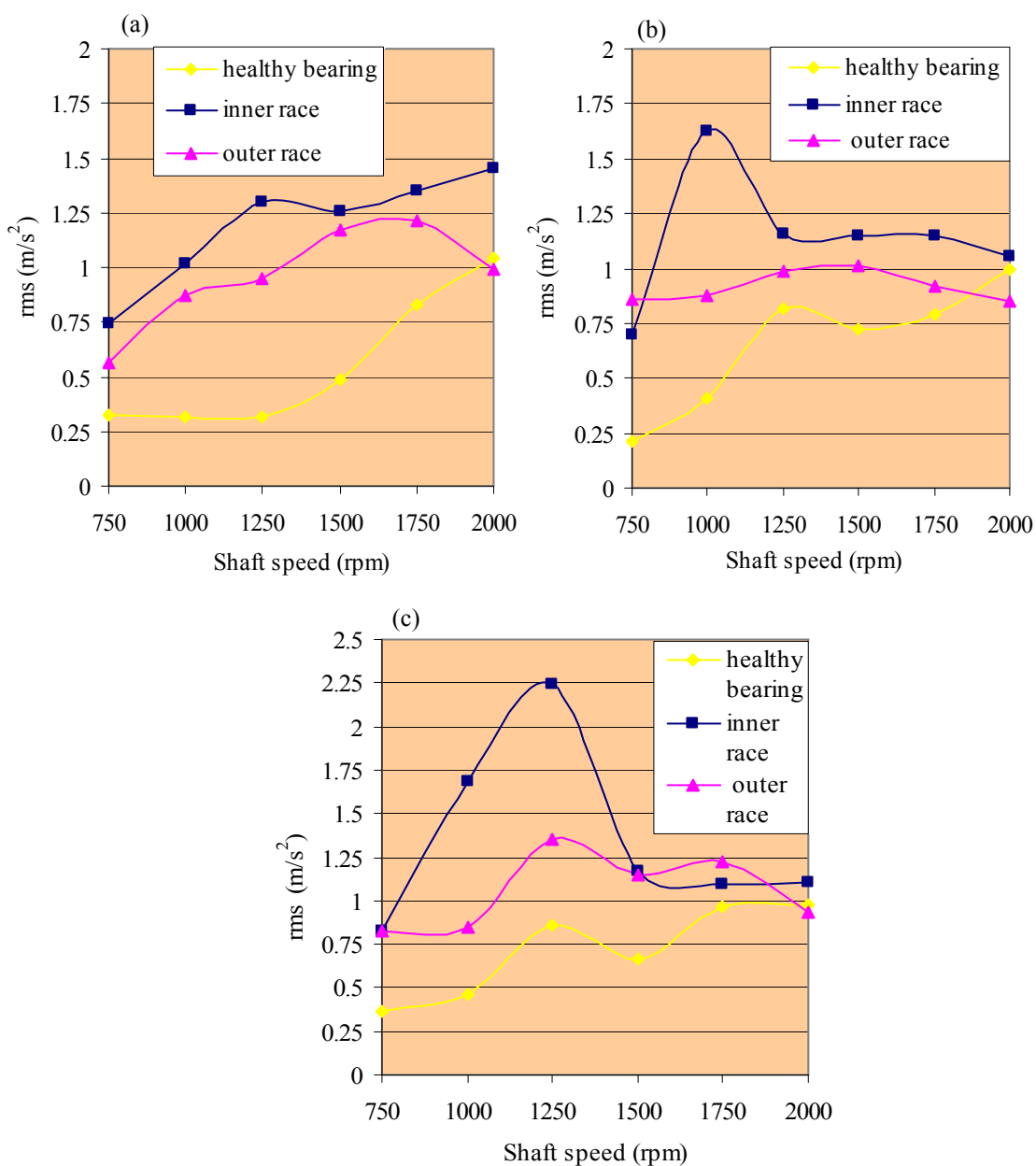
Figure 5.13 Rms values of acceleration signals under a) L0, b) L1 and c) L2 load cases versus shaft speed.

5.4.2 Kurtosis Values of Acceleration Signals

Kurtosis values of raw acceleration signals are given in Figure 5.14. The kurtosis values of healthy bearing are lower than those obtained for defected bearings at some limited shaft speeds, but generally the kurtosis values do not have diagnostic informations for inner and outer race defects.
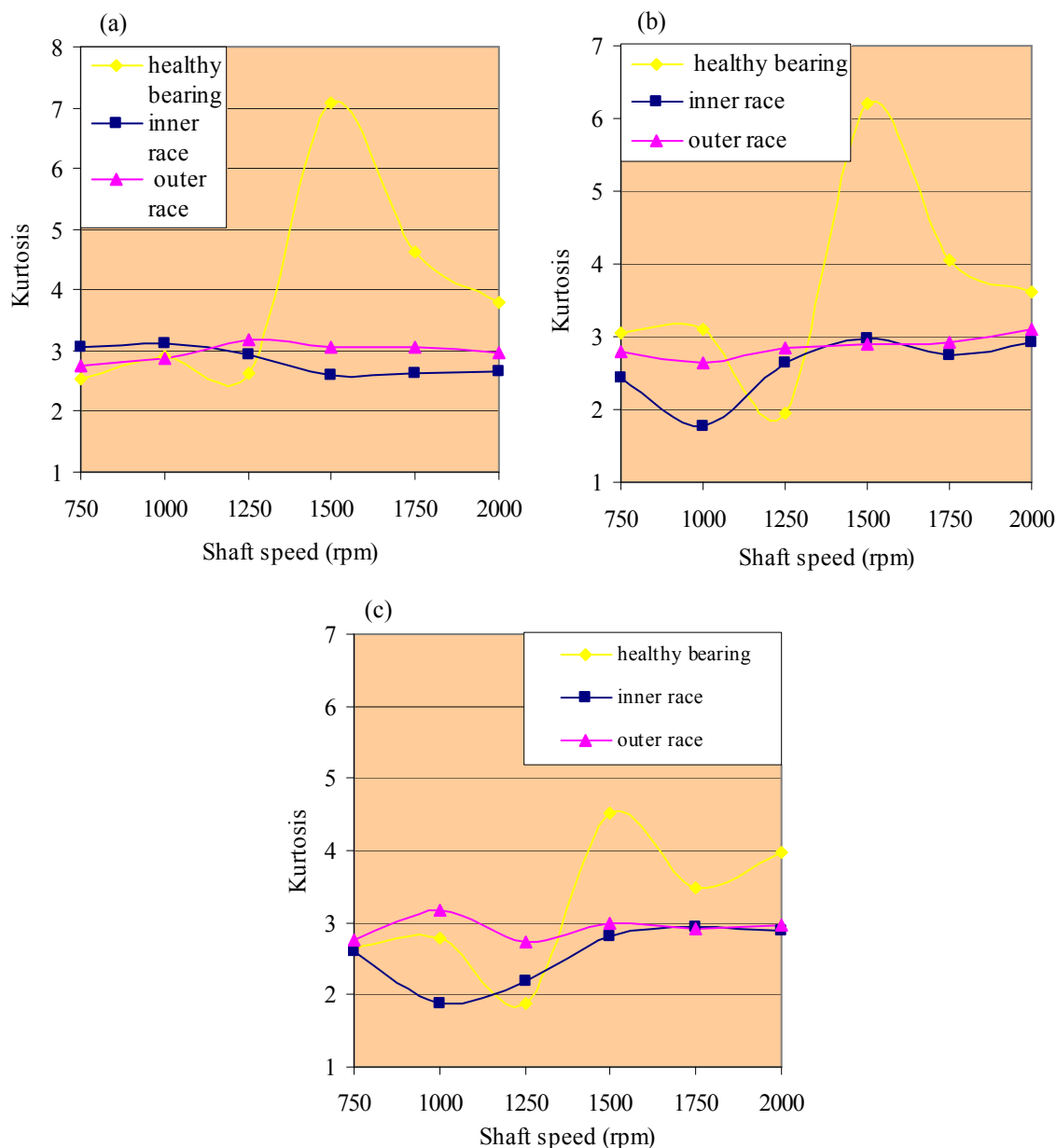
Figure 5.14 Kurtosis values of acceleration signals under a) L0, b) L1 and c) L2 load cases versus shaft speed.

5.4.3 Peak to Peak Values of Acceleration Signals

Peak to peak values of raw acceleration signals are given in Figure 5. 15. The p2p values of acceleration signals are speed dependent and the p2p ratios between the defected and healthy bearing are very high indicating the existence of bearing fault. Both the inner and outer race defects can be captured by p2p values of acceleration signals for a broad range of shaft speed.
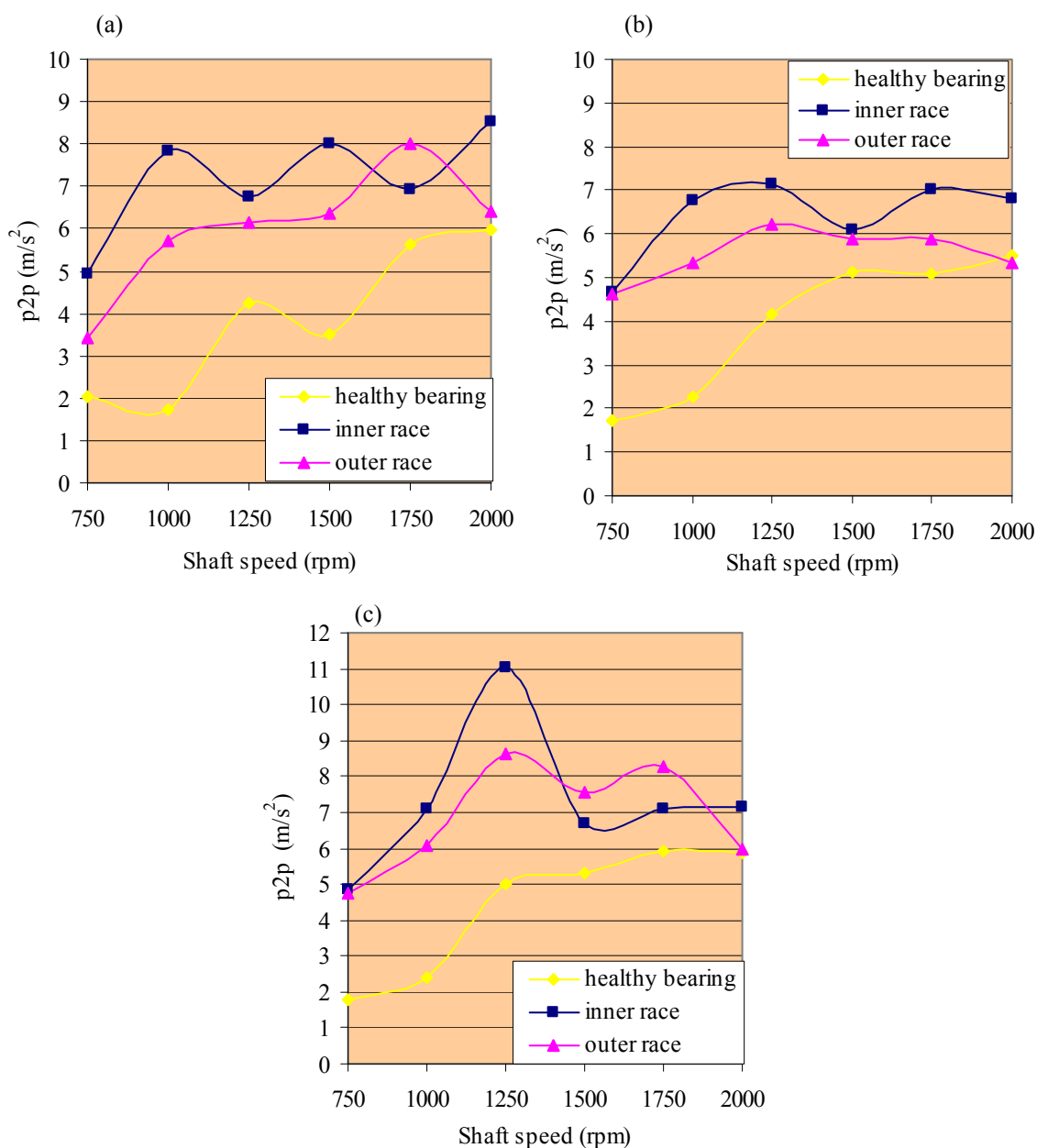
Figure 5.15   P2p values of acceleration signals under a) L0, b) L1 and c) L2 load cases versus shaft speed.

CHAPTER SIX
FREQUENCY DOMAIN ANALYSES

Each component of a rolling element bearing has characteristic rotational frequency due to the geometry of the rolling element bearing. These characteristic frequencies are used to identify the bearing defects in the frequency spectrum of a time signal.

6.1 Bearing Characteristic Frequencies

Bearing characteristic frequencies are known as the defect frequencies. This requencies indicate the location of faults, if there is a defect on any components of rolling element bearing. In the faulty situation, these frequencies are observed in the frequency spectrum. These frequencies depend on rolling element bearing geometry, number of rolling element and shaft rotational speed. Bearing characteristic frequencies (Tandon, & Choudhury, 1999) are calculated by the formula given in Equations 6.1 - 6.5. The properties of the rolling element bearing used in this study are given in Figure 6.1.

Outer diameter $D = 52$ mm
Bore diameter $d = 25$ mm
Pitch diameter $d_m = 39$ mm
Ball diameter $d_b = 8$ mm
Raceway width $w = 15$ mm
Contact angle $\alpha = 0°$
Number of balls $Z = 9$
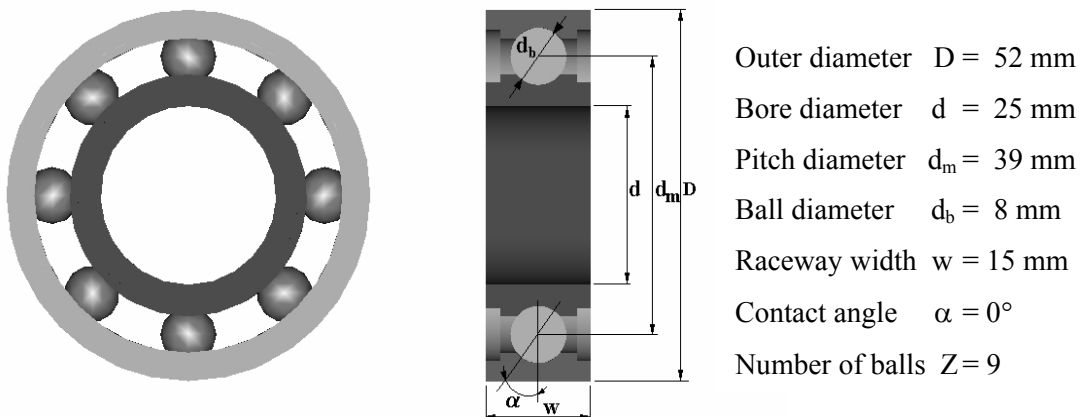
Figure 6.1 Geometry of rolling element bearing (ORS 6205).

$$f_o = \frac{Zf_s}{2}\left(1 - \frac{d_b}{d_m}\cos\alpha\right) \tag{6.1}$$

$$f_i = \frac{Zf_s}{2}\left(1 + \frac{d_b}{d_m}\cos\alpha\right) \tag{6.2}$$

$$f_{re} = f_s\frac{d_p}{d}\left(1 - \frac{d_b^{\,2}}{d_m^{\,2}}\cos^2\alpha\right) \tag{6.3}$$

$$f_{sp} = \frac{f_{re}}{2} = f_s\frac{d_m}{2d_b}\left(1 - \frac{d_b^{\,2}}{d_m^{\,2}}\cos^2\alpha\right) \tag{6.4}$$

$$f_c = \frac{f_s}{2}\left(1 - \frac{d_b}{d_m}\cos\alpha\right) \tag{6.5}$$

The sembols used in above equations are

d_b: rolling element diameter

d_p: pitch diameter

Z: number of rolling elements

f_s : shaft speed

f_o : characteristic frequency of outer race

f_i : characteristic frequency of inner race

f_{re} : characteristic frequency of rolling element

f_{sp} : spin frequency of rolling element

f_c : characteristic frequency of cage

The bearing characteristic frequencies of ORS 6205 for different shaft speeds are given Table 6.1.

Table 6.1 Characteristic frequencies of ORS 6205.

Shaft speed(rpm)	f_o [Hz]	f_i [Hz]	f_{re} [Hz]	f_{sp} [Hz]	f_c [Hz]
750	44,826	67,673	59,014	29,507	4,980
1000	59,769	90,230	78,686	39,343	6,641
1250	74,711	112,788	98,357	49,178	8,301
1500	89,653	135,346	118,029	59,014	9,961
1750	104,596	157,903	137,700	68,850	11,621
2000	119,538	180,461	157,372	78,686	13,282

6.2 The Fast Fourier Transform

The frequency contents of the vibration signals are calculated by the Fast Fourier Transform (FFT). The FFTs of the experimental vibration signals are calculated by MATLAB software. For a continous time signal, the Fourier transform is calculated by the equation given below.

$$F(i\omega) = \int_{-\infty}^{\infty} f(t) e^{-i\omega t} dt \tag{6.6}$$

If vibration signal is a discrete signal having n samples, the Fast Fourier Transform is calculated as

$$X(k) = \sum_{i=1}^{n} x(i) e^{-i\frac{2\pi(k-1)*(i-1)}{n}} \qquad 1<k<n \tag{6.7}$$

6.3 Dynamic Properties of the Test Rig

In the scope of the vibration measurements, the dynamic response of the test rig is measured by a non-contact laser measurement system in order to find the natural frequencies of the test rig. Determination of the natural frequencies of the test rig is important to identify some frequency components which appear in the frequency spectrum of the bearing vibration signals. The experimental set-up for measuring the free response of the test rig is shown in Figure 6.2.
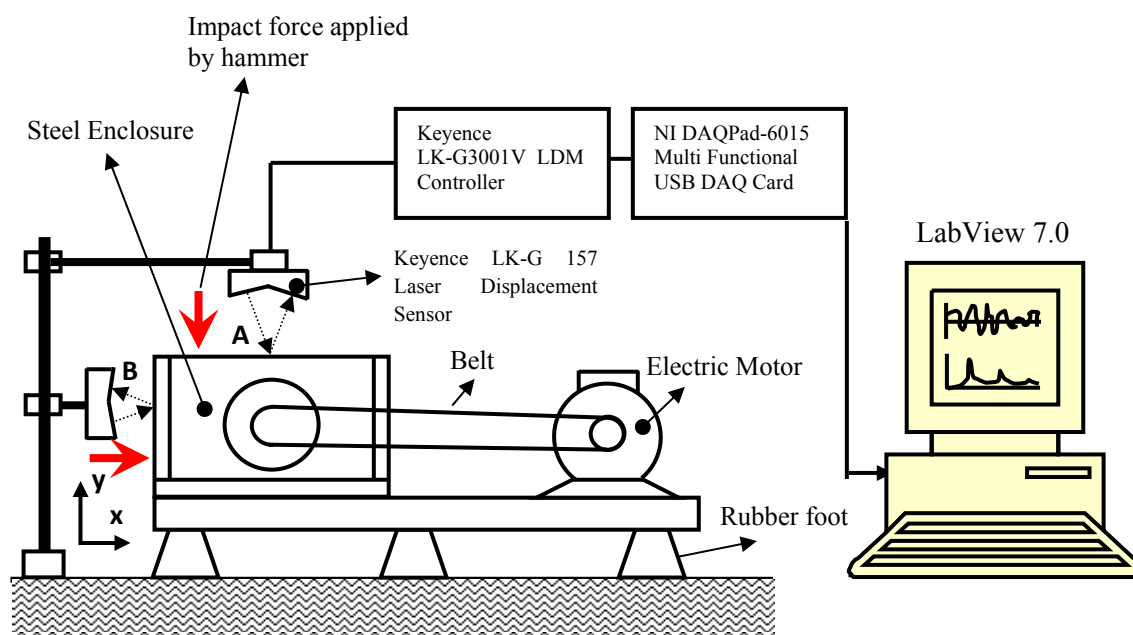
Figure 6.2. Schematic view of the experimental set-up for measuring the natural frequencies of the test rig.

The test rig is excited by a standard hammer to initiate its free vibration. The free vibration of the test rig is measured in terms of displacement by a non-contact laser displacement meter (LDM). The vibration signal measured by the laser sensor is amplified by a LDM controller and then is sent to the National Instrument DAQ Card in order to transfer the signal to the computer. Displacement signal is stored in the computer via a code written in LabView program. The measurement range and the sensitivity of the laser displacement sensor are 150±40 mm and 0.5 μm, respectively. The test rig is excited by an impact force using hammer from points A and B shown in Figure 6.2, and the free vibration responses are measured for the point A and B. In this way, the natural frequencies of the test rig in x and y directions are extracted from the frequency spectrum of the free responses. The real view of the experimental set-up is shown in Figure 6.3.
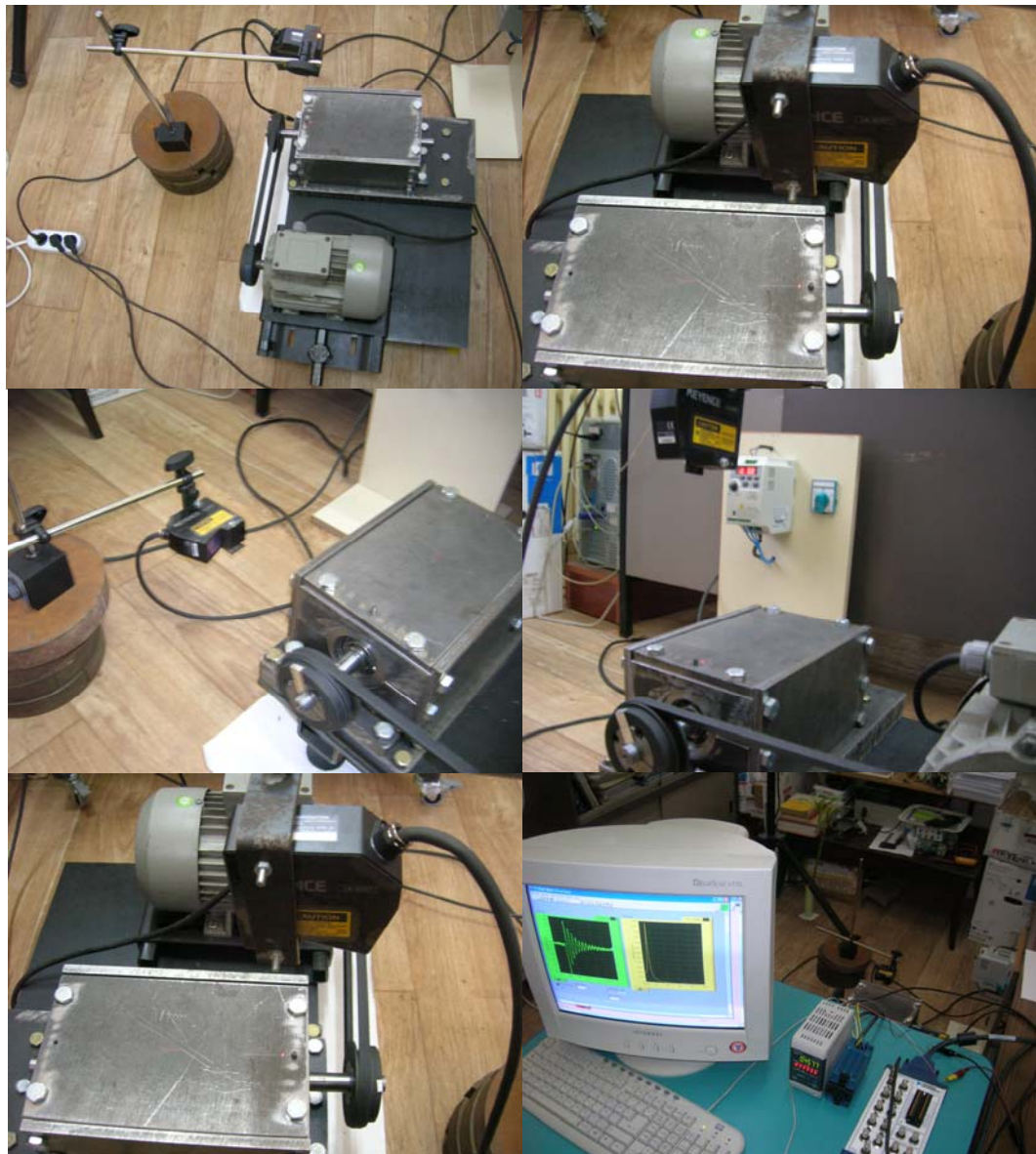
Figure 6.3. Real views of the experimental set-up.

Figure 6.4 illustrates the free response and the frequency spectrum of the test rig measured at point A when the test rig is excited from the top of the bearing housing. As seen from the figure that, the natural frequency of the test rig in y direction appears at 22.58 Hz.
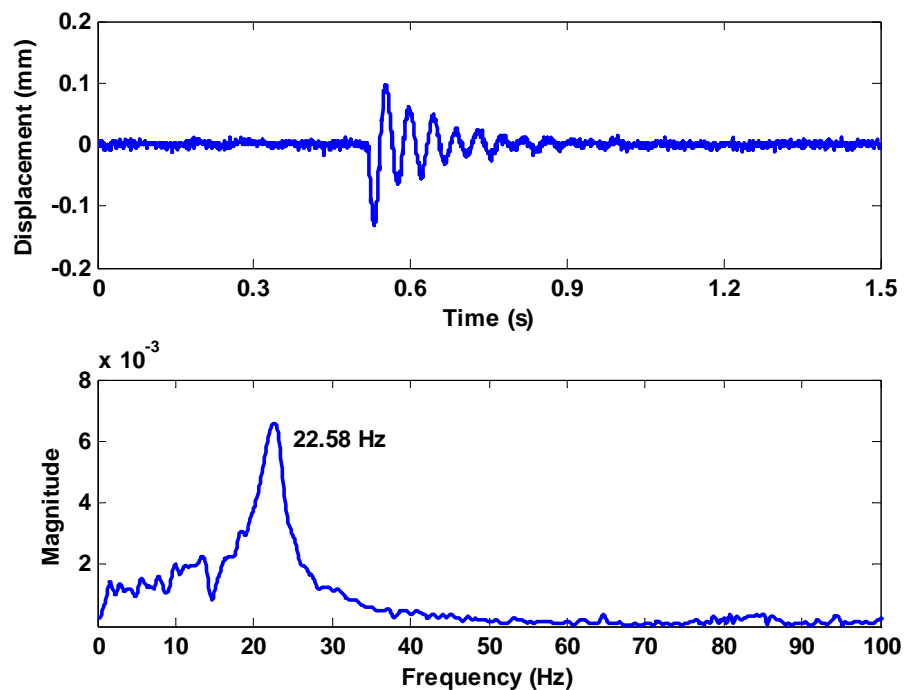
Figure 6.4. Free response and the frequency spectrum of the test rig measured at point A when the impact is in y direction.

Figure 6.5 shows the free response and the frequency spectrum of the test rig measured at point B when the test rig is excited from the side of the bearing housing. As seen from the figure that, the natural frequencies of the test rig in x direction appear at 12.329 Hz and 481 Hz.

Figure 6.6 shows the displacement response of the test rig measured at point B while the rotation speed is changed. The frequency content of the vibration signal is shown in the spectrogram plot in Figure 6.6. The first and second natural frequencies can be seen in the spectrogram graph.
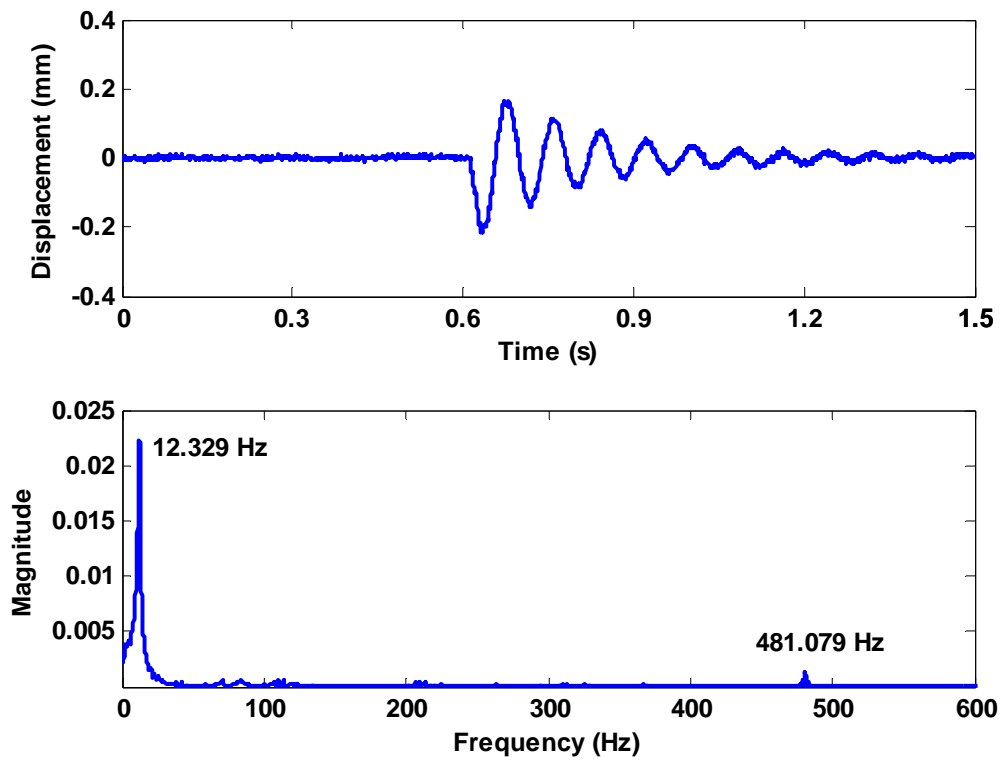
Figure 6.5 Free response and the frequency spectrum of the test rig measured at point B when the impact is in x direction.
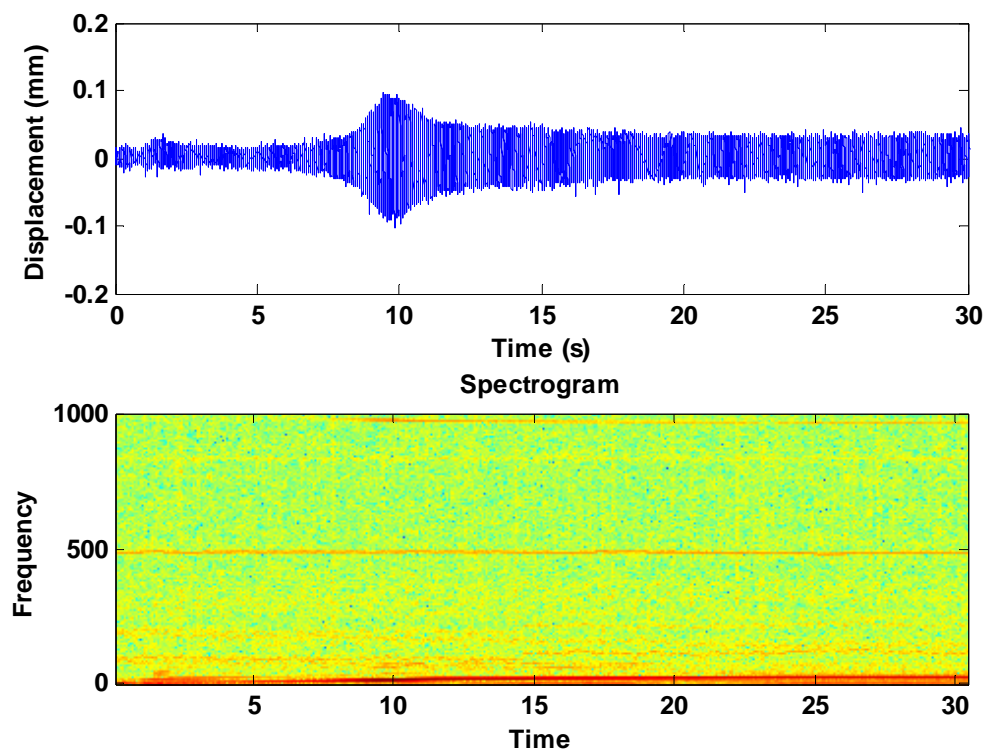
Figure 6.6 Free response and the frequency spectrum of the test rig measured at point B when the impact is in x direction.

6.4 Raw Signals

In this section, raw (unprocessed) vibration signals are examined under various load cases at different shaft speeds ranging from 750 rpm to 2000 rpm with the speed increment 250 rpm. The vibration signals and its frequency spectrums are given for displacement, velocity and acceleration responses only at 1000 rpm and 2000 rpm for healthy and faulty bearing cases.

6.4.1 Vibration Responses for Healthy Bearing

Raw signals obtained for healty bearing and their frequency spectrums are given in this section.

6.4.1.1 Displacement Responses for Healthy Bearing

Displacement signals and their frequency spectrums for L0, L1 and L2 load cases at 1000 rpm are shown in figures from 6.7 to 6.9, respectively. Shaft rotation frequency is 16.67 Hz and can be seen clearly in these figures. An increase in the spectrum amplitude at the shaft frequency is observed as the level of the unbalance increases as expected.
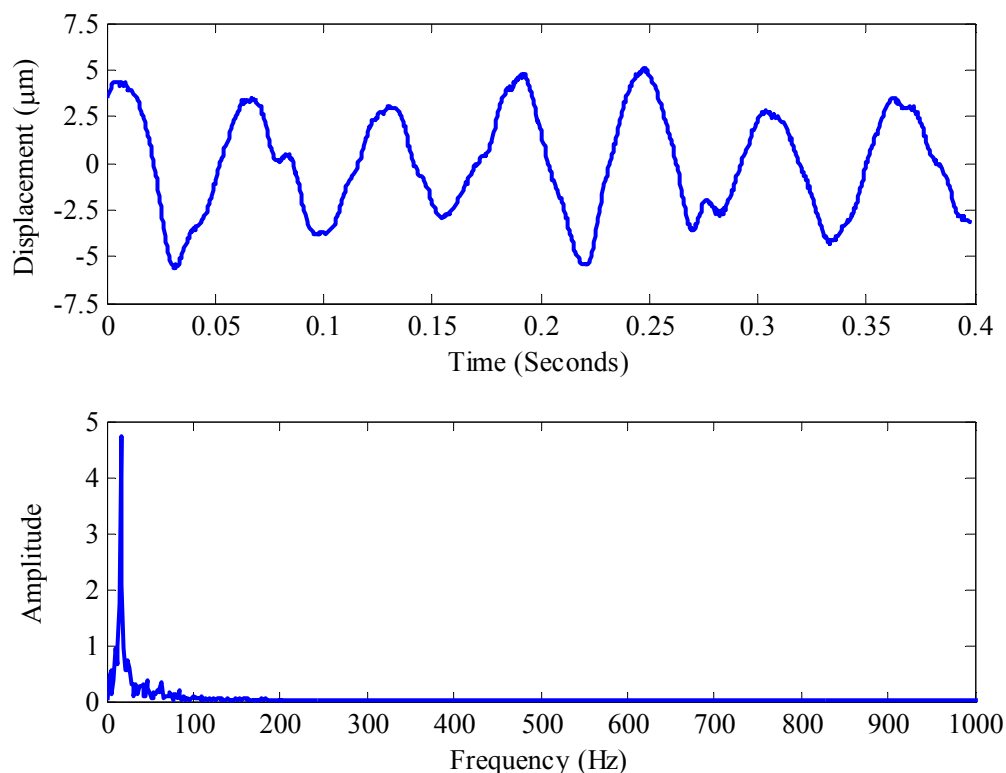
Figure 6.7 Displacement signal and its frequency spectrum at 1000 rpm under L0 load case (healthy bearing).
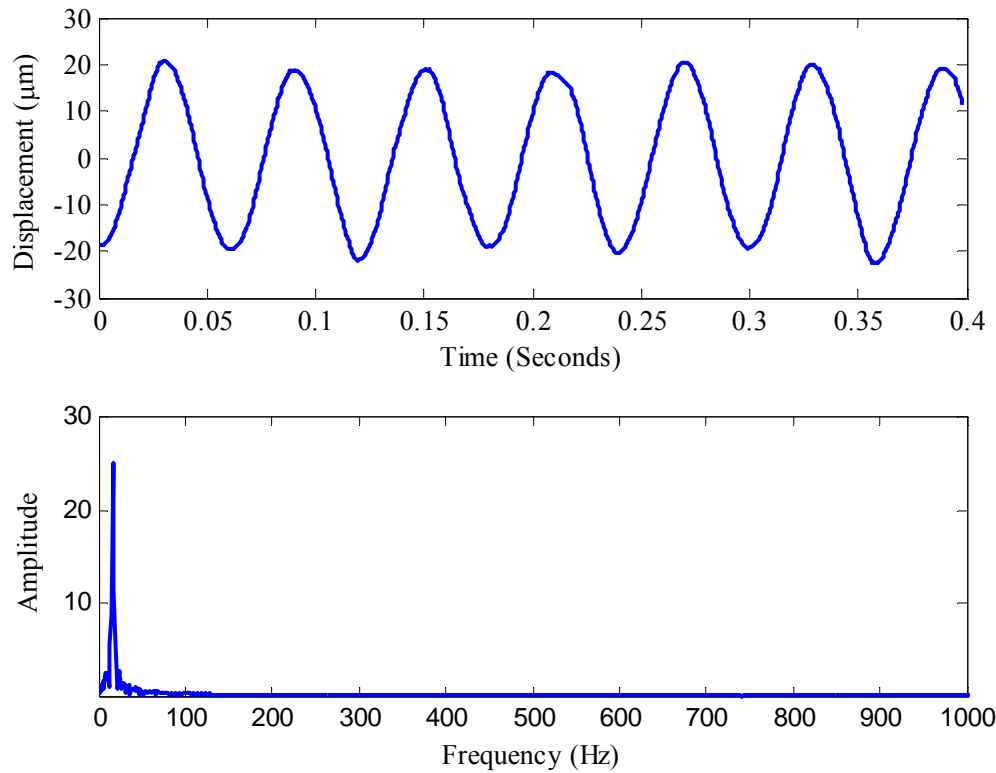
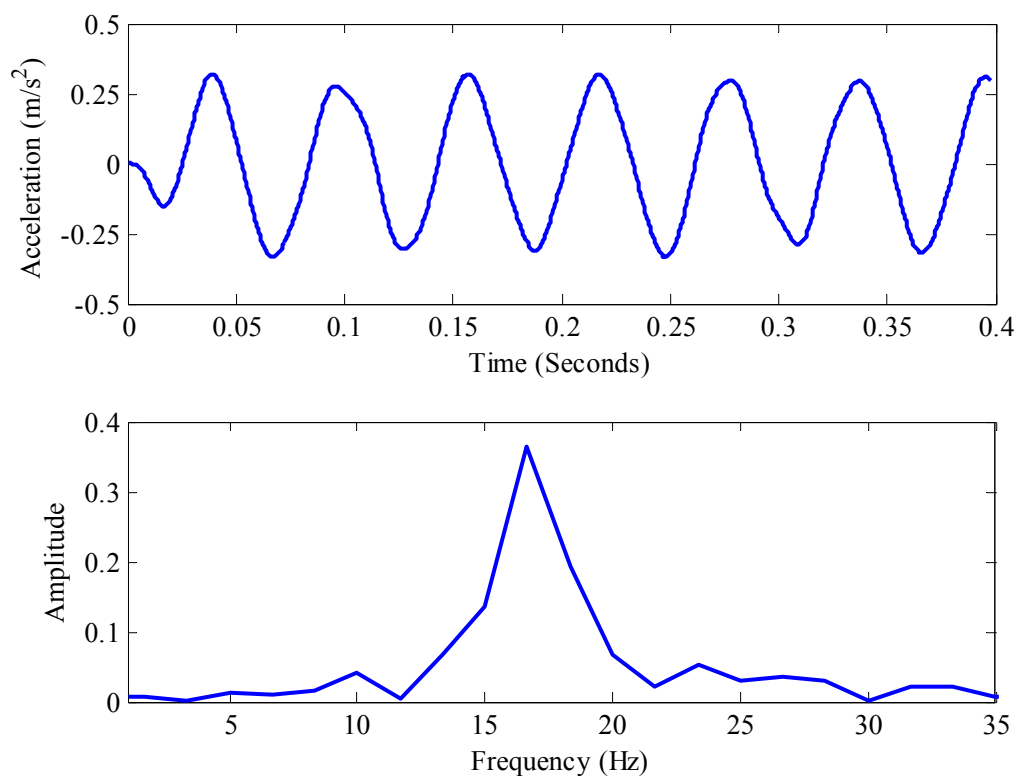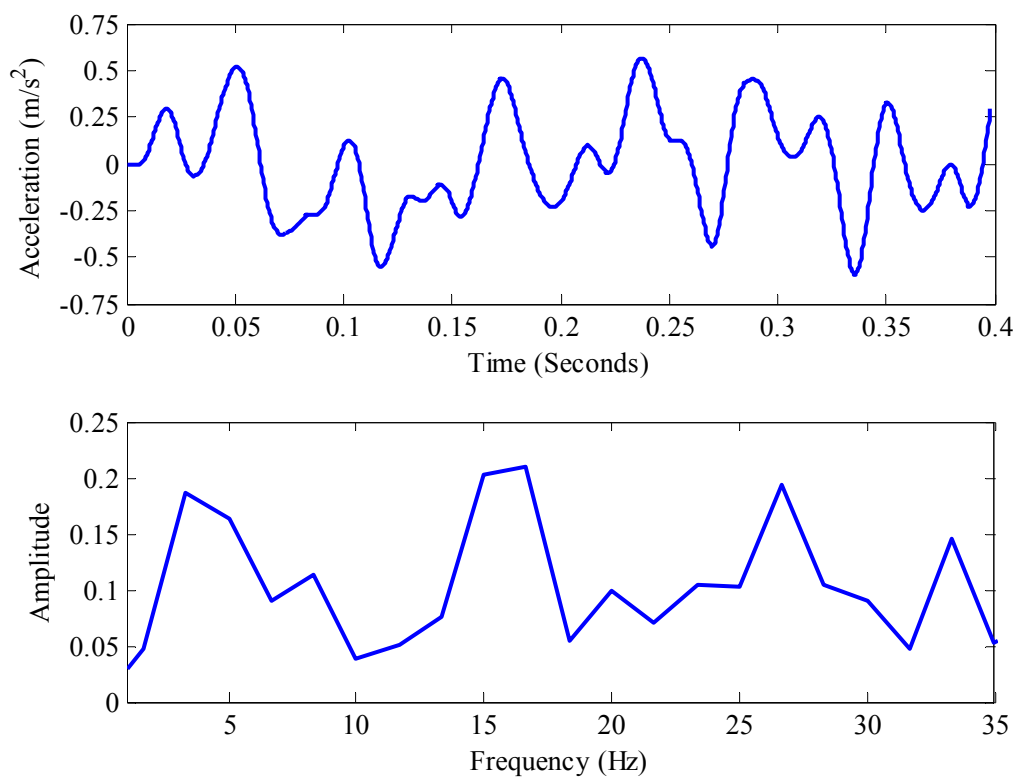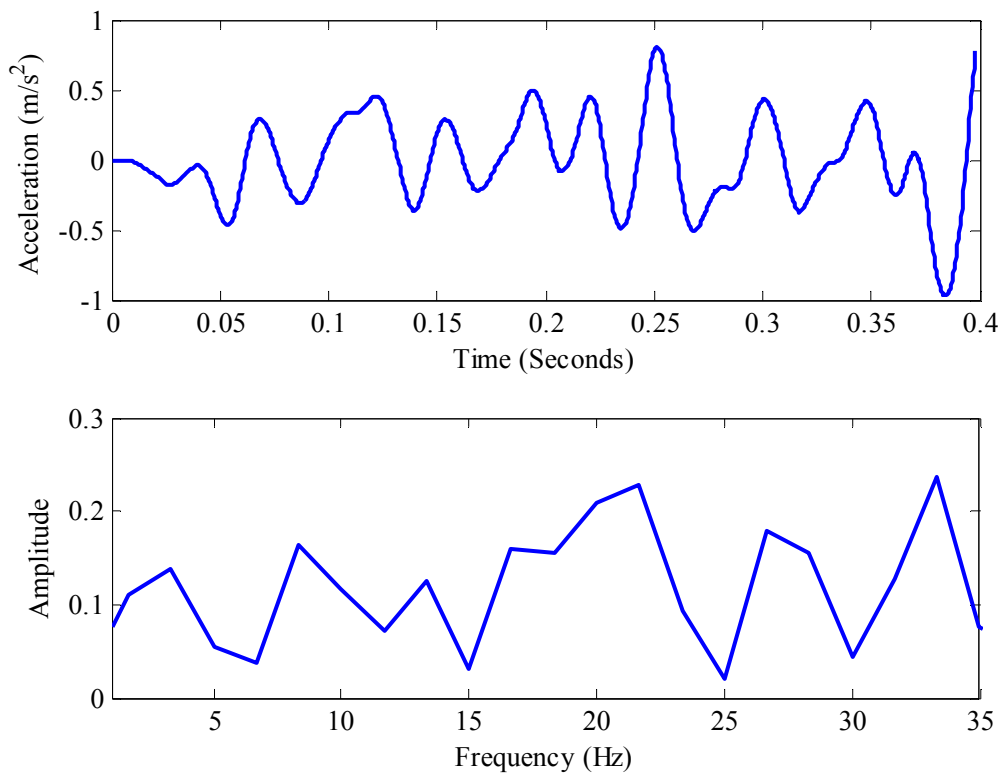Figure 6.8 Displacement signal and its frequency spectrum at 1000 rpm under L1 load case (healthy bearing).
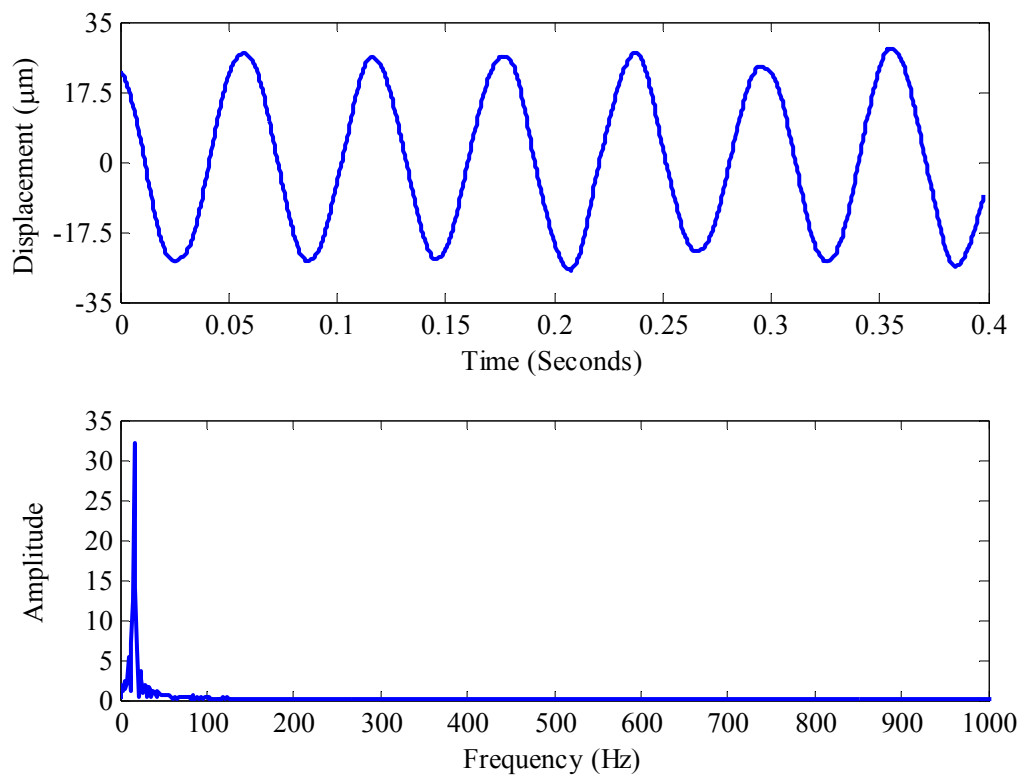
Figure 6.9 Displacement signal and its frequency spectrum at 1000 rpm under L2 load case (healthy bearing).

Displacement responses and the associated frequency spectrums for three different load cases at 2000 rpm are given in figures from 6.10 to 6.12. The shaft rotational frequency is 33.33 Hz. The shaft rotational frequency and its harmonics are seen in the frequency spectrums and some side bands also appear near the shaft frequency. The spectrum amplitude at the shaft frequency increases as the level of the shaft unbalance increases. On the other hand, some different frequencies appear in the frequency spectrum and they are interpretted as the structural components.
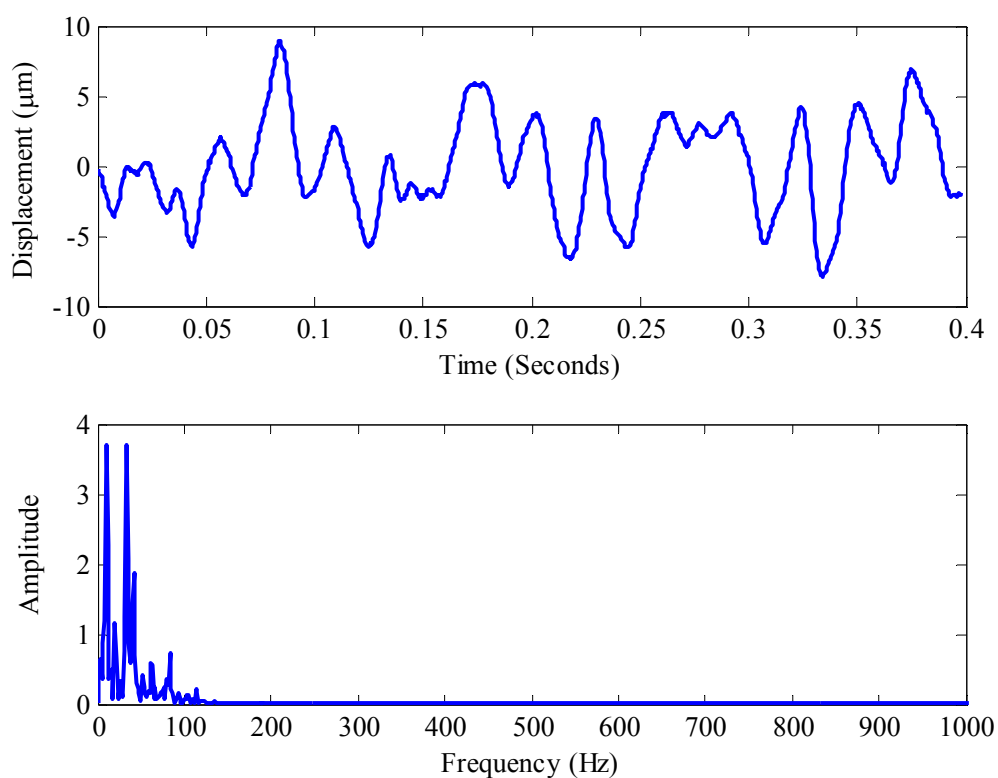
Figure 6.10 Displacement signal and its frequency spectrum at 2000 rpm under L0 load case (healthy bearing).
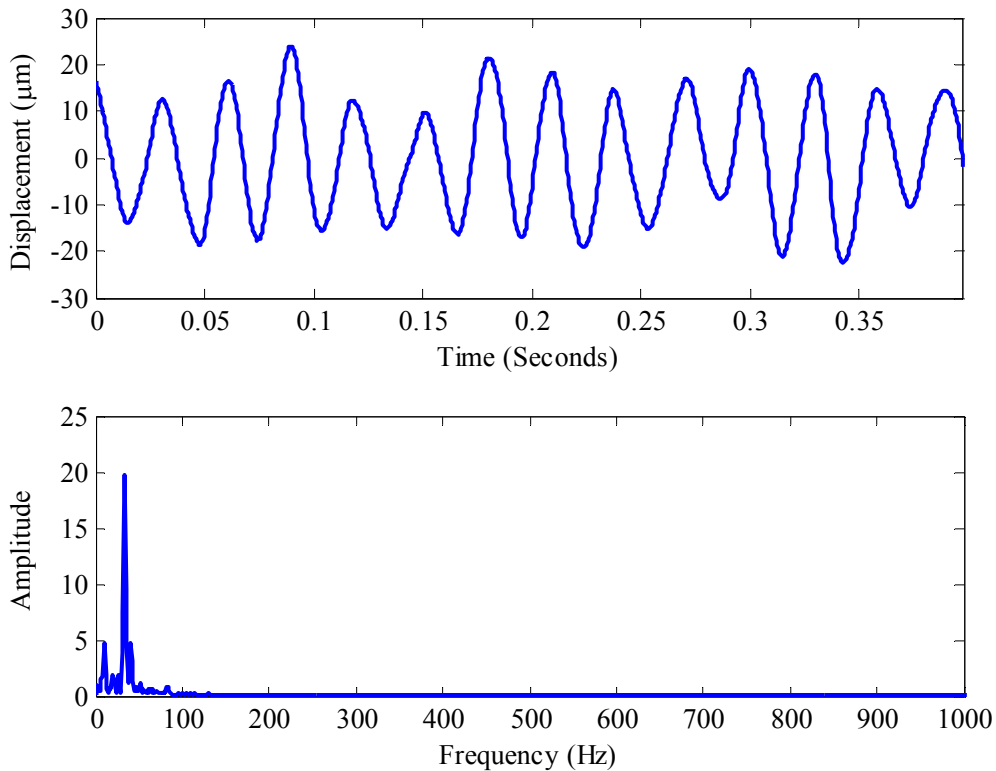
Figure 6.11 Displacement signal and its frequency spectrum at 2000 rpm under L1 load case (healthy bearing).
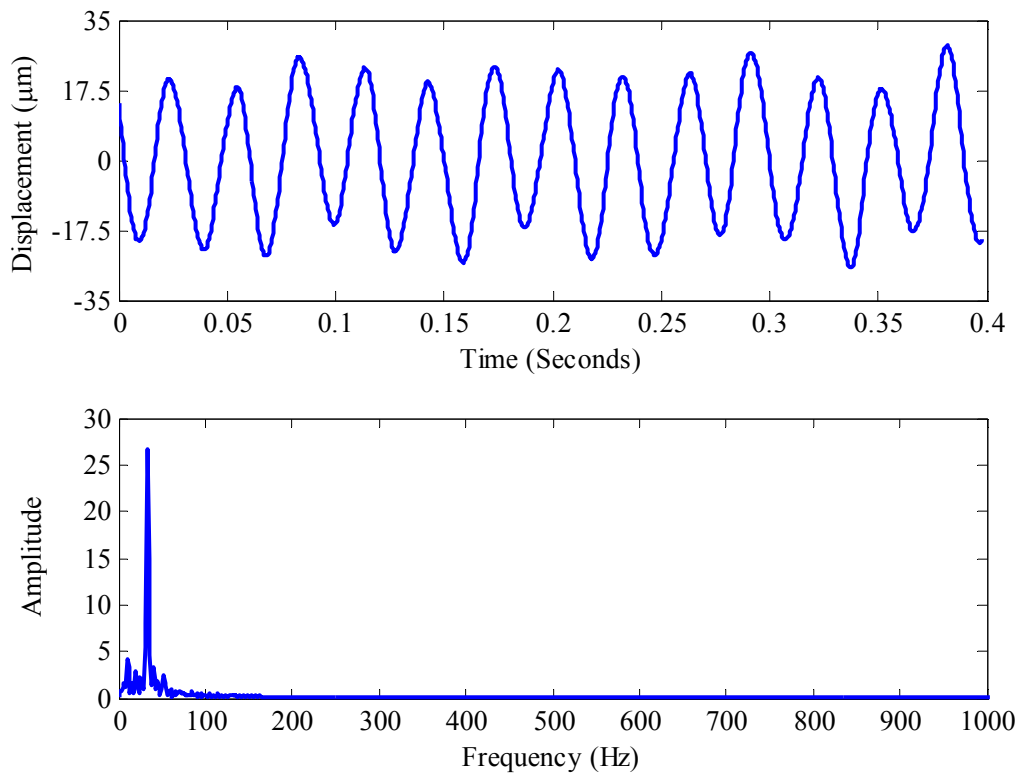
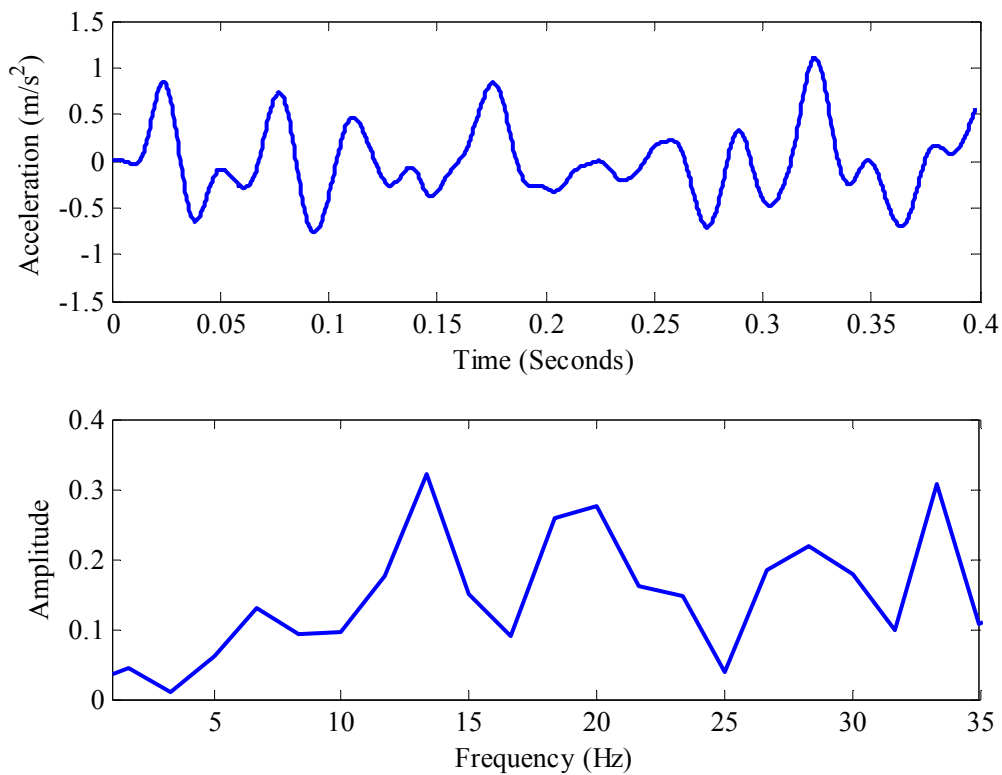Figure 6.12 Displacement signal and its frequency spectrum at 2000 rpm under L2 load case (healthy bearing).

6.4.1.2 Velocity Responses For Healthy Bearing

Velocity responses and their frequency spectrums at 1000 rpm are given for examined load cases in Figures 6.13-6.15. Shaft rotational frequency is 16.67 Hz at this speed. Shaft frequency can be seen in the frequency spectrum. Besides, there is a small peak at 480 Hz, which is one of the natural frequency of the test rig. The spectrum amplitudes increases as the unbalance increases. The pattern of the velocity response gets a harmonic form as the unbalance increases. There are some small peaks at about 700 Hz and these peaks can be attributed to the structural frequencies.
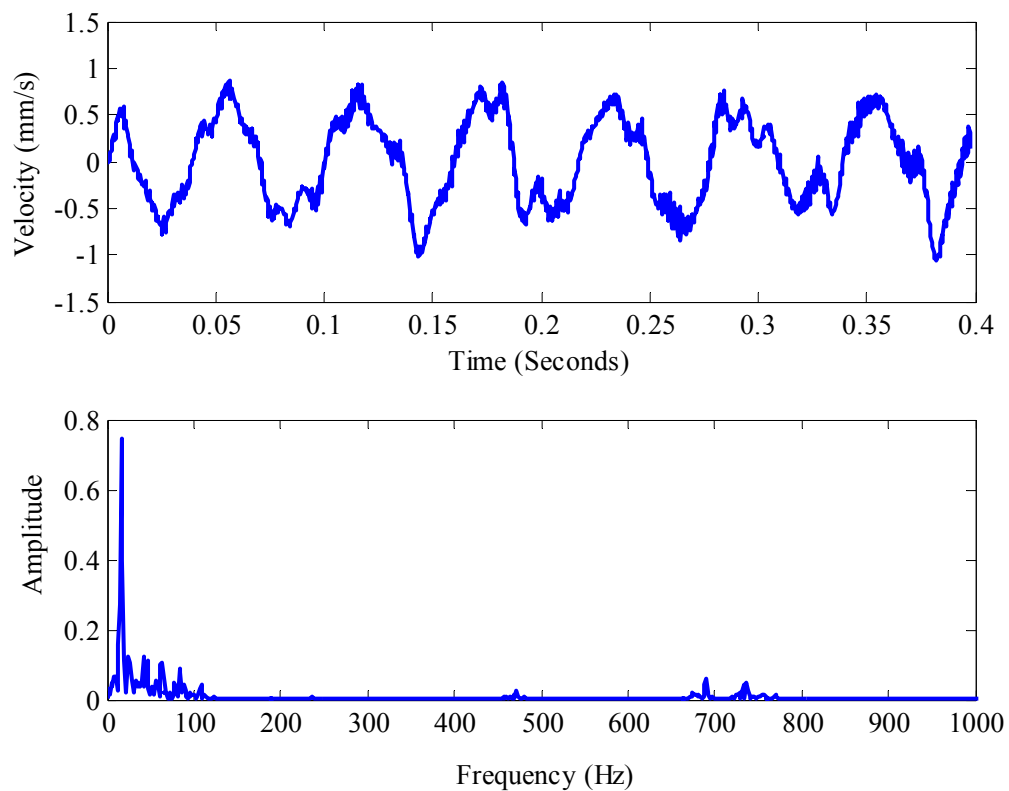
Figure 6.13 Velocity signal and its frequency spectrum at 1000 rpm under L0 load case (healthy bearing).
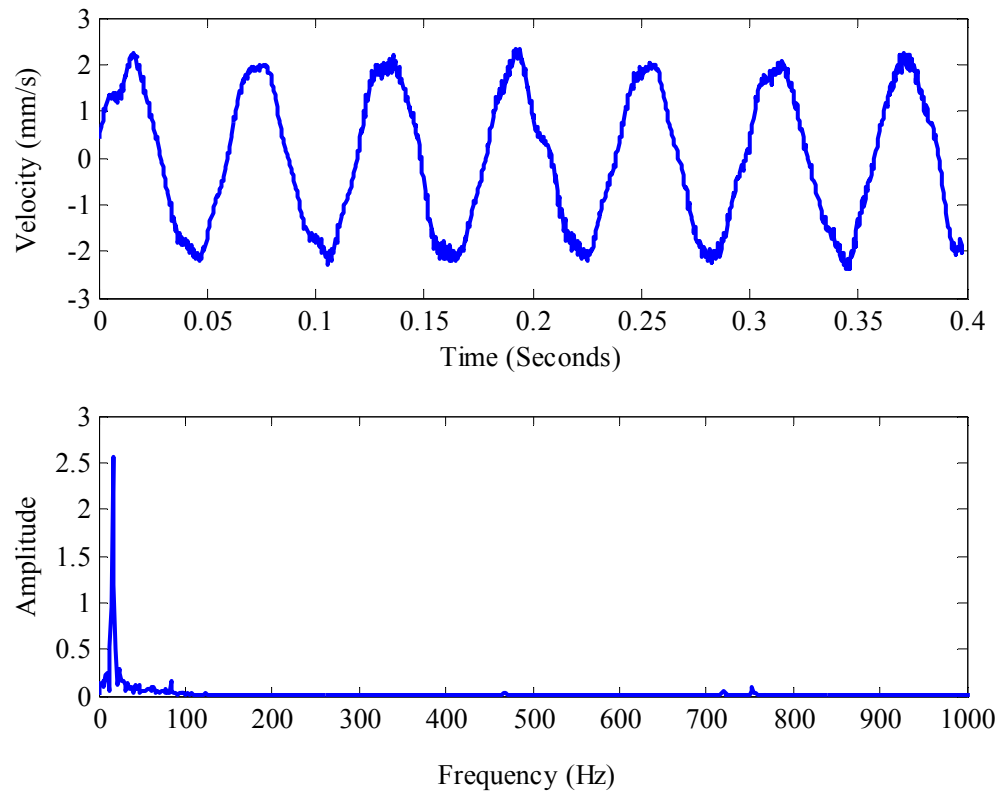
Figure 6.14 Velocity signal and its frequency spectrum at 1000 rpm under L1 load case (healthy bearing).
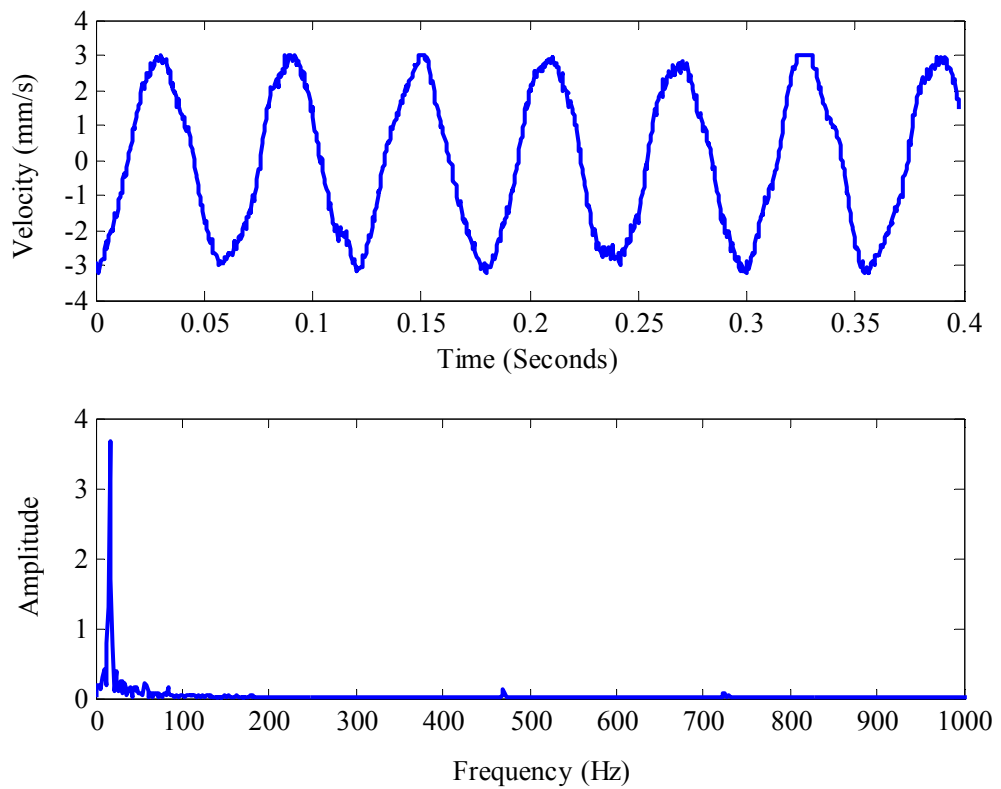
Figure 6.15 Velocity signal and its frequency spectrum at 1000 rpm under L2 load case (healthy bearing).

Velocity responses and their frequency spectrums at 2000 rpm are given for examined load cases in Figures 6.16-6.18. Shaft rotational frequency is 33.33 Hz at this speed. The same observations obtained for 1000 rpm are valid for 2000 rpm.
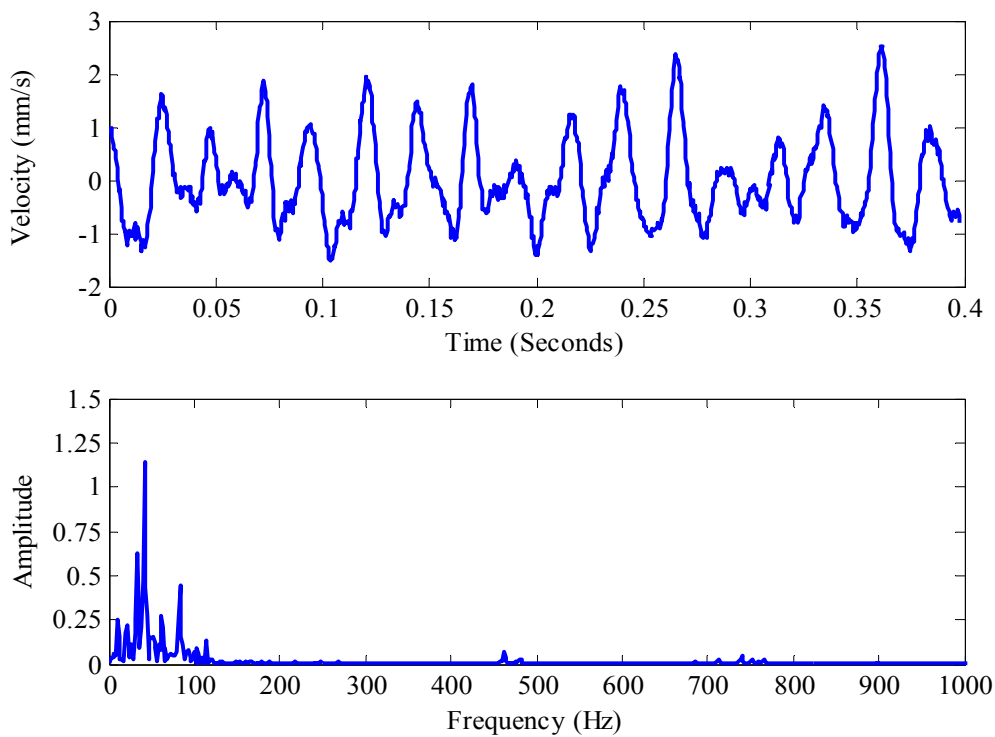
Figure 6.16 Velocity signal and its frequency spectrum at 2000 rpm under L0 load case (healthy bearing).
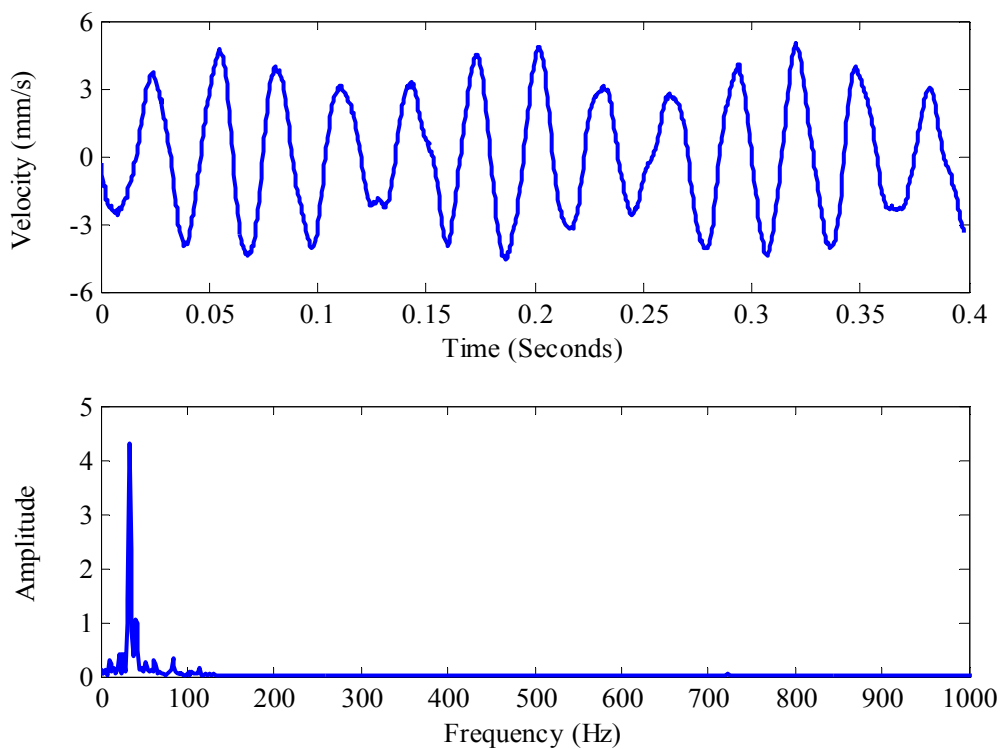
Figure 6.17 Velocity signal and its frequency spectrum at 2000 rpm under L1 load case (healthy bearing).
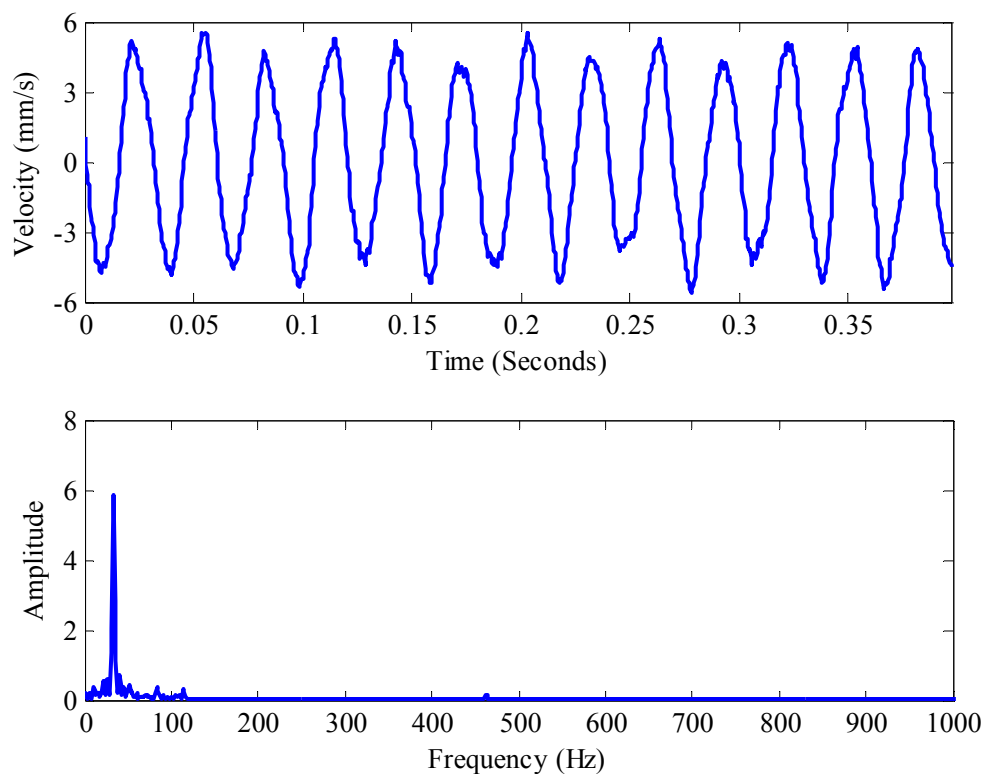
Figure 6.18 Velocity signal and its frequency spectrum at 2000 rpm under L2 load case (healthy bearing).

6.4.1.3 Acceleration Responses for Healthy Bearing

Acceleration responses and their frequency spectrums at 1000 rpm are given for healthy bearing in Figures 6.19-6.21. Shaft frequency is 16.67 Hz for 1000 rpm shaft speed and it appears in the frequency spectrum clearly. On the other hand, the peaks at 480 Hz and around 700 Hz can be seen with large amplitudes. The spectrum amplitude at shaft frequency increases as the level of unbalance increases. As seen from the figures, high frequency components dominate the frequency spectrum.

The acceleration response has also a harmonic pattern combined with the high frequency structural componnets. This is the general nature of the the acceleration responses. Acceleration responses and their frequency spectrums at 2000 rpm is given in Figures 6.22-6.24. The frequency spectrum for 2000 rpm is more complex than those of 1000 rpm.
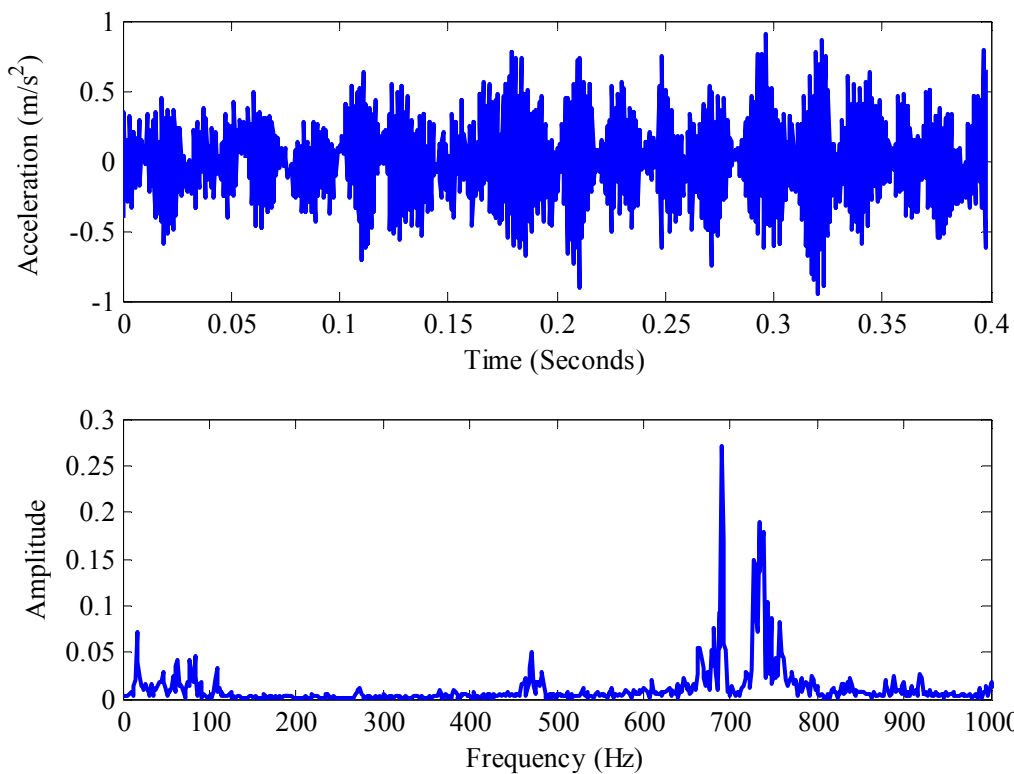
Figure 6.19 Acceleration signal and its frequency spectrum at 1000 rpm under L0 load case (healthy bearing).
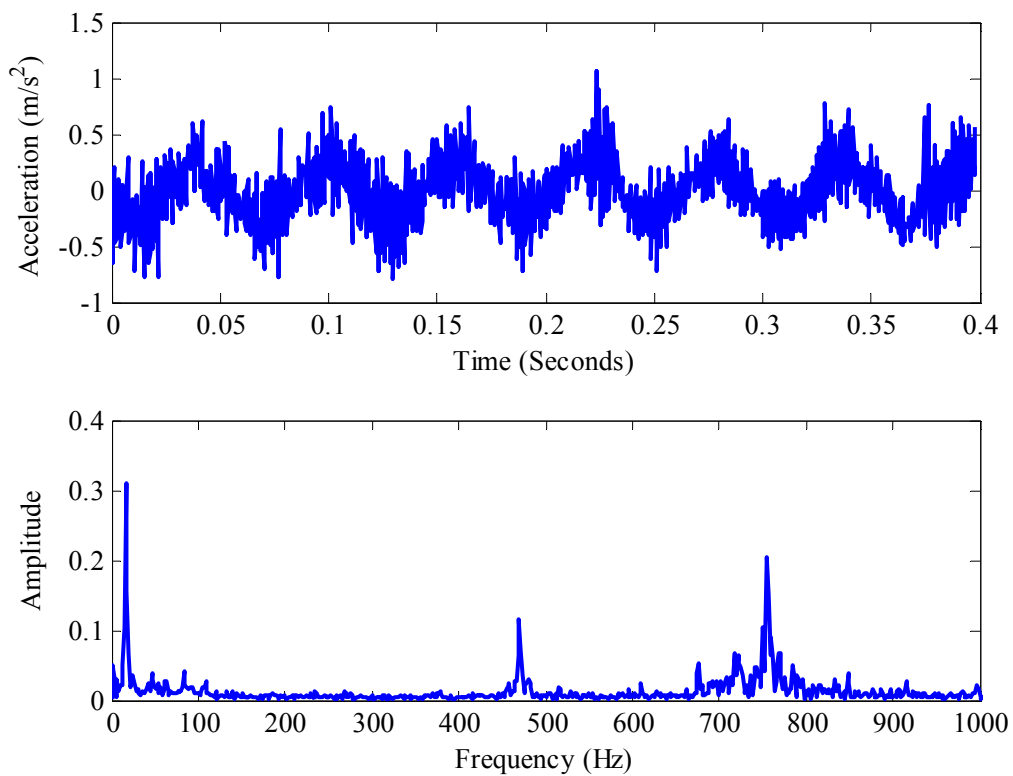
Figure 6.20 Acceleration signal and its frequency spectrum at 1000 rpm under L1 load case (healthy bearing).
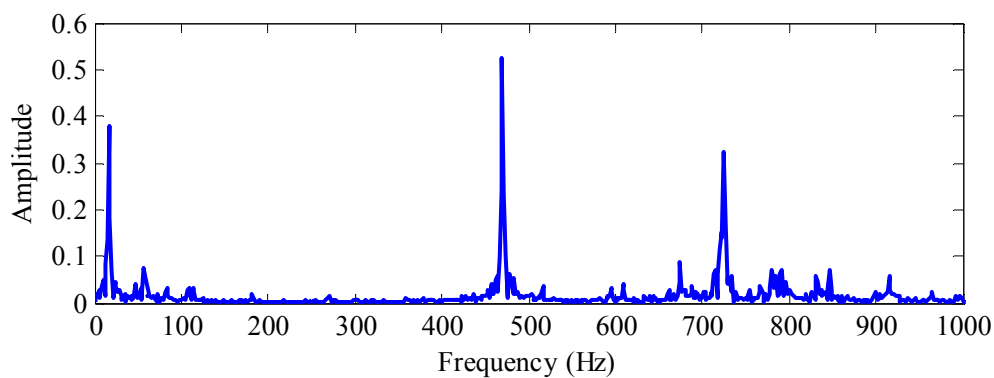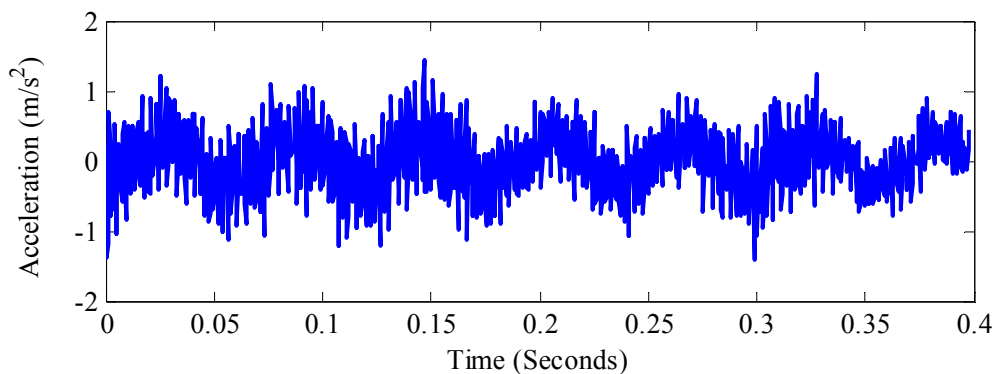
Figure 6.21 Acceleration signal and its frequency spectrum at 1000 rpm under L2 load case (healthy bearing).
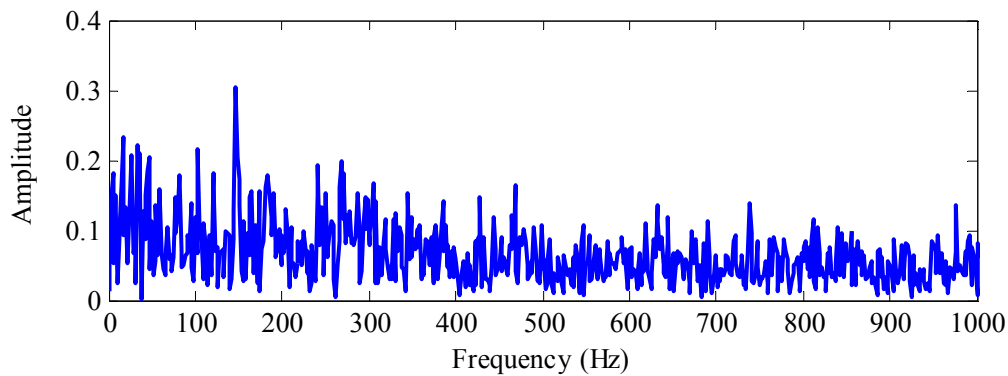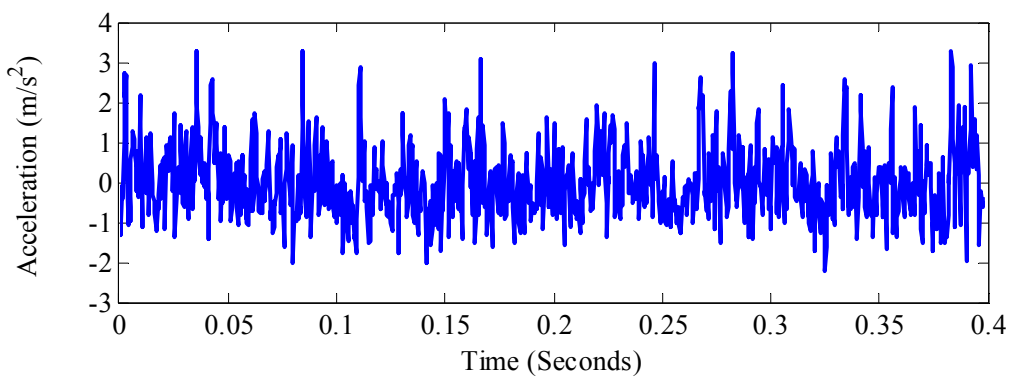
Figure 6.22 Acceleration signal and its frequency spectrum at 2000 rpm under L0 load case (healthy bearing).
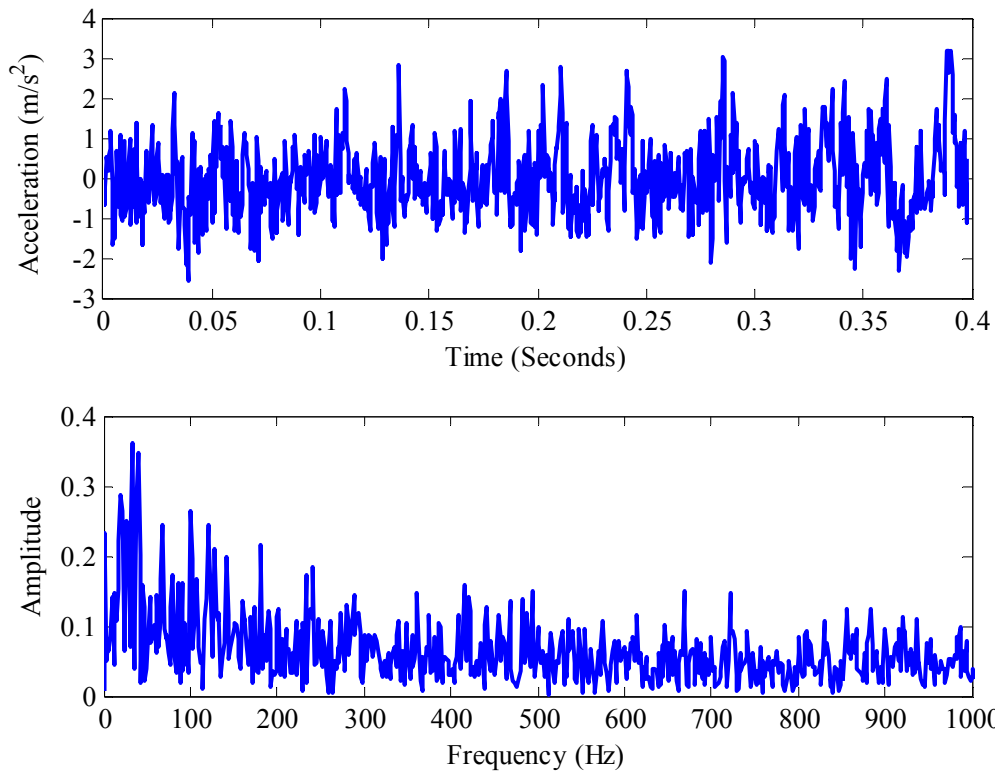
Figure 6.23 Acceleration signal and its frequency spectrum at 2000 rpm under L1 load case (healthy bearing).
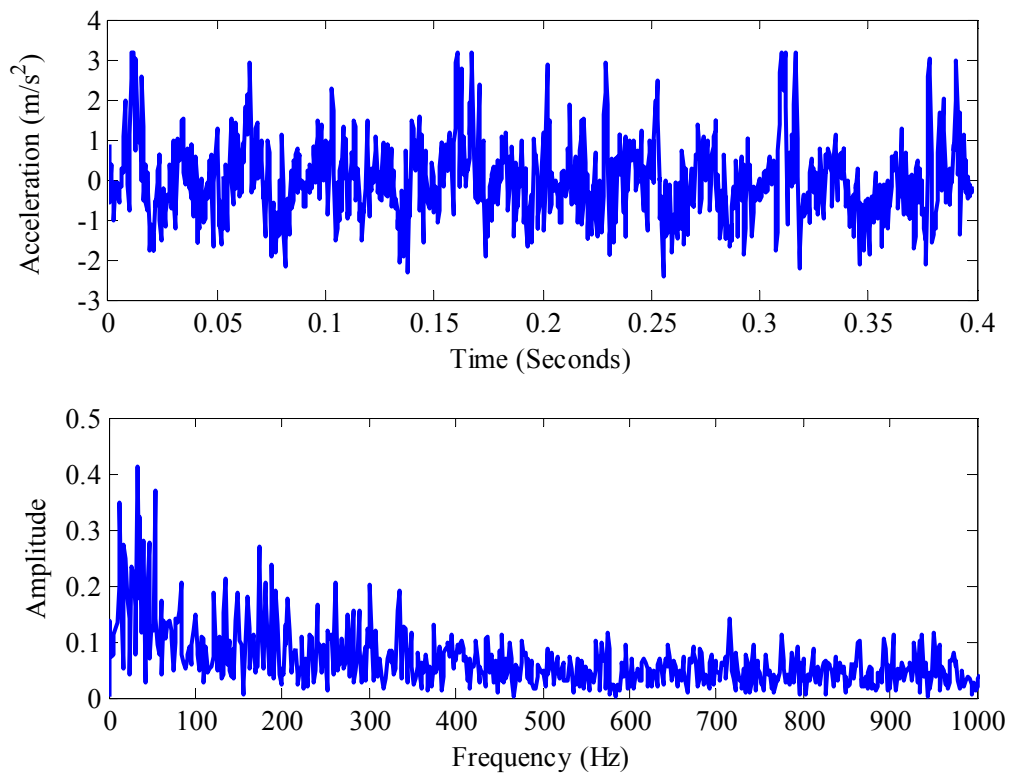
Figure 6.24 Acceleration signal and its frequency spectrum at 2000 rpm under L2 load case (healthy bearing).

6.4.2 Vibration Responses for Outer Race Defect Case

In this section, the vibration responses and the associated frequency spectrums for the outer race defect case measured at 1000 rpm and 2000 rpm are given for different load cases.

6.4.2.1 Displacement Responses for Outer Race Defect Case

Displacement responses at 1000 rpm shaft speed and their frequency spectrums are given for different load cases in figures form 6.25 to 6.27. The shaft frequency is seen in the frequency spectrums with increasing FFT magnitudes due to the increasing unbalance. The outer race defect frequency is 59.769 Hz at 1000 rpm and there is small peak showing this defect frequency. The outer race defect frequency can not be seen for L1 and L2 load cases.
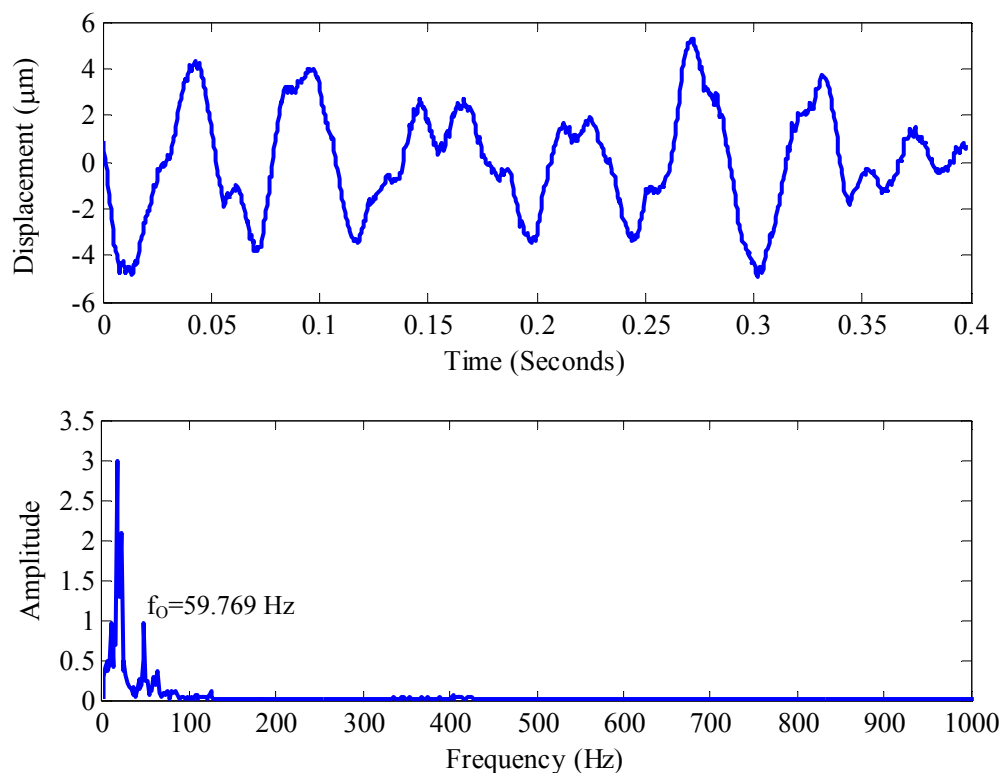
Figure 6.25 Displacement signal and its frequency spectrum at 1000 rpm under L0 load case (outer race defect).
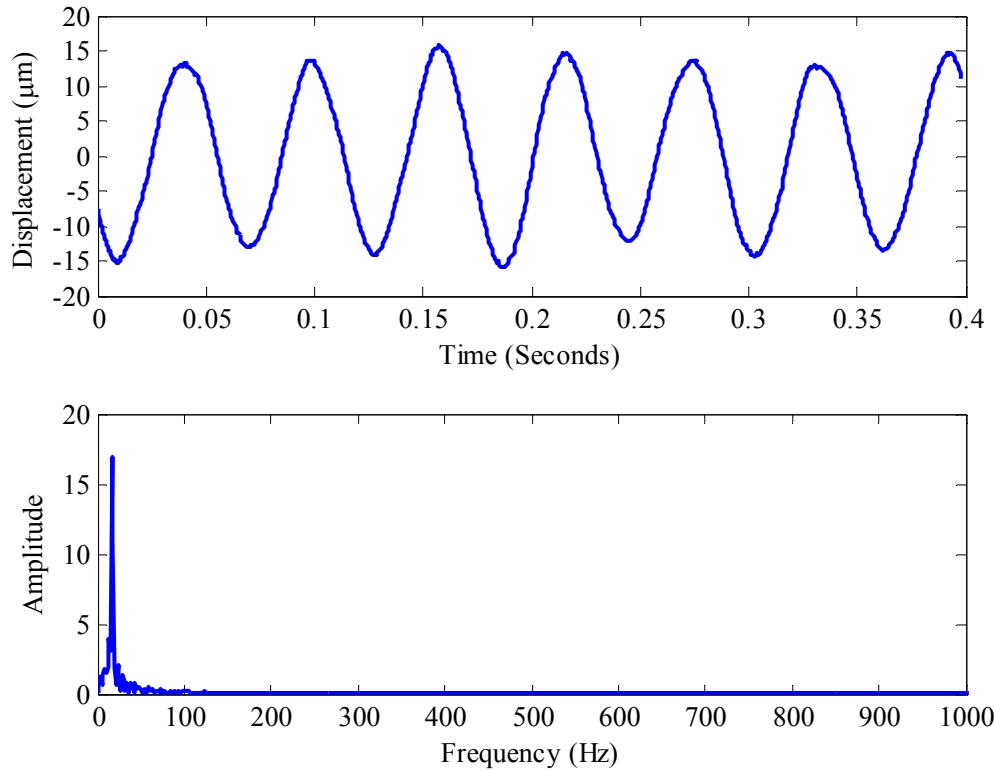
Figure 6.26 Displacement signal and its frequency spectrum at 1000 rpm under L1 load case (outer race defect).
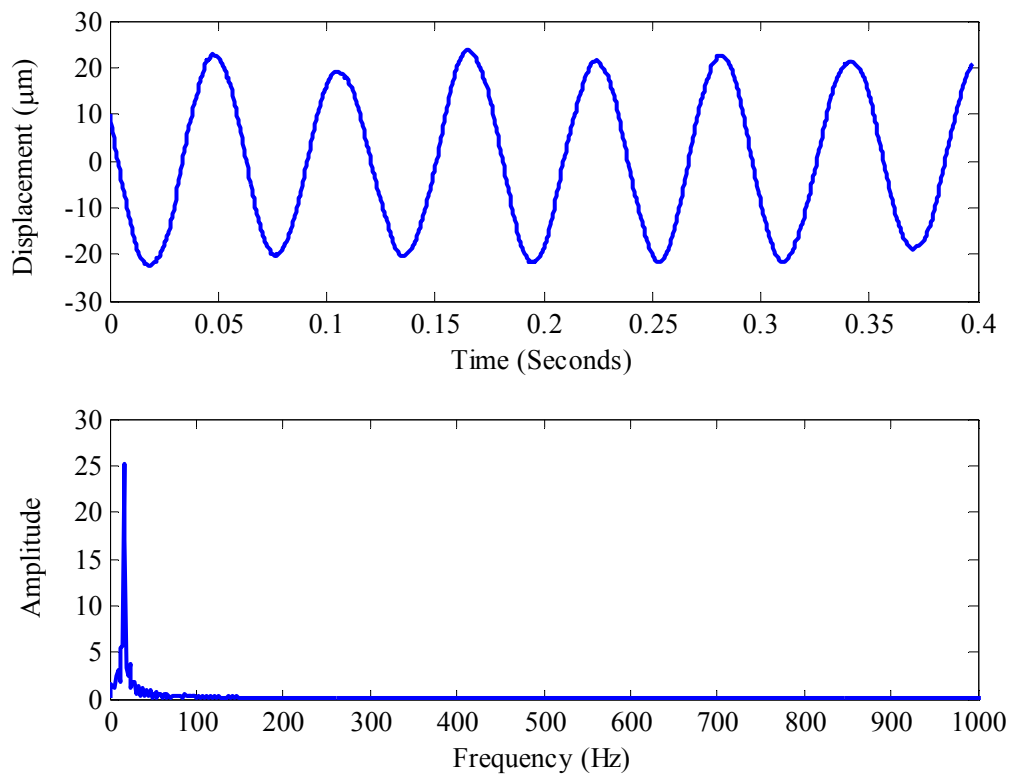
Figure 6.27 Displacement signal and its frequency spectrum at 1000 rpm under L2 load case (outer race defect).

Displacement responses at 2000 rpm shaft speed and their frequency spectrums are examined for varying load cases in Figures 6.28-6.30. The outer race defect frequeny is 119.538 Hz for 2000 rpm shaft speed. The shaft frequency and the outer race defect frequency are observed for L0 load case in Figure 6.28. There are two peaks at 11 Hz and 21 Hz representing the natural frequencies in horizontal and vertical directions, respectively. The outer race defect frequency is not observed for L1 and L2 load cases.
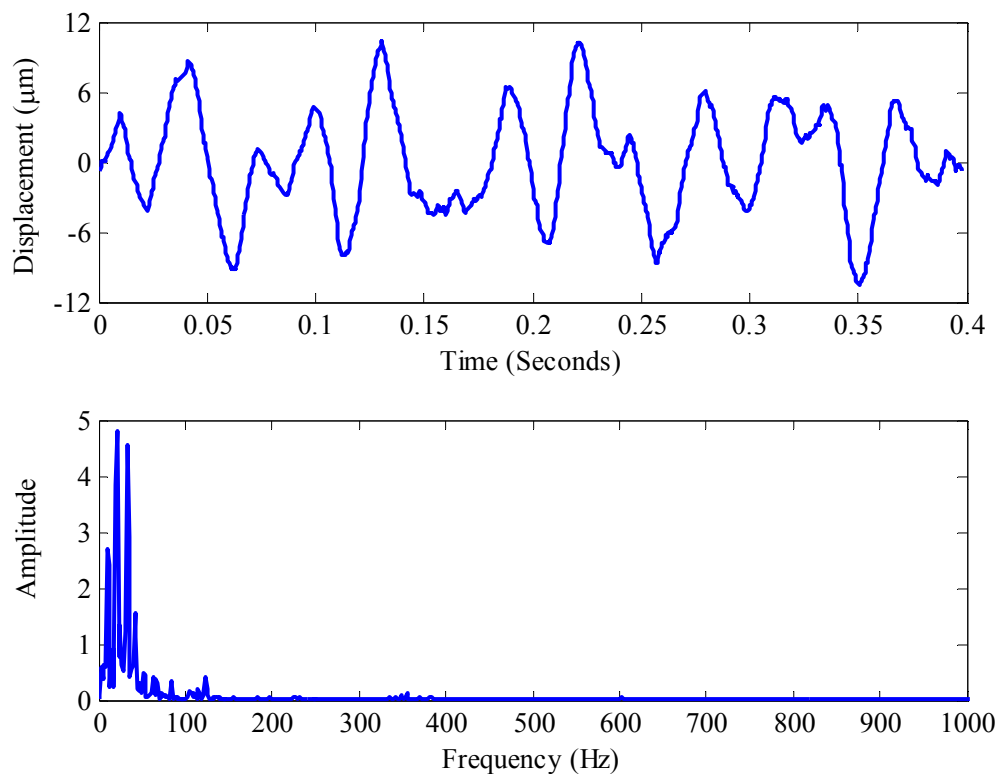
Figure 6.28 Displacement signal and its frequency spectrum at 2000 rpm under L0 load case (outer race defect).
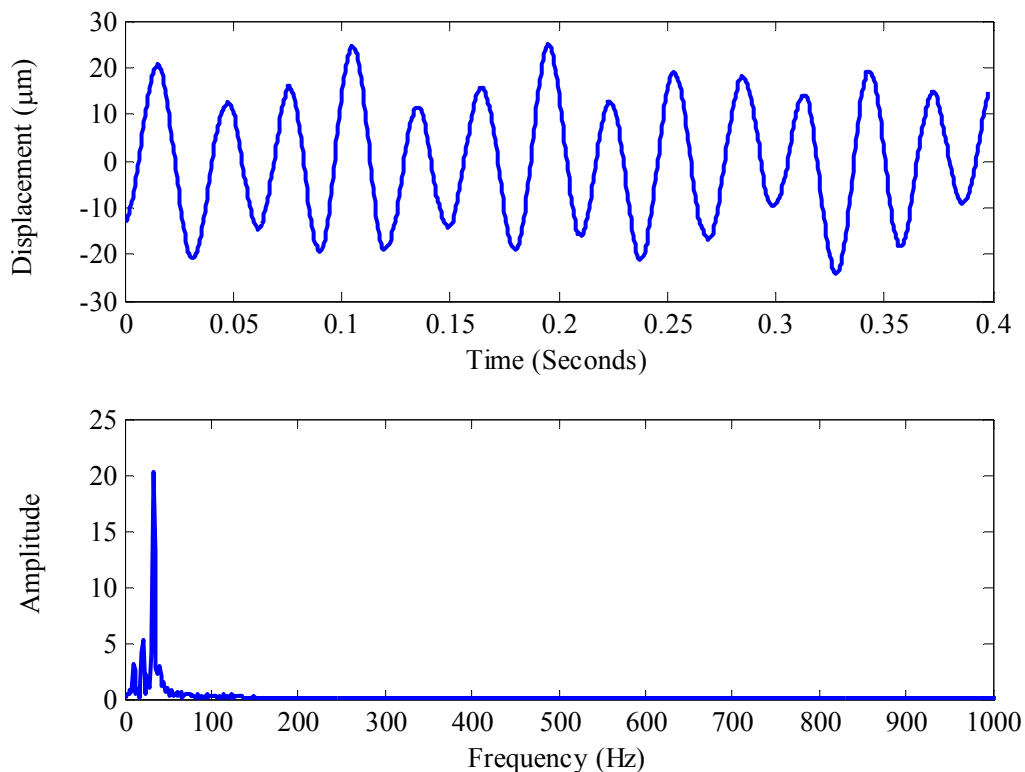
Figure 6.29 Displacement signal and its frequency spectrum at 2000 rpm under L1 load case (outer race defect).
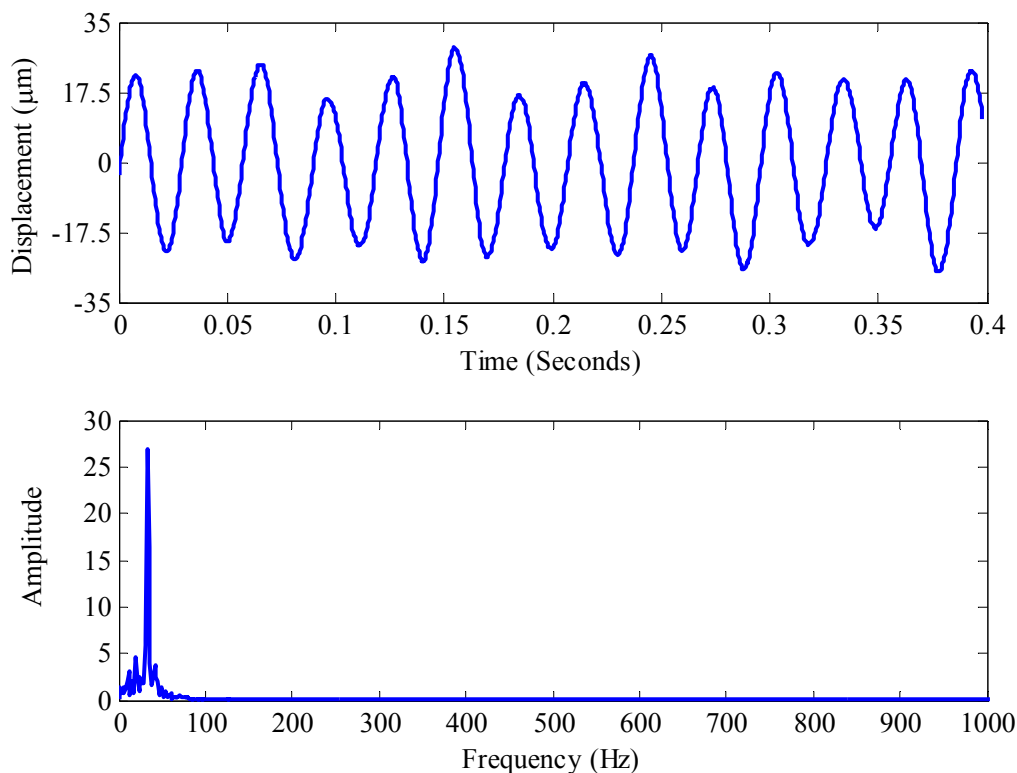
Figure 6.30 Displacement signal and its frequency spectrum at 2000 rpm under L2 load case (outer race defect).

6.4.2.2 Velocity Responses for Outer Race Defect Case

Velocity responses at 1000 rpm shaft speed and their frequency spectrums are given for examined load cases in Figures 6.31-6.33. The outer race defect frequency is 59.769 Hz for 1000 rpm shaft speed. The natural frequency in vertical direction and the outer race defect frequency can be seen in the frequency spectrum given in Figure 6.31. The outer race defect frequency can not be seen in the frequency spectrums for L1 and L2 load cases.
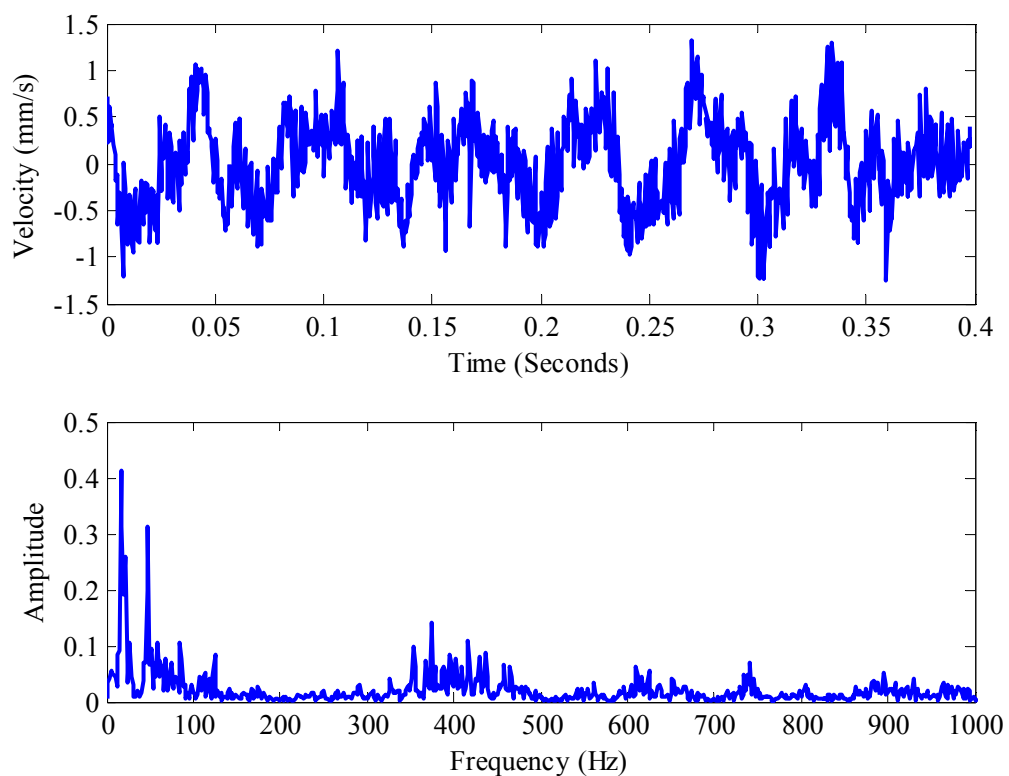
Figure 6.31 Velocity signal and its frequency spectrum at 1000 rpm under L0 load case (outer race defect).
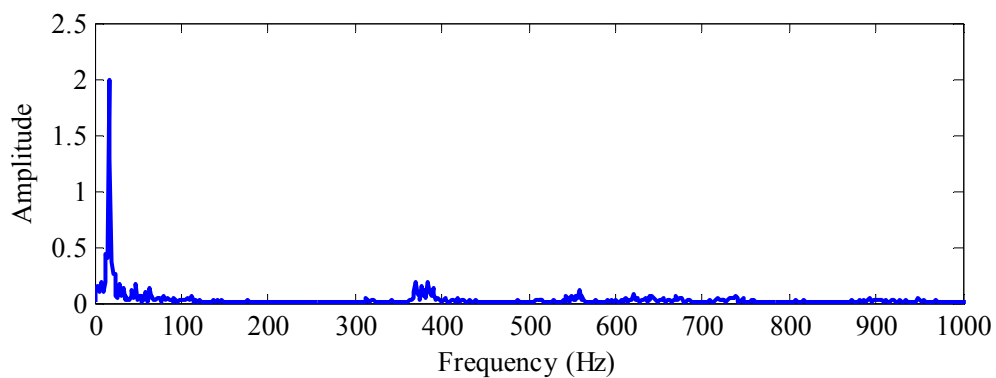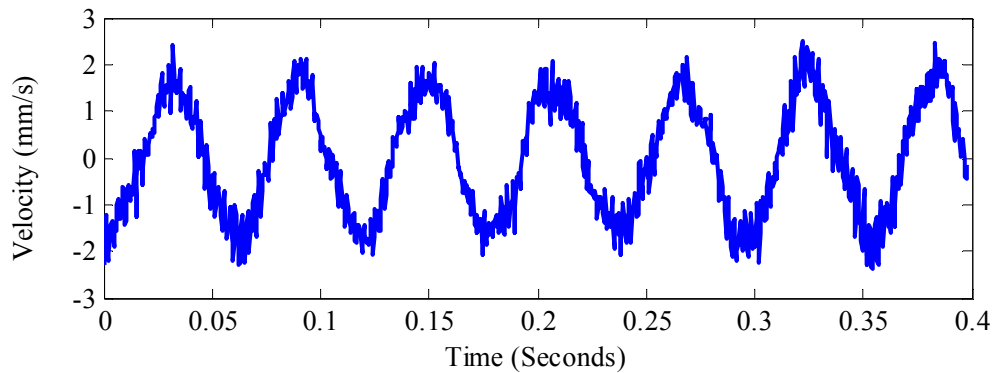
Figure 6.32 Velocity signal and its frequency spectrum at 1000 rpm under L1 load case (outer race defect).
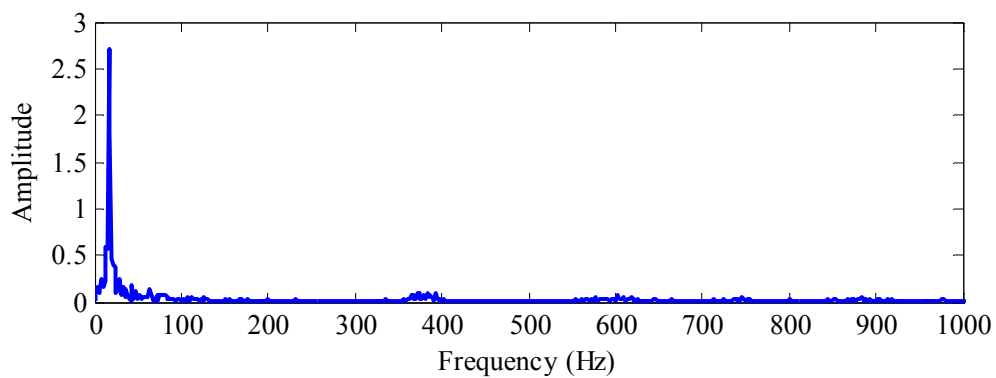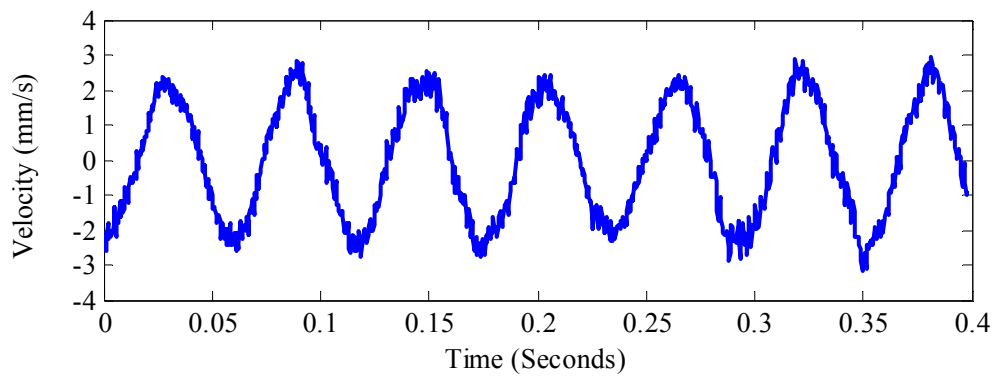
Figure 6.33 Velocity signal and its frequency spectrum at 1000 rpm under L2 load case (outer race defect).

Velocity responses at 2000 rpm shaft speed and their frequency spectrums are given in Figures 6.34-6.36. The outer race defect frequency can be seen in the frequency spectrum for L0 load case.
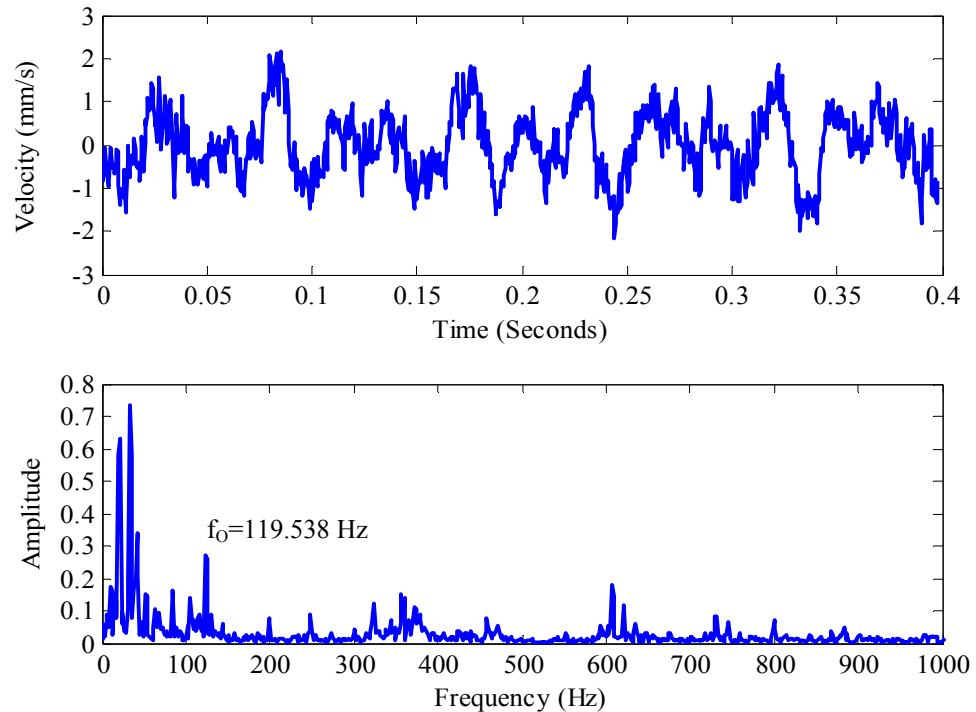
Figure 6.34 Velocity signal and its frequency spectrum at 2000 rpm under L0 load case (outer race defect).
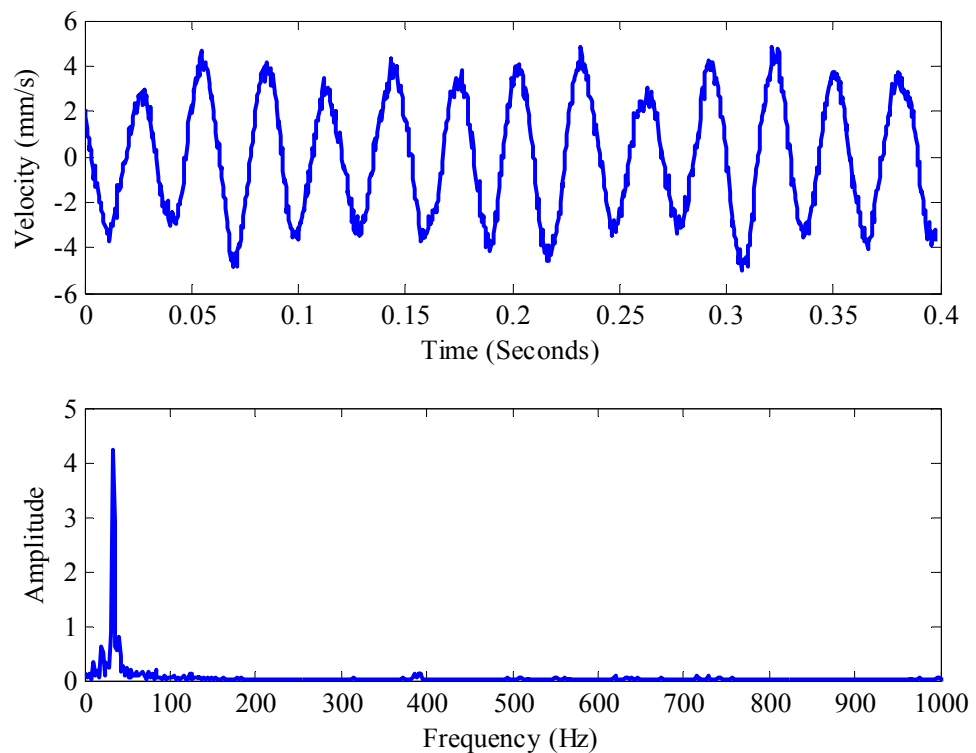
Figure 6.35 Velocity signal and its frequency spectrum at 2000 rpm under L1 load case (outer race defect).
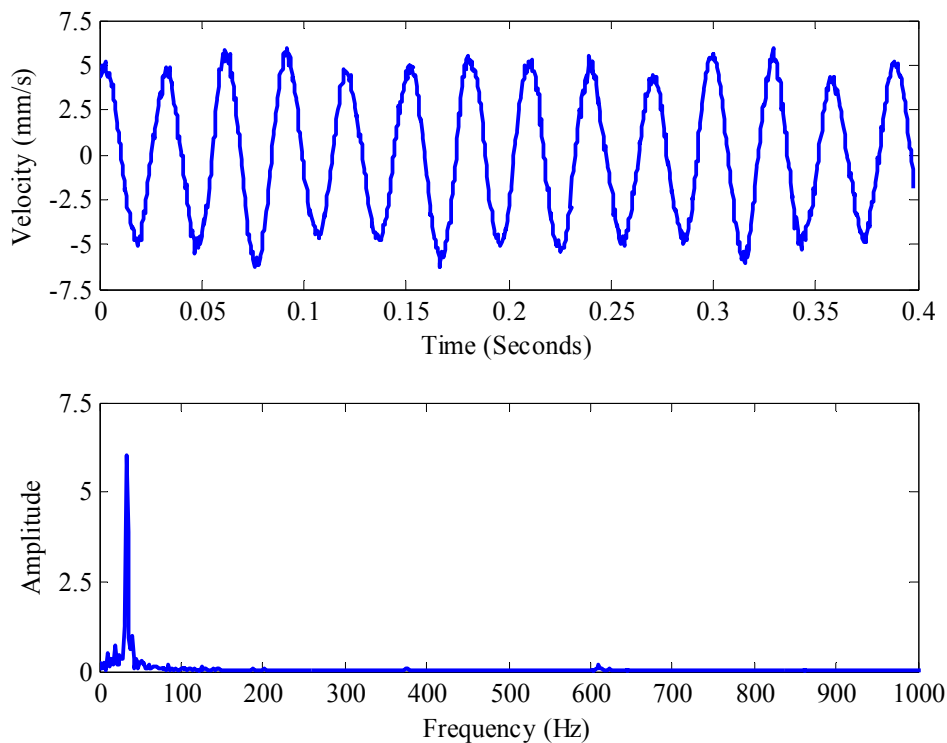
Figure 6.36 Velocity signal and its frequency spectrum at 2000 rpm under L2 load case (outer race defect).

6.4.2.3 Acceleration Responses for Outer Race Defect Case

Acceleration responses at 1000 rpm shaft speed and their frequency spectrums are given in Figures 6.37-6.39 for outer race defect case.
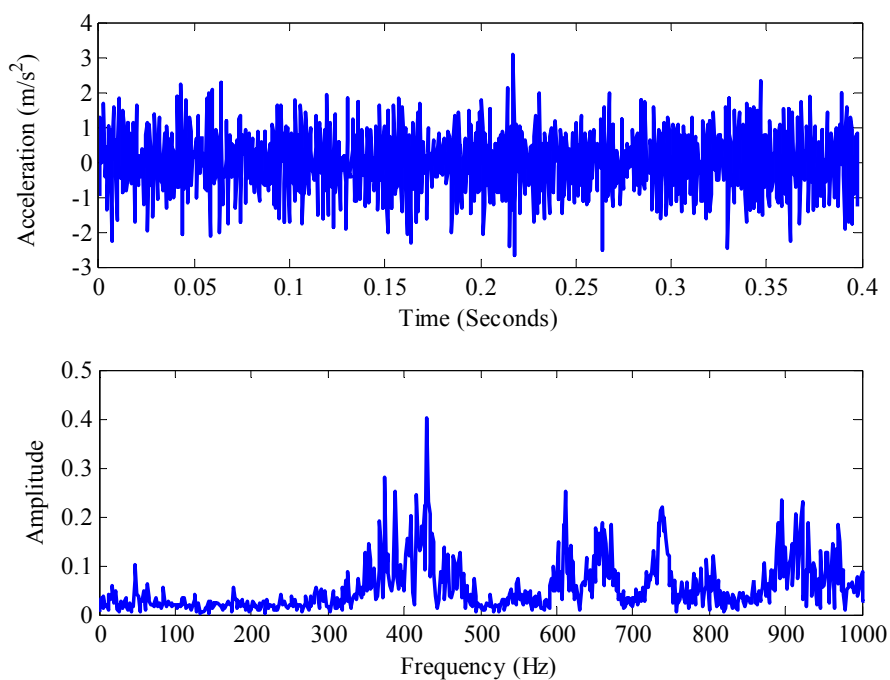
Figure 6.37 Acceleration signal and its frequency spectrum at 1000 rpm under L0 load case (outer race defect).
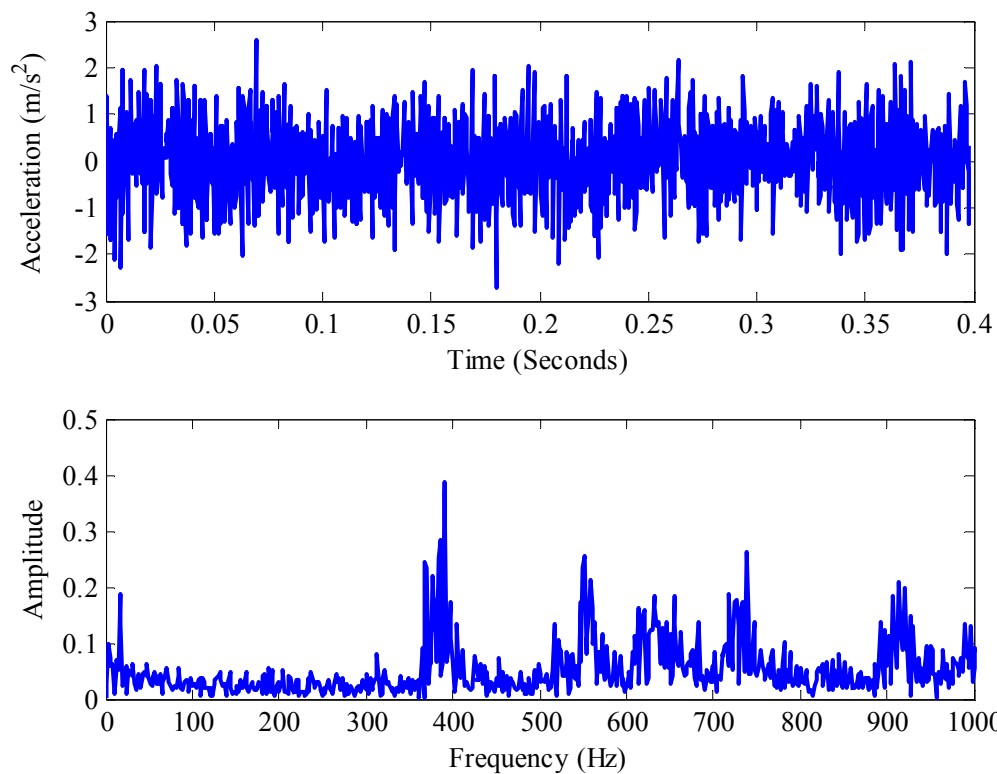
Figure 6.38 Acceleration signal and its frequency spectrum at 1000 rpm under L1 load case (outer race defect).
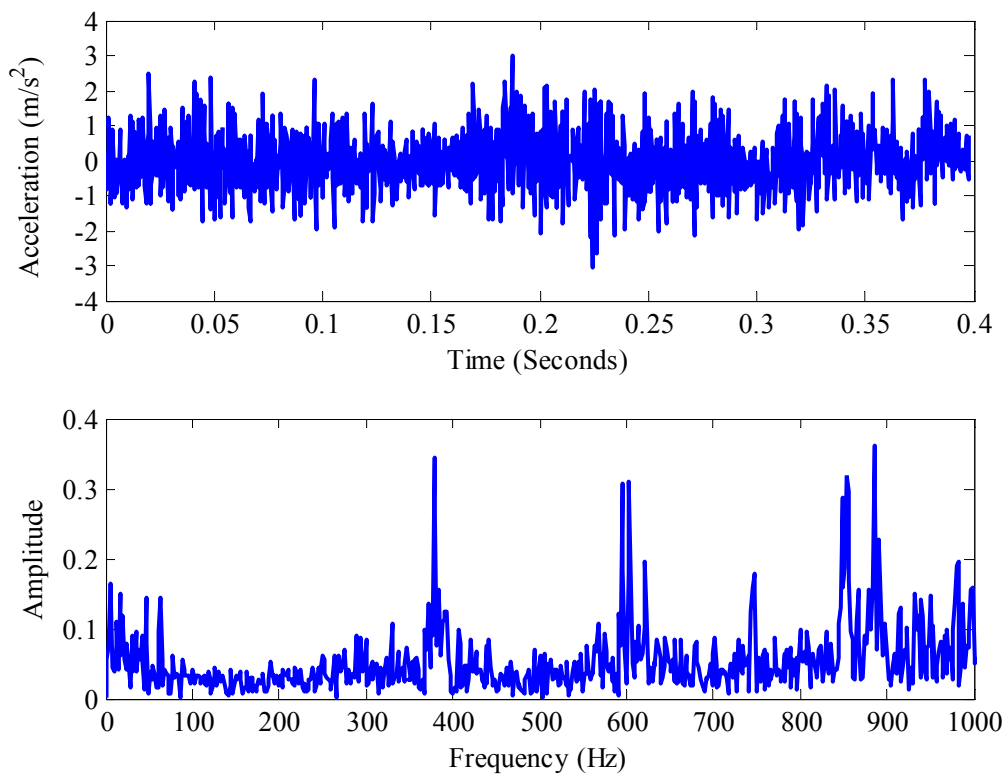
Figure 6.39 Acceleration signal and its frequency spectrum at 1000 rpm under L2 load case (outer race defect).

Acceleration responses at 2000 rpm shaft speed and their frequency spectrums are given in Figures 6.40-6.42. The outer race defect frequency appears in the frequency spectrum for L0 load case.
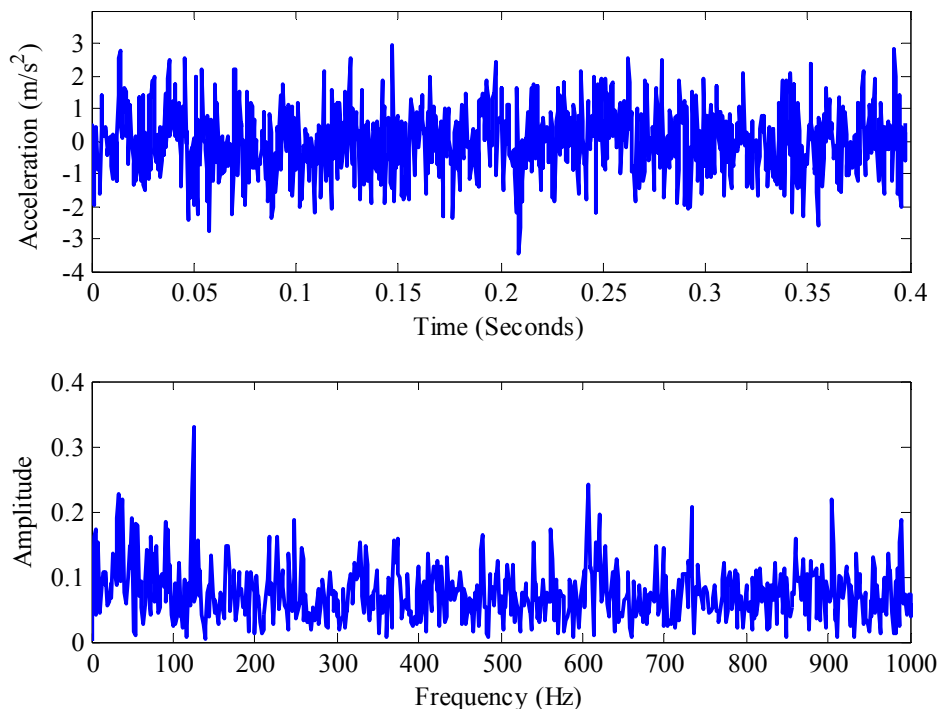
Figure 6.40 Acceleration signal and its frequency spectrum at 2000 rpm under L0 load case (outer race defect).
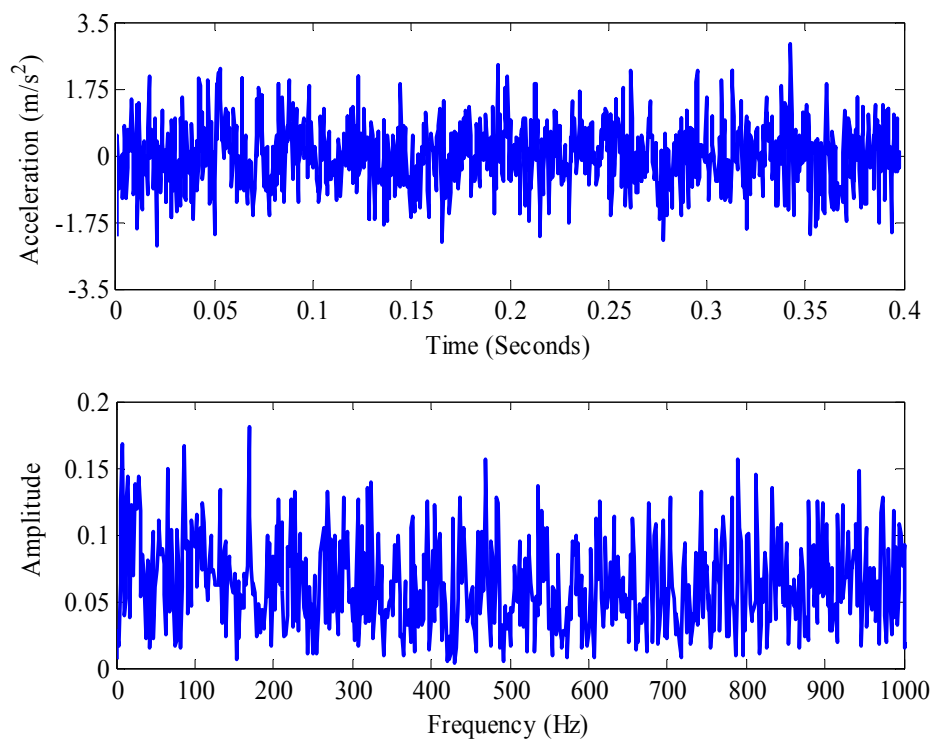
Figure 6.41 Acceleration signal and its frequency spectrum at 2000 rpm under L1 load case (outer race defect).
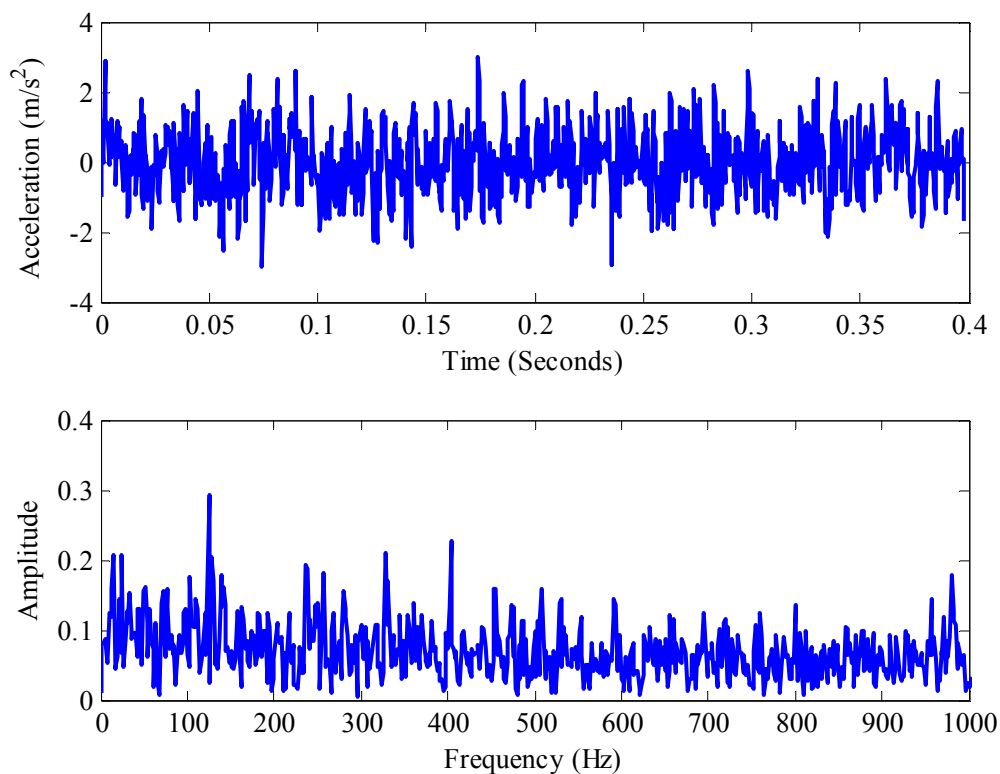
Figure 6.42 Acceleration signal and its frequency spectrum at 2000 rpm under L2 load case (outer race defect).

6.4.3 Vibration Responses for Inner Race Defect Case

In this section, the vibration responses and related frequency spectrums for inner race defect case are given under L0, L1 and L2 load cases at 1000 rpm and 2000 rpm shaft speeds.

6.4.3.1 Displacement Responses for Inner Race Defect Case

Displacement responses for iner race defect case at 1000 rpm shaft speed and their frequency spectrums are given in Figures 6.43-6.45 for different load cases. The shaft frequency can be seen clearly in all frequency spectrums. The spectrum amplitudes increases as the unbalance increases. Inner race defect frequeny is 90.230 Hz for 1000 rpm shaft speed and can not be seen clearly in the frequency spectrums for all load cases.
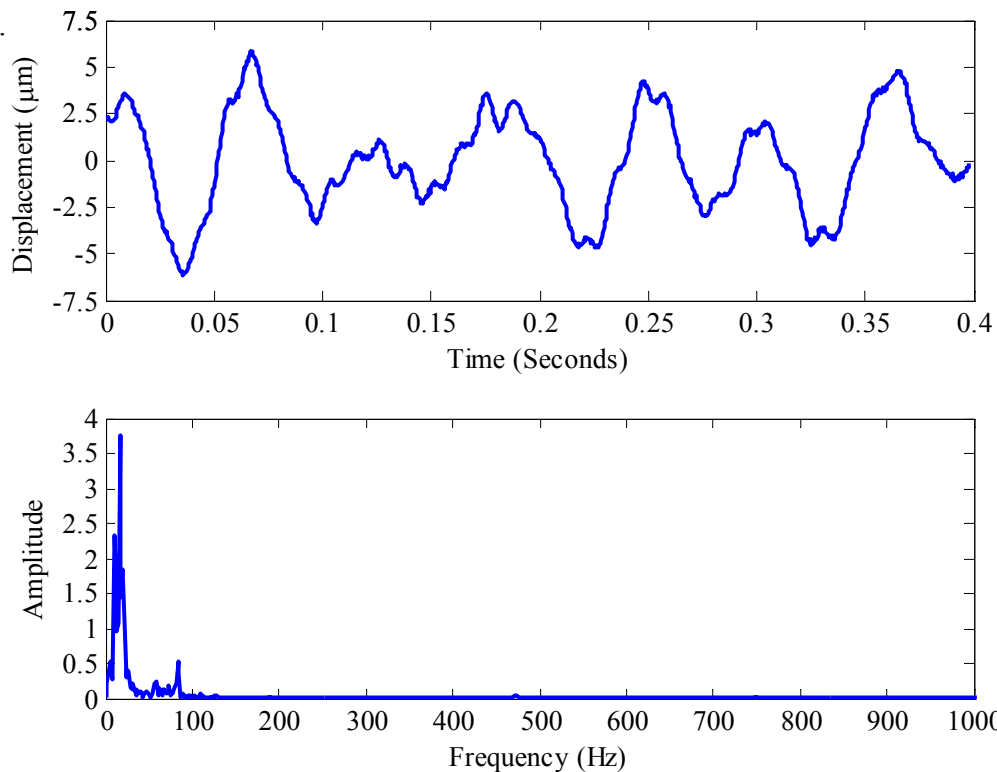
Figure 6.43 Displacement signal and its frequency spectrum at 1000 rpm under L0 load case (inner race defect).
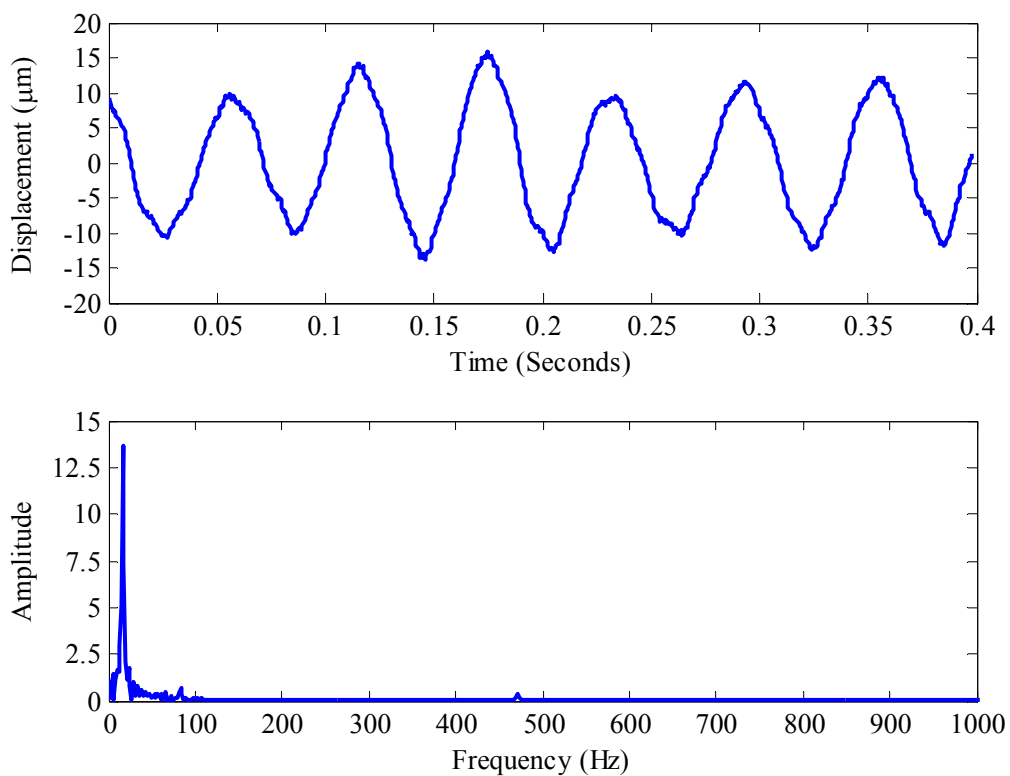
Figure 6.44 Displacement signal and its frequency spectrum at 1000 rpm under L1 load case (inner race defect).
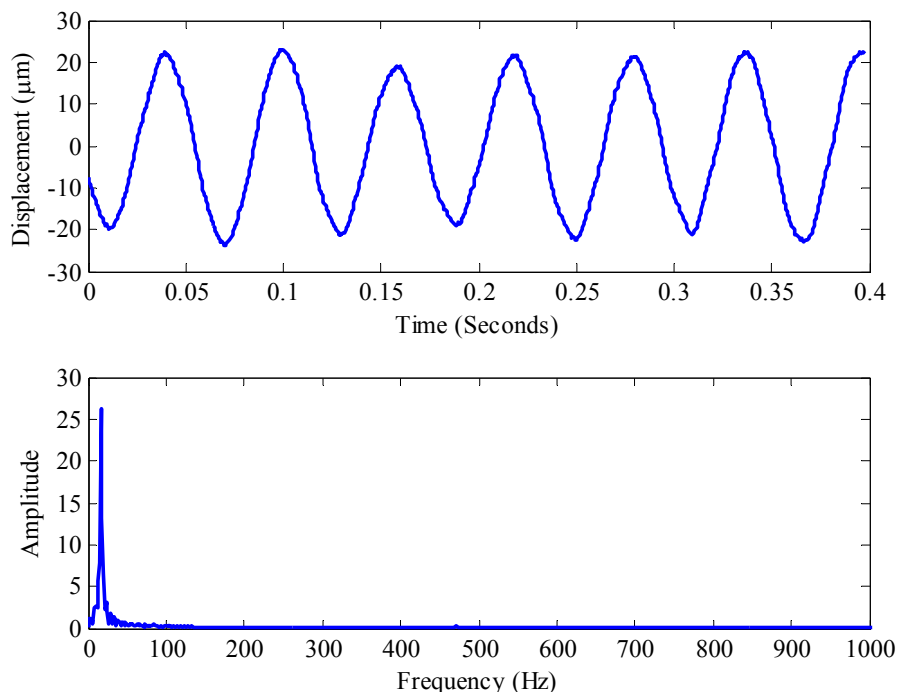
Figure 6.45 Displacement signal and its frequency spectrum at 1000 rpm under L2 load case (inner race defect).

Displacement responses at 2000 rpm shaft speed and their frequency spectrums are given in Figures 6.46-6.48. The natural frequency of the test rig in vertical direction can be seen in the low frequency region in Figure 6.46. The inner race defect frequeny is 180.4 Hz for 2000 rpm shaft speed, but this frequency component can not be observed in any load case.
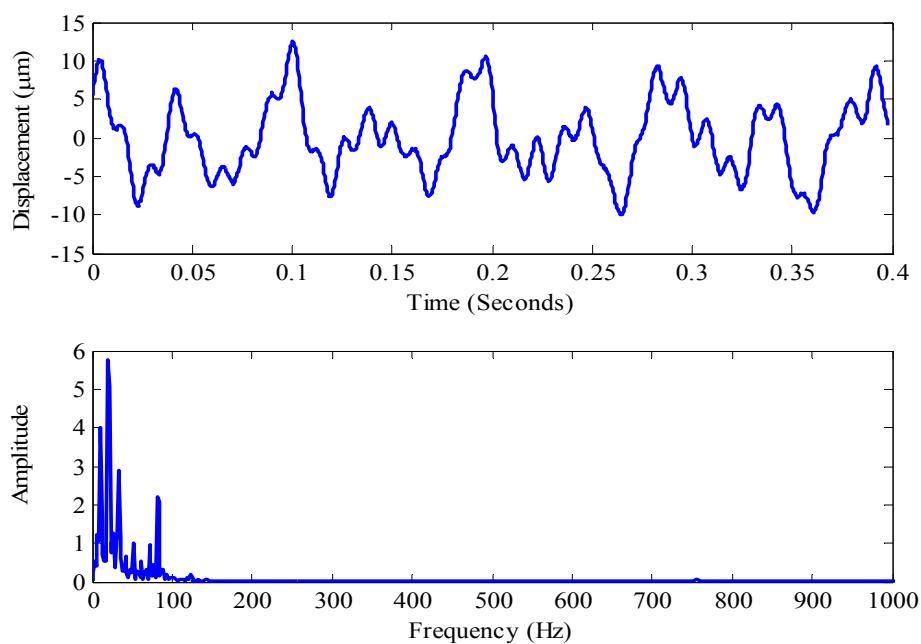
Figure 6.46 Displacement signal and its frequency spectrum at 2000 rpm under L0 load case (inner race defect).
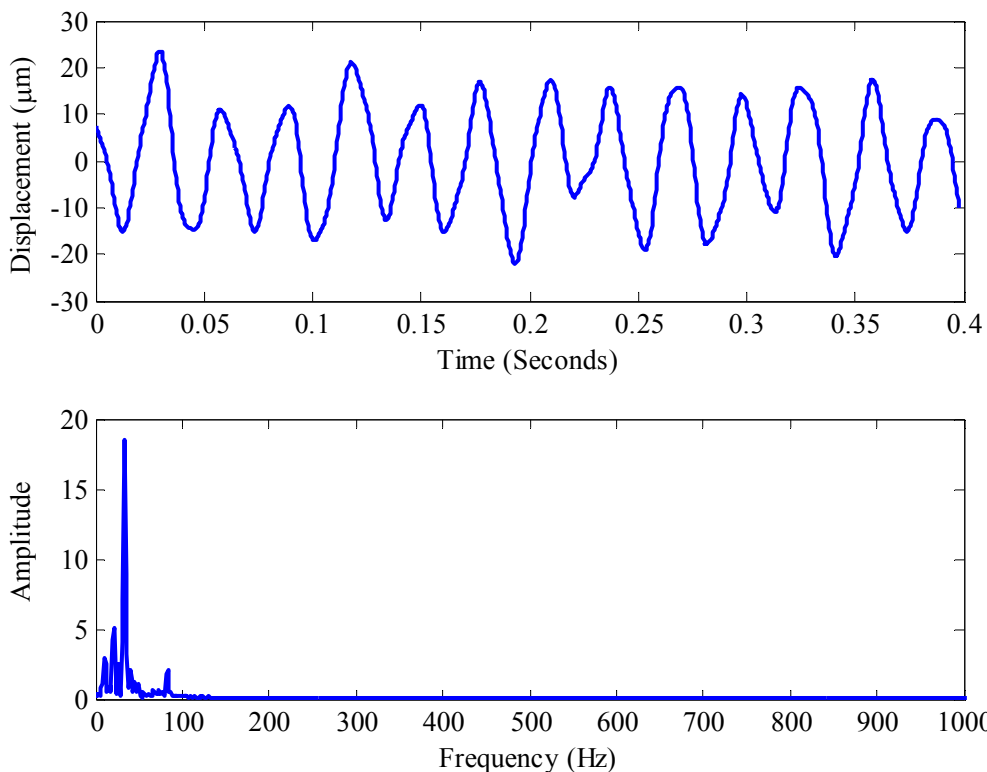
Figure 6.47 Displacement signal and its frequency spectrum at 2000 rpm under L1 load case (inner race defect).
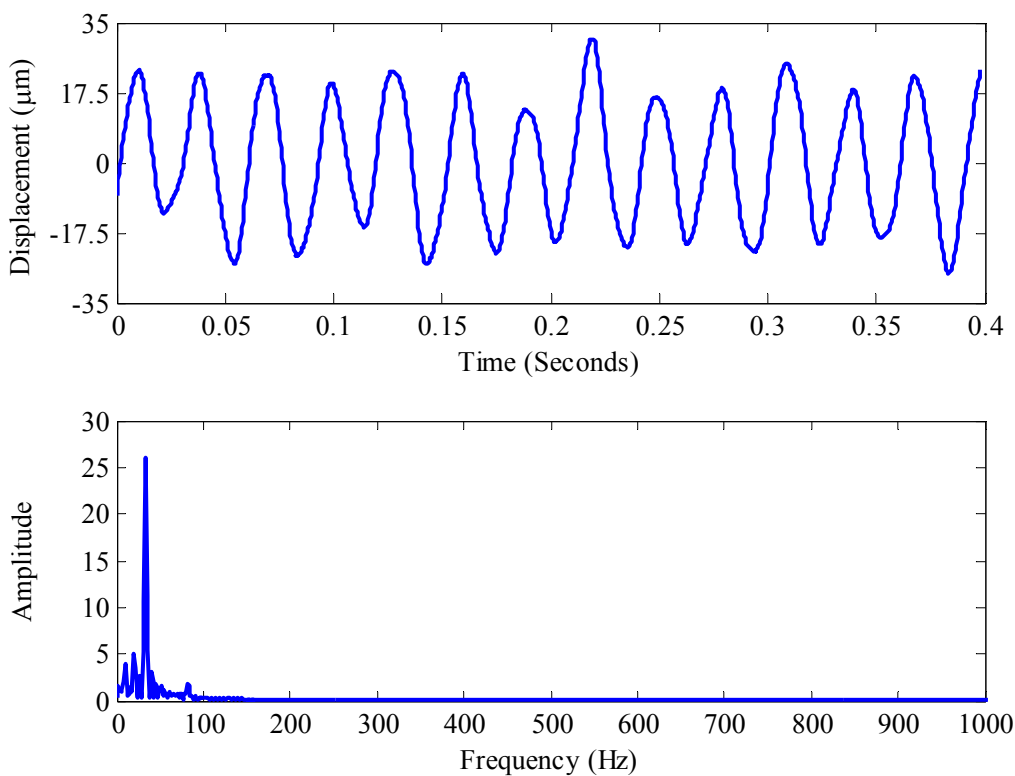
Figure 6.48 Displacement signal and its frequency spectrum at 2000 rpm under L2 load case (inner race defect).

6.4.3.2 Velocity Responses for Inner Race Defect Case

Velocity responses for inner race defect case at 1000 rpm shaft speed and their frequency spectrums are given in Figures 6.49-6.51. The shaft rotation frequency can be observed clearly in all load cases. The inner race defect frequency is 90.2 Hz for 1000 rpm shaft speed. There is a peak in the spectrum at about 470 Hz, which can be interpretted as one of the natural frequencies of the test rig in horizontal direction.
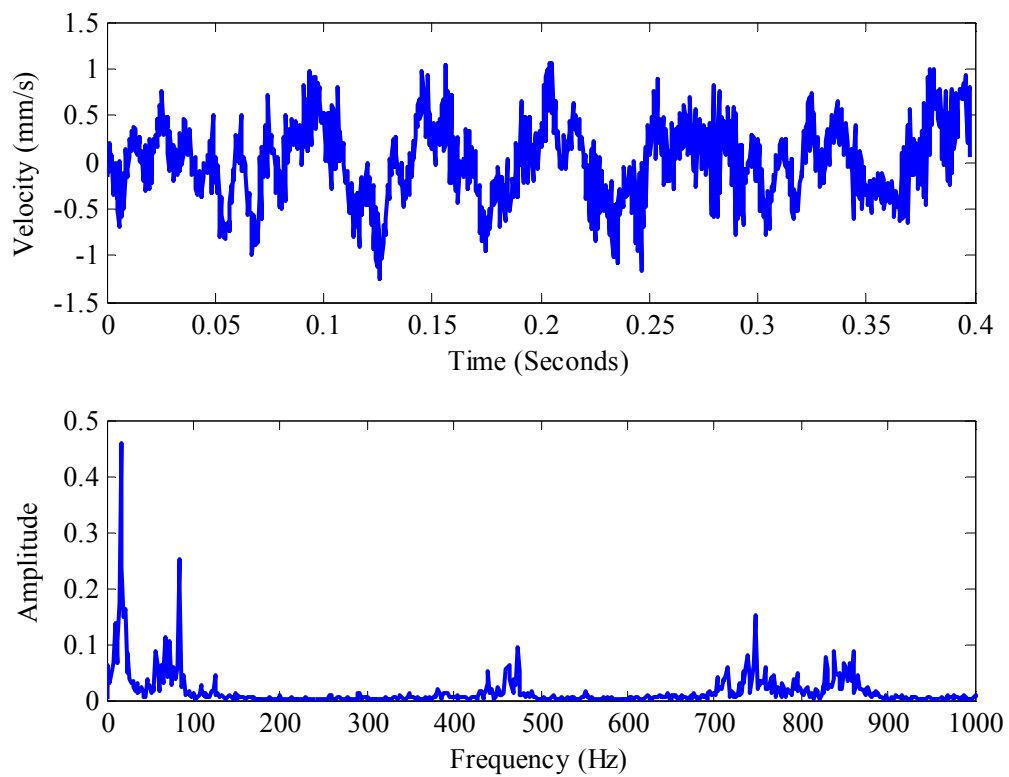
Figure 6.49 Velocity signal and its frequency spectrum at 1000 rpm under L0 load case (inner race defect).
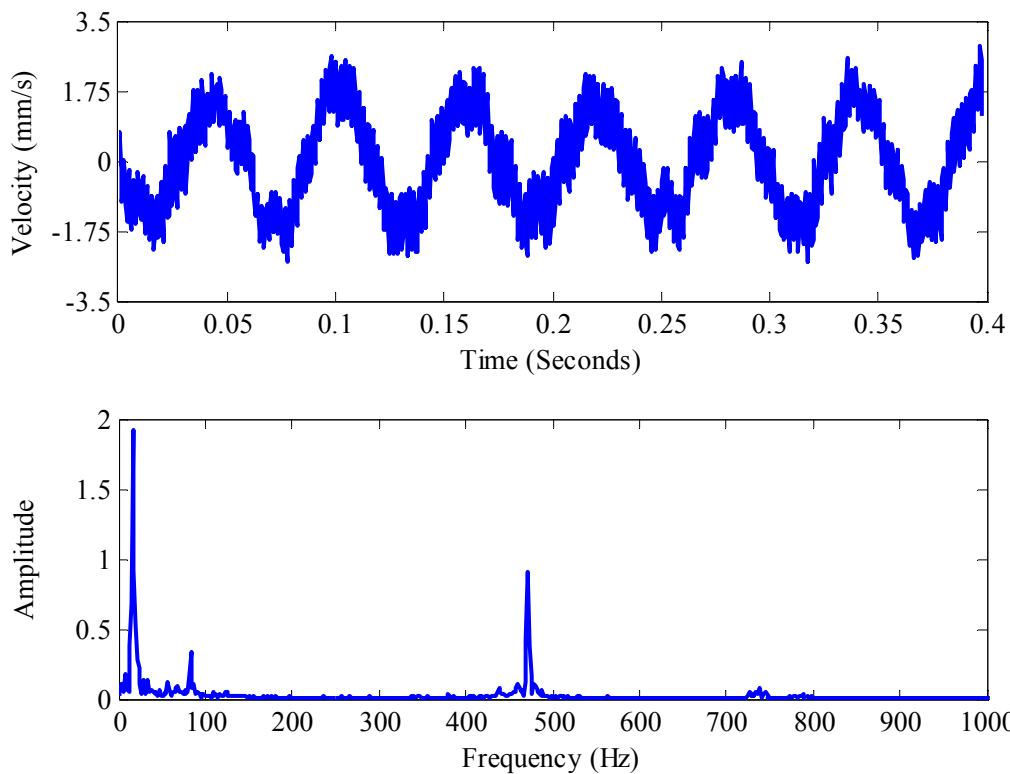
Figure 6.50 Velocity signal and its frequency spectrum at 1000 rpm under L1 load case (inner race defect).
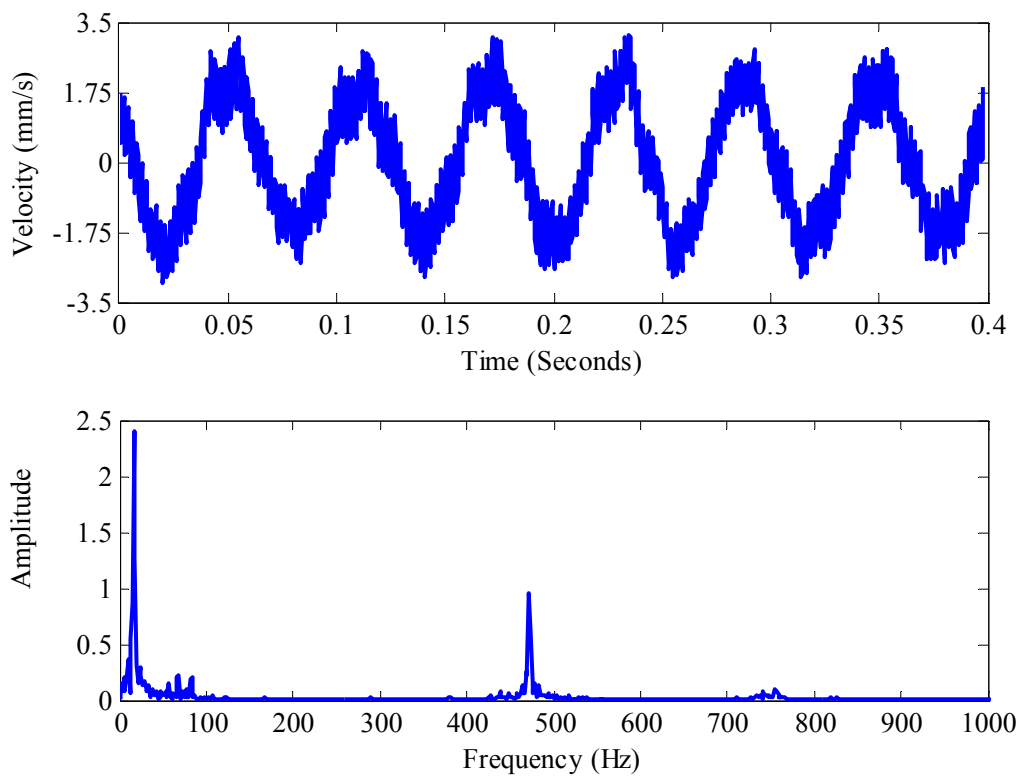
Figure 6.51 Velocity signal and its frequency spectrum at 1000 rpm under L2 load case (inner race defect).

Velocity responses at 2000 rpm shaft speed and their frequency spectrums are given in Figures 6.52-6.54. The inner race defect frequeny is 180.46 Hz for 2000 rpm shaft speed, but there are no peaks about 180 Hz for all load cases.
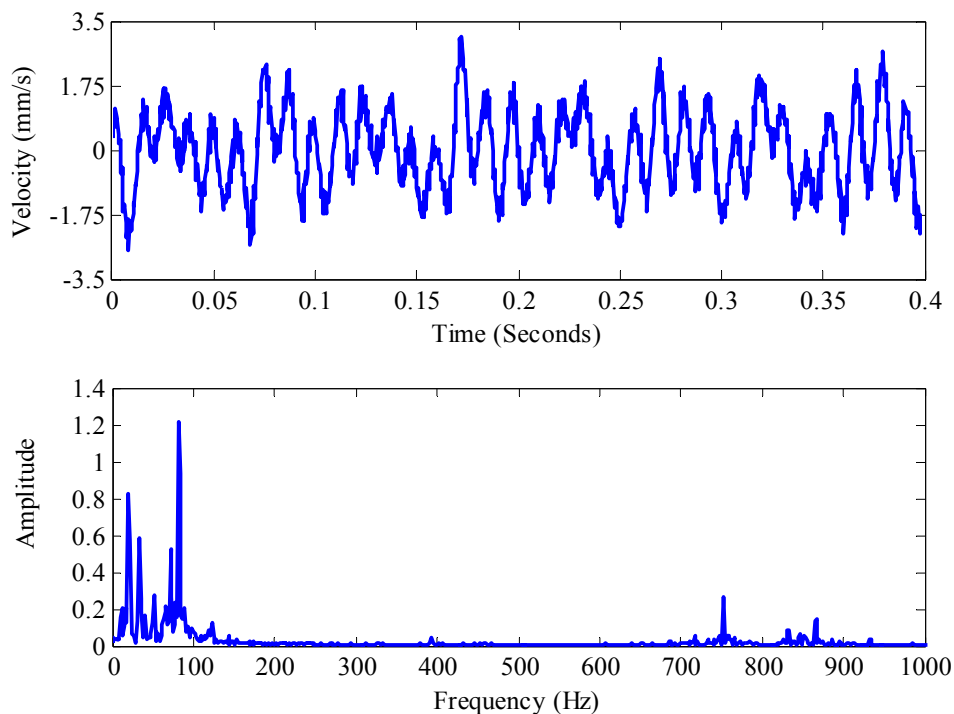
Figure 6.52 Velocity signal and its frequency spectrum at 2000 rpm under L0 load case (inner race defect).
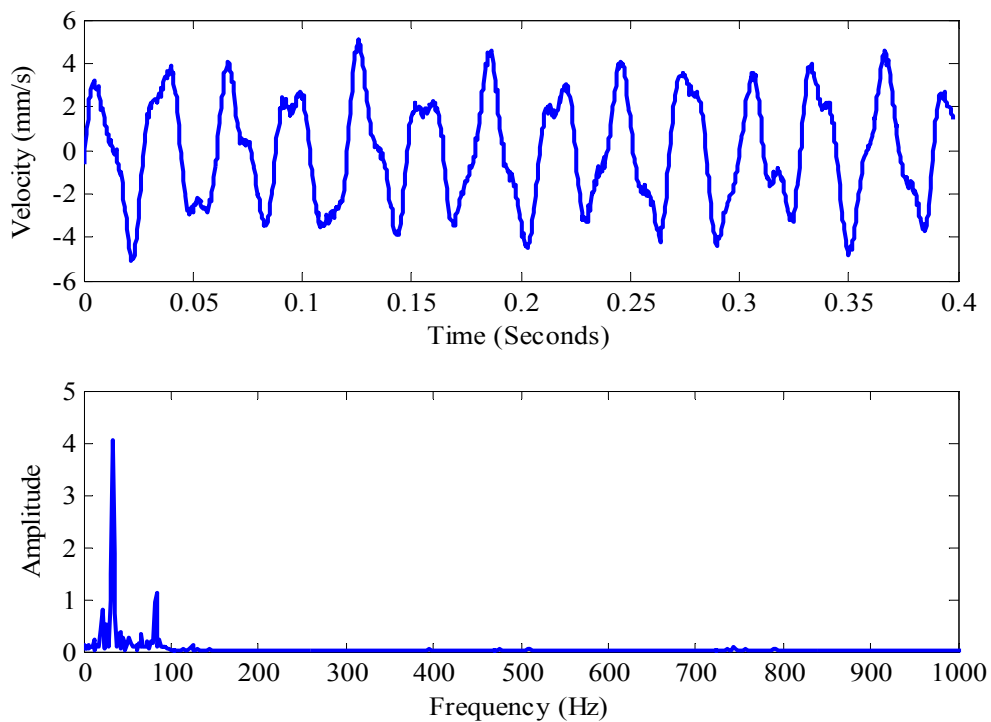
Figure 6.53 Velocity signal and its frequency spectrum at 2000 rpm under L1 load case (inner race defect).
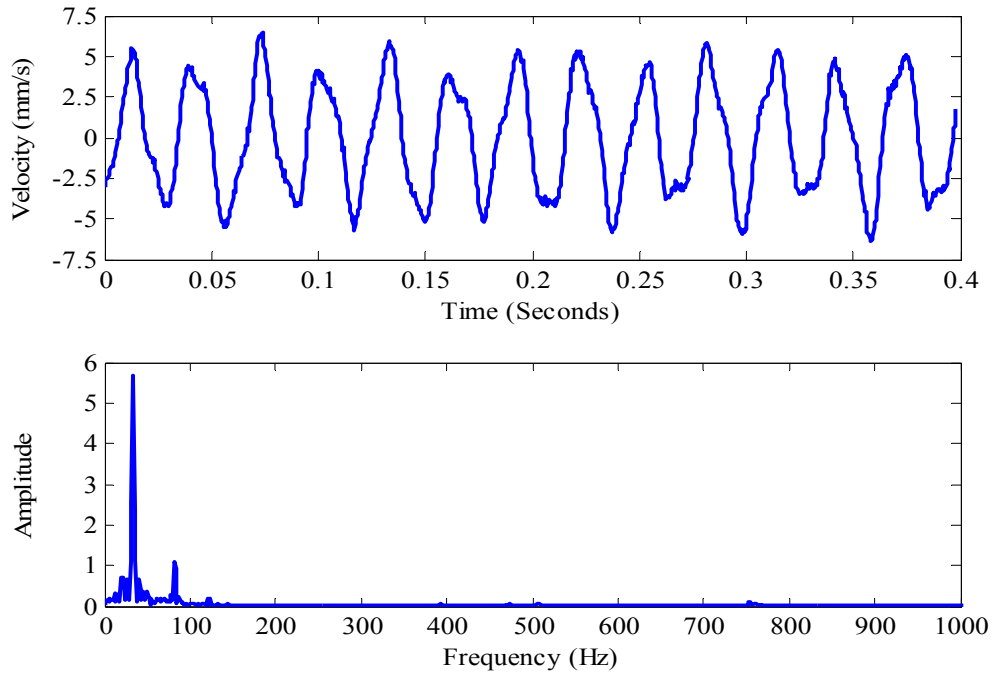
Figure 6.54 Velocity signal and its frequency spectrum at 2000 rpm under L2 load case (inner race defect).

6.4.3.3 AccelerationResponses for Inner Race Defect Case

Acceleration responses at 1000 rpm shaft speed and their frequency spectrums are given in Figures 6.55-6.57.
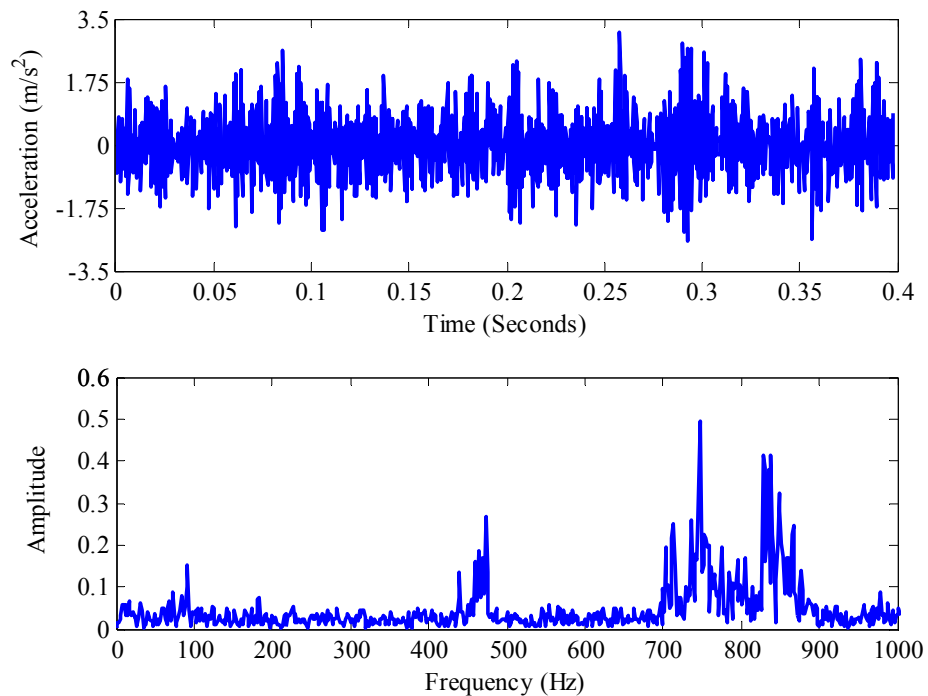
Figure 6.55 Acceleration signal and its frequency spectrum at 1000 rpm under L0 load case (inner race defect).

The inner race defect frequency appears in Figure 6.55. The FFT magnitudes in high frequency region are also high for all load cases.
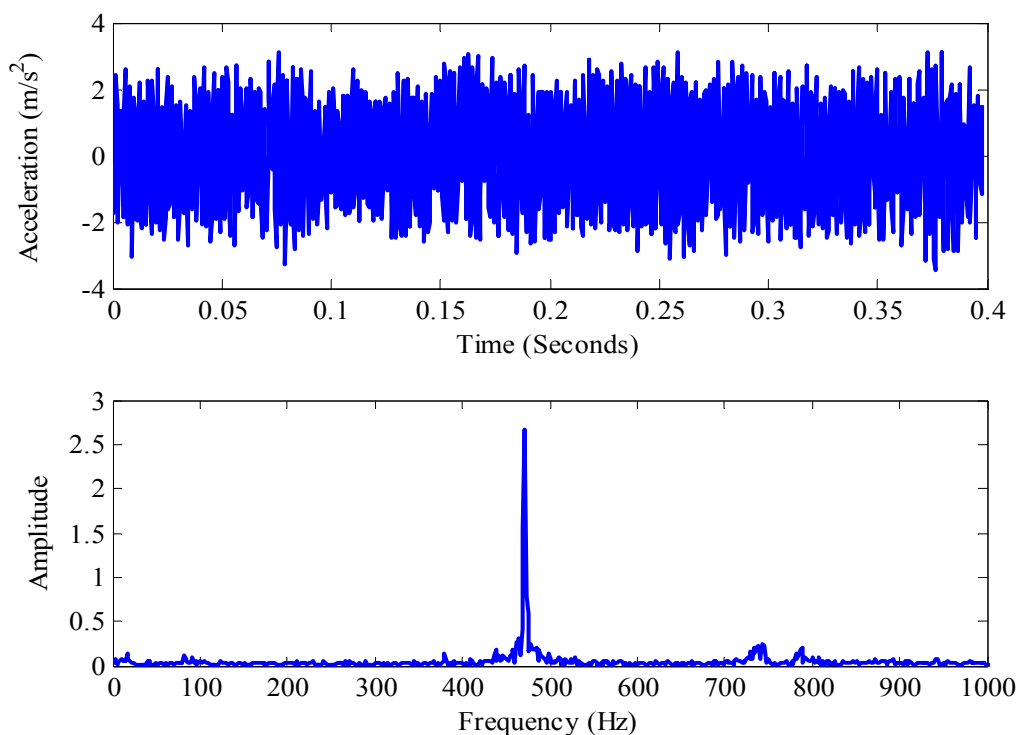
Figure 6.56 Acceleration signal and its frequency spectrum at 1000 rpm under L1 load case (inner race defect).
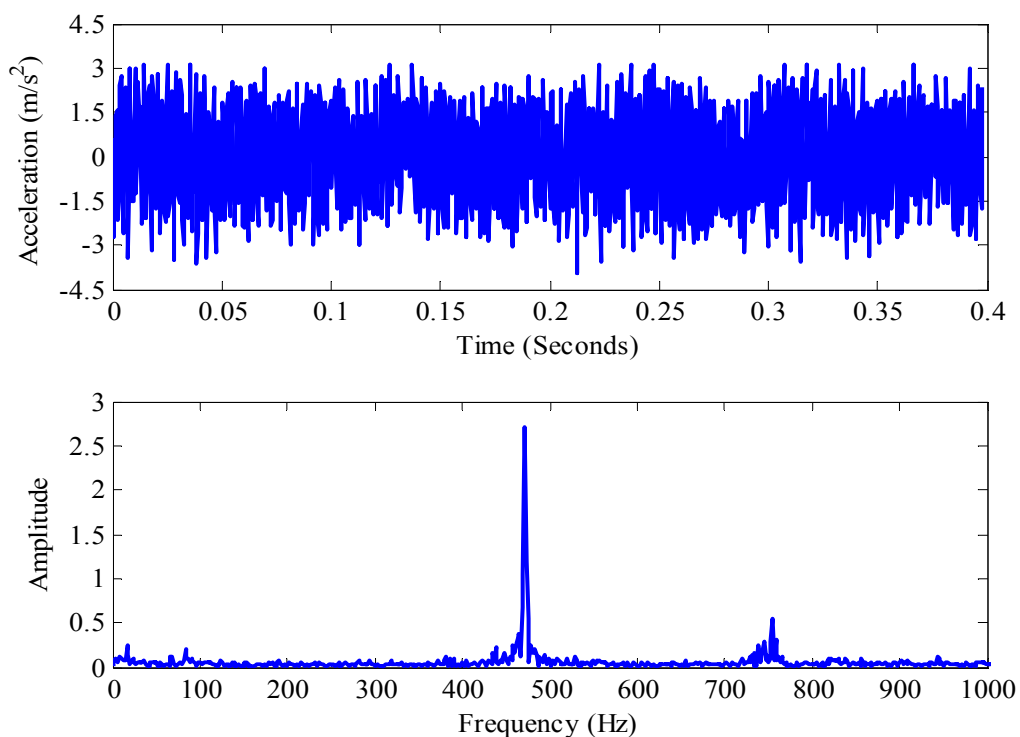
Figure 6.57 Acceleration signal and its frequency spectrum at 1000 rpm under L2 load case (inner race defect).

Acceleration responses at 2000 rpm shaft speed and their frequency spectrums are given in Figures 6.58-6.60. The inner race defect frequeny is 180.5 Hz for 2000 rpm shaft speed. Inner race defect frequeny is observed for all load cases.
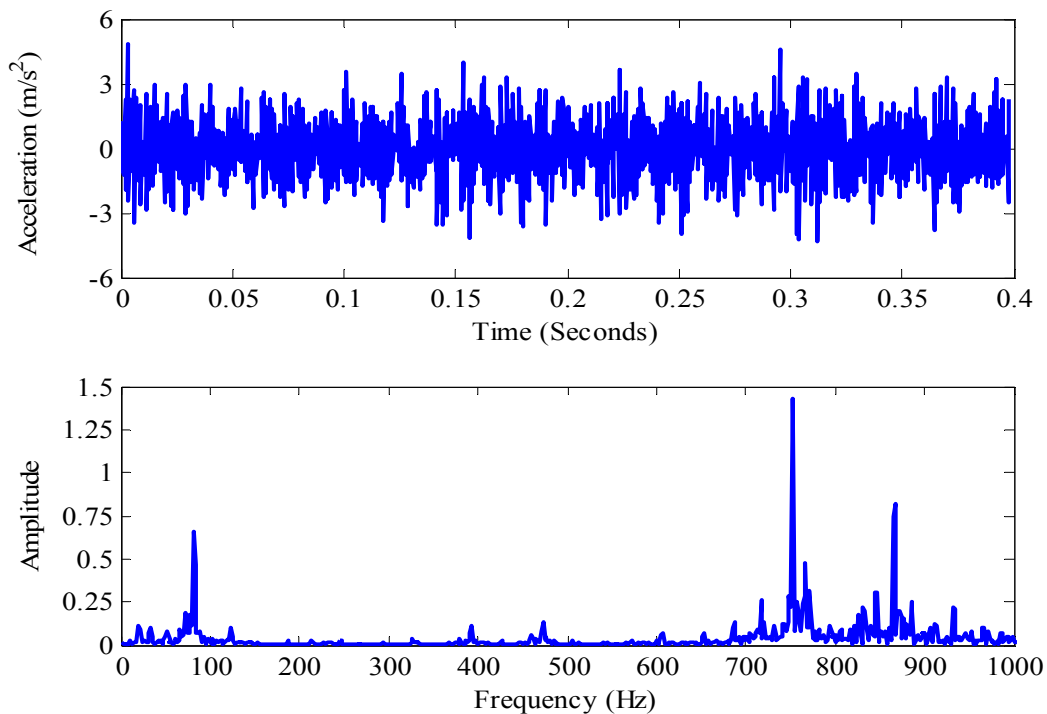
Figure 6.58 Acceleration signal and its frequency spectrum at 2000 rpm under L0 load case (inner race defect).
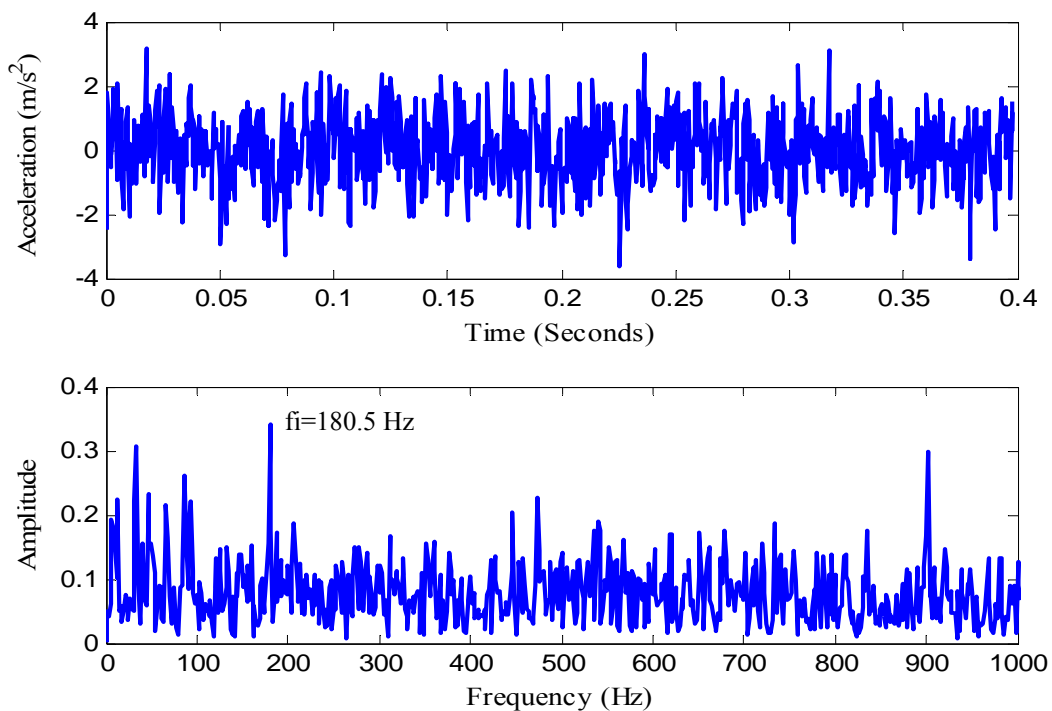
Figure 6.59 Acceleration signal and its frequency spectrum at 2000 rpm under L1 load case (inner race defect).
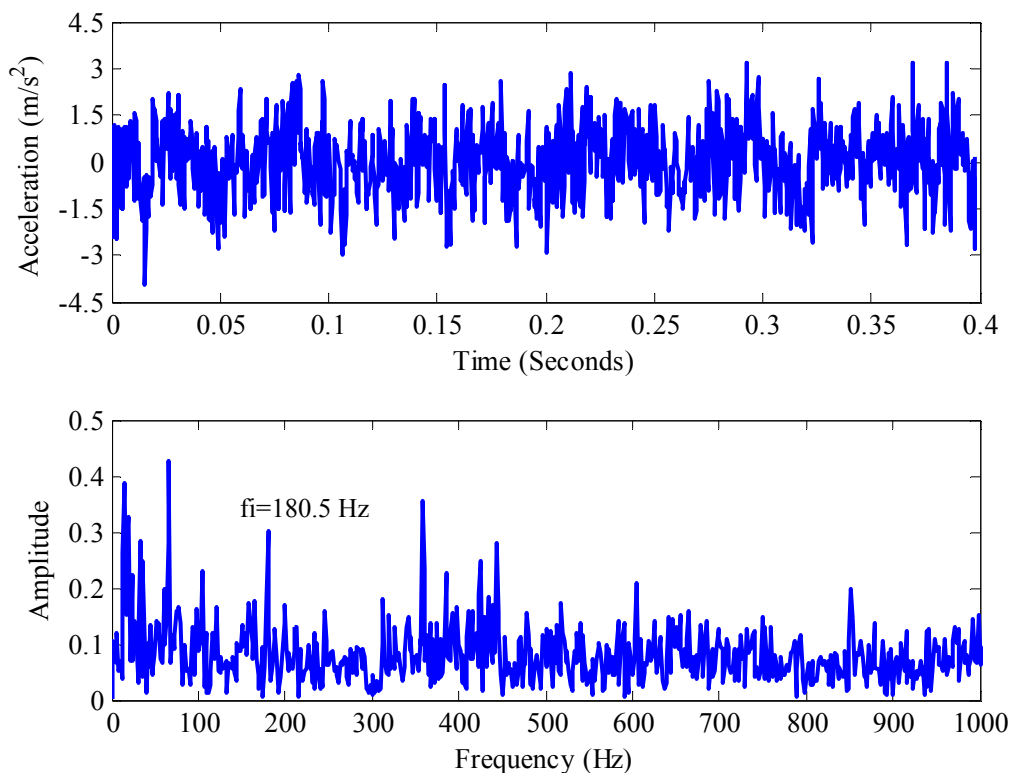
Figure 6.60 Acceleration signal and its frequency spectrum at 2000 rpm under L2 load case (inner race defect).

6.5 Filtered Acceleration Signals

In this sction, 4th order bandpass butterworth filter is applied to the acceleration signals in order to see the bearing defect frequencies more clearly. Then, the FFT is applied to the filtered acceleration signals to obtain the frequency spectrums.

6.5.1 Filtered Acceleration Responses for Healthy Bearing

The 4th order butterworth filter with a passband from 1 to 35 Hz is applied to the acceleration signals for healthy bearing. Filtered acceleration signals at 1000 rpm and 2000 rpm with their frequency spectrums are given in Figures 6.61-6.66 for three different load cases. The shaft frequencies appear in the frequency spectrums. The cage defect frequency 13.282 Hz appears in the frequency spectrums at 2000 rpm.
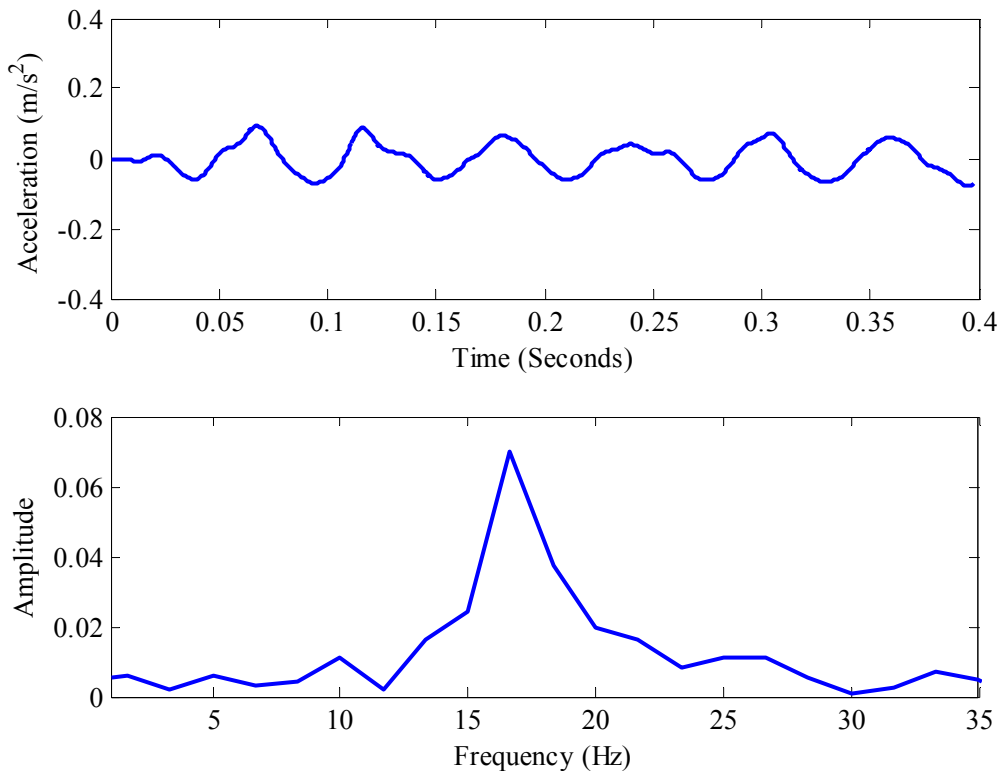
Figure 6.61 Filtered acceleration signal and its frequency spectrum at 1000 rpm under L0 load case (healthy bearing).
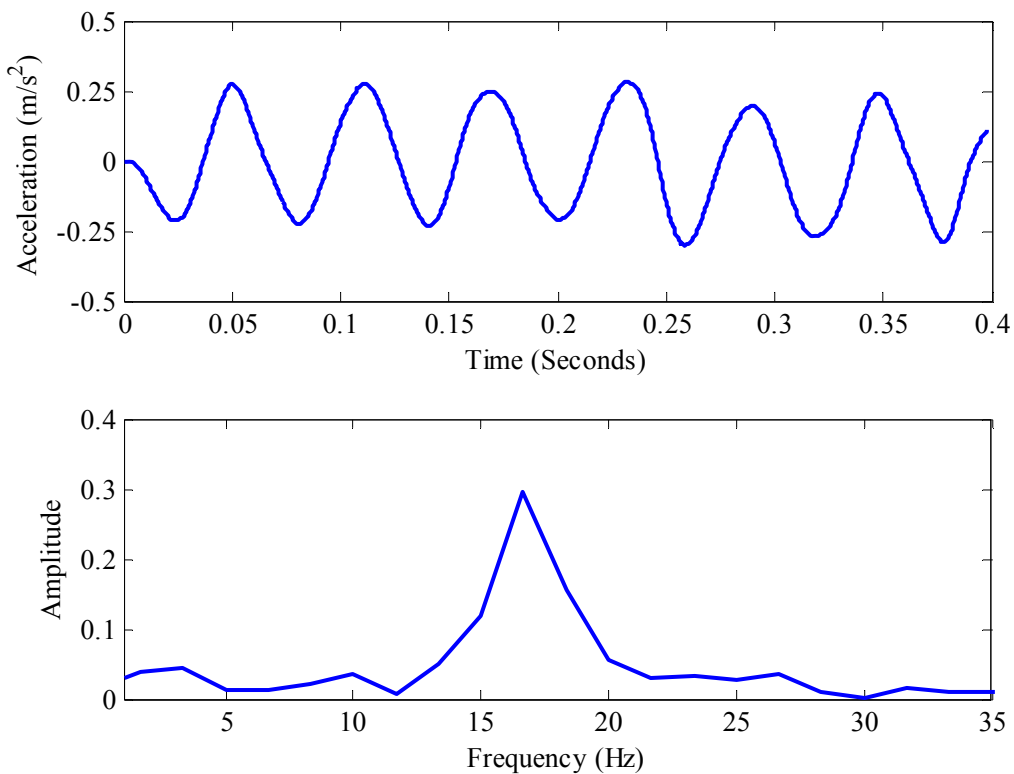
Figure 6.62 Filtered acceleration signal and its frequency spectrum at 1000 rpm under L1 load case (healthy bearing).

Figure 6.63 Filtered acceleration signal and its frequency spectrum at 1000 rpm under L2 load case (healthy bearing).

Figure 6.64 Filtered acceleration signal and its frequency spectrum at 2000 rpm under L0 load case (healthy bearing).

Figure 6.65 Filtered acceleration signal and its frequency spectrum at 2000 rpm under L1 load case (healthy bearing).

Figure 6.66 Filtered acceleration signal and its frequency spectrum at 2000 rpm under L2 load case (healthy bearing).

6.5.2 Filtered Acceleration Responses for Outer Race Defect Case

The bandpass Butterworth filter with a passband $0.5f_o<f<1.5f_o$ is applied to the acceleration signals for outer race defect case.

The outer race defect frequency is 59.769 Hz at 1000 rpm. Filtered acceleration signals at this shaft speed and their frequency spectrums are shown in Figures 6.67-6.69. But the outer race defect frequency can not be seen for L1 and L2 load cases.
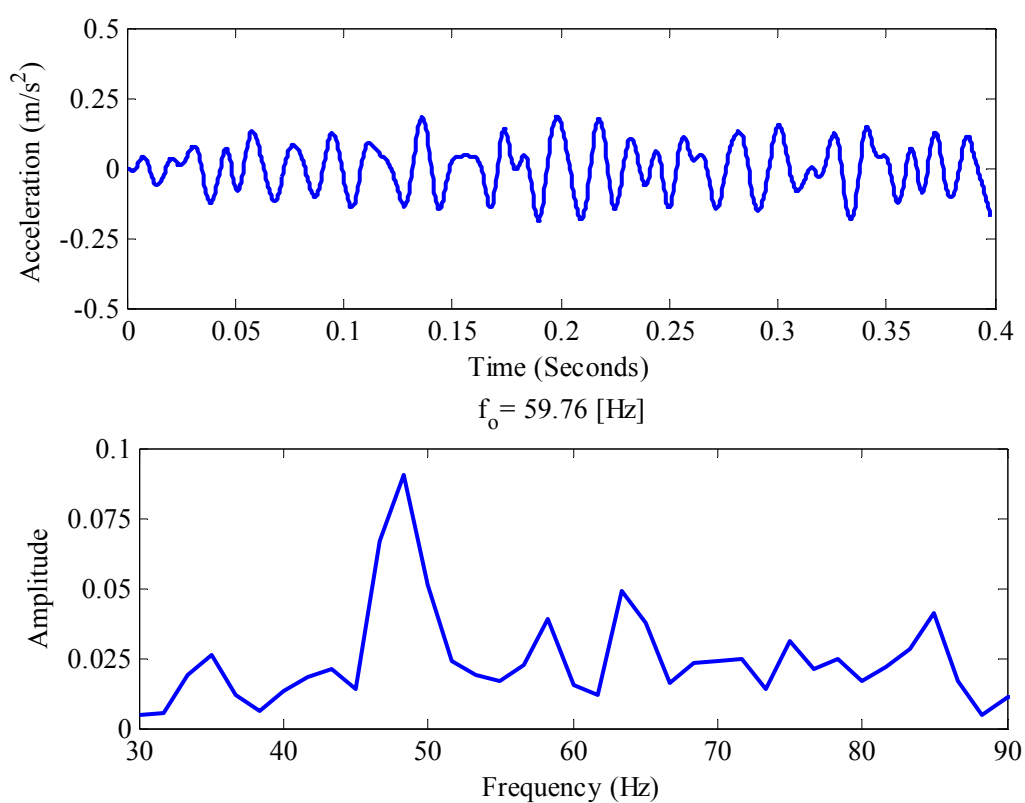
Figure 6.67 Filtered acceleration signal and its frequency spectrum at 1000 rpm under L0 load case (defect on outer race).
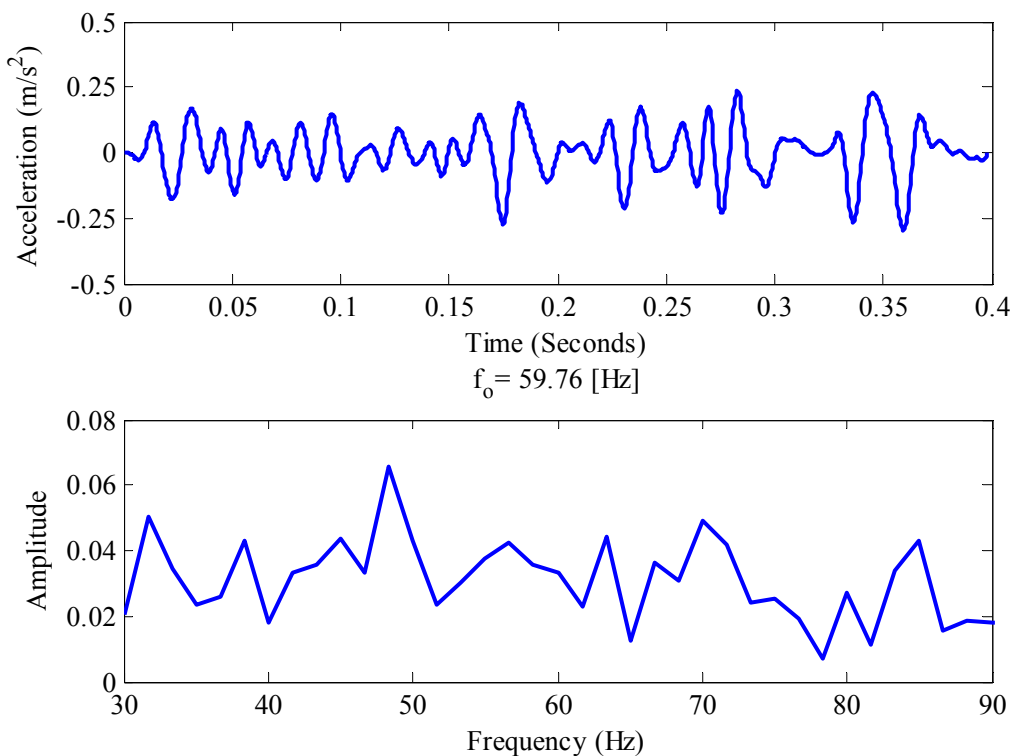
Figure 6.68 Filtered acceleration signal and its frequency spectrum at 1000 rpm under L1 load case (defect on outer race).
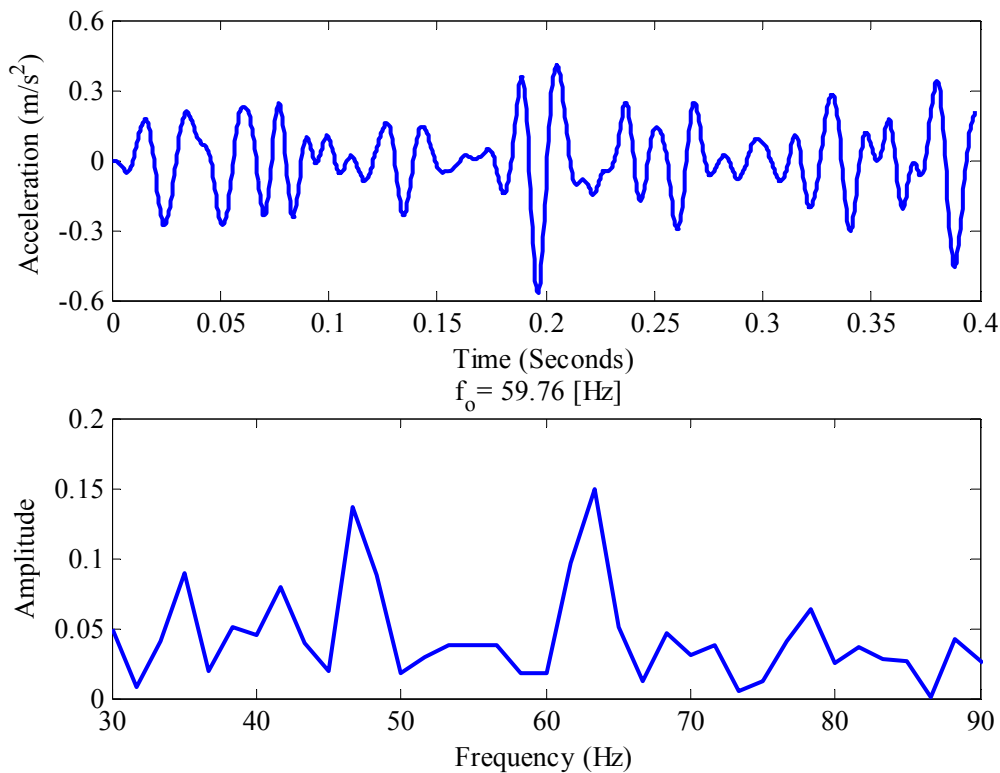
Figure 6.69 Filtered acceleration signal and its frequency spectrum at 1000 rpm under L2 load case (defect on outer race).

Filtered acceleration signals at 2000 rpm and their frequency spectrums are given in Figures 6.70-6.72. The outer race defect frequency can be shown for all load cases.
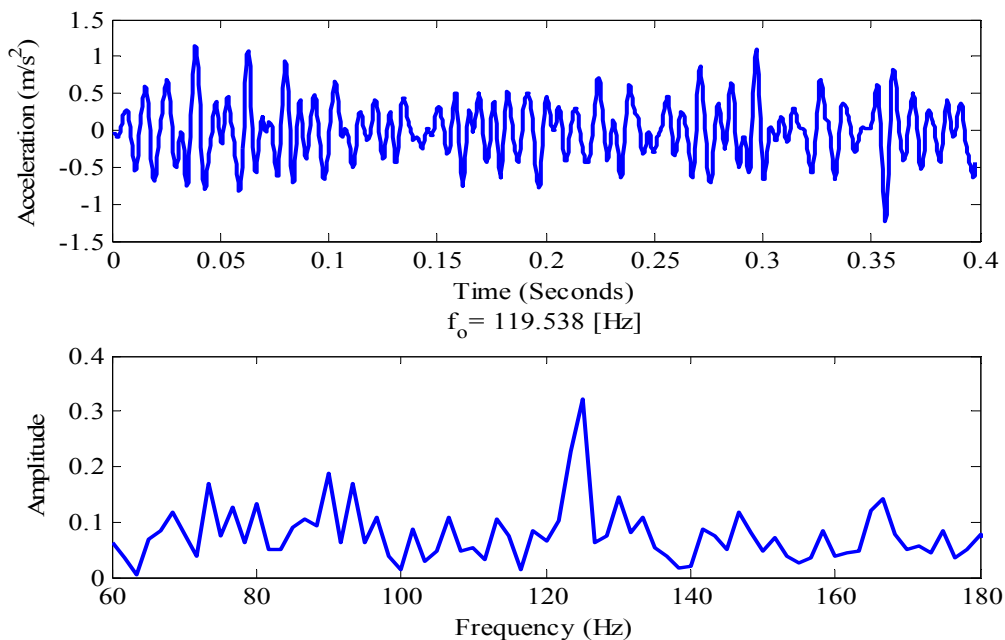
Figure 6.70 Filtered acceleration signal and its frequency spectrum at 2000 rpm under L0 load case (defect on outer race).
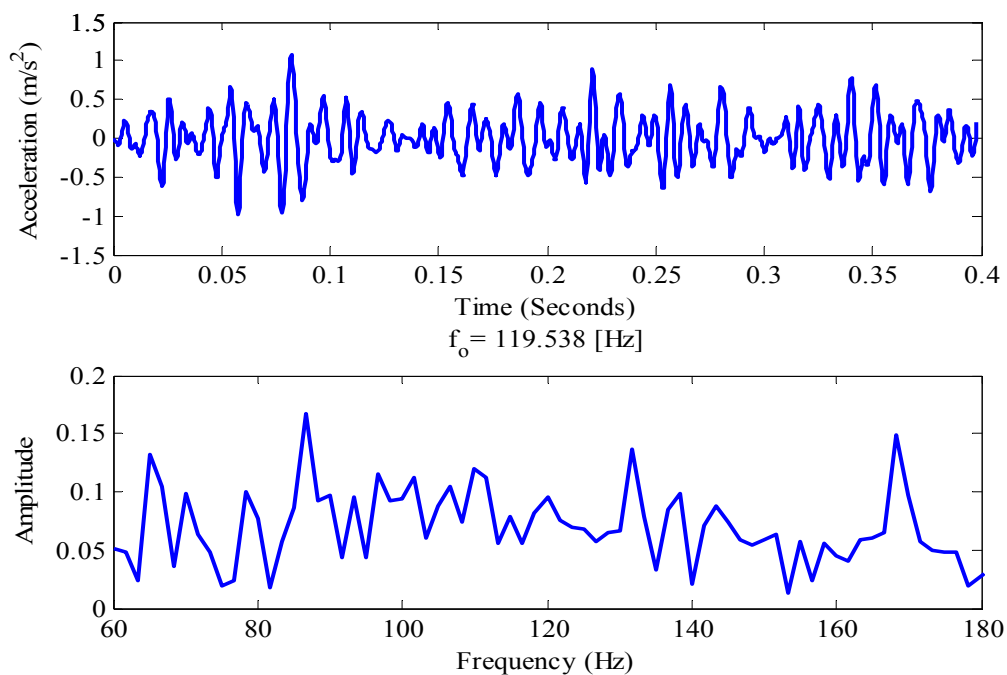
Figure 6.71 Filtered acceleration signal and its frequency spectrum at 2000 rpm under L1 load case (defect on outer race).
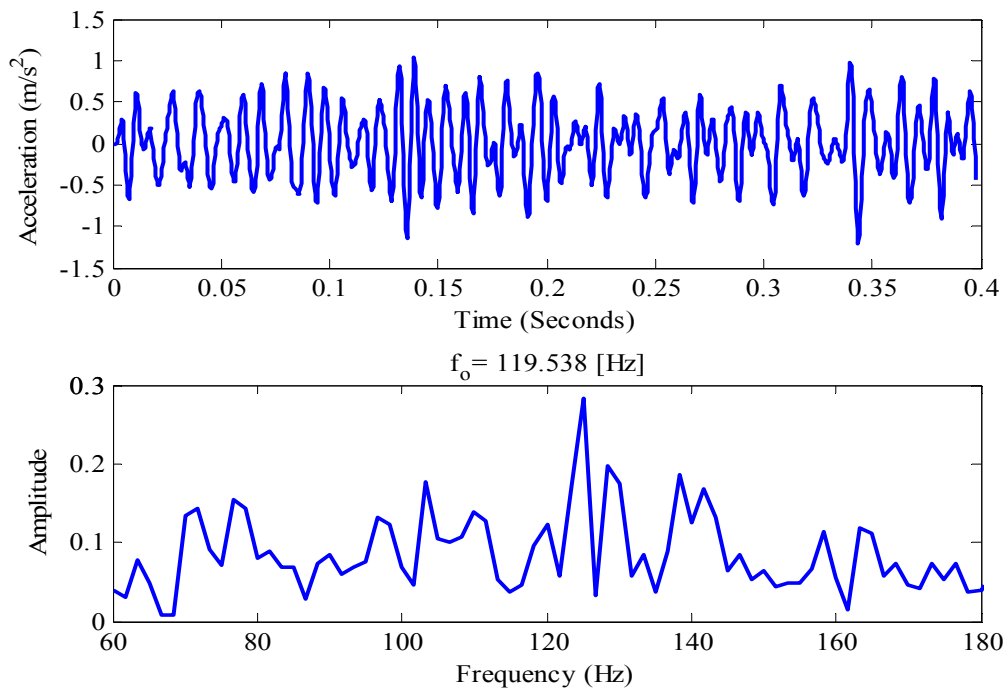
Figure 6.72 Filtered acceleration signal and its frequency spectrum at 2000 rpm under L2 load case (defect on outer race).

6.5.3 Filtered Acceleration Responses for Inner Race Defect Case

The bandpass Butterworth filter with a passband $0.5f_i<f<1.5f_i$ is applied to the acceleration signals for inner race defect case.

Filtered acceleration responses at 1000 rpm and their frequency spectrums are given in Figures 6.73-6.75. The inner race defect frequency 90.230 Hz for this shaft speed can be seen in the frequency spectrums for all load cases. The filtered acceleration responses at 1500 are given in Figures 6.76-6.78. The inner race defect frequency for this shaft speed is 135.346 Hz and it appears in the frequency spectrum for all load cases.

The filtered acceleration responses at 2000 rpm are given in Figures 6.79-6.81. The inner race defect frequency for this shaft speed is 180.461 Hz and it appears in the frequency spectrum for all load cases.
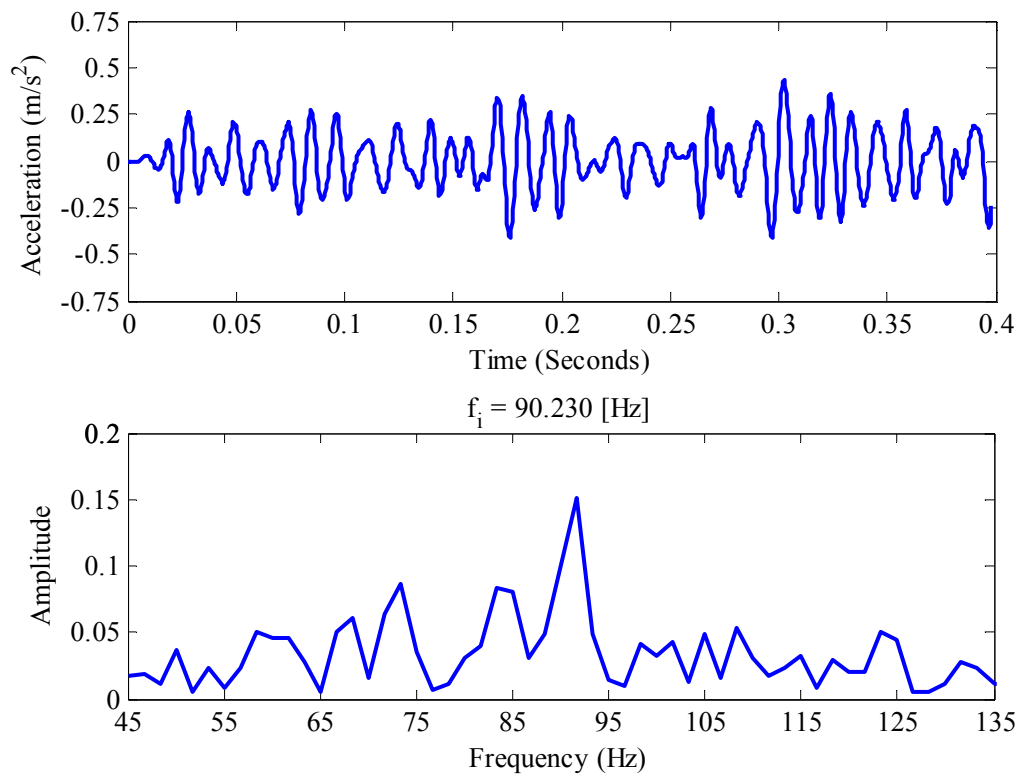
Figure 6.73 Filtered acceleration signal and its frequency spectrum at 1000 rpm under L0 load case (defect on inner race).
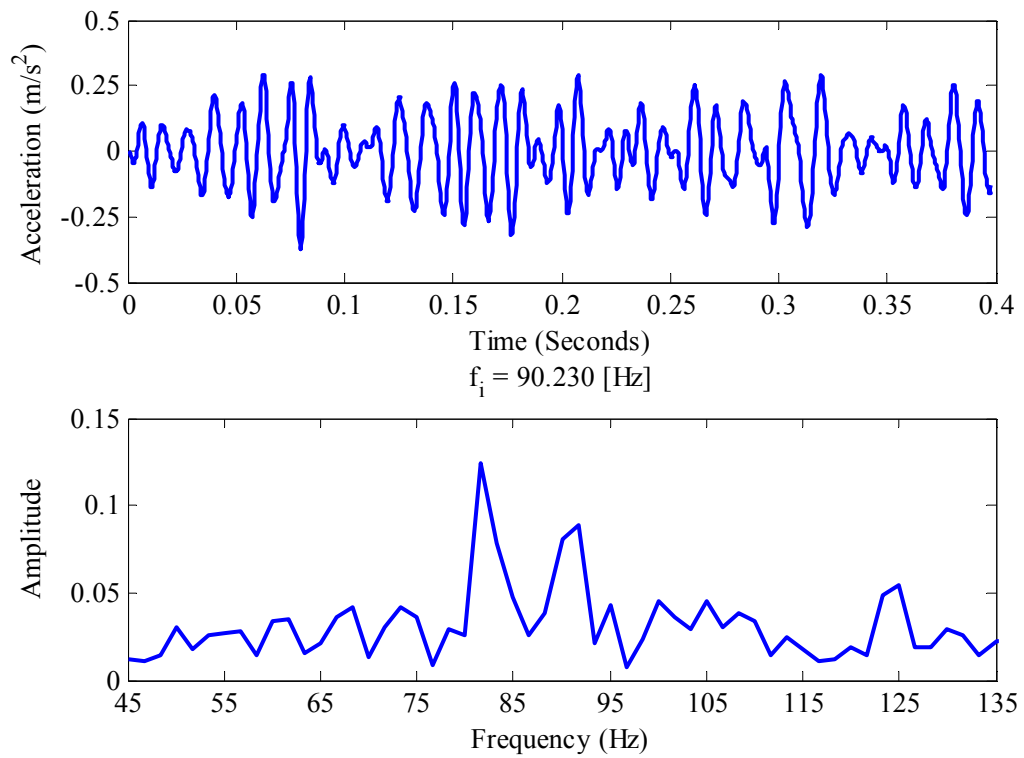
Figure 6.74 Filtered acceleration signal and its frequency spectrum at 1000 rpm under L1 load case (defect on inner race).
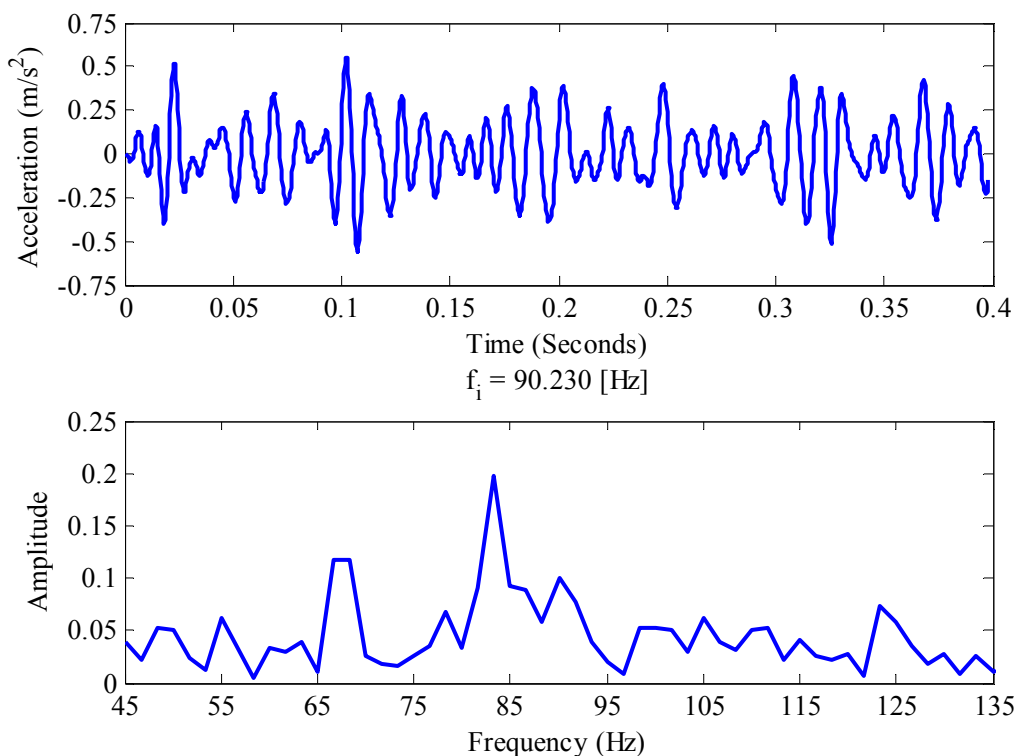
Figure 6.75 Filtered acceleration signal and its frequency spectrum at 1000 rpm under L2 load case (defect on inner race).
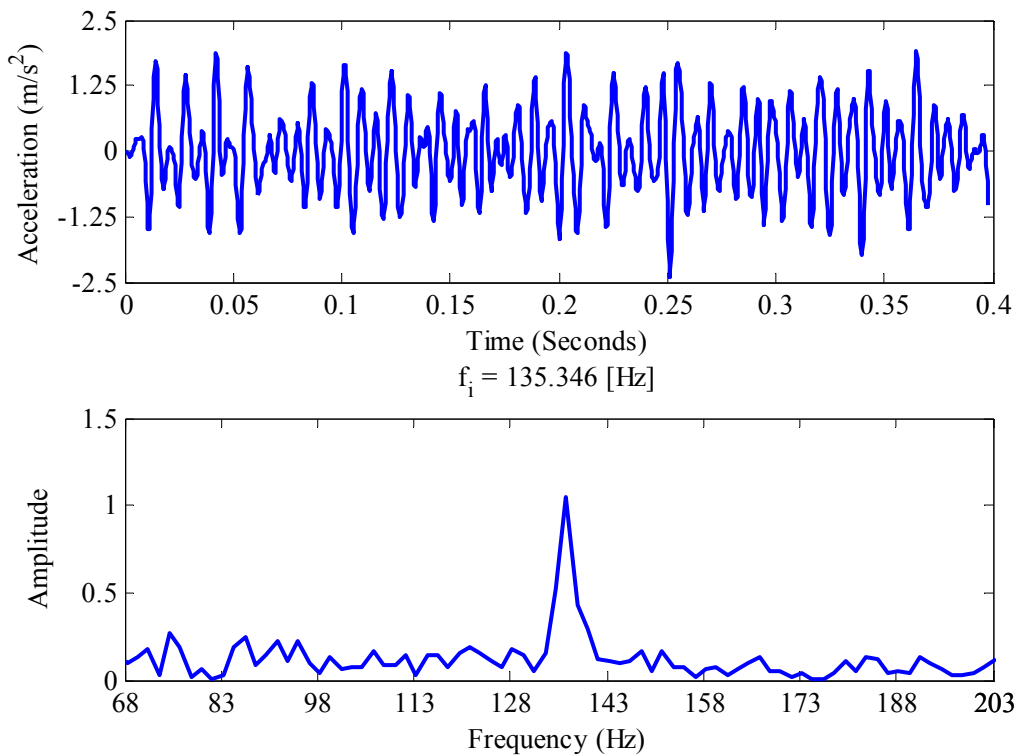
Figure 6.76 Filtered acceleration signal and its frequency spectrum at 1500 rpm under L0 load case (defect on inner race).
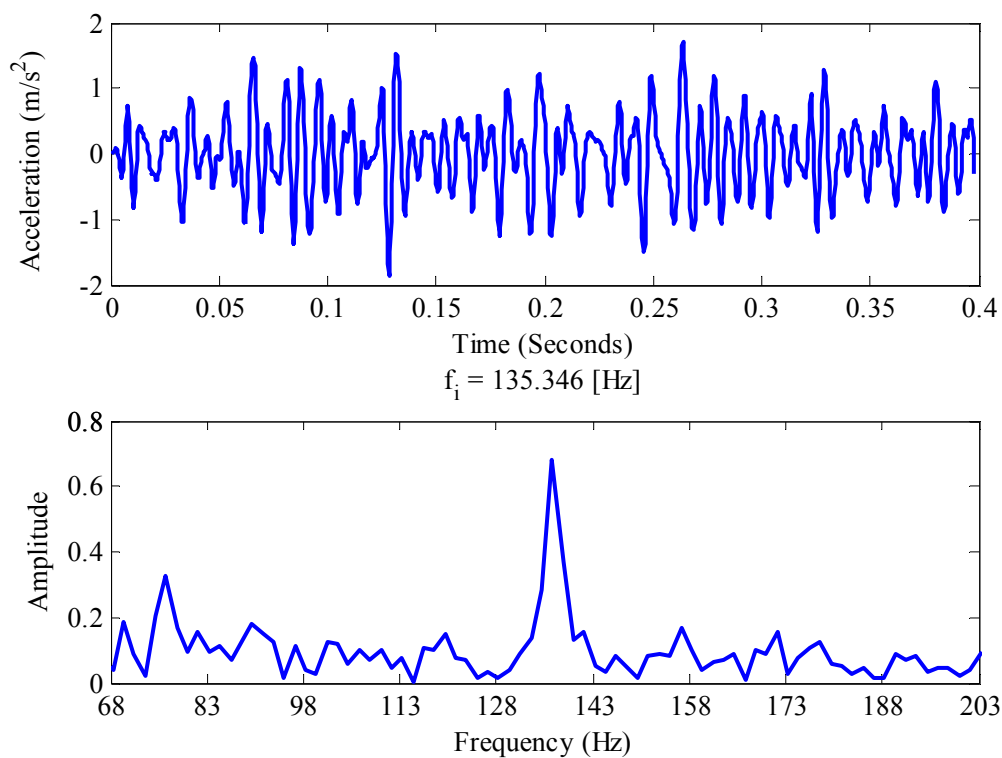
Figure 6.77 Filtered acceleration signal and its frequency spectrum at 1500 rpm under L1 load case (defect on inner race).
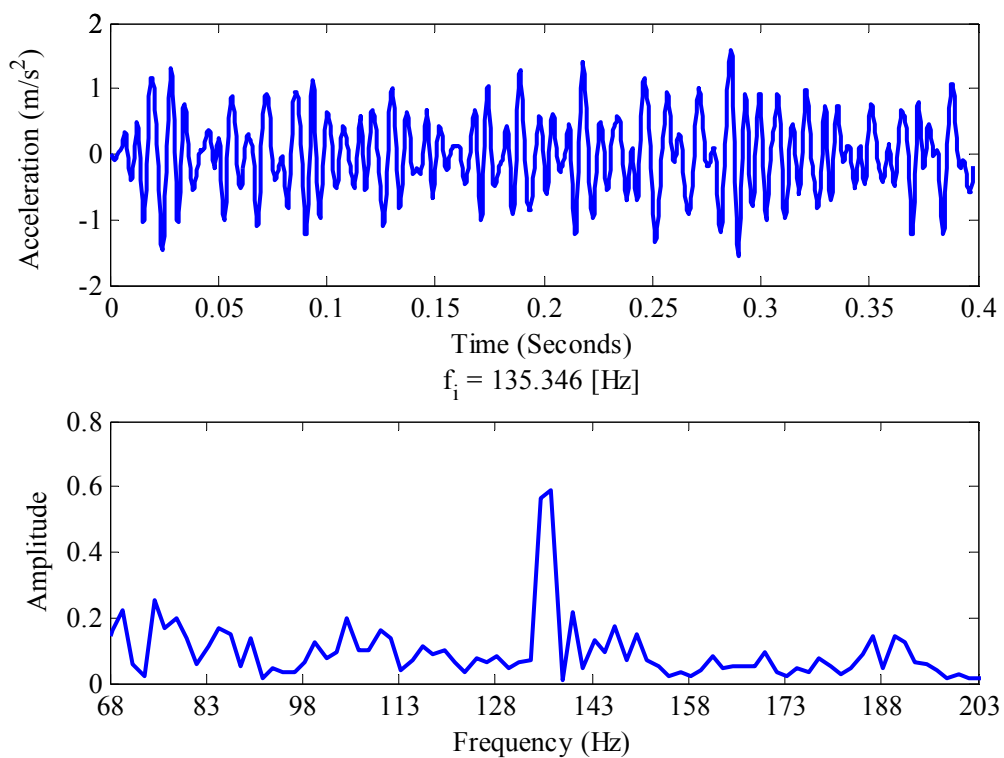
Figure 6.78 Filtered acceleration signal and its frequency spectrum at 1500 rpm under L2 load case (defect on inner race).
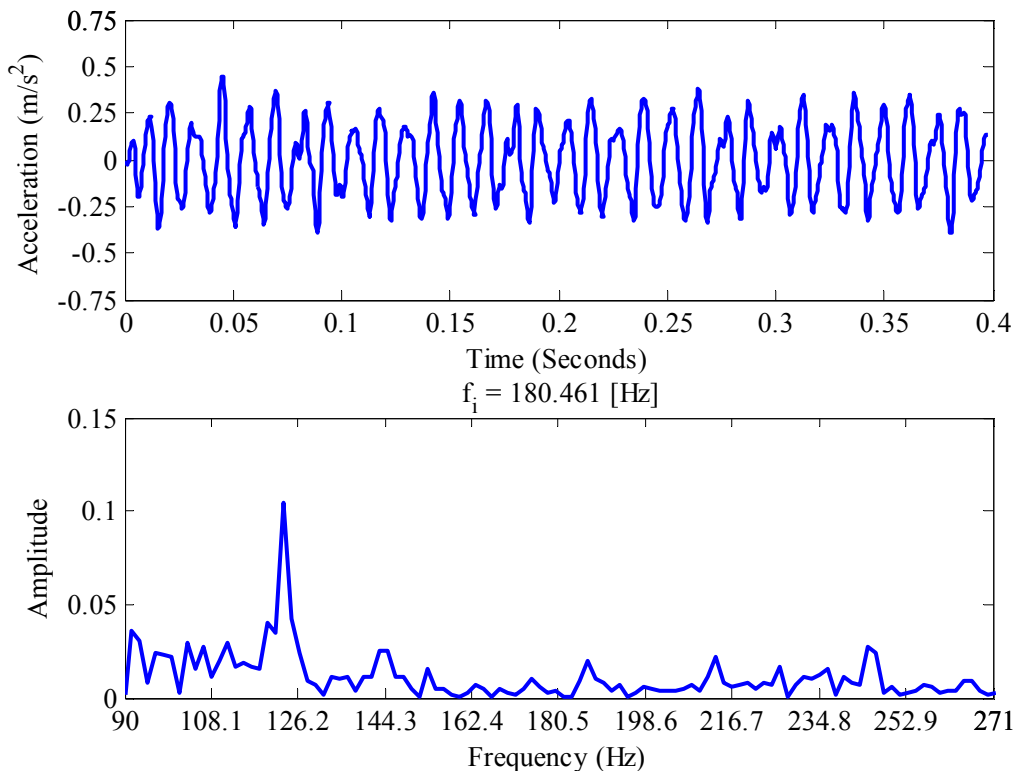
Figure 6.79 Filtered acceleration signal and its frequency spectrum at 2000 rpm under L0 load case (defect on inner race).
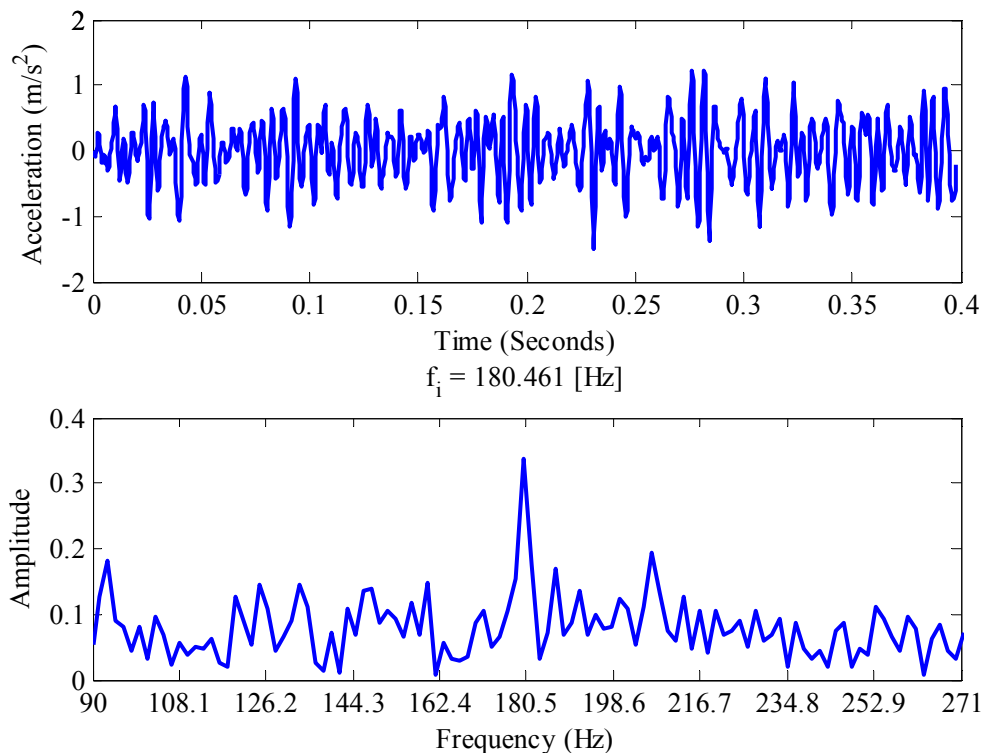
Figure 6.80 Filtered acceleration signal and its frequency spectrum at 2000 rpm under L1 load case (defect on inner race).
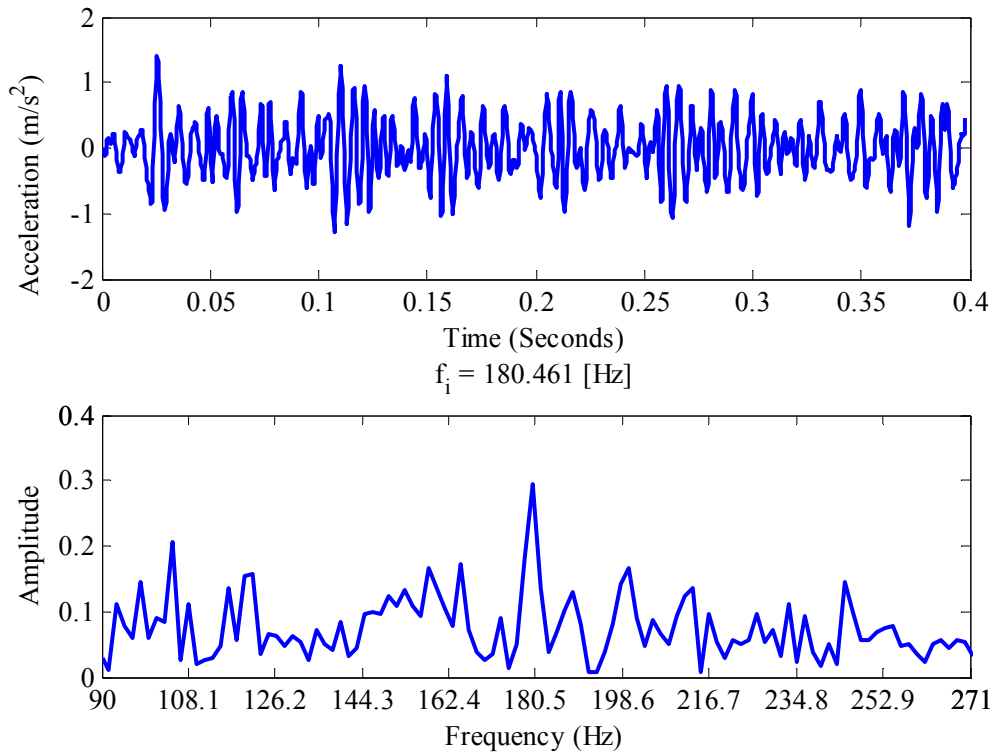
Figure 6.81 Filtered acceleration signal and its frequency spectrum at 2000 rpm under L2 load case (defect on inner race).

6.6 The Short Time Fourier Transform (STFT)

The Short Time Fourier Transforms (STFT) of experimental vibration signals are calculated by MATLAB's spectrogram command in order to show the time dependence of the freqency components.

The Short Time Fourier Transform of a time signal x(t) is described by Eq.(6.8) and further information about the STFT can be obtained from study of Misiti M., Misiti Y., Oppenheim,& Poggi.

$$X(\tau,\omega) = \int_{-\infty}^{\infty} x(t)\omega(t-\tau)e^{-j\omega t}dt \qquad (6.8)$$

where ω is the window used in the transformation. The STFT is a joint time-frequency transformation and gives the frequency contents of a time signal with their occurrence times.

6.6.1 STFT for Outer Race Defect Case

The Short Time Fourier Transforms of acceleration responses at 1750 rpm are given in Figures 6.82-6.84 for L0, L1 and L2 load cases. The shaft frequency is 29.16 Hz and the outer race defect frequeny is 104.596 Hz for this shaft speed. There are many frequency components at different time segments in spectrograms. One of them is shown at about 110 Hz in Figure 6.82. It can be attributed as the outer race defect frequeny. The spectrogram graph for L1 load case is given in Figure 6.83. In this figure, the frequency component at about 110 Hz can be seen for time segments intermittently. The spectrogram for L2 load case is given in Figure 6.84 and the the same frequency component can be seen at all time intervals.
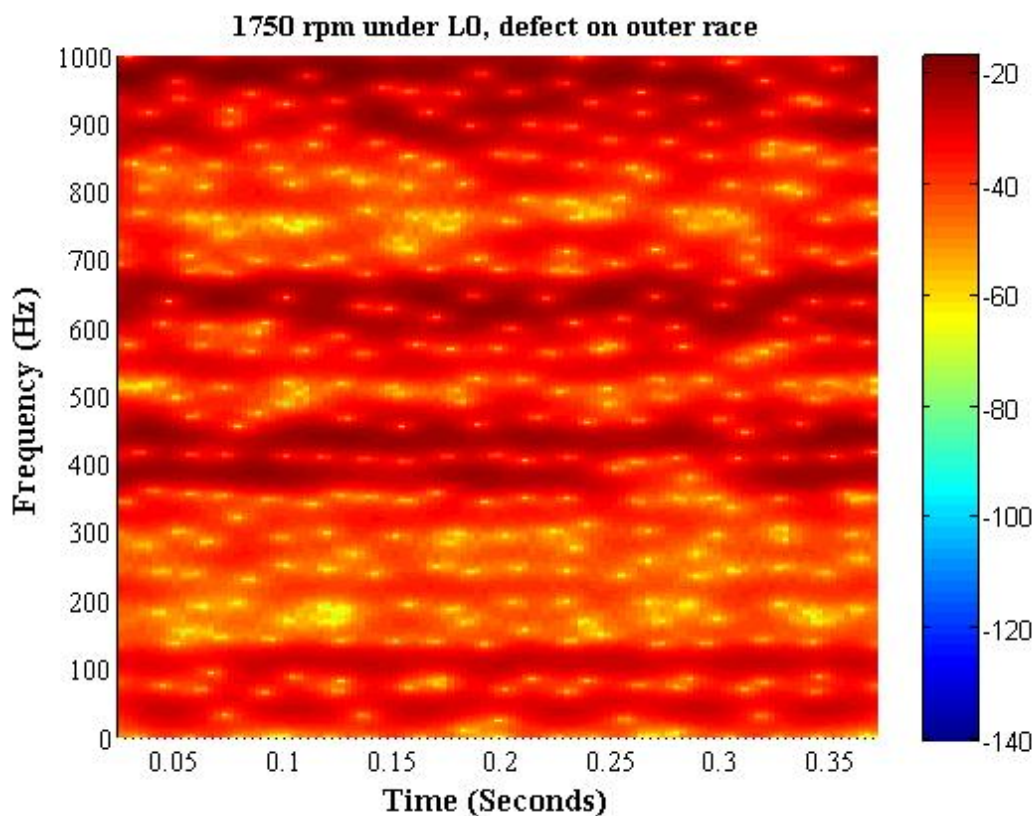
Figure 6.82 STFT of acceleration signal at 1750 rpm shaft speed under L0 load case (defect on outer race).
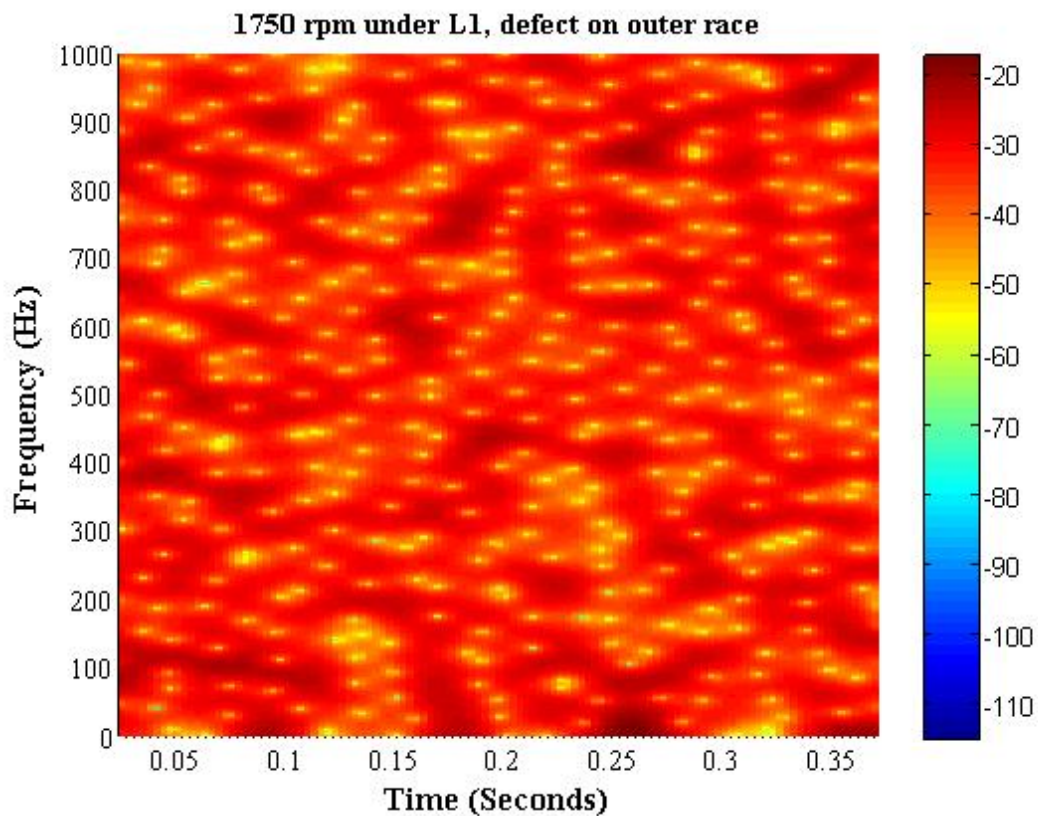
Figure 6.83 STFT of acceleration signal at 1750 rpm shaft speed under L1 load case (defect on outer race).
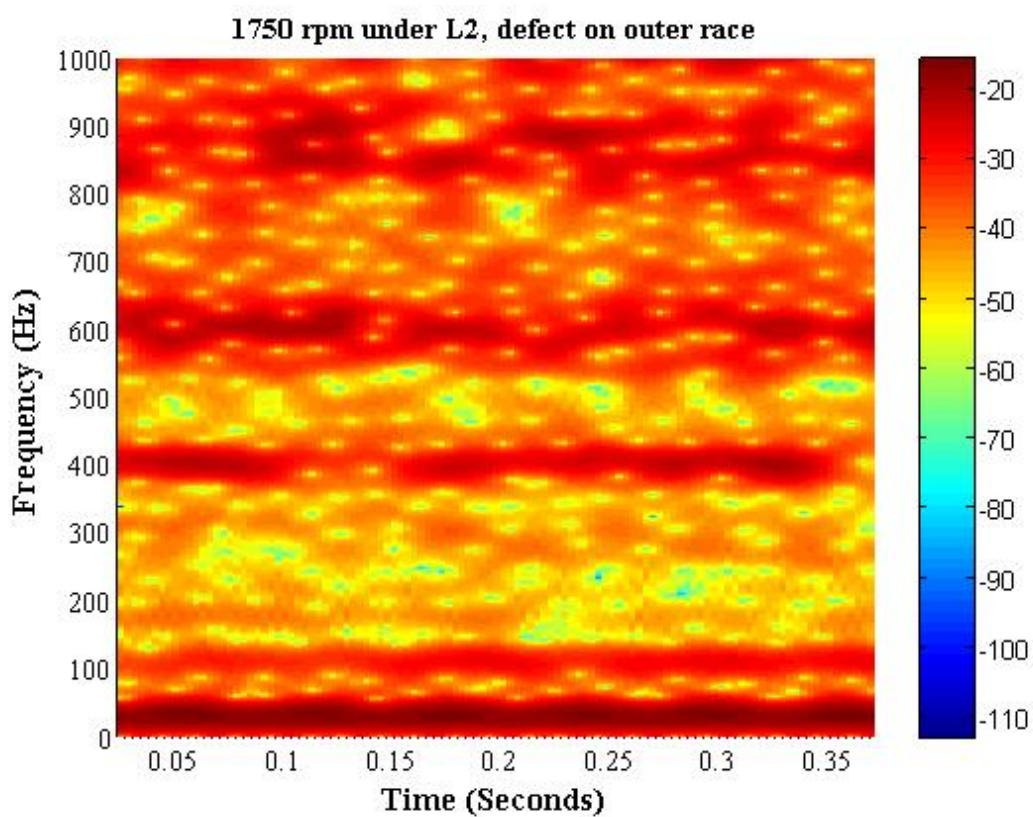
Figure 6.84 STFT of acceleration signal at 1750 rpm shaft speed under L2 load case (defect on outer race).

6.6.2 STFT for Inner Race Defect Case

STFT spectogram of acceleration response for inner race defect case at 1000 rpm shaft speed is given in Figure 6.85 for L0 load case. The inner race defect frequency for this speed is 90.230 Hz and this frequency appears in the spectrogram for regular time intervals. The STFT spectrogram for L1 load case is given in Figure 6.86. As seen in this figure, the resonance frequency dominates the STFT graph at all time intervals.
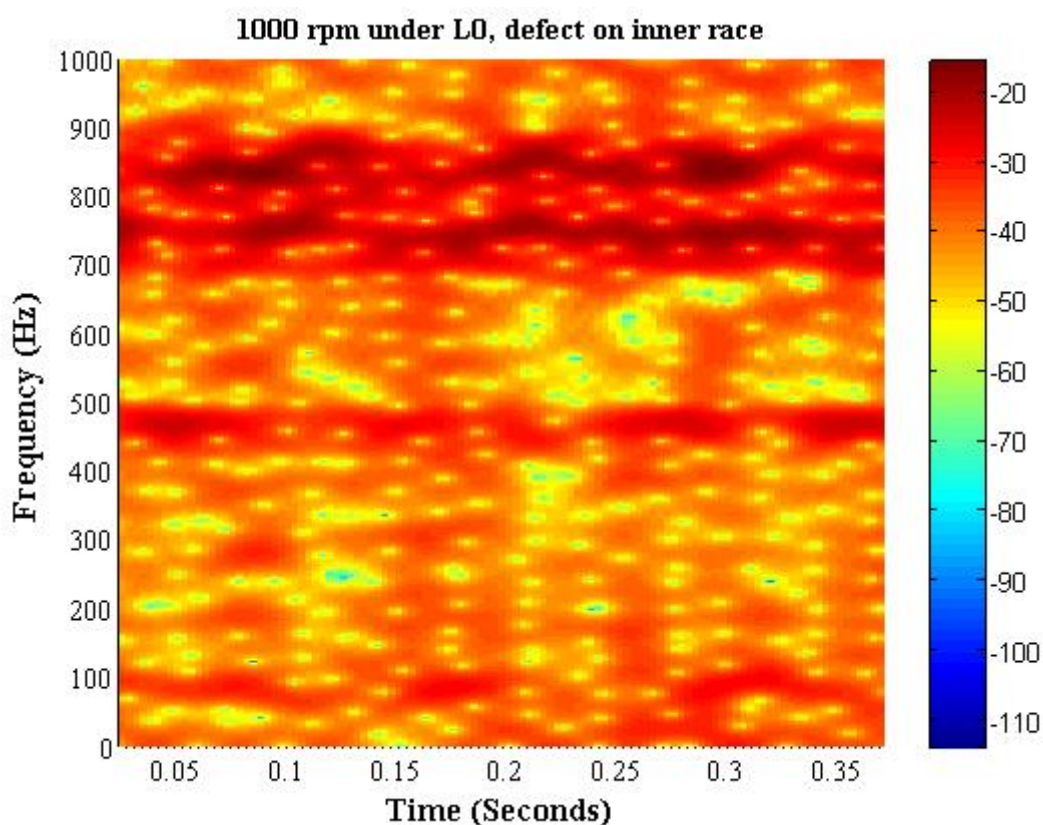
Figure 6.85 STFT of acceleration signal at 1000 rpm shaft speed under L0 load case (defect on inner race).

The STFT graph at 1500 rpm shaft speed is given in Figures 6.87-6.87 for examined load cases. The inner race defect frequency is 135.346 Hz and this frequency appears in the spectrogram for all load cases.
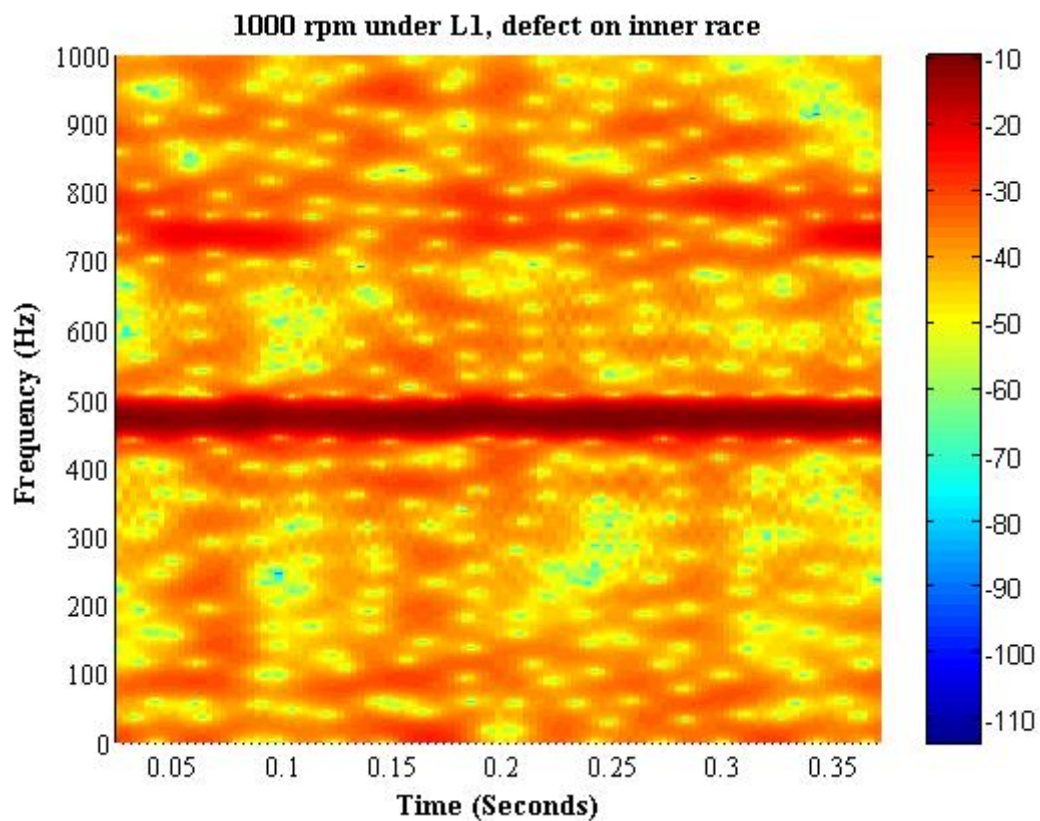
Figure 6.86 STFT of acceleration signal at 1000 rpm shaft speed under L1 load case (defect on inner race).
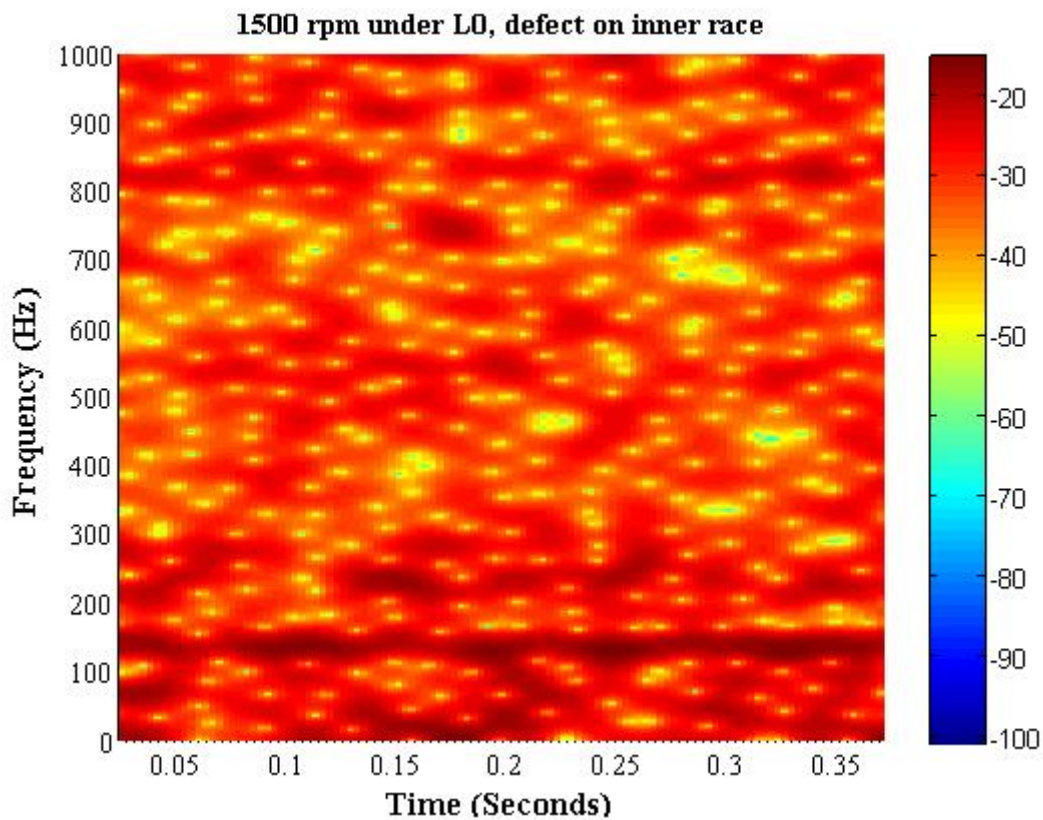
Figure 6.87 STFT of acceleration signal at 1500 rpm shaft speed under L0 load case (defect on inner race).
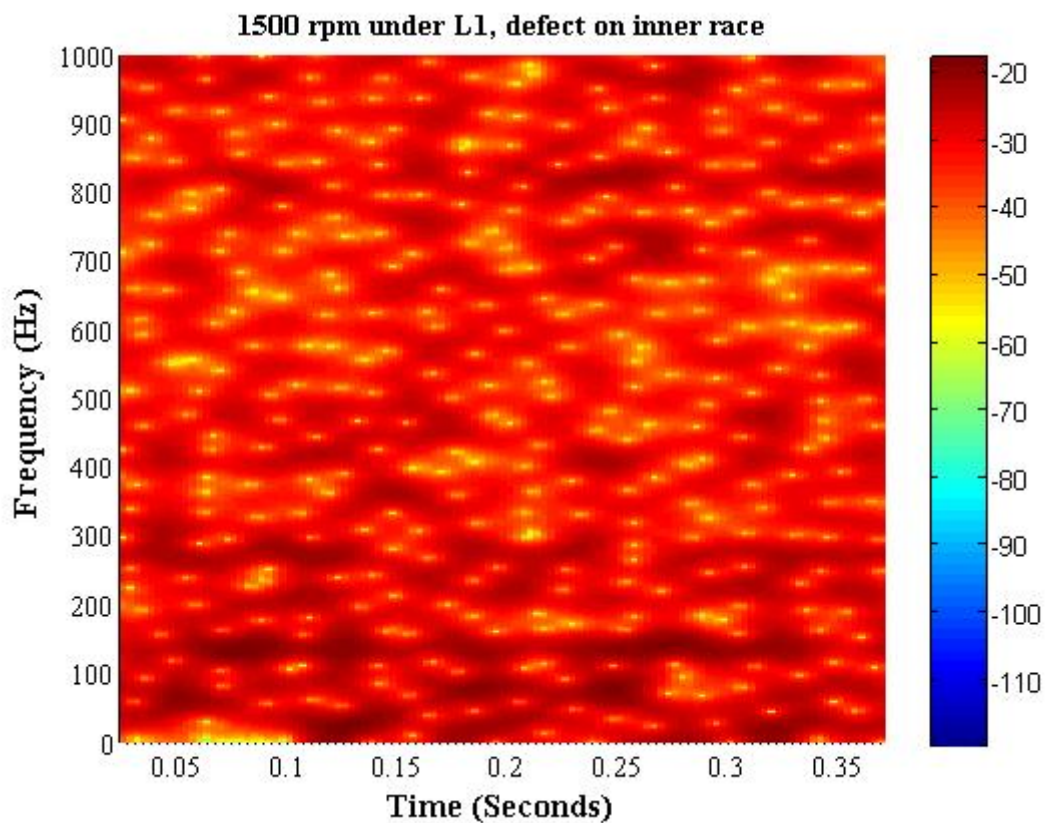
Figure 6.88 STFT of acceleration signal at 1500 rpm shaft speed under L1 load case (defect on inner race).
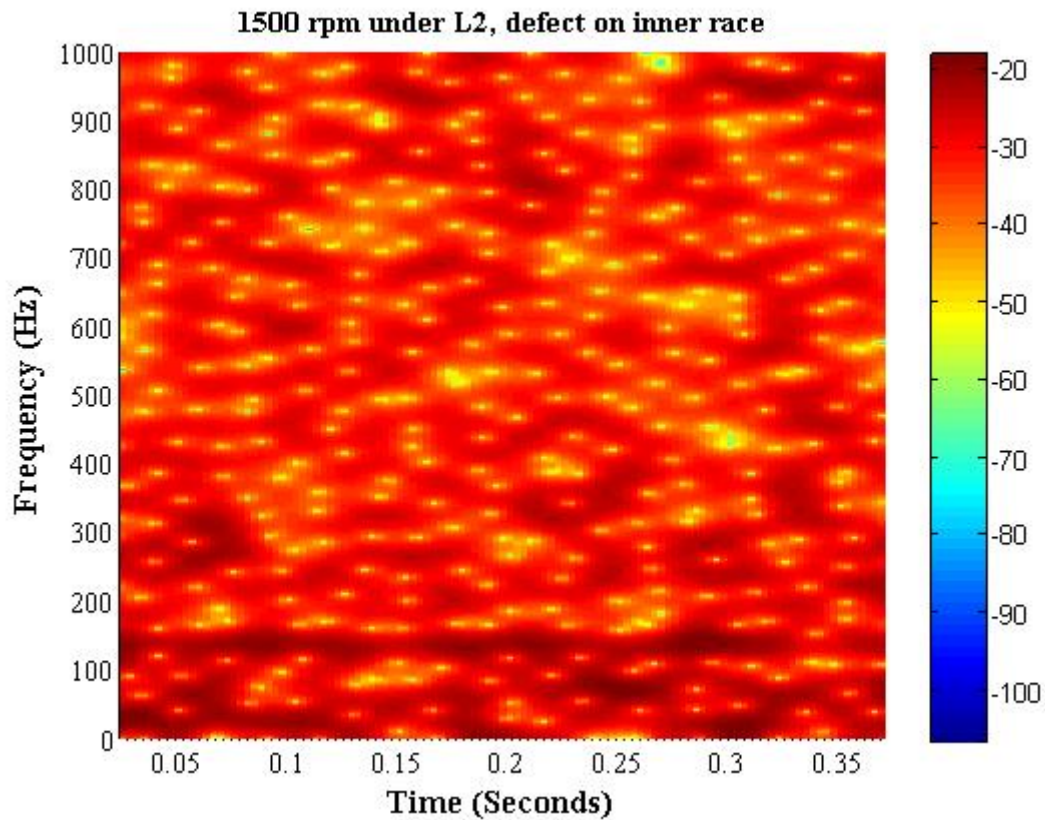
Figure 6.89 STFT of acceleration signal at 1500 rpm shaft speed under L2 load case (defect on inner race).

The STFT spectogram of acceleration response at 1750 rpm shaft speed is given in Figure 6.90 for L0 load case. The inner race defect frequency is 157.903 Hz and can be extracted from the spectrogram nearly at all time intervals.
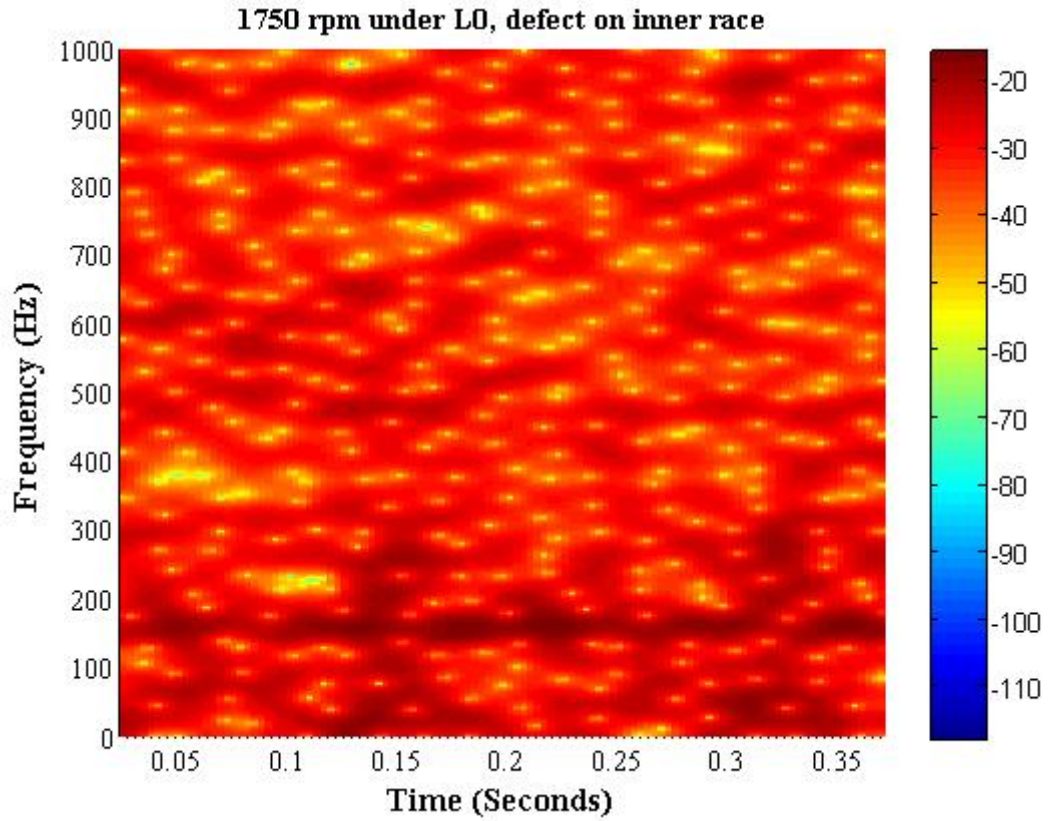
Figure 6.90 STFT of acceleration signal at 1750 rpm shaft speed under L0 load case (defect on inner race).

CHAPTER SEVEN
THE CURVE LENGTH TRANSFORM

7.1 Definition of the Curve Length Transform

In this study, the vibration responses collected from the test rig for healthy and faulty cases are processed by a time based transform named as the Curve Length Transform (CLT).

The curve length transform is a nonlinear time based transform in which the discrete values of a time signal are used. The total curve length, which is the sum of the lengths of the straight lines defined between the adjacent measurement points is calculated for a specified window length w as shown next Figure. The curve length transform is generally used for QRS complex detection and feature extraction in ECG analysis.
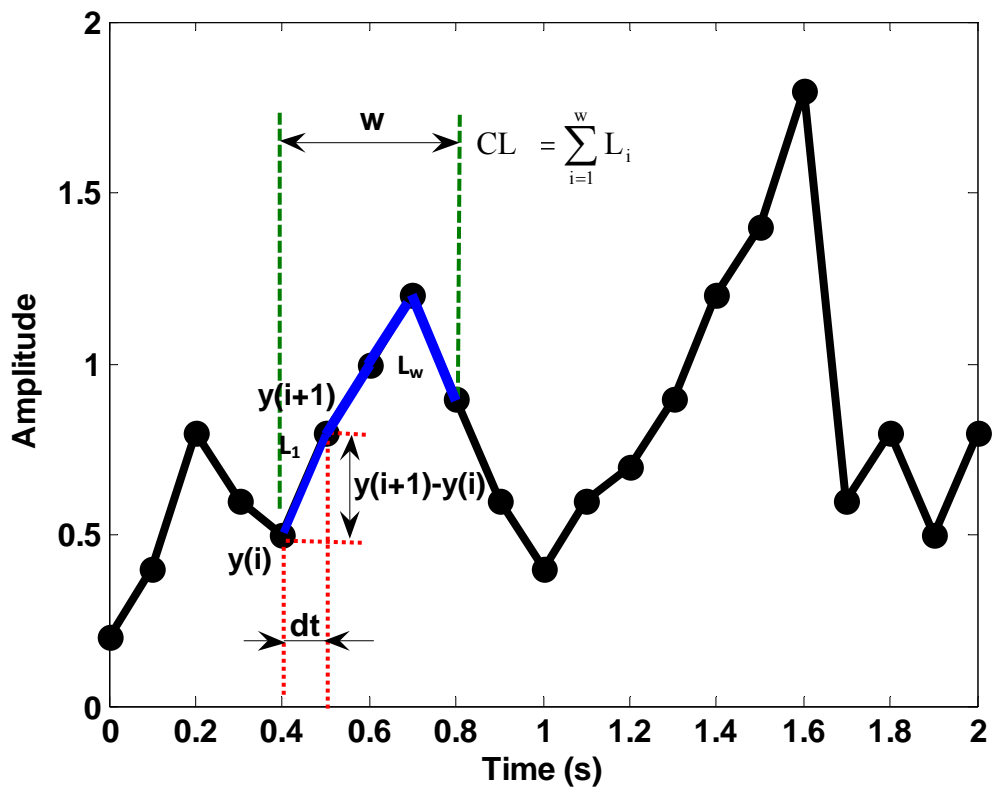
Figure 7.1 Definition of the Curve Length Transform.

The curve length transform is used in this study for diagnostic purpose of rolling element bearings. The curve length transform of a vibration signal having N samples is calculated for the window length w as

$$CL_k = \sum_{i=1}^{w} \sqrt{dt^2 + (x_{i+1} - x_i)^2} \quad (k=1,\ldots, N\text{-}w) \qquad (7.1)$$

where dt is the sampling period of the vibration signal x. Due to the nature of the faulty vibration signal, it is expected that the curve length at the ball-defect impact corresponding to the examined defect is generally longer than the other parts of the signal. The curve length transform is also defined using a scaling factor C as

$$CL_k = \sum_{i=1}^{w} \sqrt{C + (x_{i+1} - x_i)^2} \qquad (7.2)$$

A sample sheme is given for curve length transform in Figure 7.2. A simulated defect signal (Figure 7.2b) with $\omega=100$ rad/s and $\zeta=0.025$ is created and combined with the raw vibration signal (Figure 7.2a) to simulate a faulty vibration signal shown in Figure 7.2c. The results of the curve length transform calculated for faulty signal using dt=0.01 and C=1 are given in Figure 7.2d and Figure 7.2e. The curve length transform for healthy vibration signal is not given in Figure 7.2, but the results of the statistical indices are given in Table 7.1 for both healthy and faulty cases in order to show the efficiency of the curve length transform.

As seen from Table 1 that there is a extreme difference between the statistical indices calculated for raw vibration signal and its curve length transform. Only the rms value for transformed signal using scaling factor C is negatively affected. The results show that the curve length transform can be succesfully used for bearing condition monitoring.
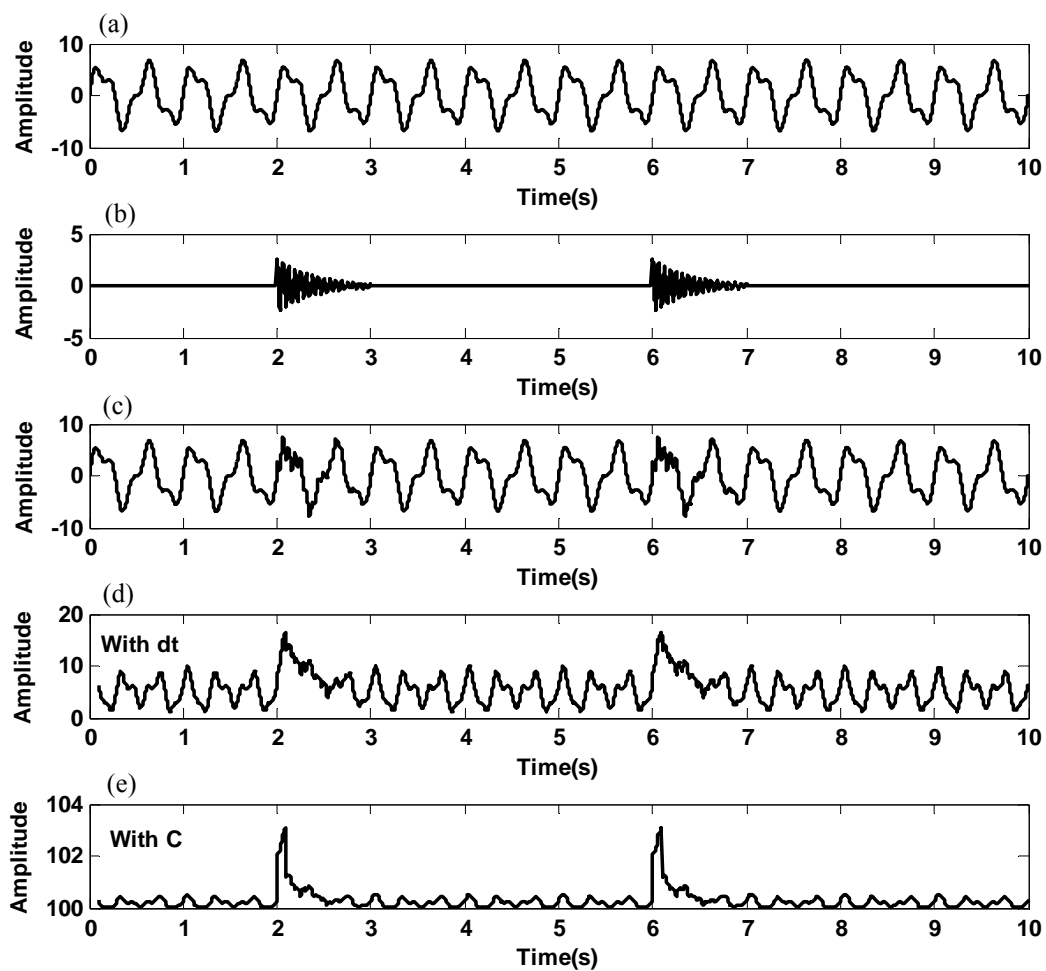
Figure 7.2 Application of the curve length transform to vibration signal a) Healthy vibration signal b) Simulated fault signal c) Faulty vibration signal d) Curve length transform of faulty signal with dt e) Curve length transform of faulty signal with C.

Table 7.1 Statistical indices for sample vibration signal and its curve length transfom.

	Healthy Signal		Faulty Signal		% Difference	
P2p	13.648		15.256		11.776	
rms	3.807		3.822		0.386	
Cf	3.584		3.991		11.345	
Kurtosis	1.856		1.882		1.400	
Curve Length Transform with dt=0.01						
	w=20	w=100	w=20	w=100	w=20	w=100
P2p	2.460	8.534	4.911	15.121	99.622	77.289
rms	1.242	5.574	1.404	6.333	12.987	13.609
Cf	1.980	1.530	3.498	2.387	76.658	55.964
Kurtosis	1.920	1.981	4.164	3.609	116.818	82.170
Curve Length Transform with C=1						
	w=20	w=100	w=20	w=100	w=20	w=100
P2p	0.154	0.499	1.947	3.042	1162.281	508.907
rms	20.039	100.194	20.057	100.287	0.093	0.093
Cf	0.007	0.005	0.097	0.030	1161.038	506.000
Kurtosis	2.947	2.177	146.697	27.847	4876.507	1178.829

7.2 Curve Length Transform of Vibration Signals and Their Moments

In this section, the curve length transform is applied to both filtered and unfiltered vibration signals. Six different window lengths, namely 5, 10, 15, 20, 50 and 100 are used for the analyses. There are no considerable differences between the curve length transforms of displacement responses for healty and defected bearings; therefore the curve length transform is applied to only the velocity and acceleration signals.

7.2.1 Curve Length Transforms of Raw Signals for C=1

The curve length transforms of raw velocity and acceleration signals are calculated for the transformation coefficient C=1. The effect of window length w on the performance of the transformation is also investigated.

7.2.1.1 Curve Length Transforms of Velocity Signals

In this section, the curve length transforms of velocity signals are given for three window length, namely 10, 20 and 100 at 1000 rpm shaft speed.

7.2.1.1.1 CLT for w=10. Figure 7.3 shows the curve length transform of velocity signals for L0 load case at 1000 rpm shaft speed. As seen from the figure, that there are considerable differences between the transforms of healthy and defected cases. Generally, the value of the transform is greater for inner race defect than those obtained for outer race defect.
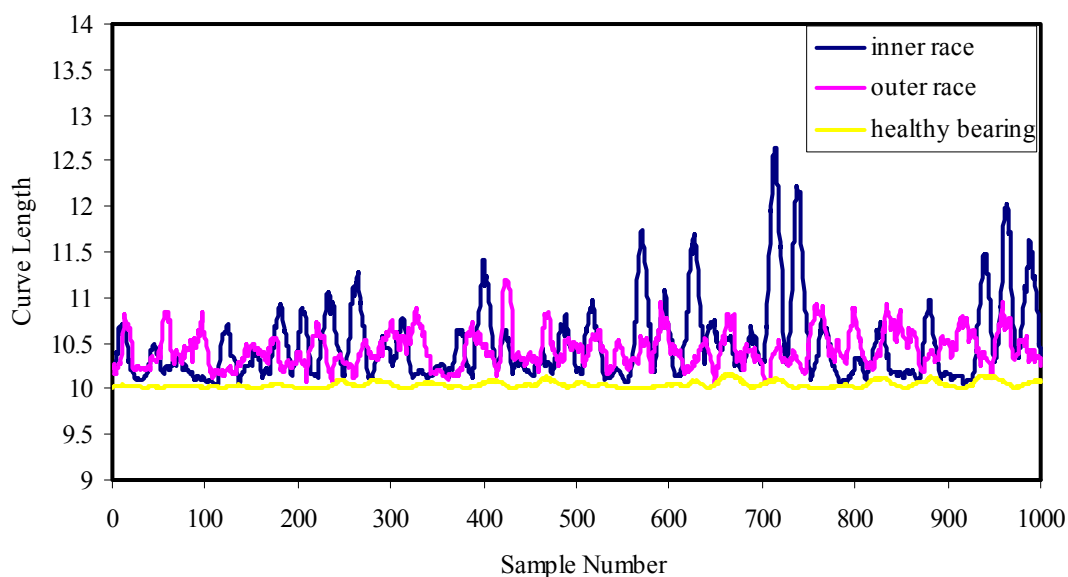
Figure 7.3 CLT of raw velocity signal under L0 load case at 1000 rpm (w=10).

The results of the CLT for L1 load case are shown in Figure 7.4. Although the amplitudes of the CLT remain unchanged, the difference between the healthy and inner race defect cases increases as the unbalance increases. The performance of the CLT is better for inner race defect detection than the detection of outer race defect. The same observations are valid for L2 load case as seen in Figure 7.5.
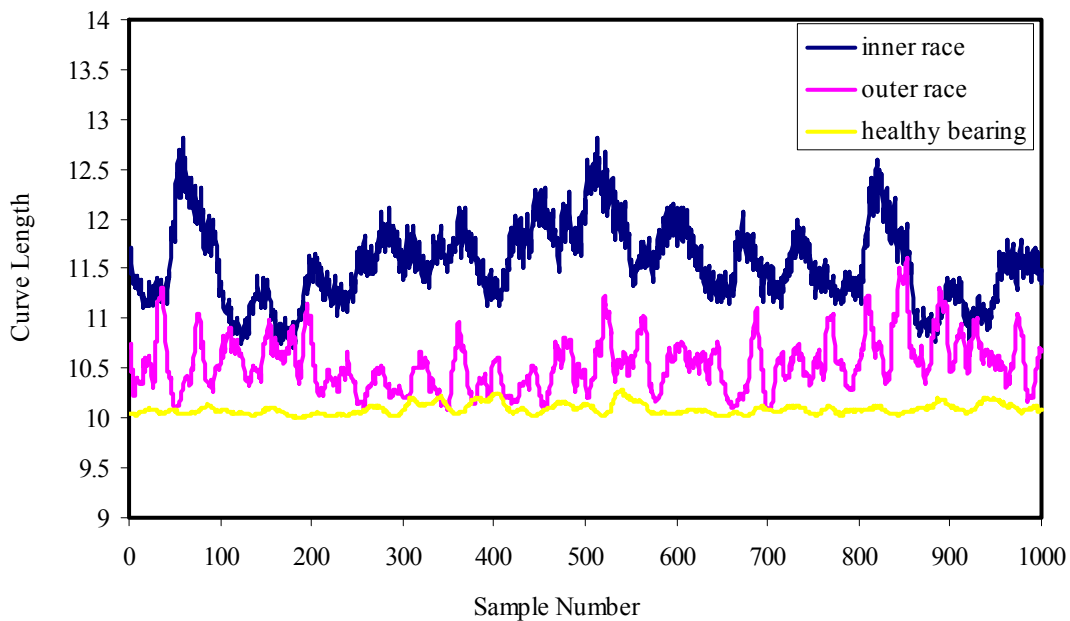
Figure 7.4 CLT of raw velocity signal under L1 load case at 1000 rpm (w=10).
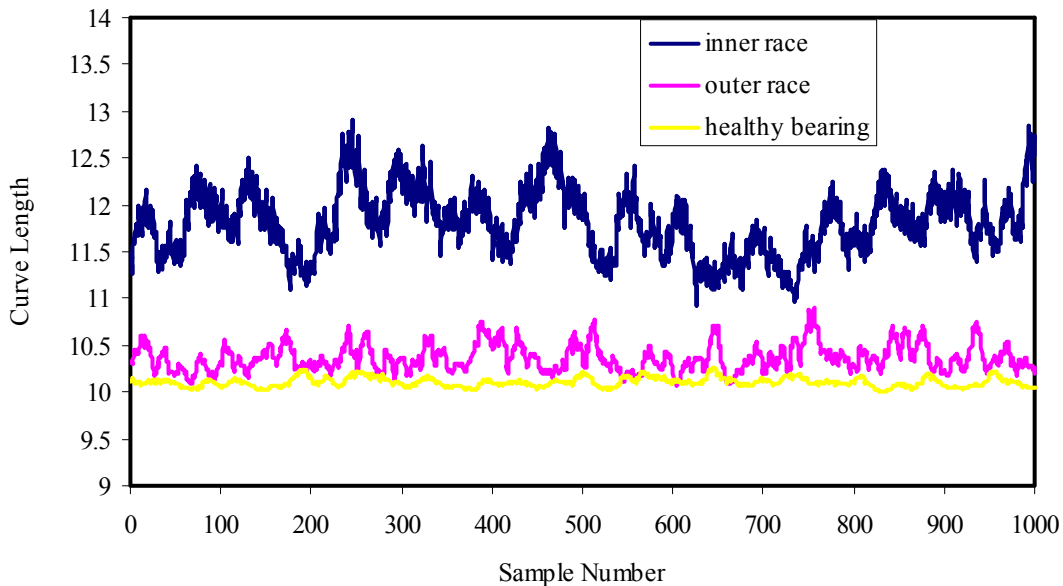
Figure 7.5 CLT of raw velocity signal under L2 load case at 1000 rpm (w=10).

The CLTs of velocity signals at 2000 rpm are given in Figures 7.6-7.8 for different load cases. The amplitude of the CLT are lower than those obtained for 1000 rpm

shaft speed and the differences between the curve length transforms are not considerable for L1 and L2 load cases.
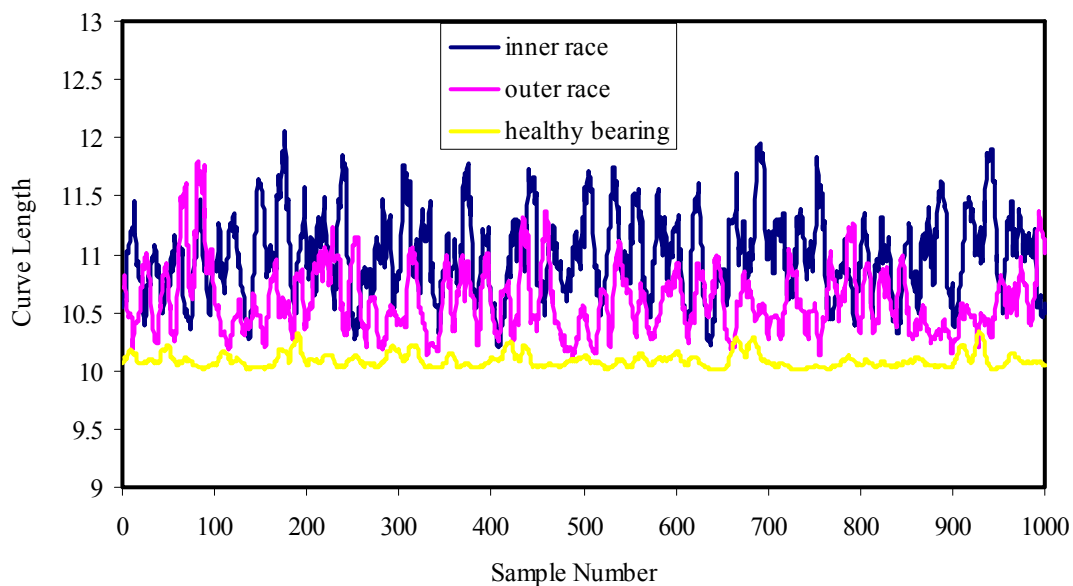
Figure 7.6 CLT of raw velocity signal under L0 load case at 2000 rpm (w=10).
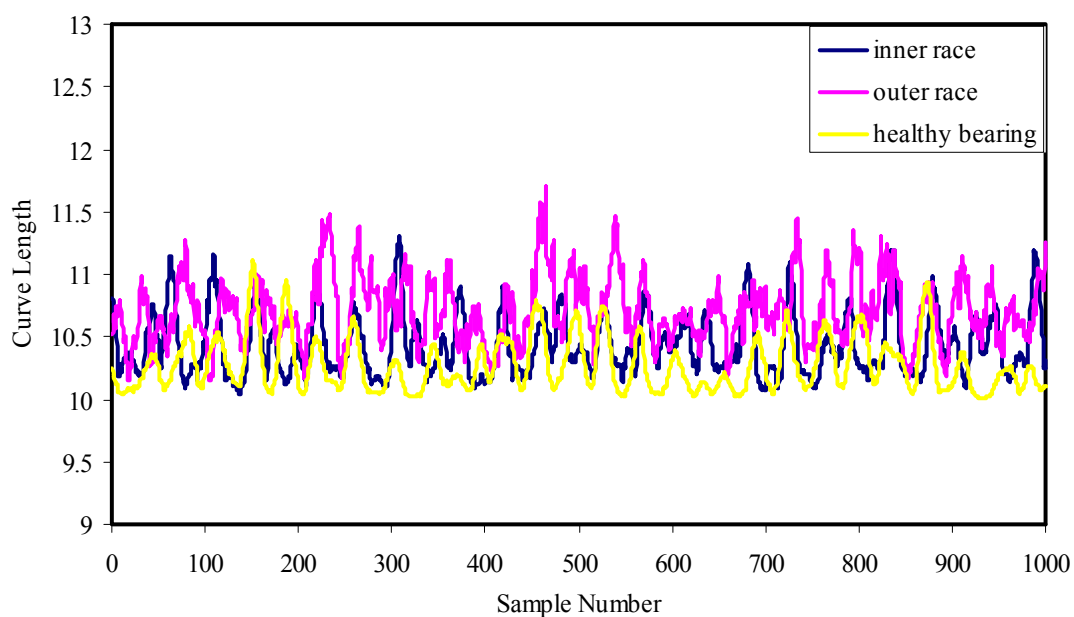
Figure 7.7 CLT of raw velocity signal that is generated under L1 load case at 2000 rpm for 10w.
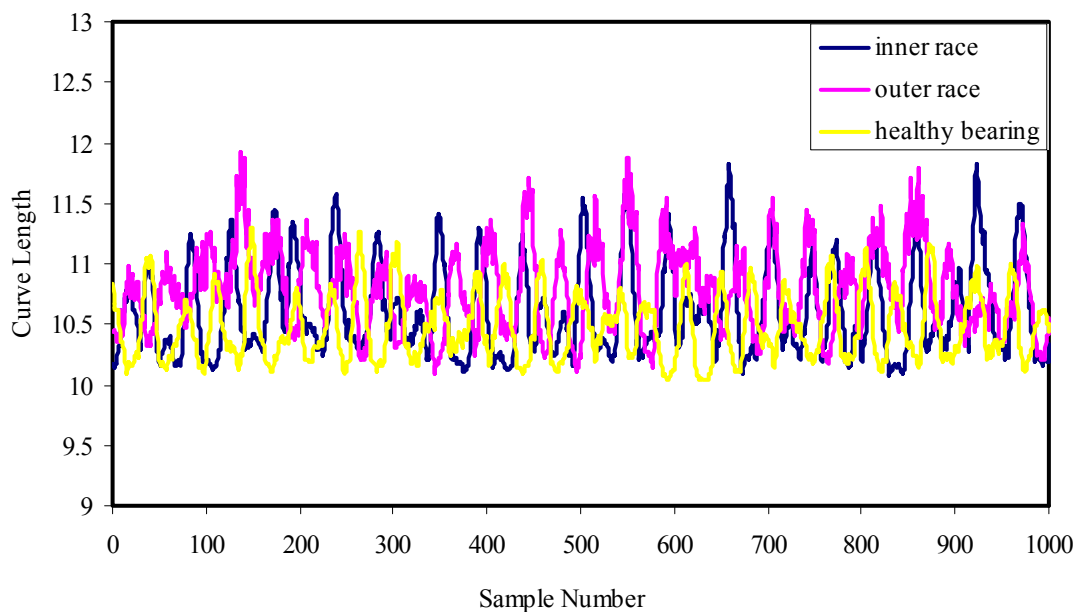
Figure 7.8 CLT of raw velocity signal under L2 load case at 2000 rpm (w=10).

7.2.1.1.2 CLT for w=20. The curve lenght transforms for the examined load cases are given in Figures 7.9-7.11. The CLT for inner race defect case differs from the CLT of healthy bearing especially for L1 and L2 load cases.
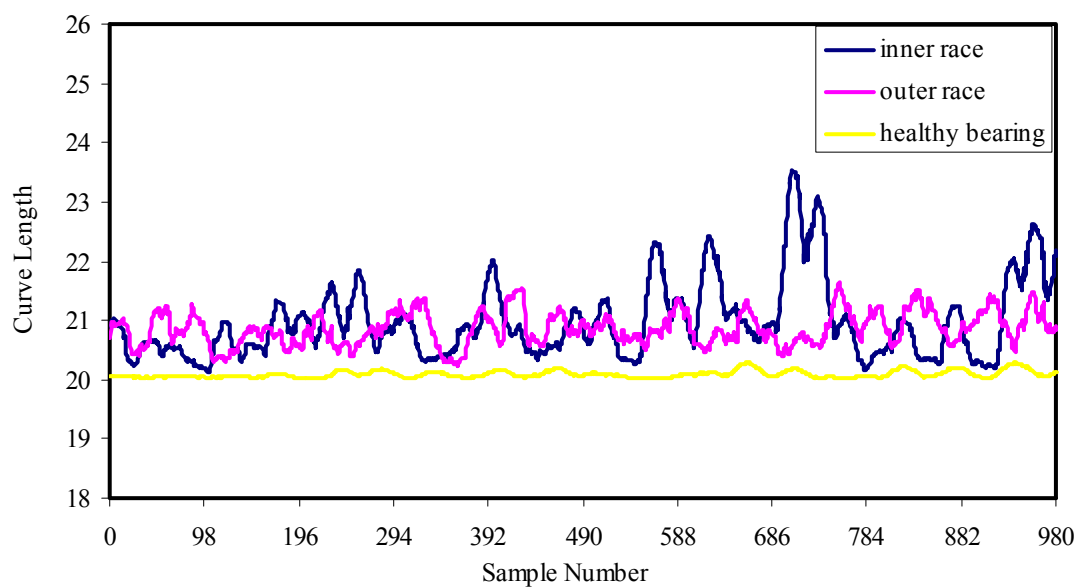
Figure 7.9 CLT of raw velocity signal under L0 load case at 1000 rpm (w=20).
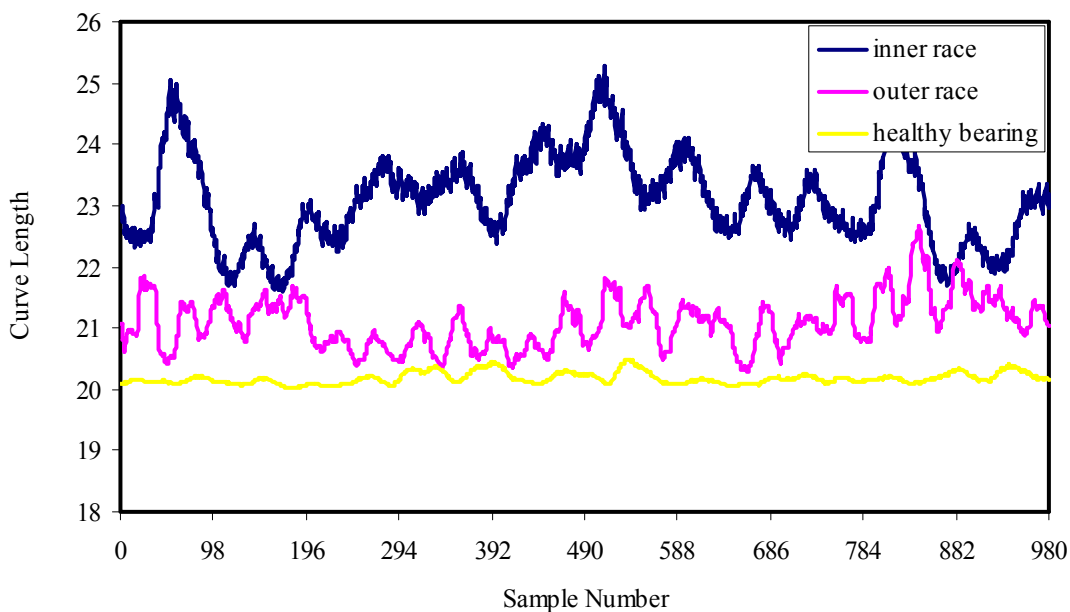
Figure 7.10 CLT of raw velocity signal under L1 load case at 1000 rpm (w=20).
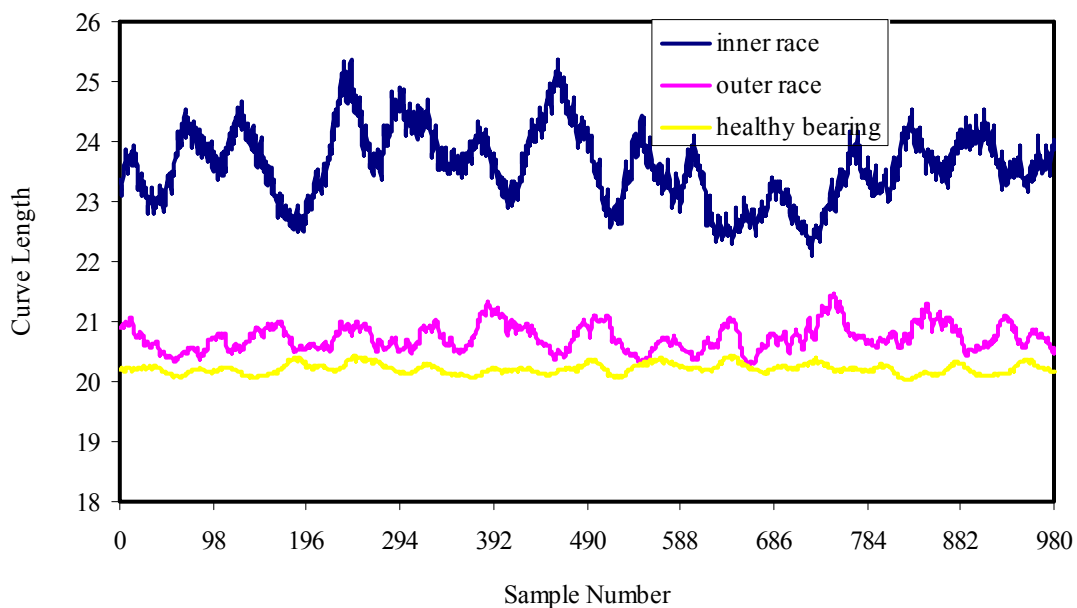
Figure 7.11 CLT of raw velocity signal under L2 load case at 1000 rpm (w=20).

The curve length transforms of velocity signals for 2000 rpm shaft speed are given in Figures 7.12-7.14. The CLT does not give useful information for L1 and L2 load cases at this shaft speed.
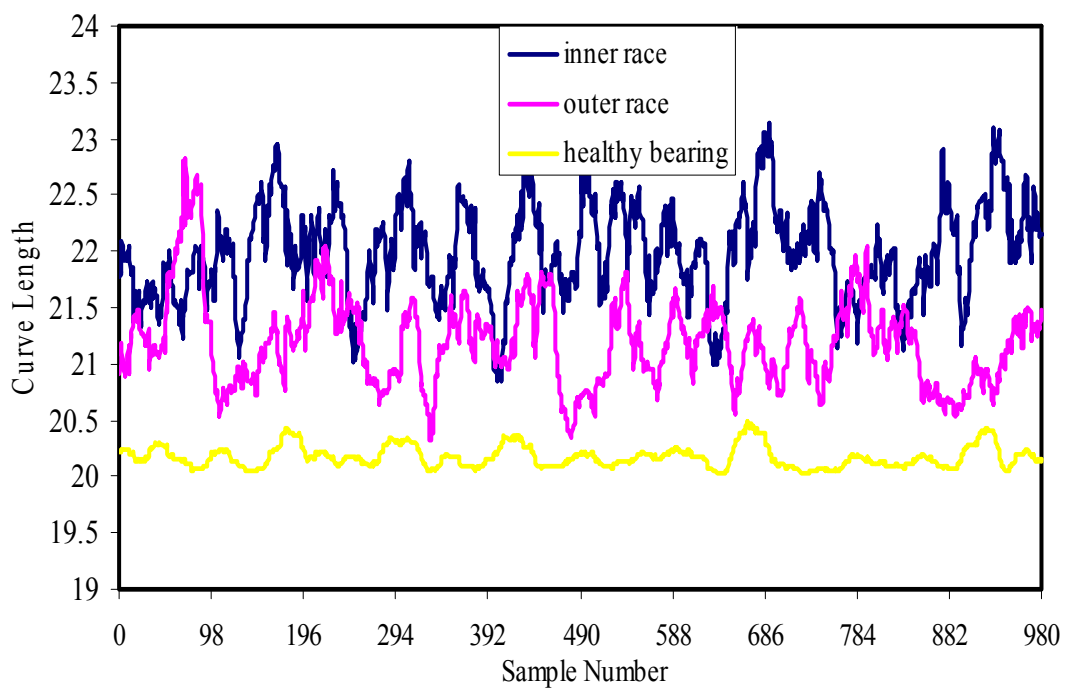
Figure 7.12 CLT of raw velocity signal under L0 load case at 2000 rpm for (w=20).
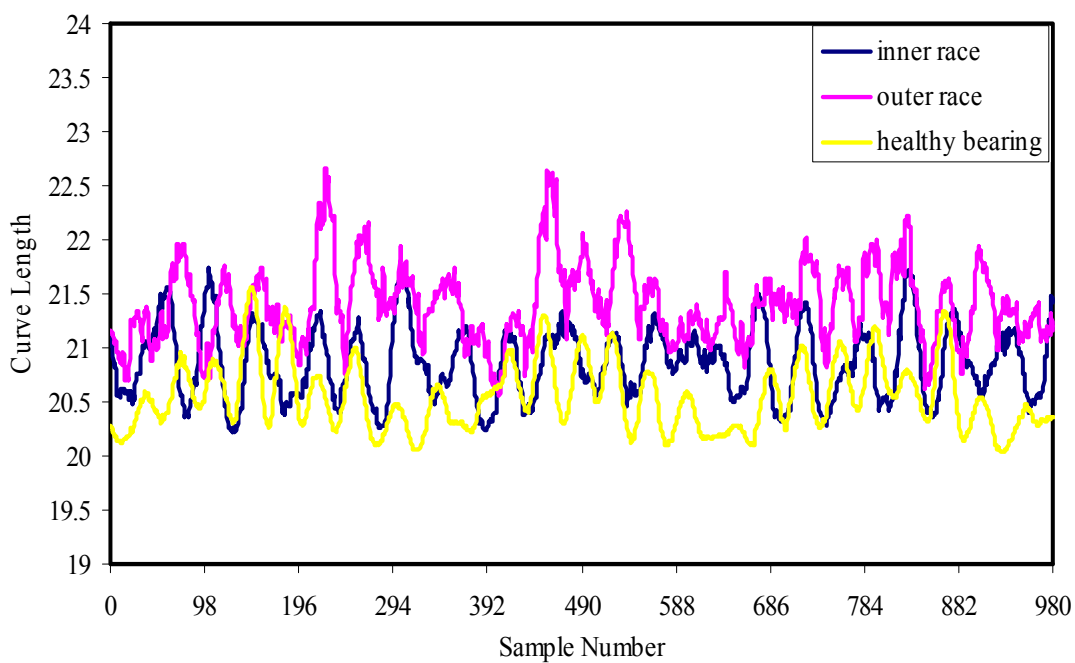
Figure 7.13 CLT of raw velocity signal under L1 load case at 2000 rpm (w=20).
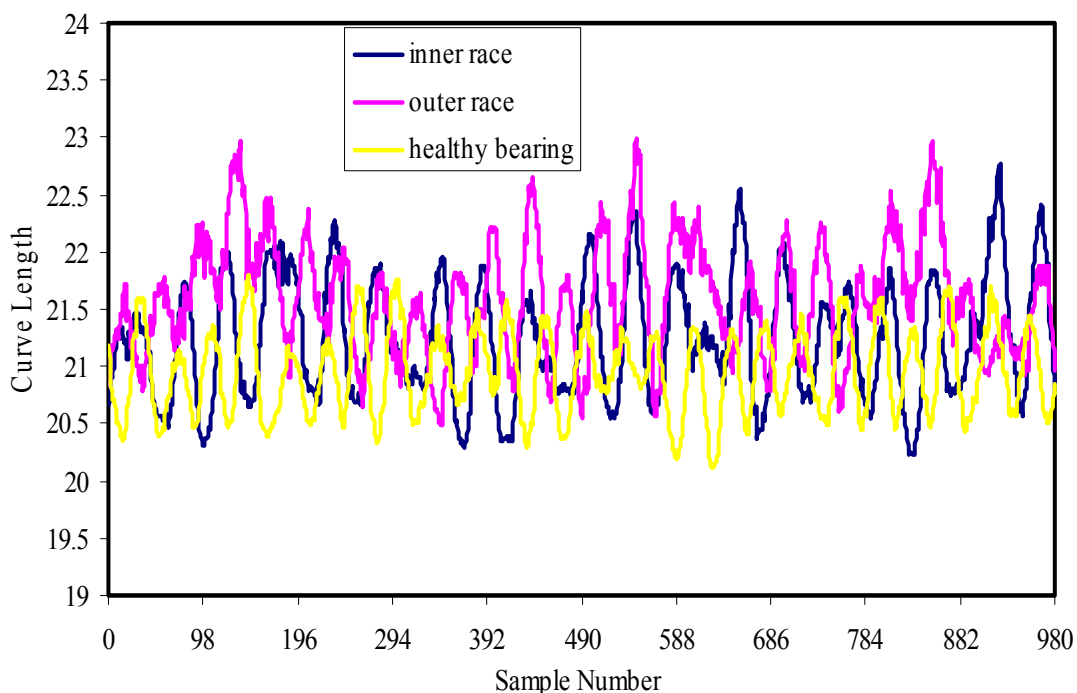
Figure 7.14 CLT of raw velocity signal under L2 load case at 2000 rpm (w=20).

7.2.1.1.3 CLT for w=100. Curve length transforms for the window lenght w=100 are given in Figures 7.15-7.17. As seen in the figures, the wavy shape of the CLT disappears as the window length increases. The detection of the inner race defect seems to be more possible by CLT for L1 and L2 load cases.
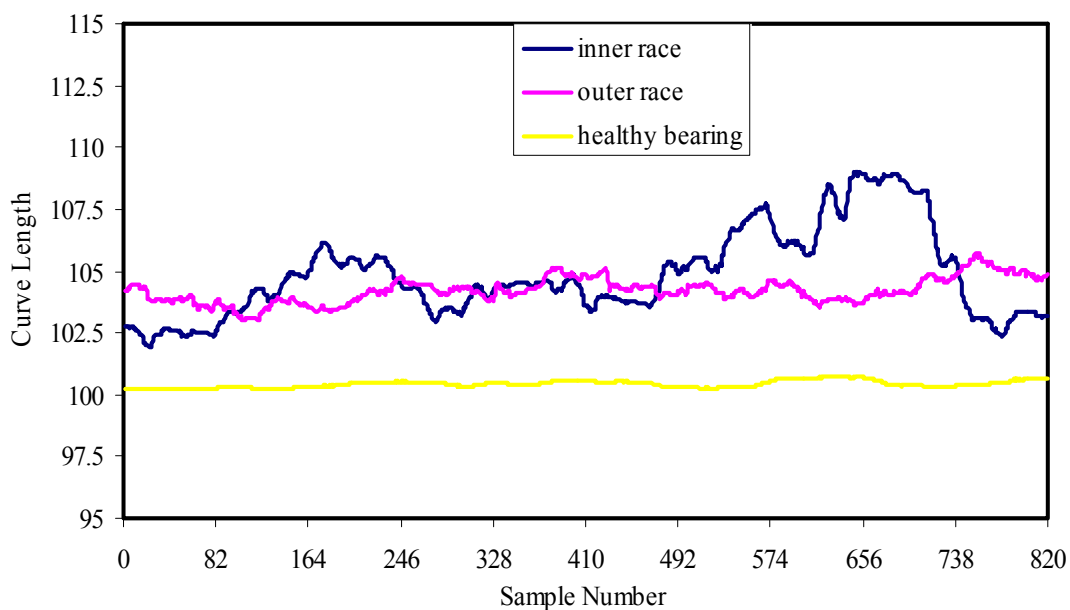
Figure 7.15 CLT of raw velocity signal under L0 load case at 1000 rpm (w=100).
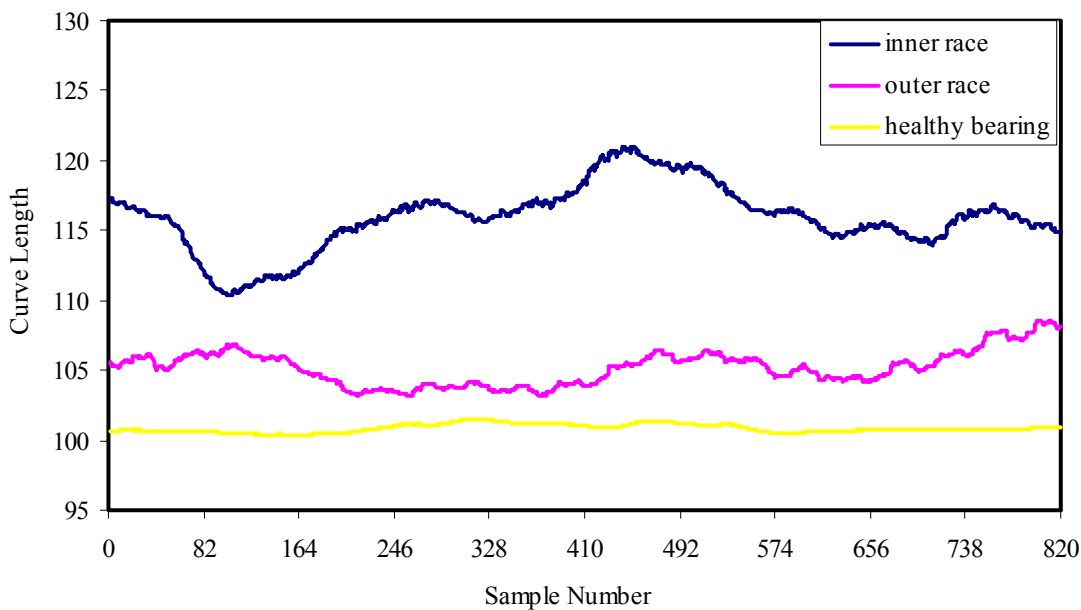
Figure 7.16 CLT of raw velocity signal under L1 load case at 1000 rpm (w=100).
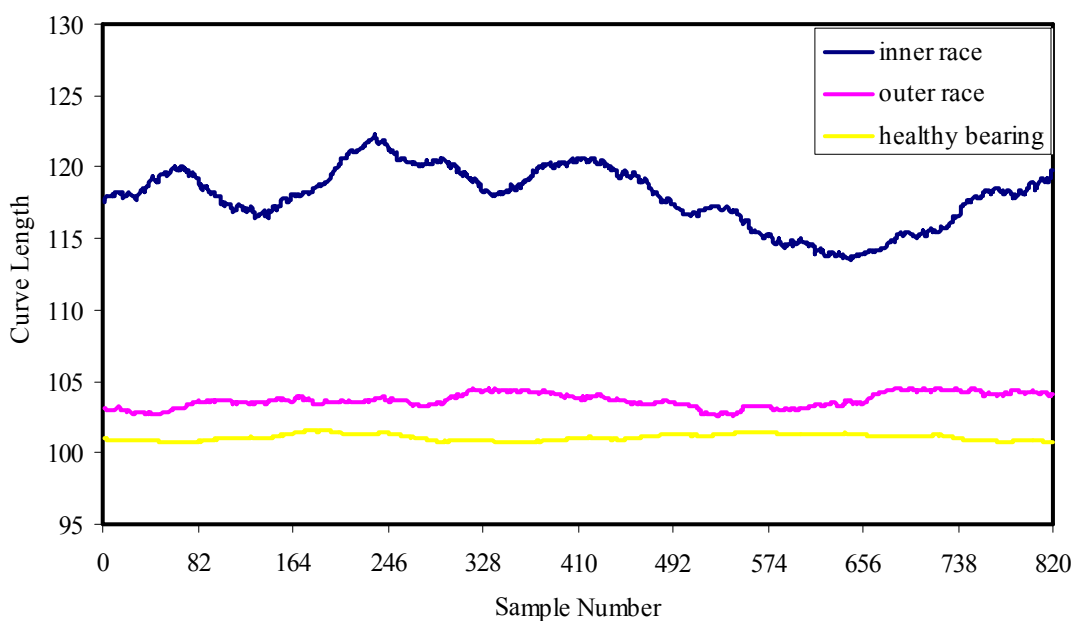
Figure 7.17 CLT of raw velocity signal under L2 load case at 1000 rpm (w=100).

The curve length transforms of velocity signals for 2000 rpm shaft speed are given in Figures 7.18-7.20. As seen from the figures, that defect detection is possible using the CLT patterns for L0 load case. In contrast with other cases, the values of CLT for outer race defect are greater than those obtained for inner race defect for L1 and L2 load cases.
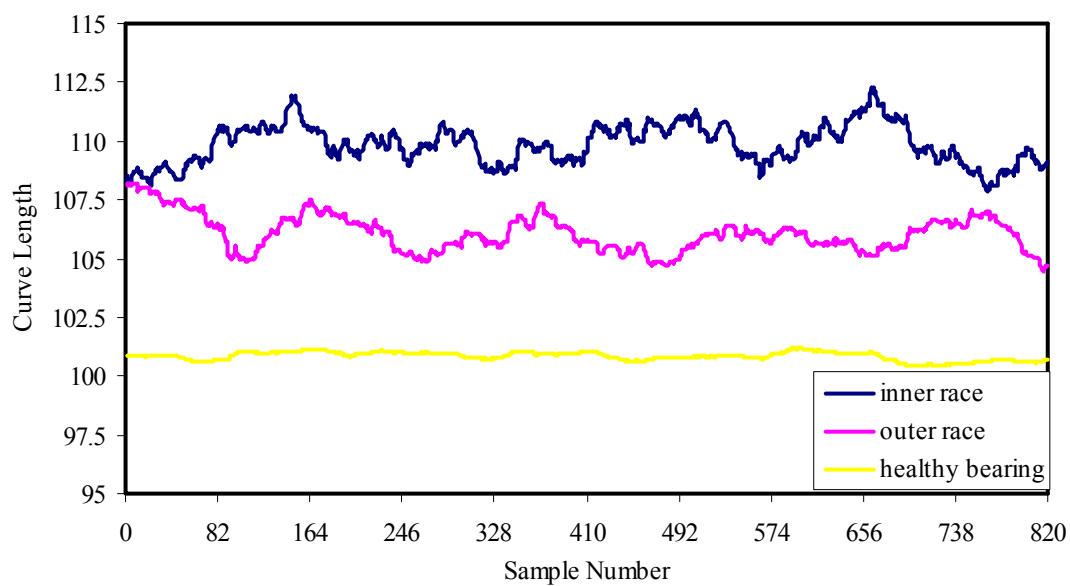
Figure 7.18 CLT of raw velocity signal under L0 load case at 2000 rpm (w=100).
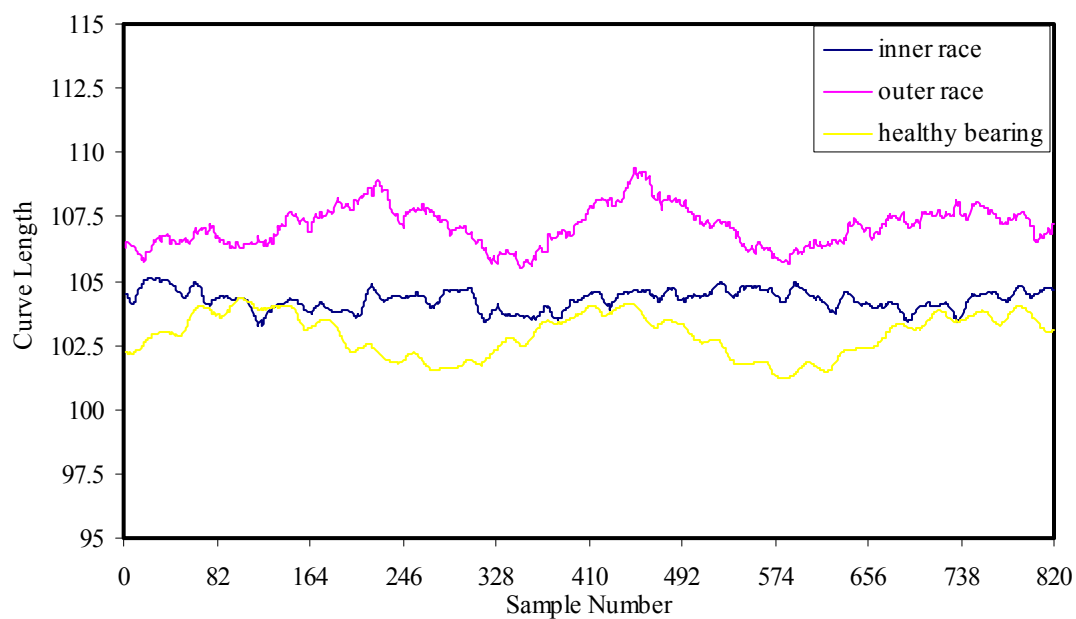
Figure 7.19 CLT of raw velocity signal under L1 load case at 2000 rpm (w=100).
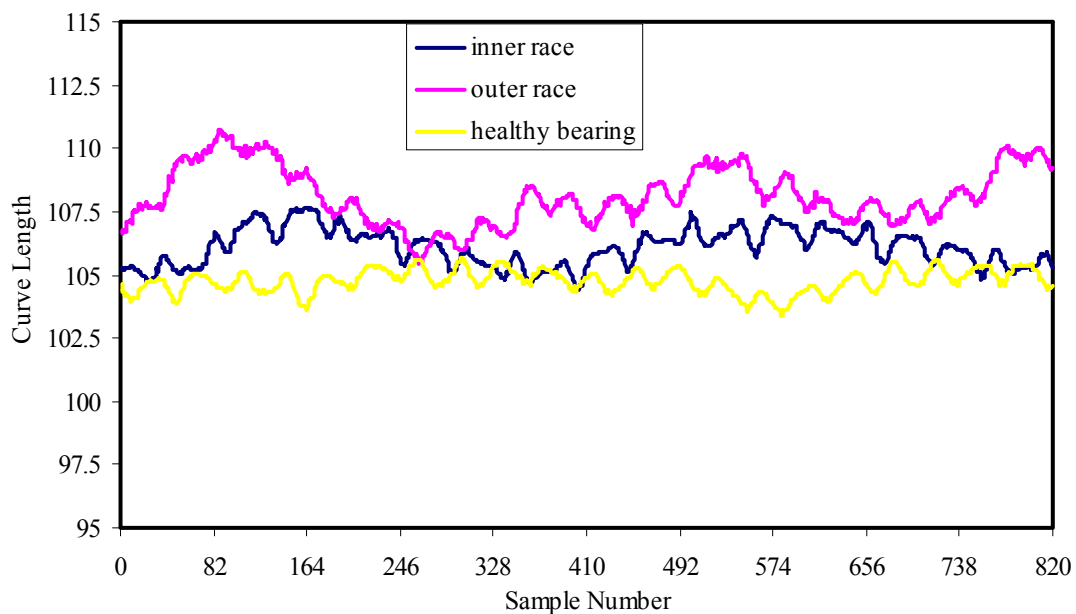
Figure 7.20 CLT of raw velocity signal under L2 load case at 2000 rpm (w=100).

7.2.1.2 Curve Length Transforms of Acceleration Signals

In this section, the curve length transforms of raw acceleration signals are calculated for the transformation coefficient C=1 at 1000 rpm.

7.2.1.2.1 CLT for w=10. Curve length transforms of acceleration signals for 1000 rpm shaft speed are given in Figures 7.21-7.23. The ratios between the CLT's of the healthy and faulty signals are greater for acceleration signals compared with the velocity signals. The inner race defect can be detected by CLT easier than the outer race defect.
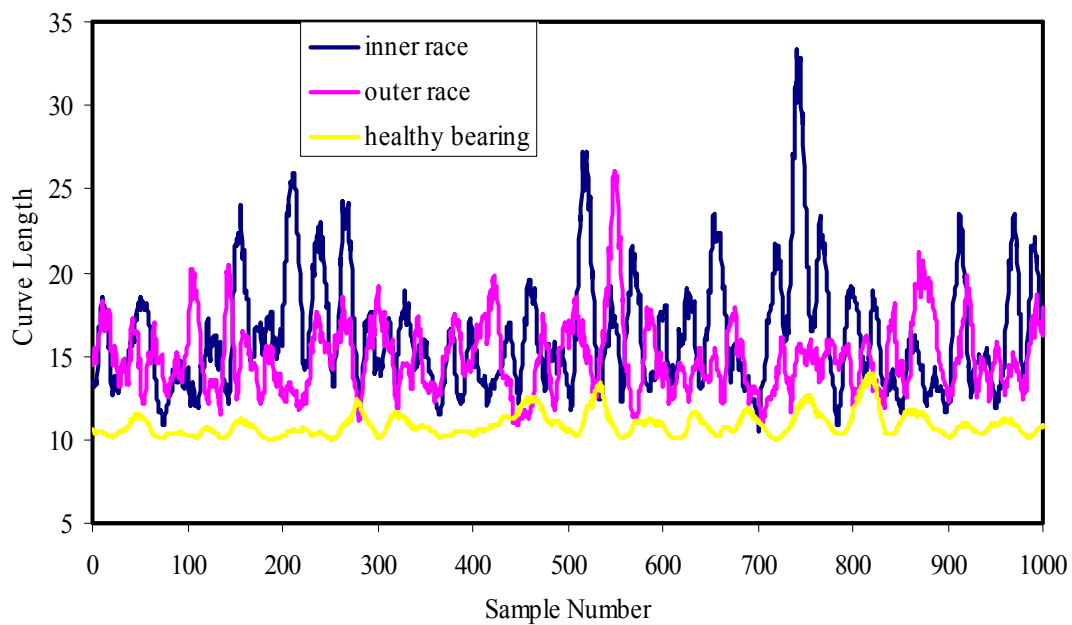
Figure 7.21 CLT of raw acceleration signal under L0 load case at 1000 rpm (w=10).
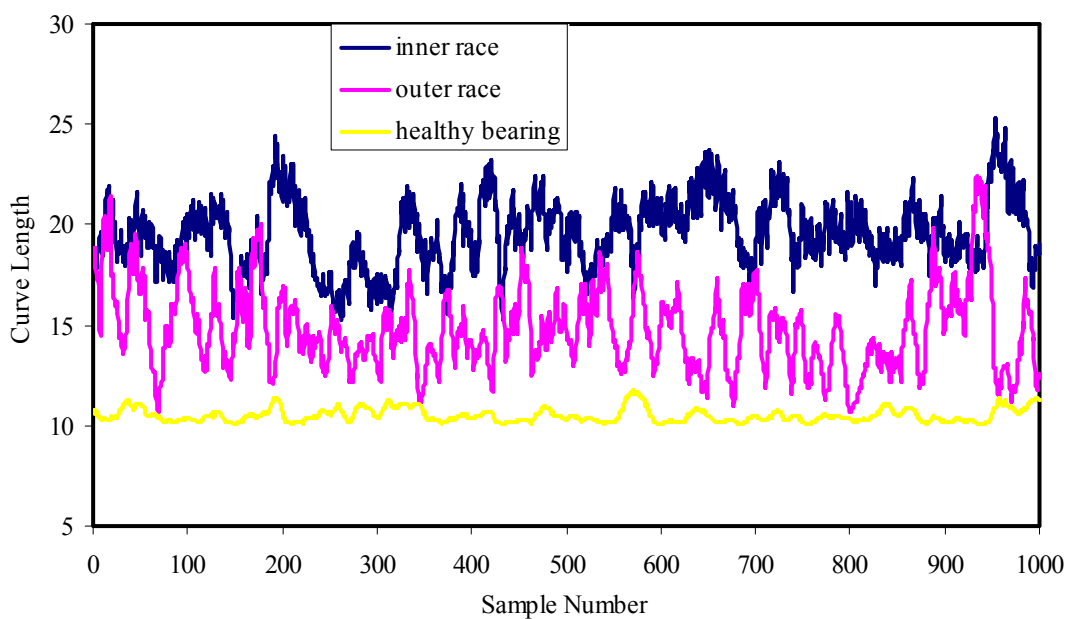
Figure 7.22 CLT of raw acceleration signal under L1 load case at 1000 rpm (w=10).
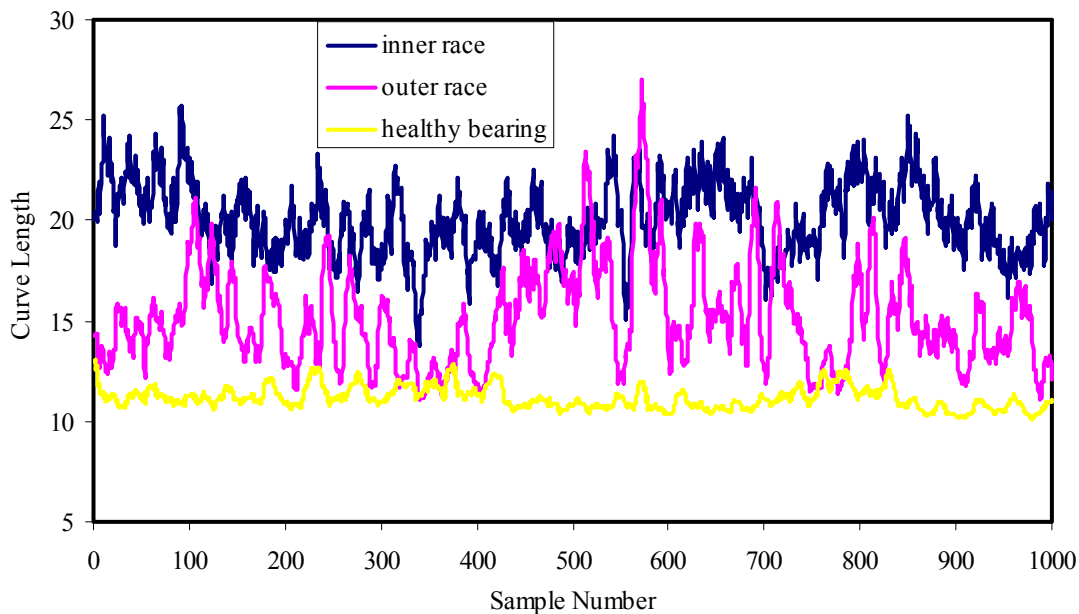
Figure 7.23 CLT of raw acceleration signal under L2 load case at 1000 rpm (w=10).

The curve length transforms of raw acceleration signals for 2000 shaft speed are given in Figures 7.24-7.26. The CLT can be used to detect the inner race defect for L0 load case, but it is not possible to detect the bearing failures by the CLT's of acceleration signals for L1 and L2 load cases.
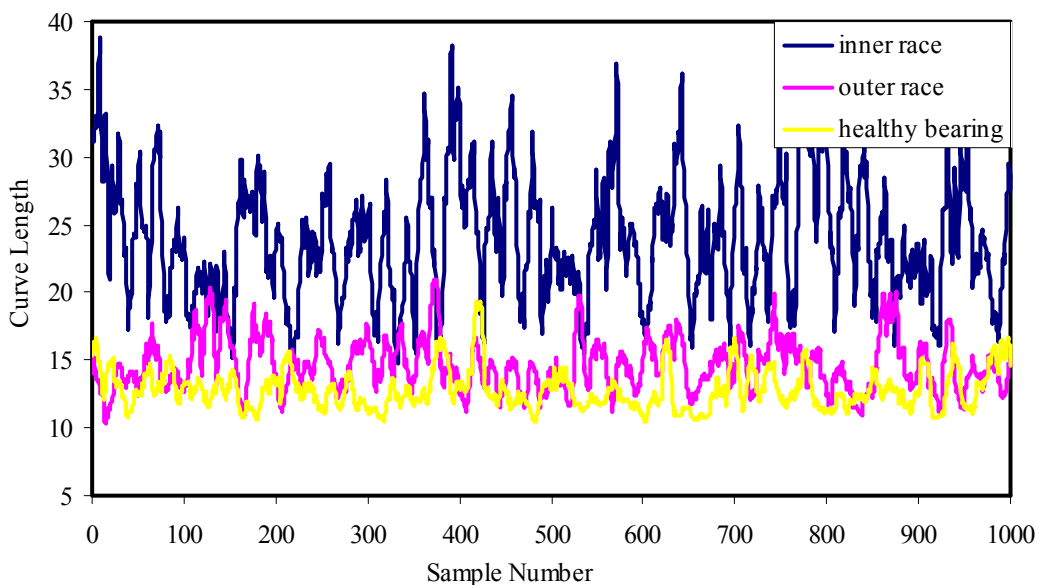
Figure 7.24 CLT of raw acceleration signal under L0 load case at 2000 rpm (w=10).
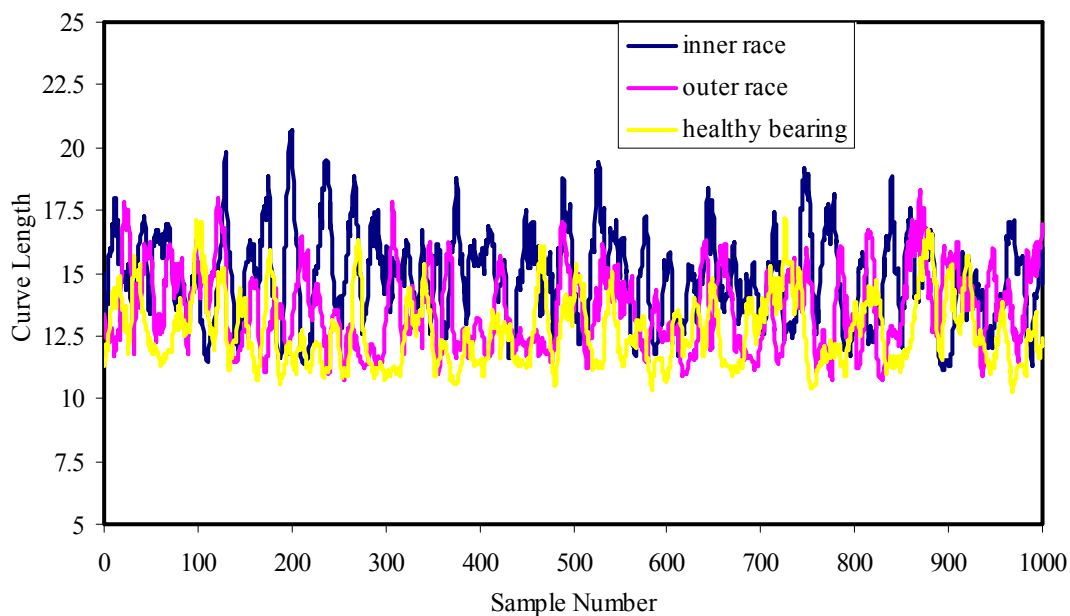
Figure 7.25 CLT of raw acceleration signal under L1 load case at 2000 rpm (w=10).
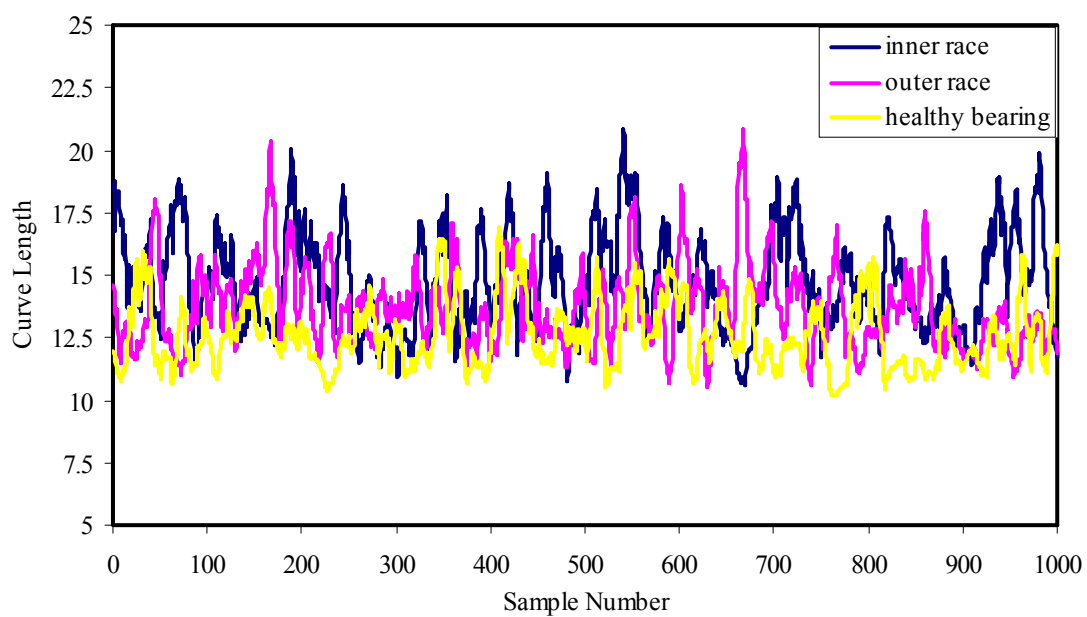
Figure 7.26 CLT of raw acceleration signal under L2 load case at 2000 rpm (w=10).

7.2.1.2.2 CLT for w=20. The CLT's of the raw acceleration signals for 1000 rpm shaft speed are given in Figures 7.27-7.29 for window length w=20.
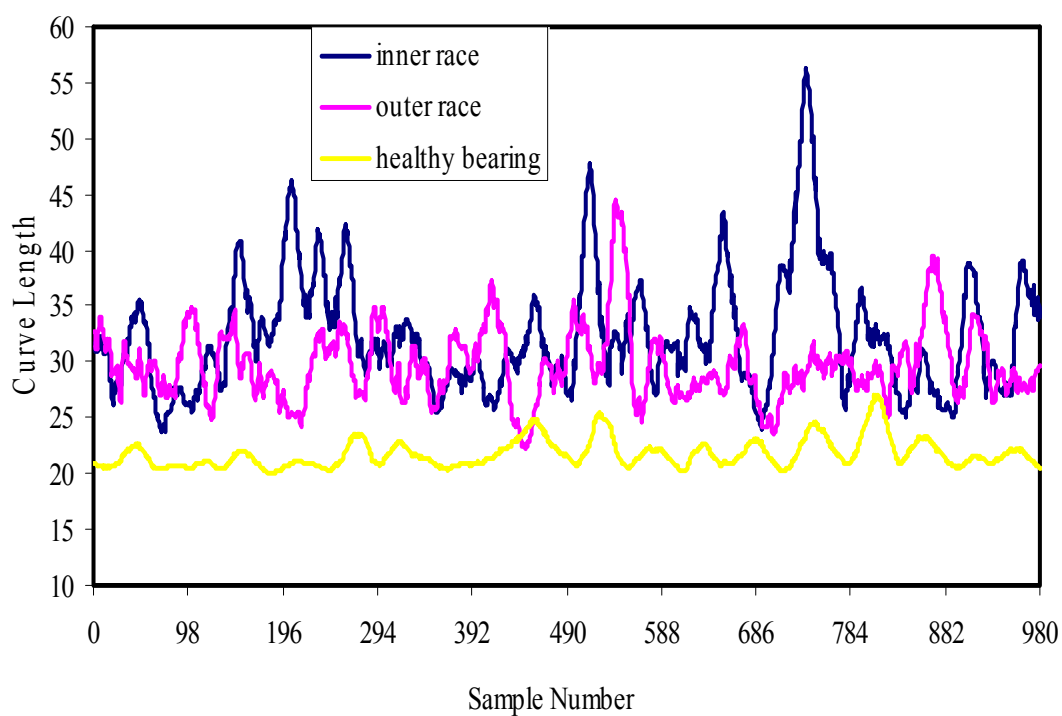
Figure 7.27 CLT of raw acceleration signal under L0 load case at 1000 rpm (w=20).
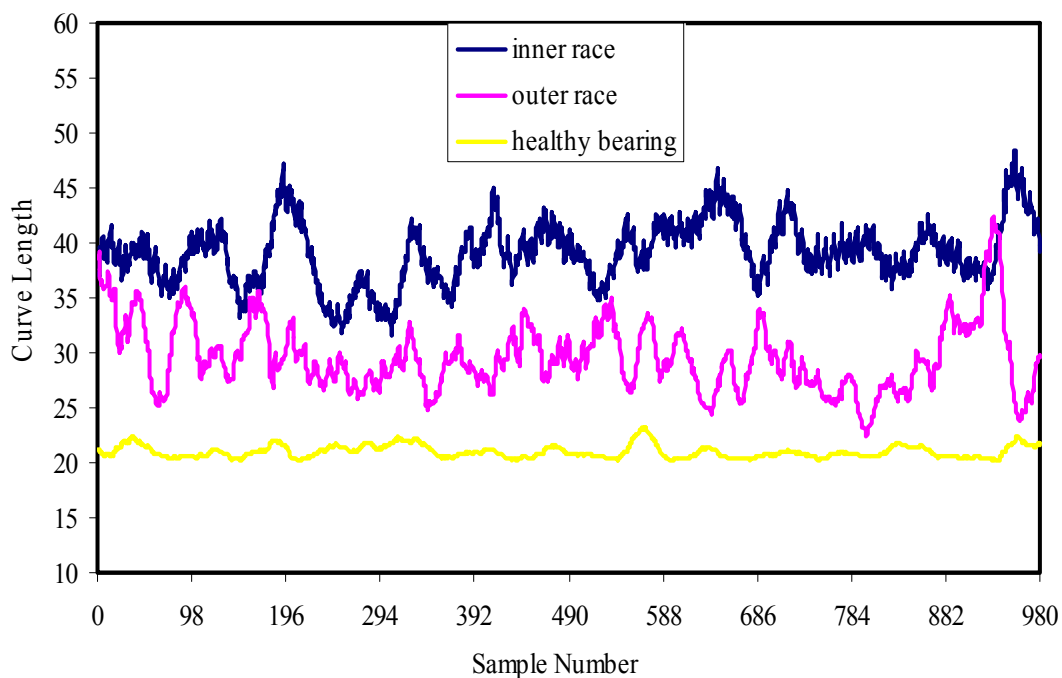
Figure 7.28 CLT of raw acceleration signal under L1 load case at 1000 rpm (w=20).
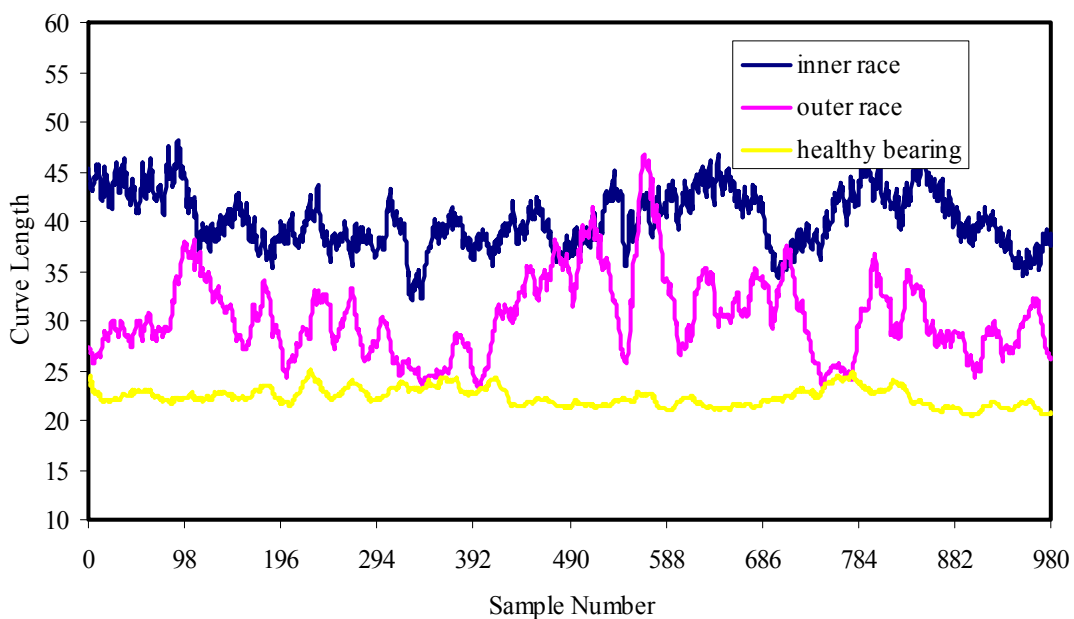
Figure 7.29 CLT of raw acceleration signal under L2 load case at 1000 rpm (w=20).

The curve length transforms of raw acceleration signals for 2000 rpm shaft speed are given in Figures 7.32-7.34. As seen from the figures, detection of inner race defect is possible only for L0 load case.
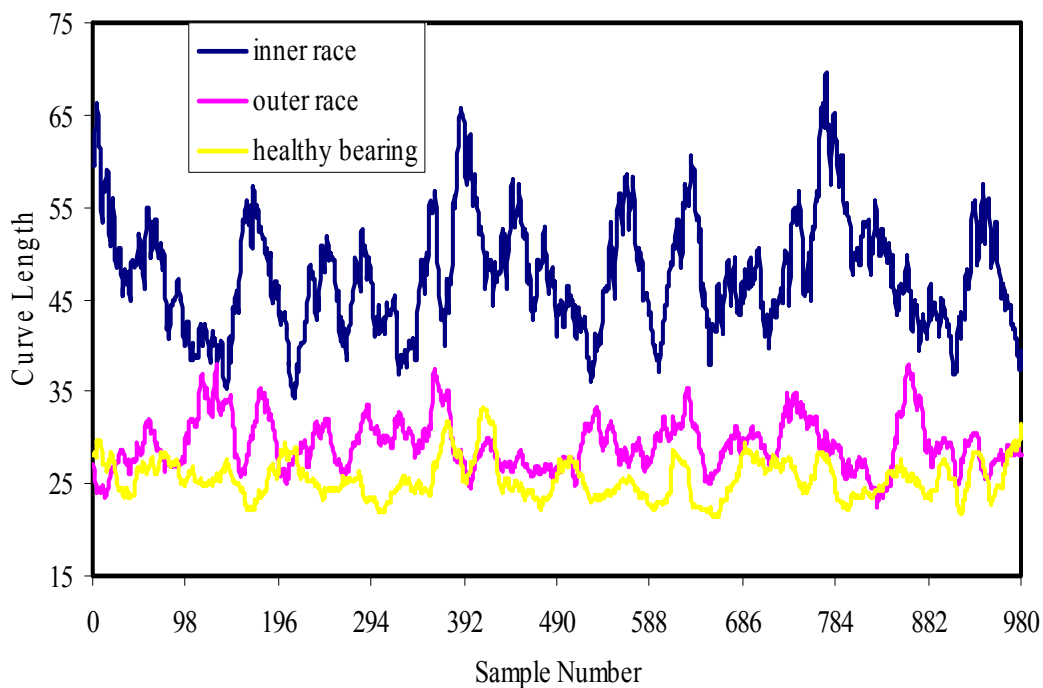
Figure 7.30 CLT of raw acceleration signal under L0 load case at 2000 rpm (w=20).
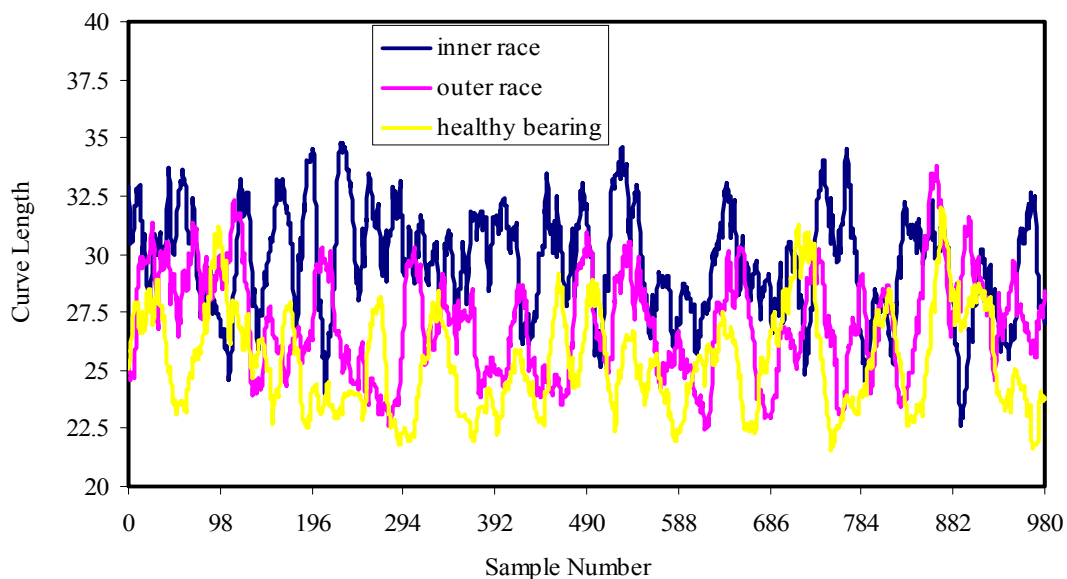
Figure 7.31 CLT of raw acceleration signal under L1 load case at 2000 rpm (w=20).
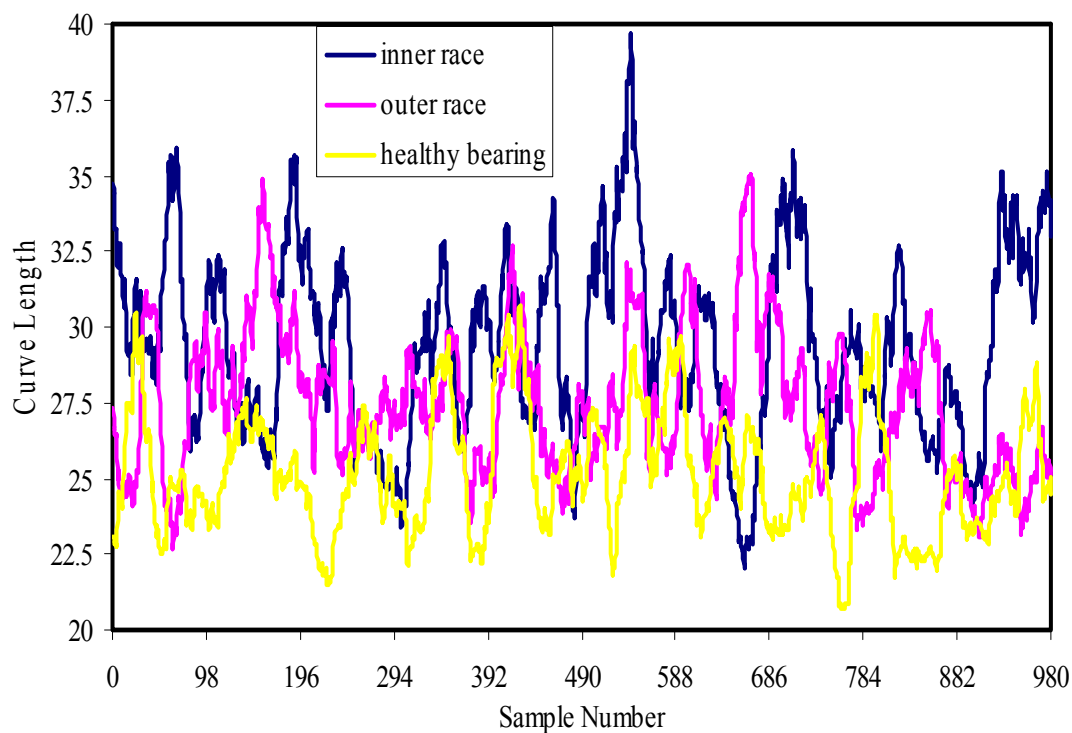
Figure 7.32 CLT of raw acceleration signal under L2 load case at 2000 rpm (w=20).

7.2.1.2.3 CLT for w=100. The curve length transforms of the acceleration signal for the window length w=100 are given in Figures 7.33-7.35. The fault detection seems to be possible for all load cases by the curve length transform.
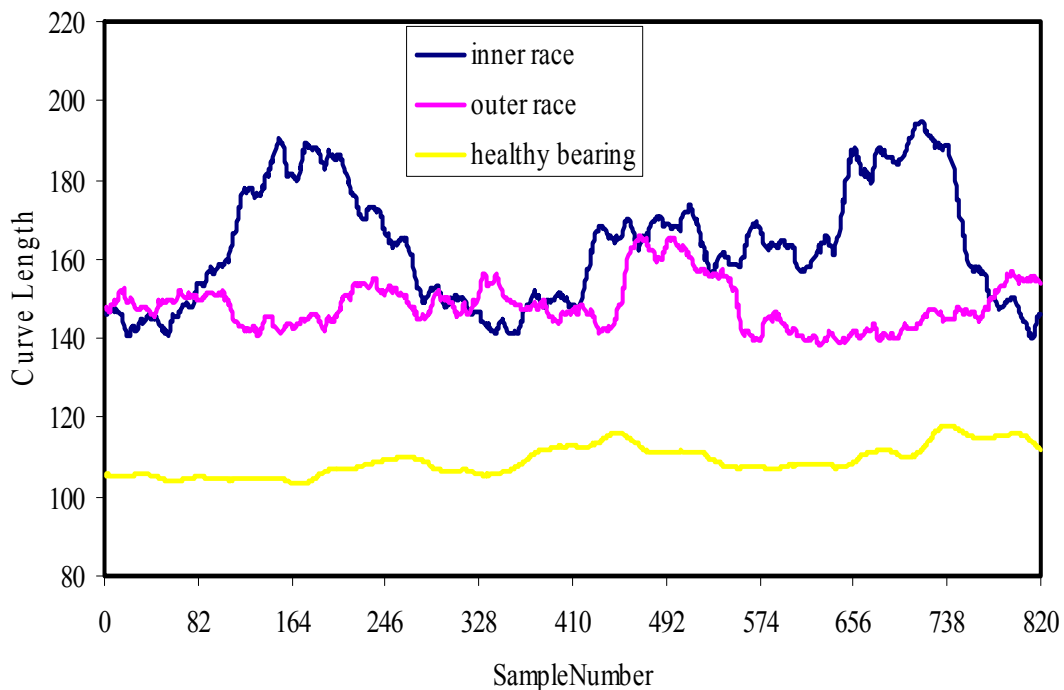
Figure 7.33 CLT of raw acceleration signal under L0 load case at 1000 rpm (w=100).
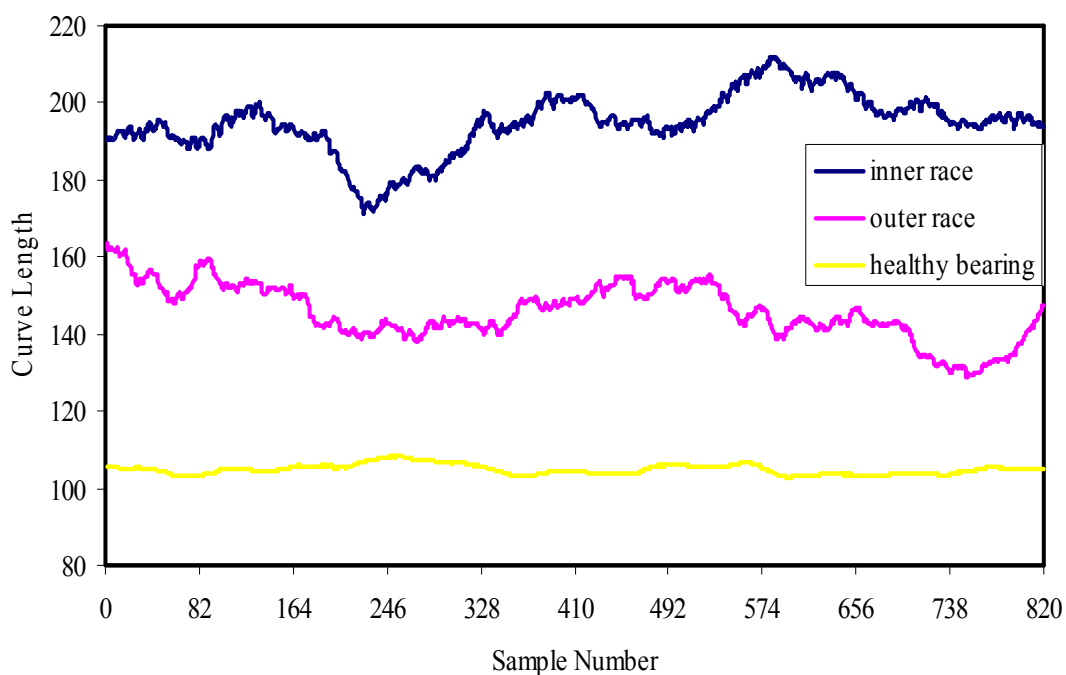
Figure 7.34 CLT of raw acceleration signal under L1 load case at 1000 rpm (w=100).
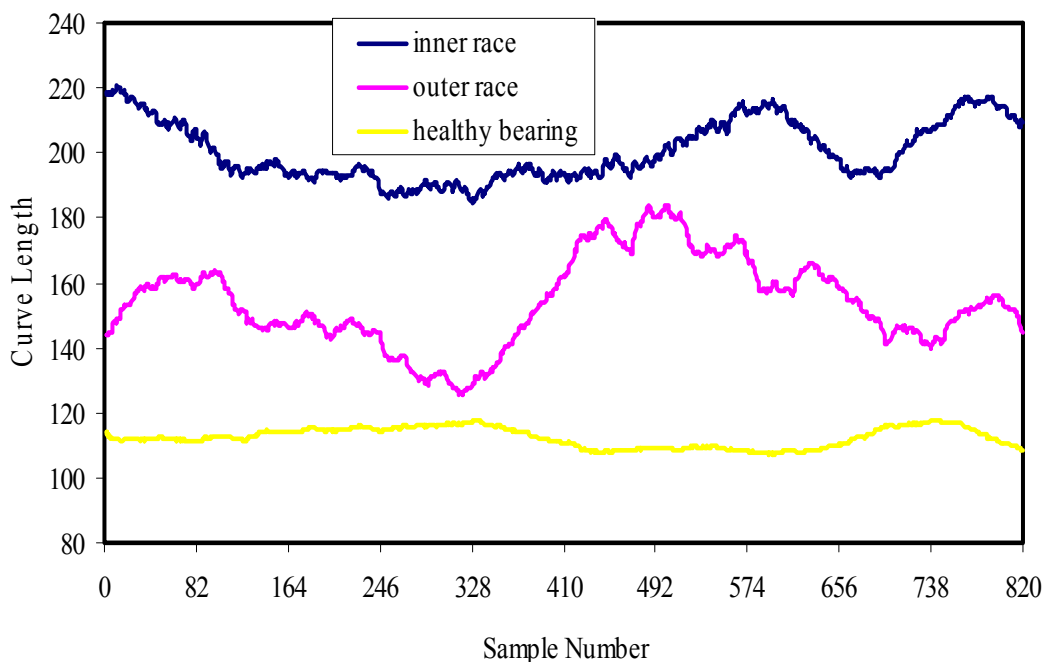
Figure 7.35 CLT of raw acceleration signal under L2 load case at 1000 rpm (w=100).

The curve length transforms of the acceleration signals for 2000 rpm shaft speed are given in Figures 7.36-7.38. Inner race defects can be captured using the CLT of the acceleration signal at 2000 rpm.
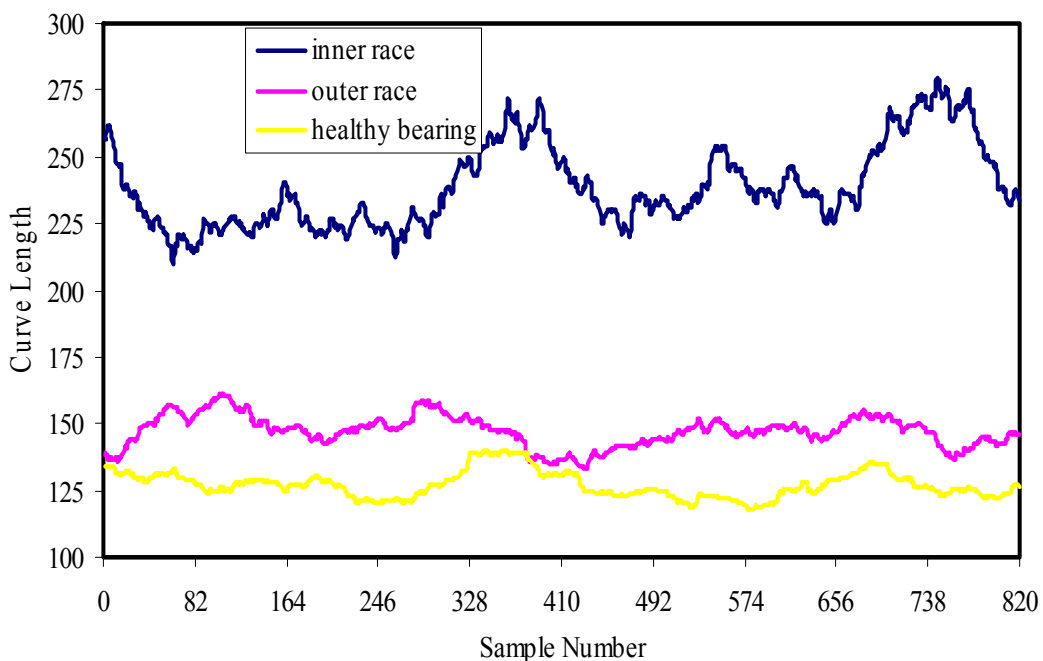
Figure 7.36 CLT of raw acceleration signal under L0 load case at 2000 rpm (w=100).
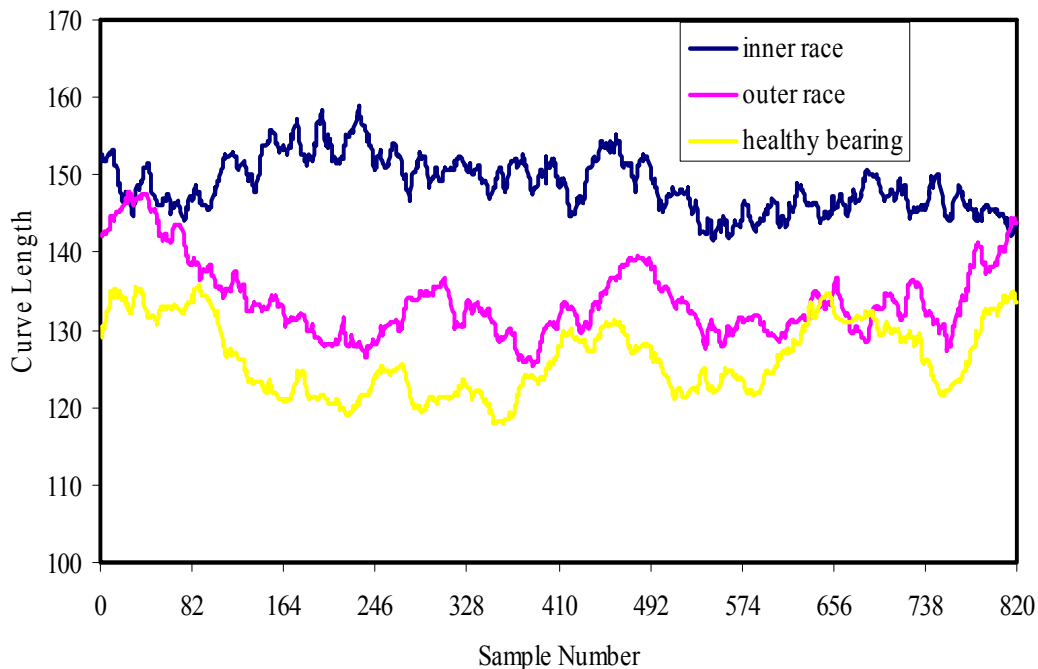
Figure 7.37 CLT of raw acceleration signal under L1 load case at 2000 rpm (w=100).
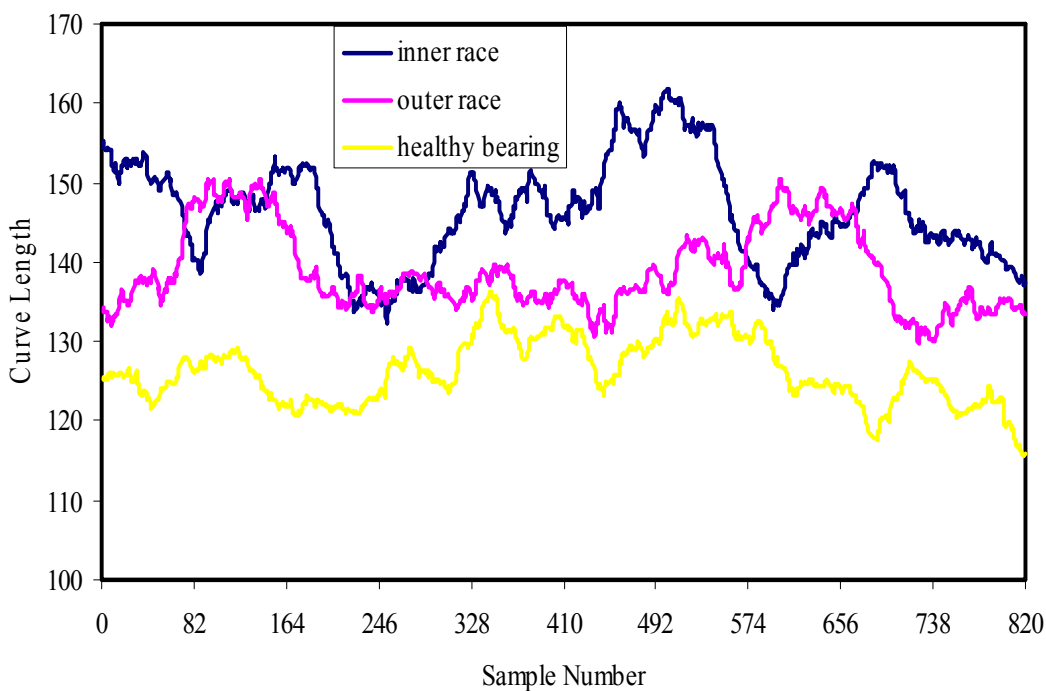
Figure 7.38 CLT of raw acceleration signal under L2 load case at 2000 rpm (w=100).

7.2.2 Statistical Moments of the CLT of Raw Vibration Signals for C=1

In this section, some statistical moments of curvelength transforms of unfiltered acceleration signals with the transformation coefficient C=1 are calculated for varying shaft speeds and load conditions for healthy and faulty cases.

7.2.2.1 Mean Value

The mean values of the CLT signals are calculated for different shaft speeds, load cases and window lengths. The mean values are given for healthy and faulty cases for comparison.

7.2.2.1.1 Mean values of CLT signals for w=10. The mean values of CLT signals for the window length w=10 are given in Figures 7.39-7.41. Figure 7.39 shows the mean values for L0 load case. The mean values for inner and outer race defect cases are greater than those obtained for healthy case as shown in the figure. The detection of inner and outer race defects is possible by using the mean values of CLT signals. The mean values for inner race defect are greater than the values for outer race defect for a broad range of shaft speed. Figure 7.40 shows the mean values for L1 load case. The mean values for faulty cases are greater than the values for healthy case for all shaft speeds. There is a recordable difference between the health and faulty cases at 1000 rpm.
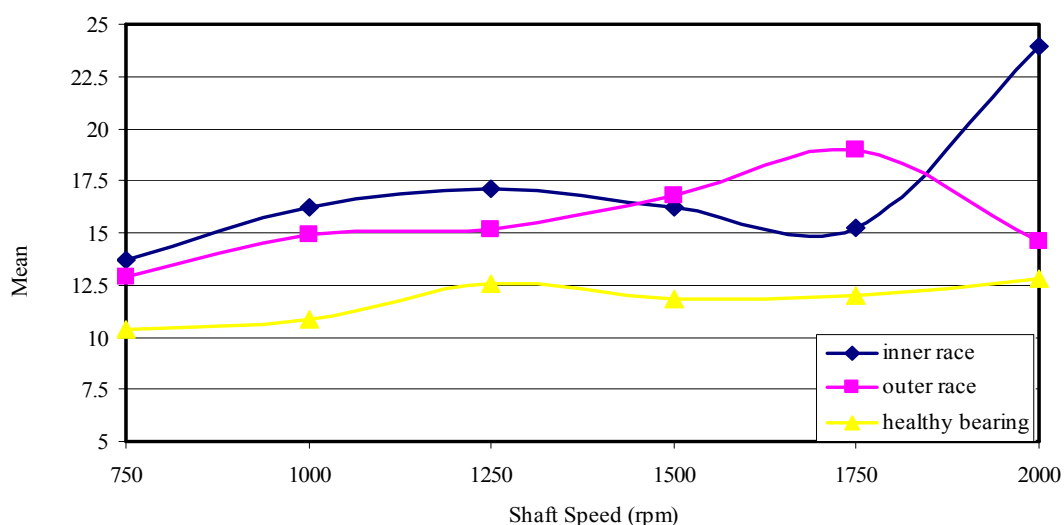
Figure 7.39 Mean values of CLT's of acceleration signals under L0 load case for w=10.

Figure 7.41 shows the mean values for L2 load case. Similar to L0 and L1 load cases, defect detection is possible for L2 load case using the difefrences between the healthy and faulty cases. The differences between the healthy and faulty cases are high for low shaft speeds.
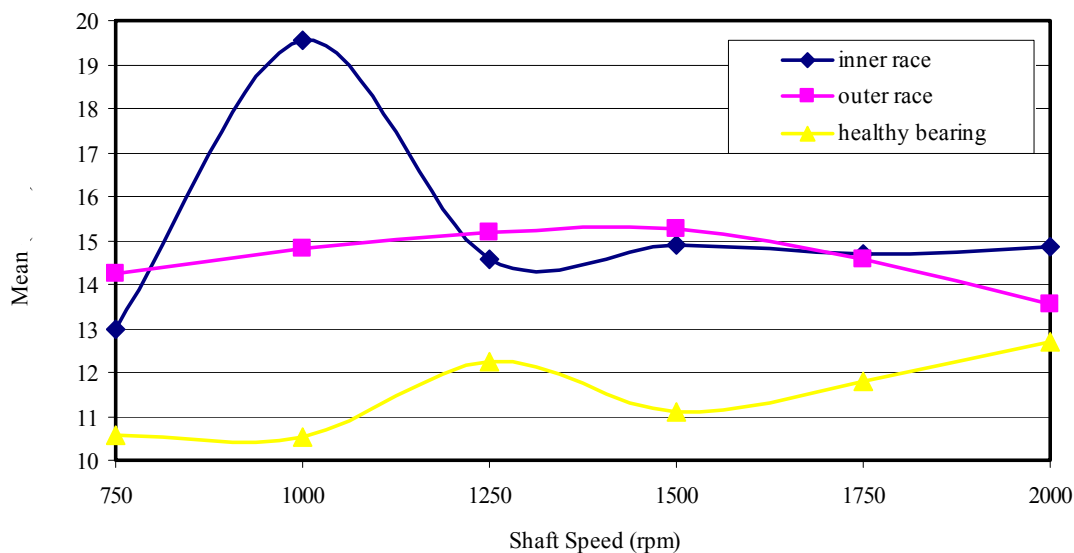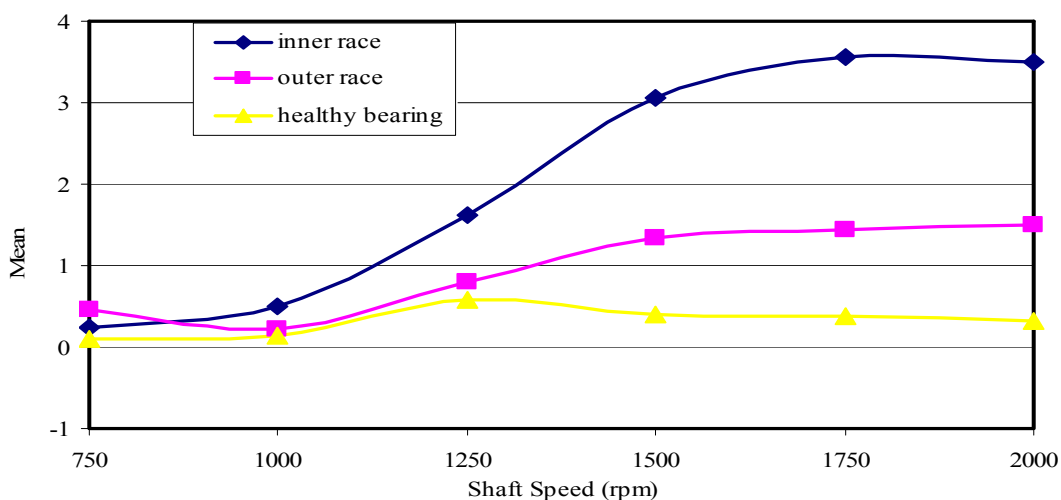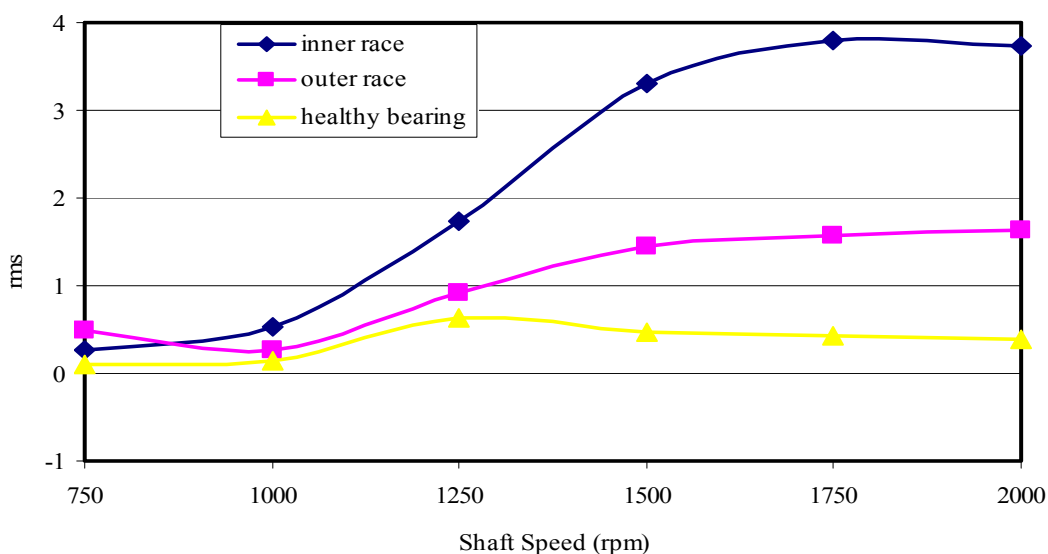

Figure 7.40 Mean values of CLT's of acceleration signals under L1 load case for w=10.
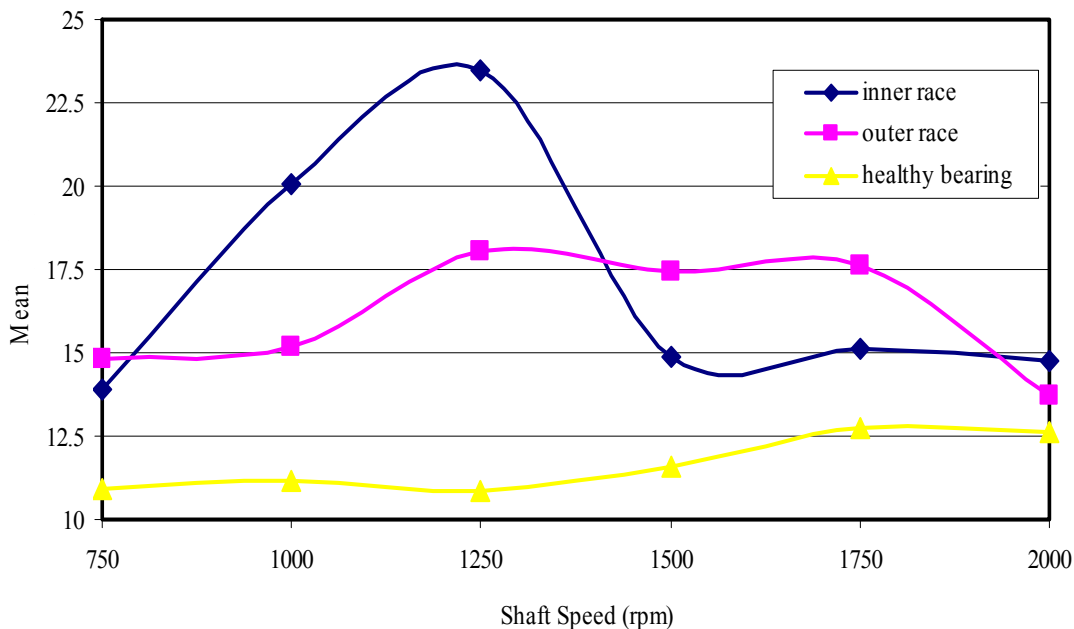
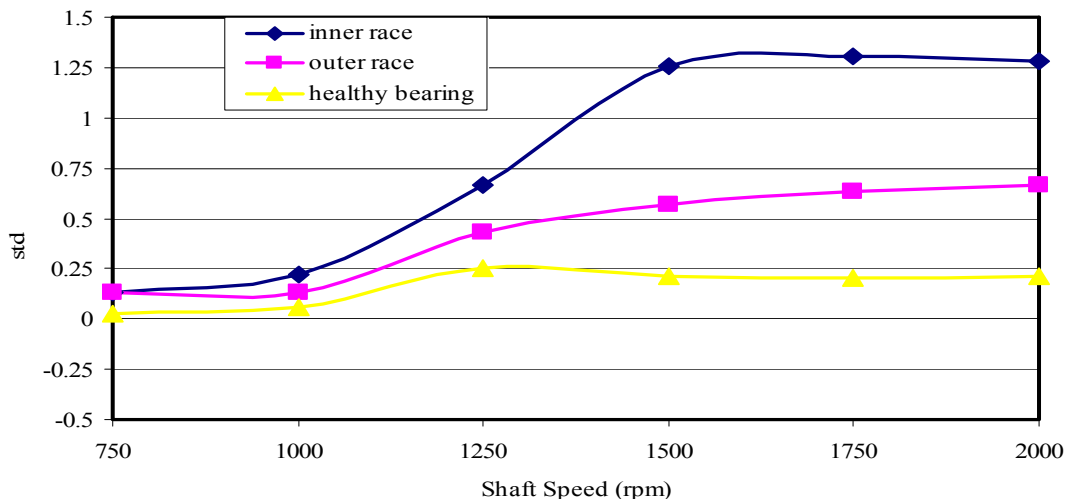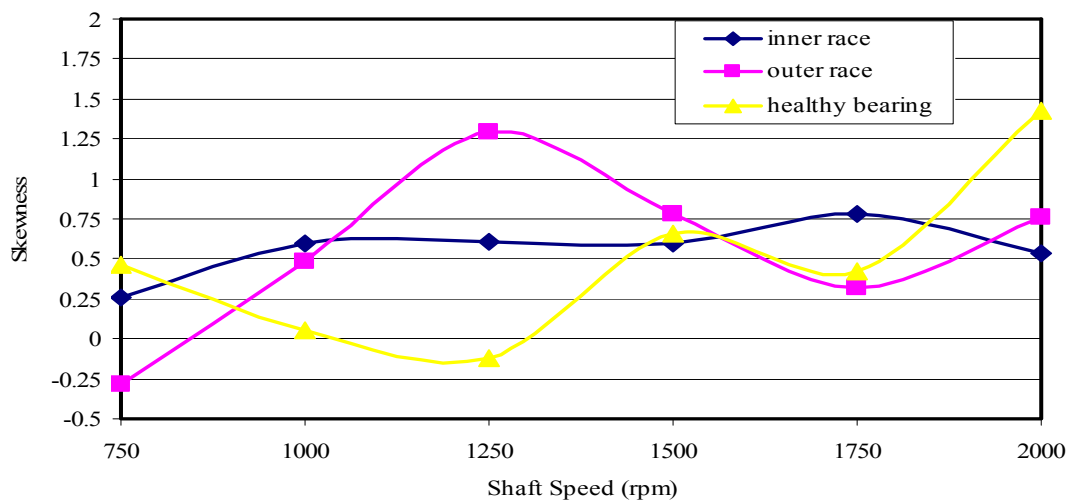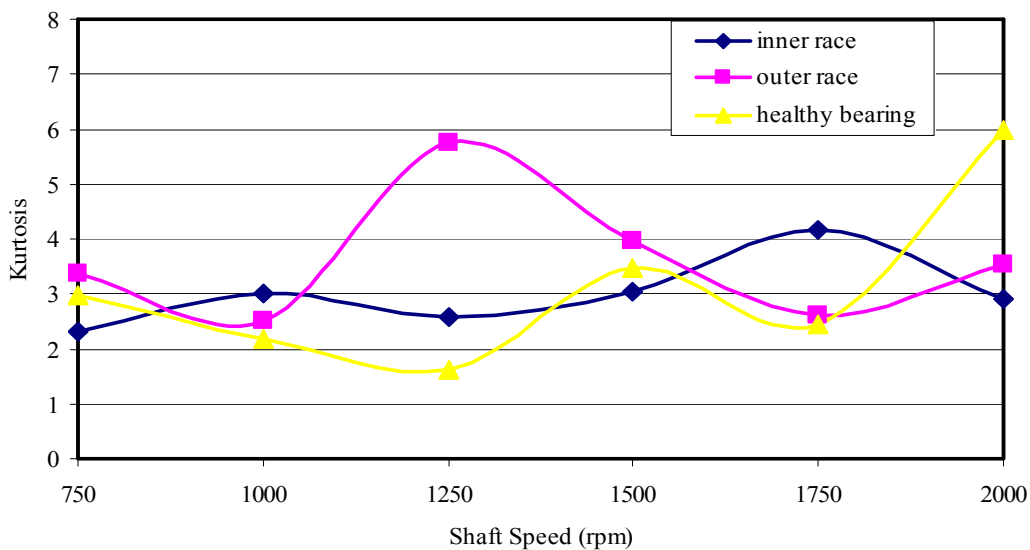Figure 7.41 Mean values of CLT's of acceleration signals under L2 load case for w=10.

7.2.2.1.2 Mean values of CLT signals for w=20. The mean values of CLT signals for the window length w=20 are given in Figures 7.42-7.44. Figure 7.42 shows the mean values for L0 load case. As seen in the figure, the mean values for faulty cases are greater than those obtained for healthy case.
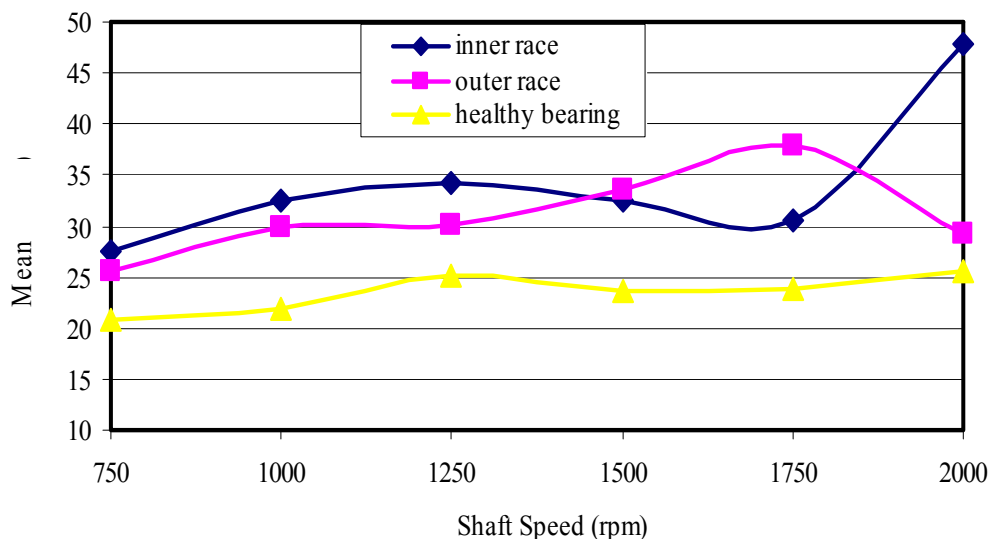
Figure 7.42 Mean values of CLT's of acceleration signals under L0 load case for w=20.
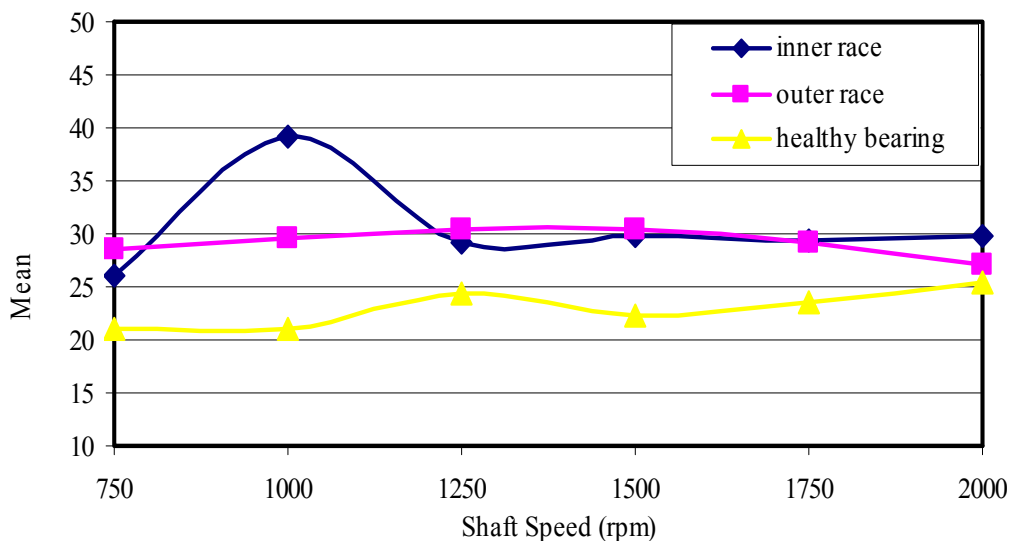
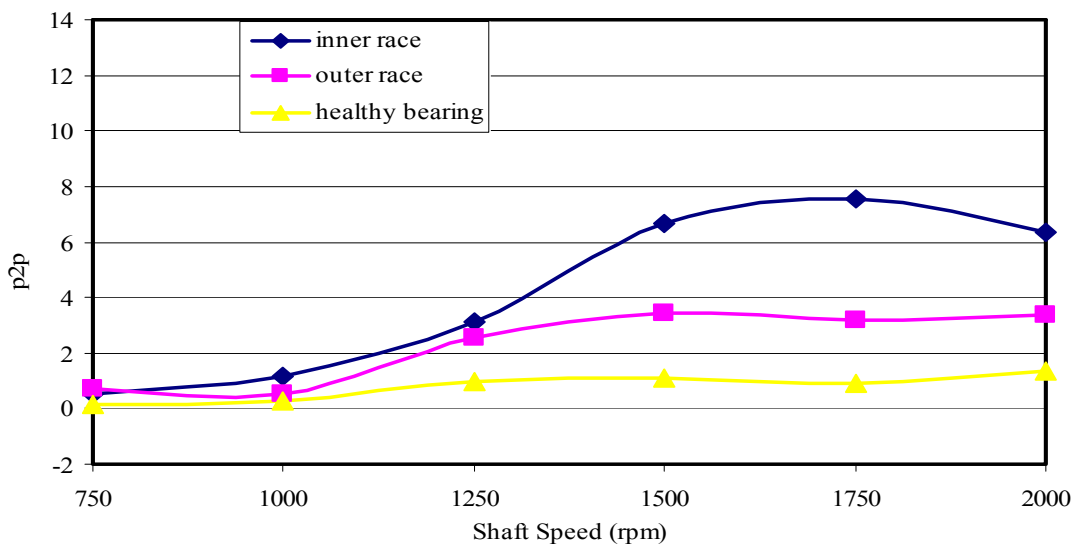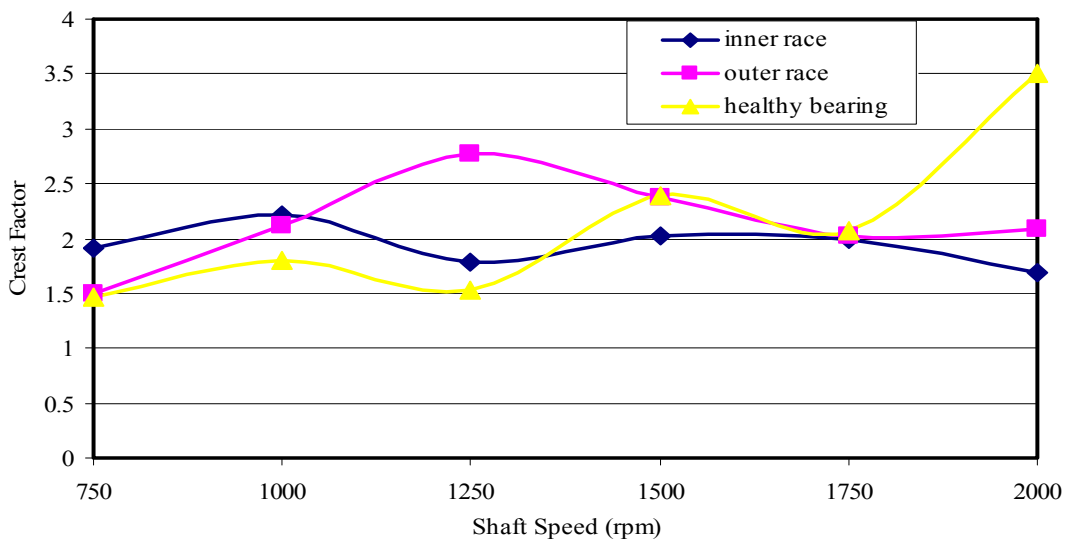Figure 7.43 Mean values of CLT's of acceleration signals under L1 load case for w=20.

Figure 7.43 and Figure 7.44 show the mean values for L1 and L2 load cases, respectively. The mean values of the CLT signals can be used as defect indicator for these load cases especially for middle speed region. The ratio between the faulty and defected cases reduces as the shaft speed increases.
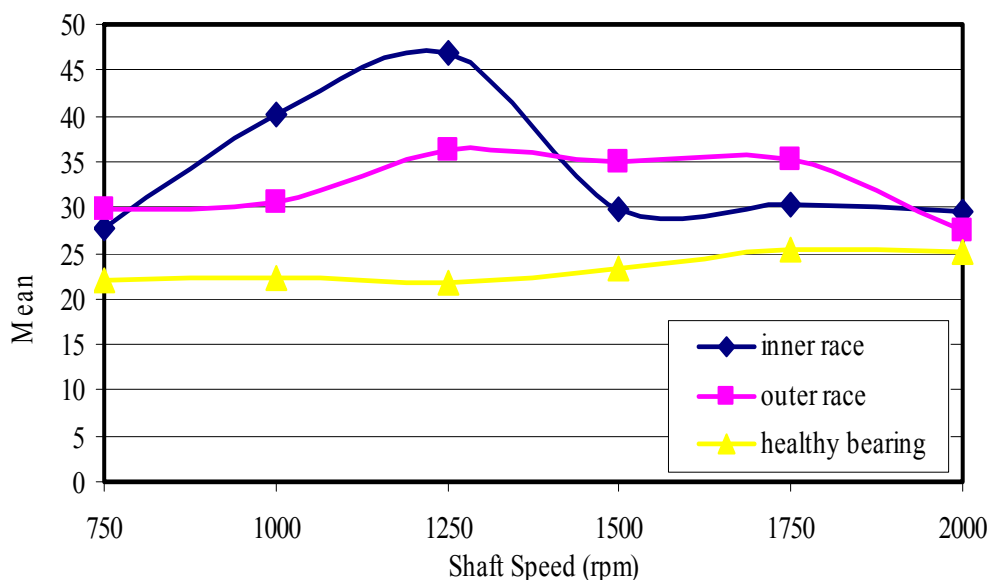
Figure 7.44 Mean values of CLT's of acceleration signals under L2 load case for w=20.

7.2.2.1.3 Mean values of CLT signals for w=100. The mean values of CLT signals for healthy and faulty cases are given for the window width w=100 in Figures 7.45-7.47. The amplitudes of the mean of the CLT signals increase as the window length increases. The ratio of the mean values between the faulty and defected bearings depends on the shaft speed. Consequently, the mean values of the CLT signals can be used as a good defect indicator under different load cases for a broad range of shaft speed.
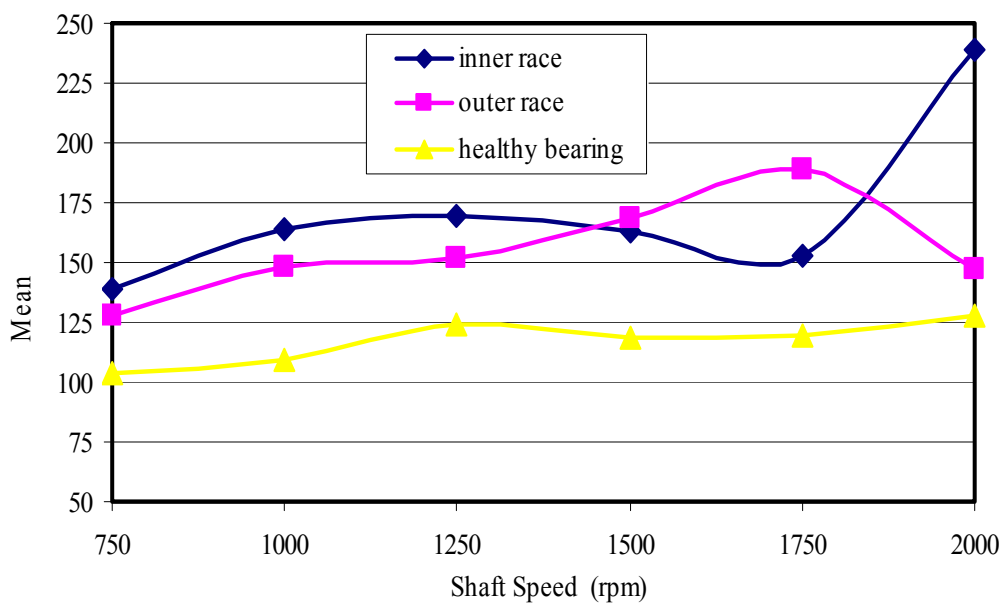
Figure 7.45 Mean values of CLT's of acceleration signals under L0 load case for w=100.
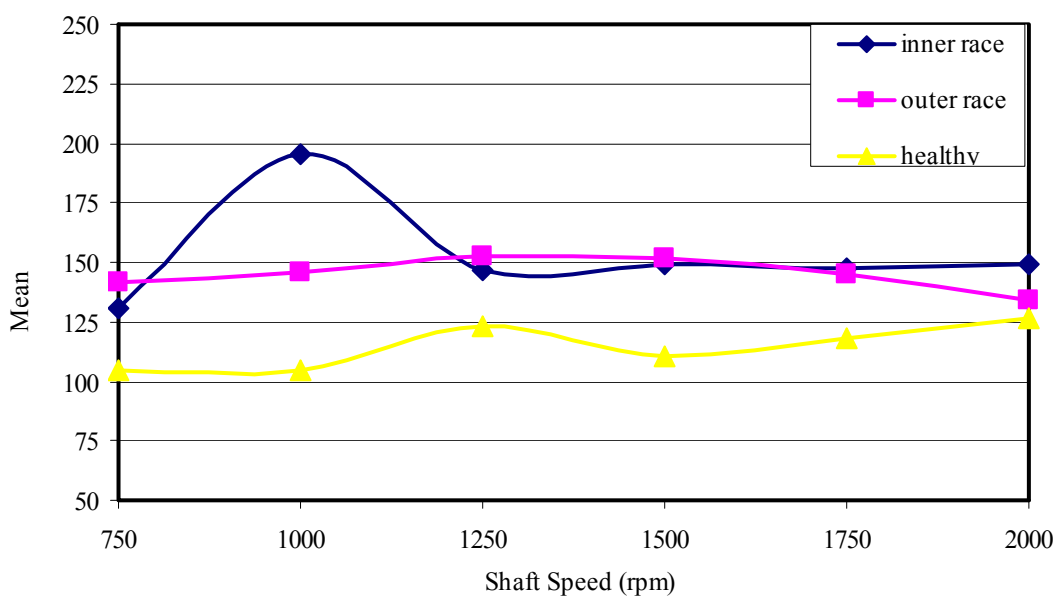
Figure 7.46 Mean values of CLT's of acceleration signals under L1 load case for w=100.
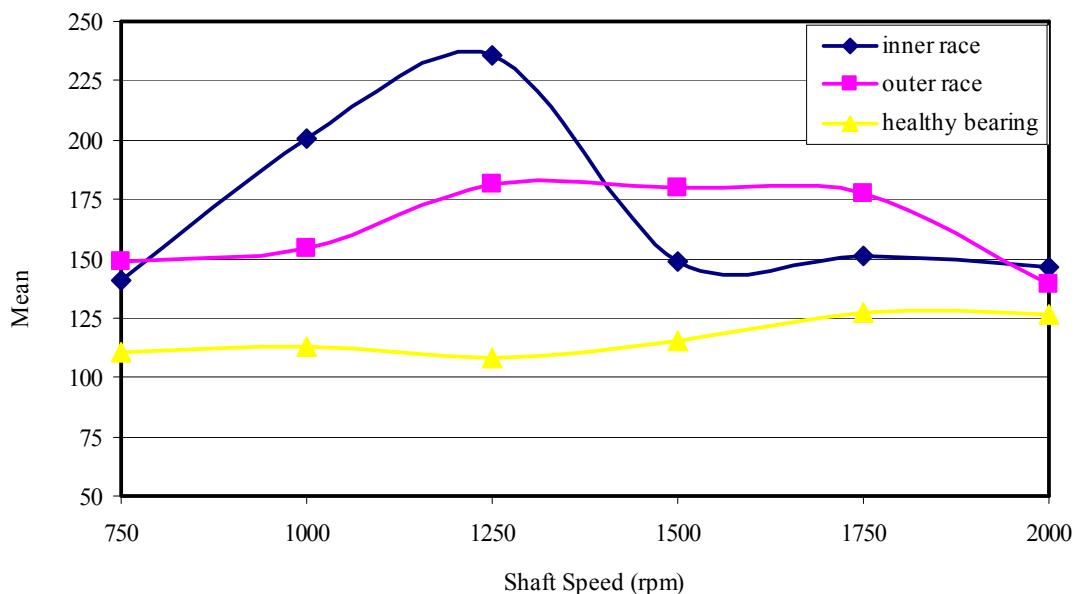
Figure 7.47 Mean values of CLT's of acceleration signals under L2 load case for w=100.

7.2.2.2 Rms Value

The mean values of the CLT signals are calculated for different shaft speeds, load cases and window lengths. The mean values are given for healthy and faulty cases for comparison.

7.2.2.2.1 Rms values of CLT signals for w=10. The rms value of the CLT signals for different window lengths and different load cases are calculated. Figure 7.48 shows the rms values for L0 load case. As seen from the figure that the rms values for faulty bearings are greater than those obtained for healthy case for all shaft speeds. The rms values for w=10 can be used to detect the bearing faults. Figure 7.49 and Figure 7.50 show the rms values for L1 and L2 load cases, respectively. The same observations with L0 load case are valid for these cases and the rms values of the CLT signals can be used as defect indicator.
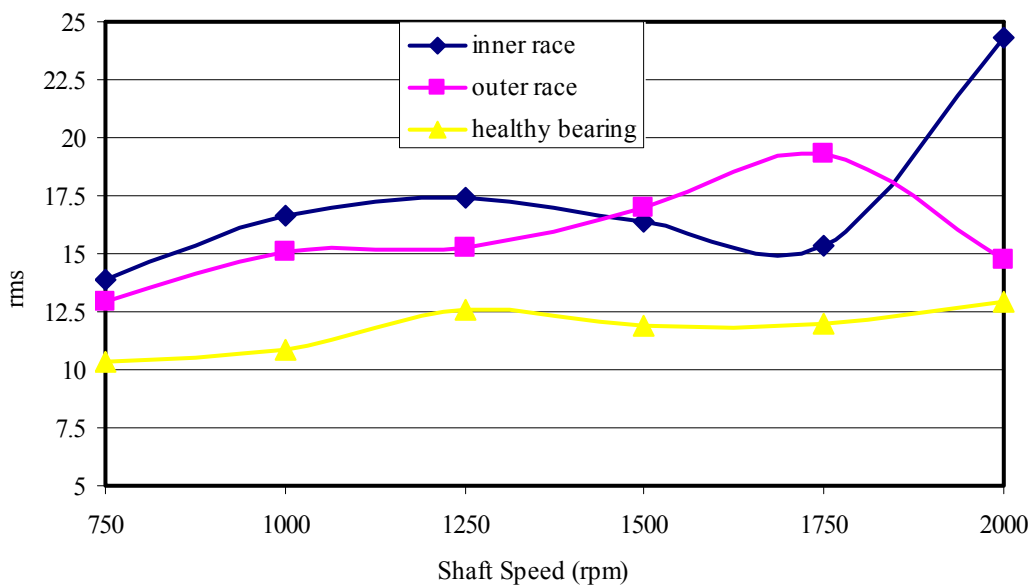
Figure 7.48 Rms values of CLT's of acceleration signals under L0 load case for w=10.
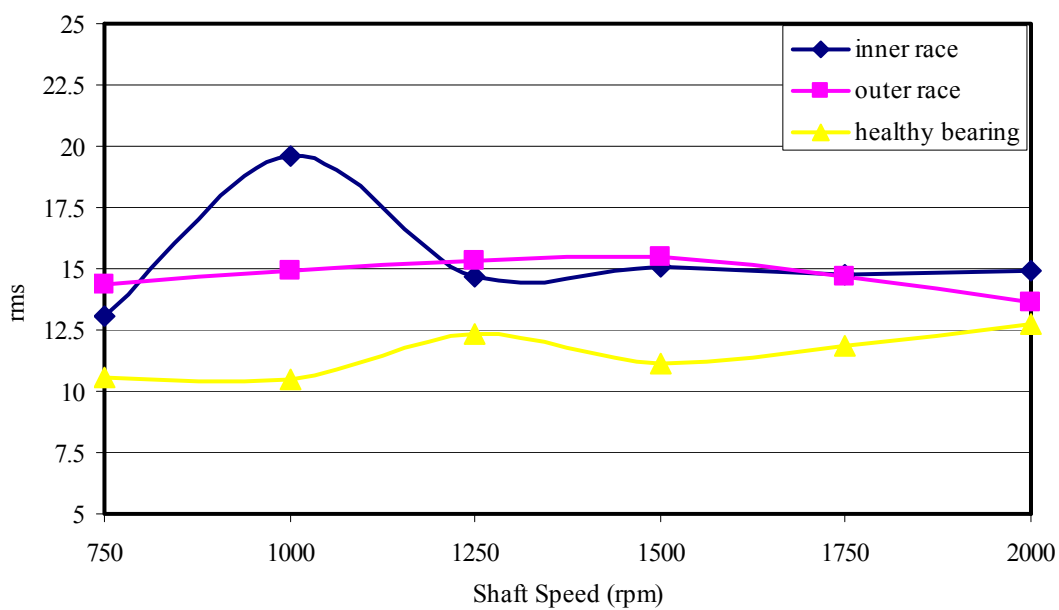
Figure 7.49 Rms values of CLT's of acceleration signals under L1 load case for w=10.
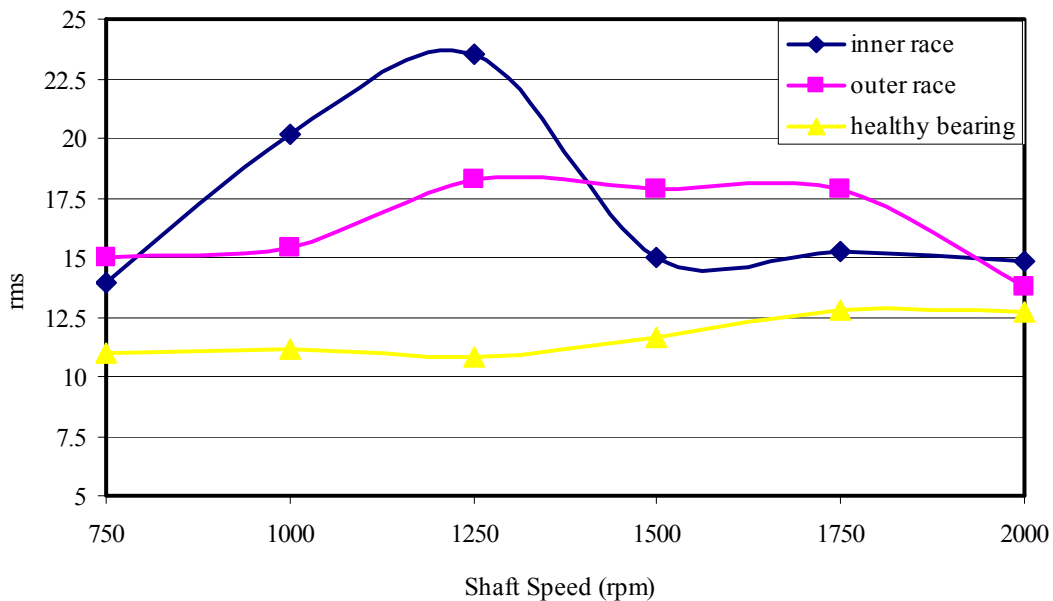
Figure 7.50 Rms values of CLT's of acceleration signals under L2 load case for w=10.

The same results are obtained for the window length w=20 and therefore the results for this window length are not given.

7.2.2.2.2 Rms values of CLT signals for w=100. The rms values of CLT signals for w=100 are given in Figures 7.51-7.53. The rms values for faulty cases are greater than those obtained for healthy cases for all shaft speeds and they can be used for defect detection.
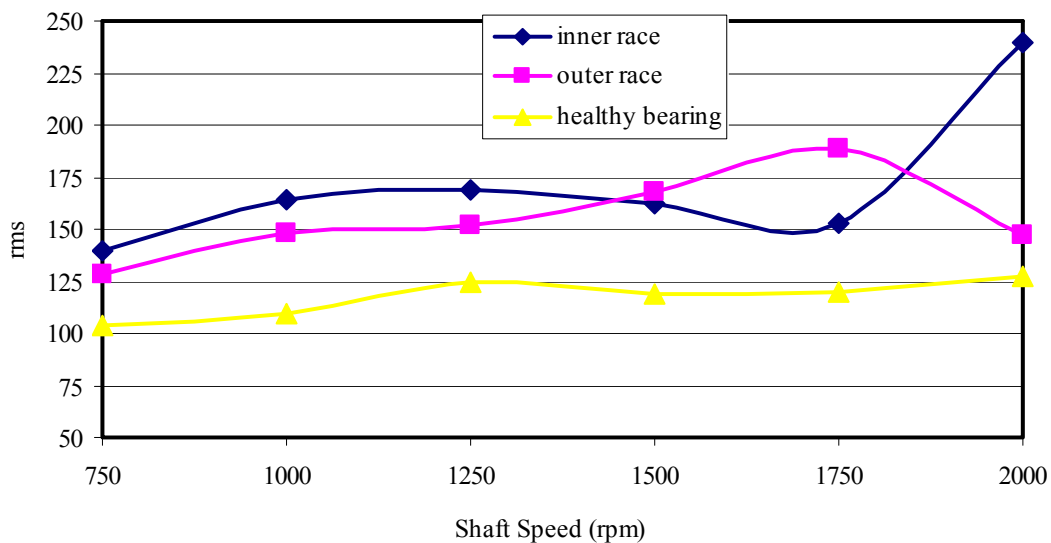
Figure 7.51 Rms values of CLT's of acceleration signals under L0 load case for w=100.
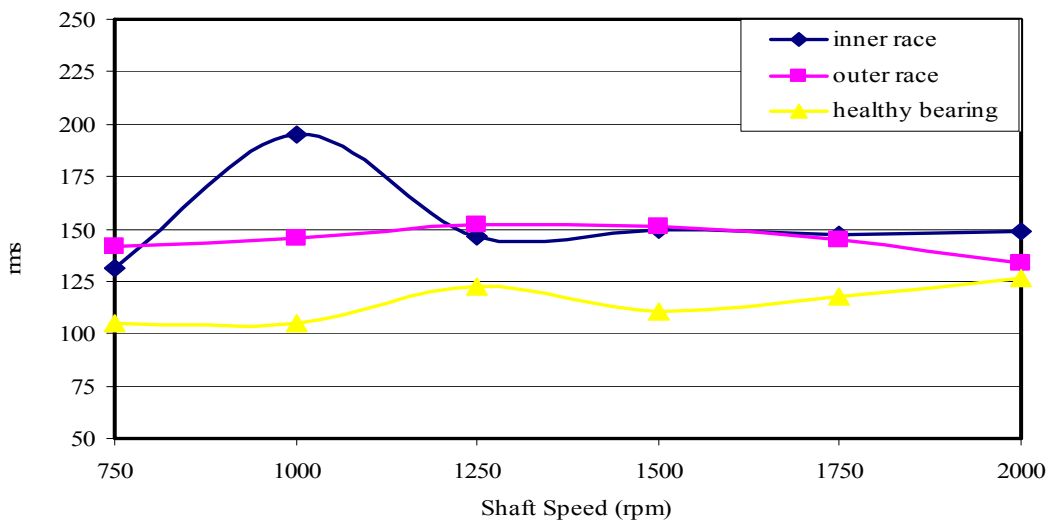
Figure 7.52 Rms values of CLT's of acceleration signals under L1 load case for w=100.
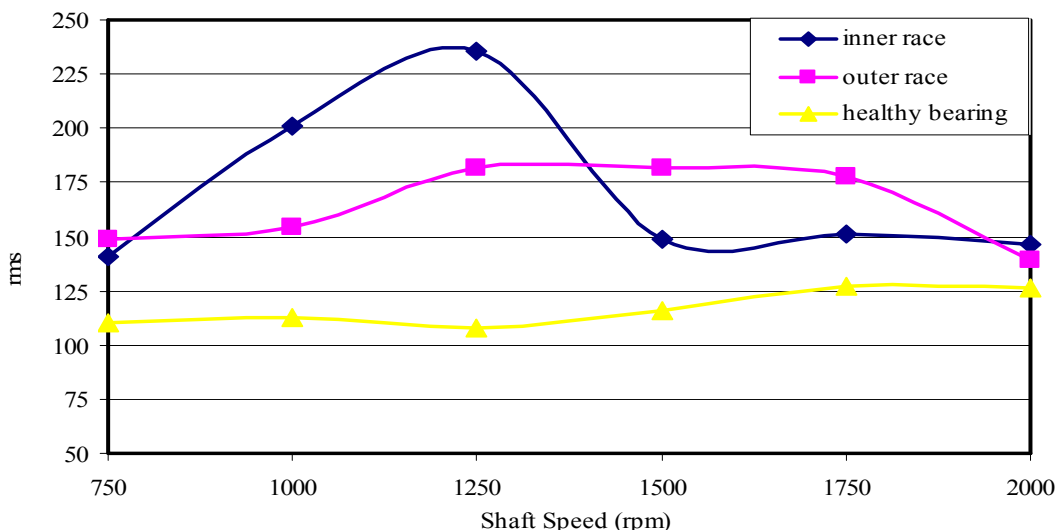
Figure 7.53 Rms values of CLT's of acceleration signals under L2 load case for w=100.

7.2.2.3 Standart Deviation (σ)

The standart deviations (std) of the CLT signals are calculated for different shaft speeds, load cases and window lengths. The std values are given for healthy and faulty cases for comparison.

7.2.2.3.1 Standart deviation values of CLT signals for w=10. The standart deviation values of the CLT signals for acceleration responses are given in Figures in 7.54-7.56. The results show that the standart deviation values can also be used in

defect detection. The std values for faulty bearings are greater than the values of healthy bearing for all shaft speeds and load cases. The std values of inner race defect for L0 load case are greater than those obtained for outer race defect. On the other hand, the std values of the outer race defect are greater than the values for inner race defect obtained for L1 and L2 load cases.
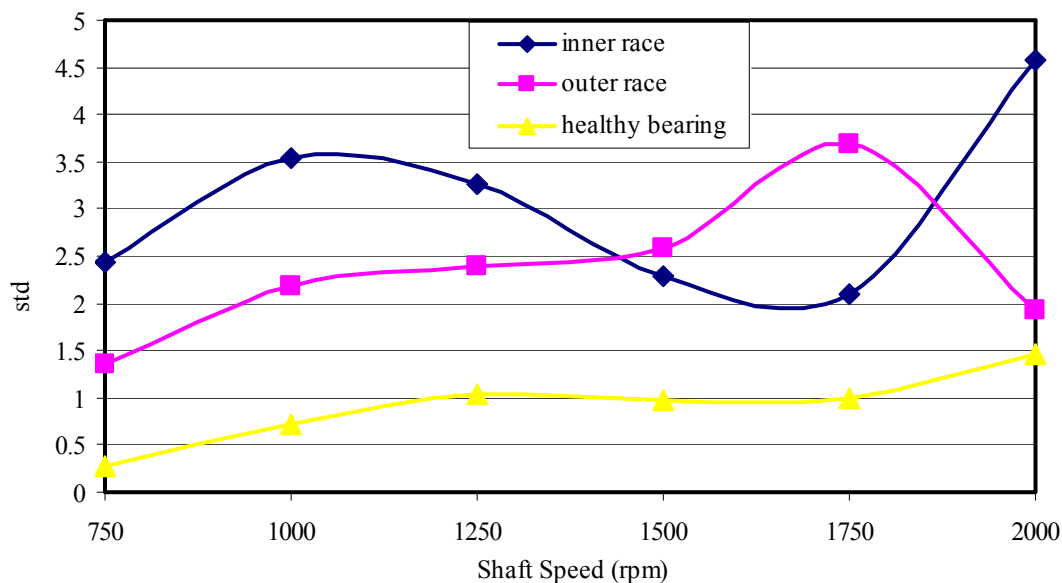
Figure 7.54 Std values of CLT's of acceleration signals under L0 load case for w=10.
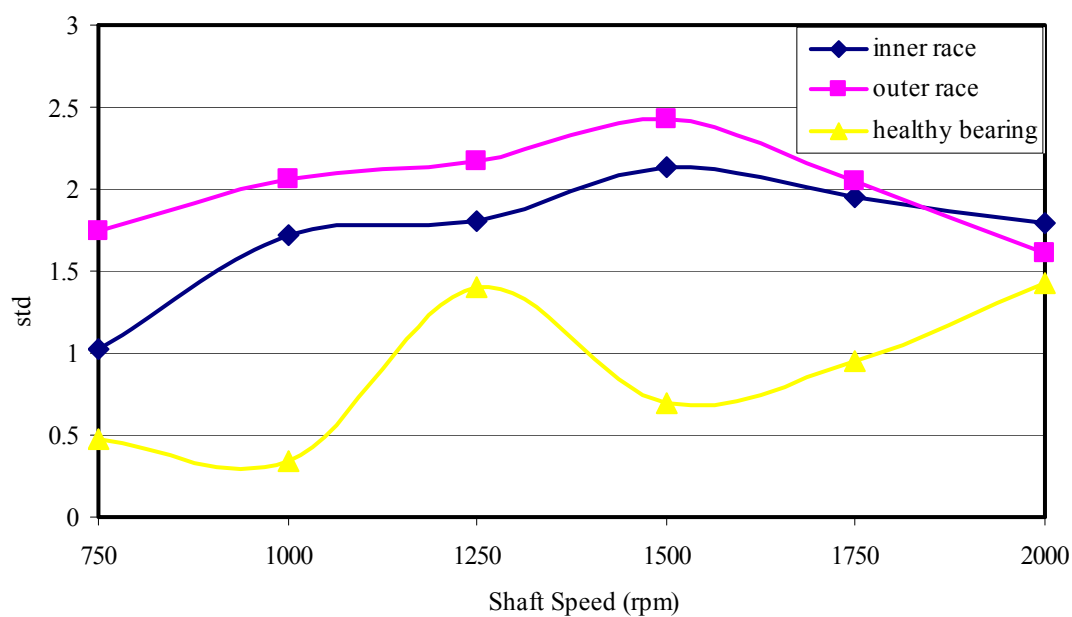
Figure 7.55 Std values of CLT's of acceleration signals under L1 load case for w=10.
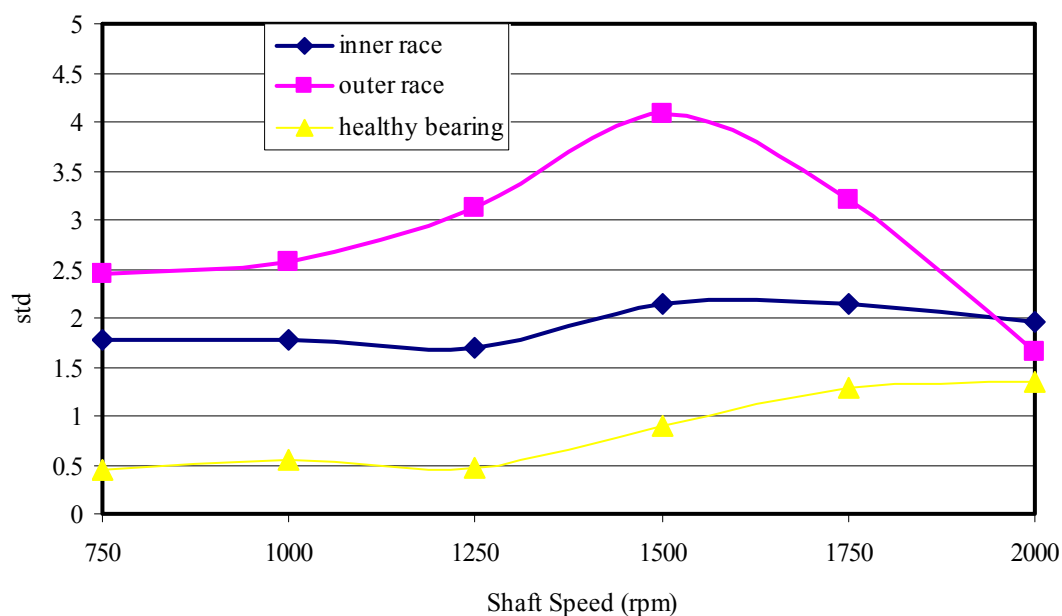
Figure 7.56 Std values of CLT's of acceleration signals under L2 load case for w=10.

7.2.2.3.2 Standart deviation values of CLT signals for w=100. The standart deviation values for the window length w=100 are given in Figures 7.57-7.59. The results show that the std values can be used successfully for detecting the rolling element bearing faults.
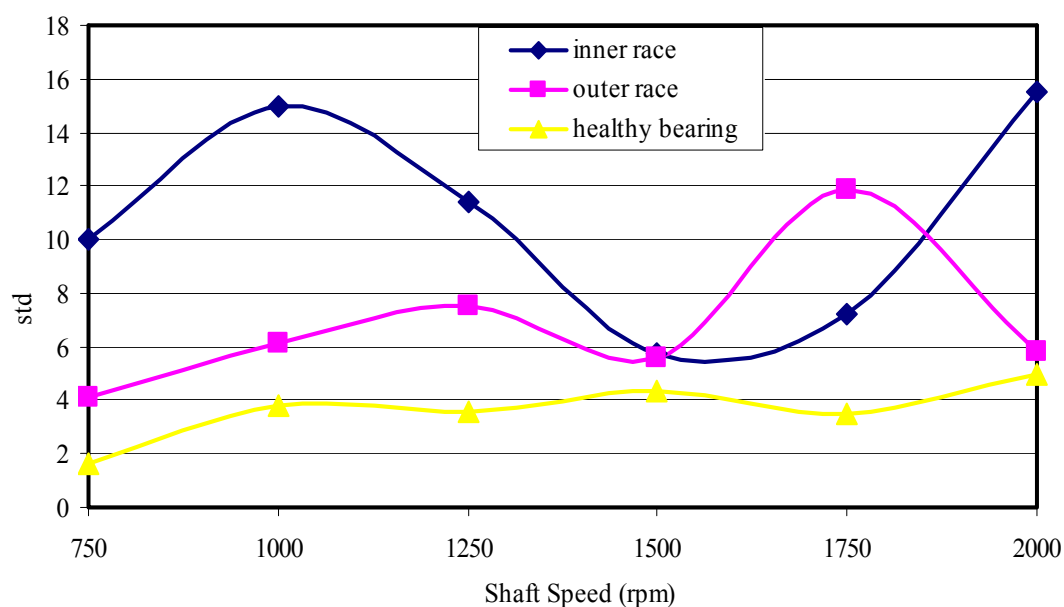
Figure 7.57 Std values of CLT's of acceleration signals under L0 load case for w=100.
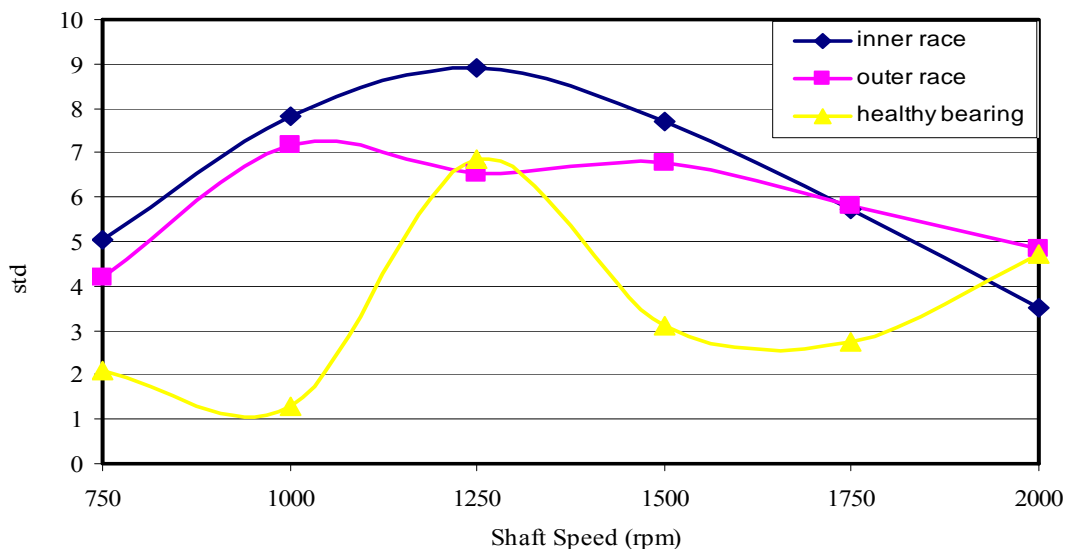
Figure 7.58 Std values of CLT's of acceleration signals under L1 load case for w=100.
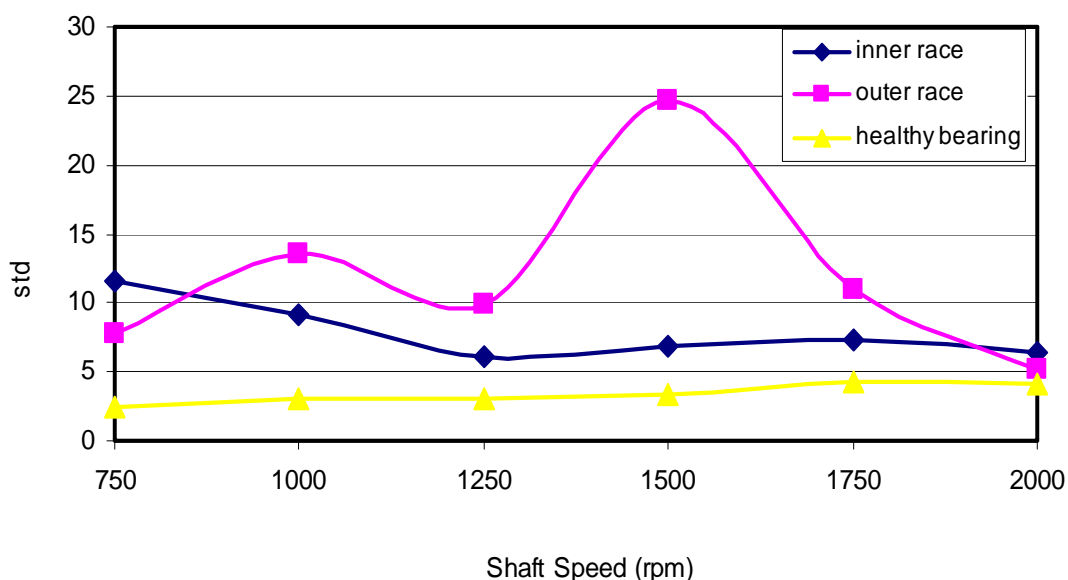
Figure 7.59 Std values of CLT's of acceleration signals under L2 load case for w=100.

7.2.2.4 Skewness

The skewness values of the CLT signals are calculated for different shaft speeds and load cases. The skewness values are given for healthy and faulty cases for comparison. Generally, the skewness parameter is not a good defect indicator and the results obtained in this study confirm this fact. Therefore, the skewness values of CLT signal are given only for the window length w=10.

7.2.2.4.1 Skewness values of CLT signals for w=10. The skewness values are given in Figures 7.60-7.62. The skewness values for healthy and faulty bearings show that the skewness parameter exhibits an irregular behaviour and defect detection may be possible for some specific shaft speeds both inner and outer race defects. But it is possible to say that the skewness parameter is not a reliable defect indicator for the examined cases.
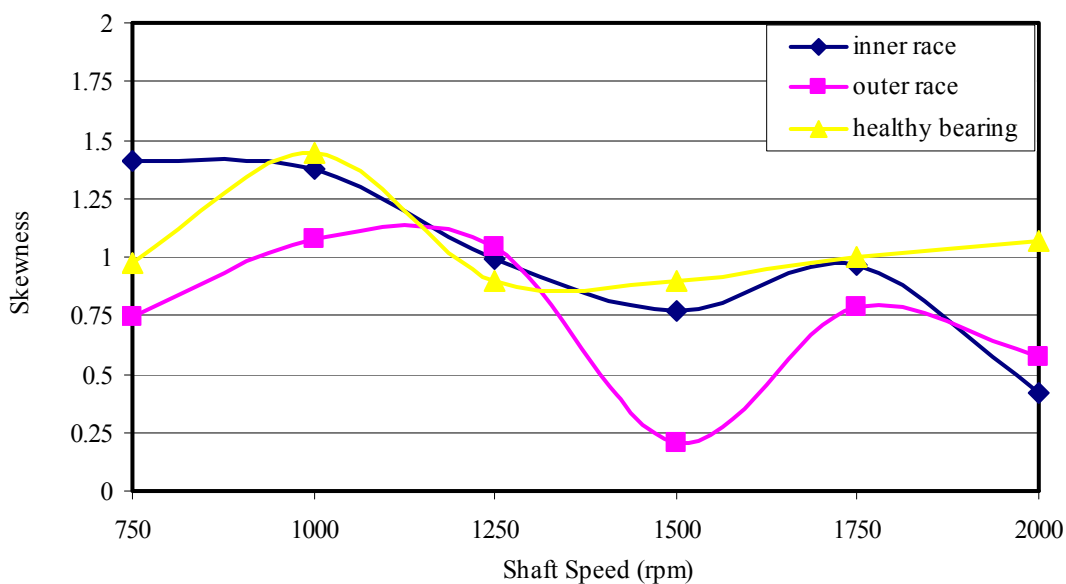
Figure 7.60 Skewness values of CLT's of acceleration signals under L0 load case for w=10.
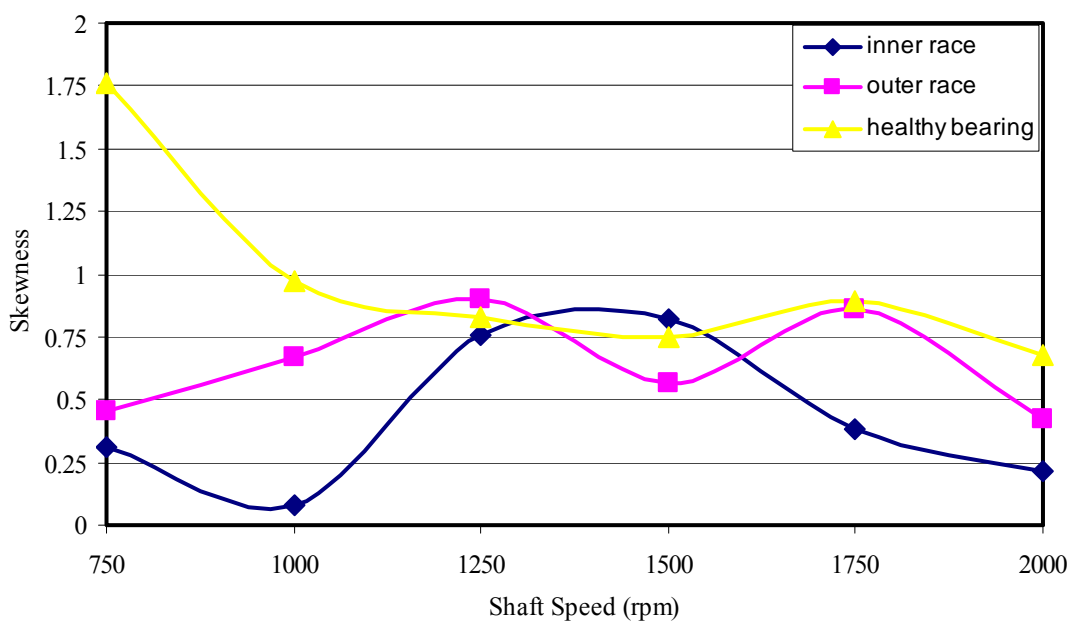
Figure 7.61 Skewness values of CLT's of acceleration signals under L1 load case for w=10.
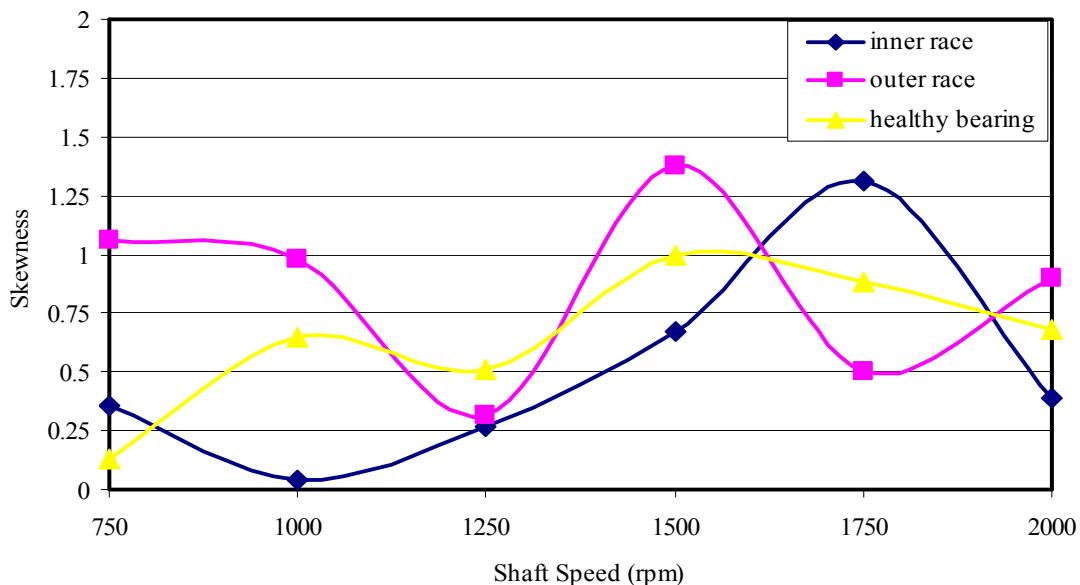
Figure 7.62 Skewness values of CLT's of acceleration signals under L2 load case for w=10.

7.2.2.5 Kurtosis

The kurtosis values of the CLT signals are calculated for different shaft speeds and load cases. The kurtosis values are given for healthy and faulty to show the efficiency of the kurtosis parameter on the defect detection. The skewness values of CLT signal are given only for the window length w=10.

7.2.2.5.1 Kurtosis values of CLT signals for w=10. The kurtosis values for the window length w=10 are given in Figures 7.63-7.65. As seen from the figures that the kurtosis parameter is not a good defect indicator for CLT signals. The kurtosis values for L2 load case at some specific shaft speeds can be used to detect the outer and inner race defects.
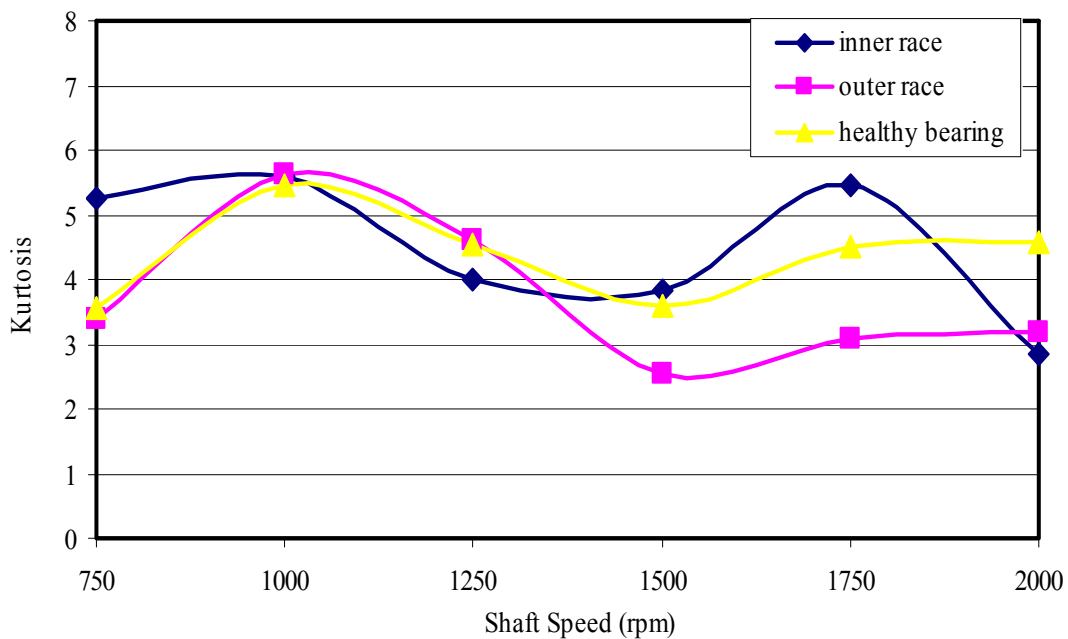
Figure 7.63 Kurtosis values of CLT's of acceleration signals under L0 load case for w=10.
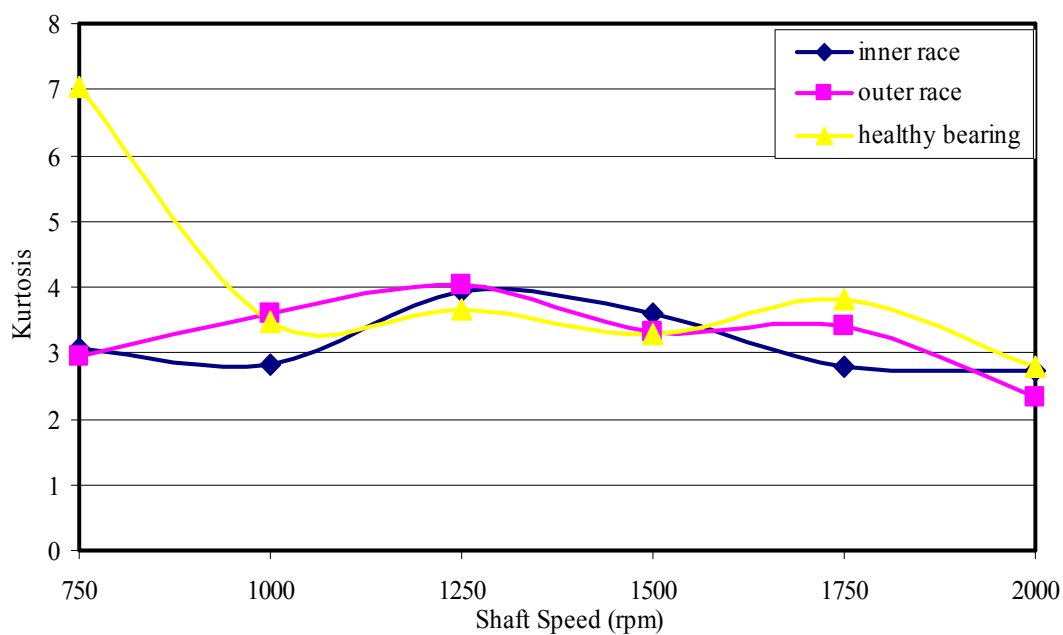
Figure 7.64 Kurtosis values of CLT's of acceleration signals under L1 load case for w=10.
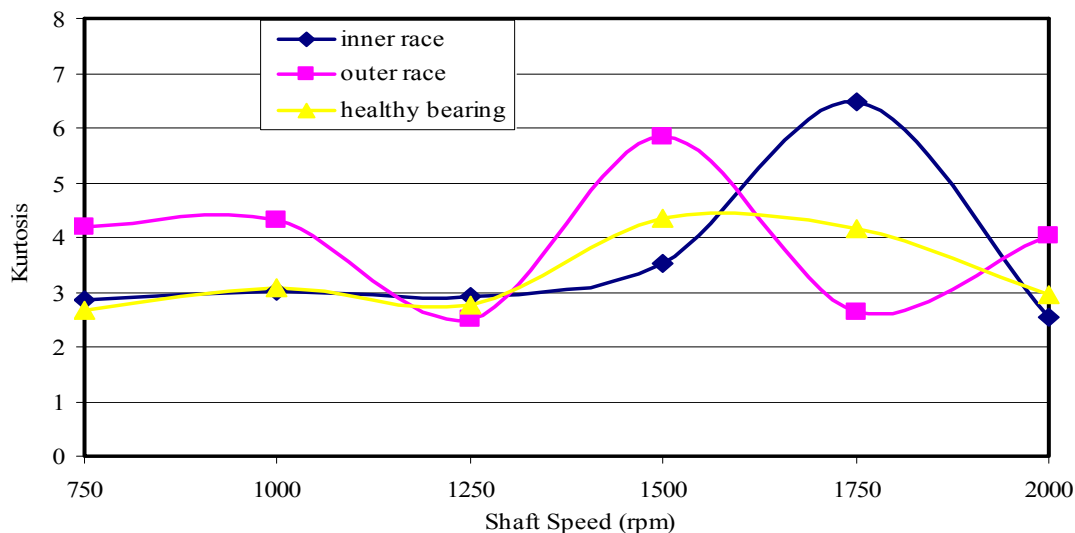
Figure 7.65 Kurtosis values of CLT's of acceleration signals under L2 load case for w=10.

7.2.2.6 Fifth Moment

The fifth moments of the CLT signals are calculated for different shaft speeds and load cases. The fifth moment values are given for healthy and faulty bearings for the window length w=10.

7.2.2.6.1 Fifth moment values of CLT signals for w=10. The fifth moment values of CLT signals are given in Figures 7.66-7.68 for the window length w=10. The trend of the fifth moment shows similar charactristics for other window lengths, so they are not given here. Similar to the skewness and kurtosis parameters, the fifth moment values are well away from being an efficient defect indicator calculated for CLT signals.
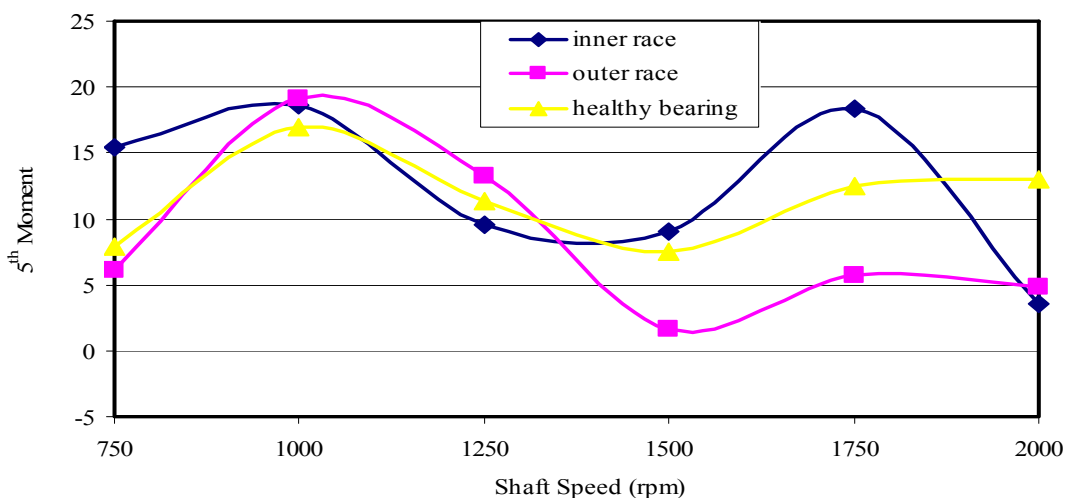
Figure 7.66 5th moment values of CLT's of acceleration signals under L0 load case for w=10.
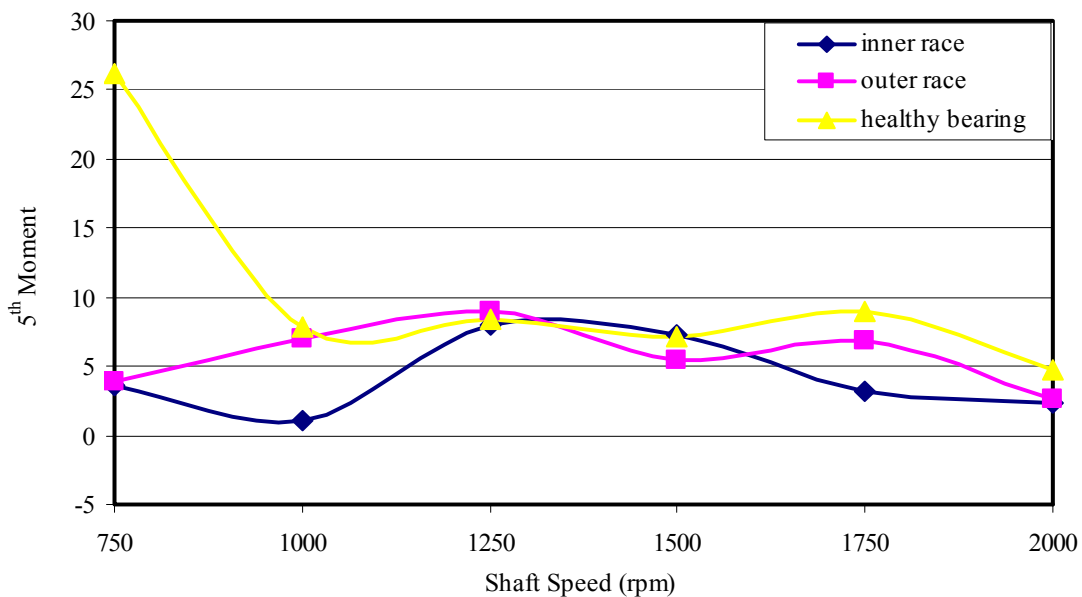
Figure 7.67 5th moment values of CLT's of acceleration signals under L1 load case for w=10.
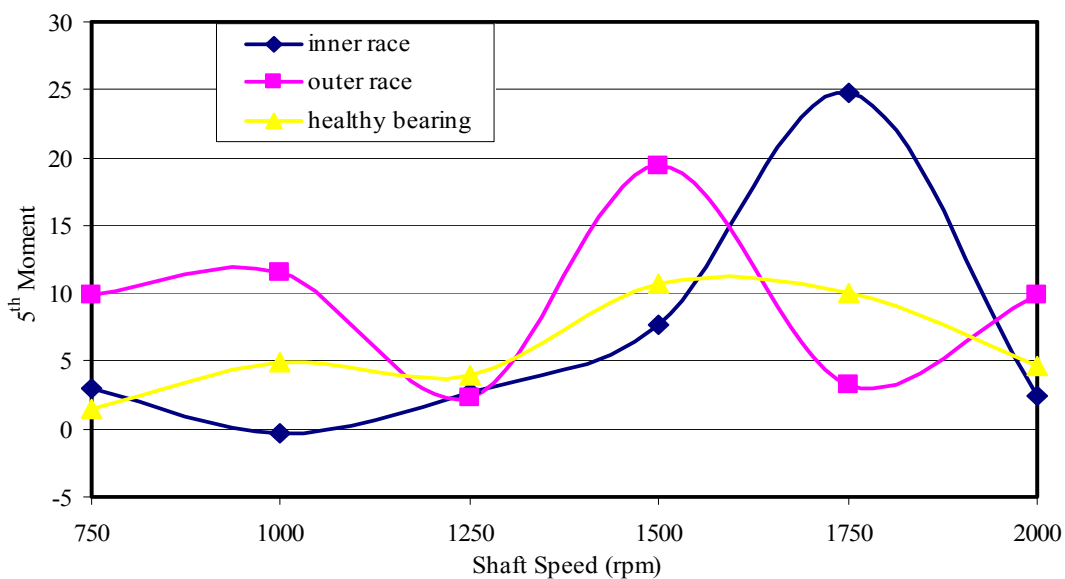
Figure 7.68 5th moment values of CLT's of acceleration signals under L2 load case for w=10.

7.2.2.7 Peak to Peak (p2p) Value

The peak to peak values of the CLT signals are calculated for different shaft speeds and load cases. The peak to peak values are given for healthy and faulty bearings for the window length w=10.

7.2.2.7.1 Peak to peak values of CLT signals for w=10. The peak to peak (p2p) values of curve length transforms calculated for acceleration signals are given in Figures 7.69-7.71. As seen from the figures that the ratios between the faulty and healthy cases are high enough to use the p2p parameter in detecting the bearing faults. The inner race faults can be detected more easily for L0 load case. On the other hand, the outer race faults can be detected efficiently for L1 and L2 load cases. The efficiency of the p2p values on the defect detection depends on the shaft speed. Similar results are obtained for other window lengths.
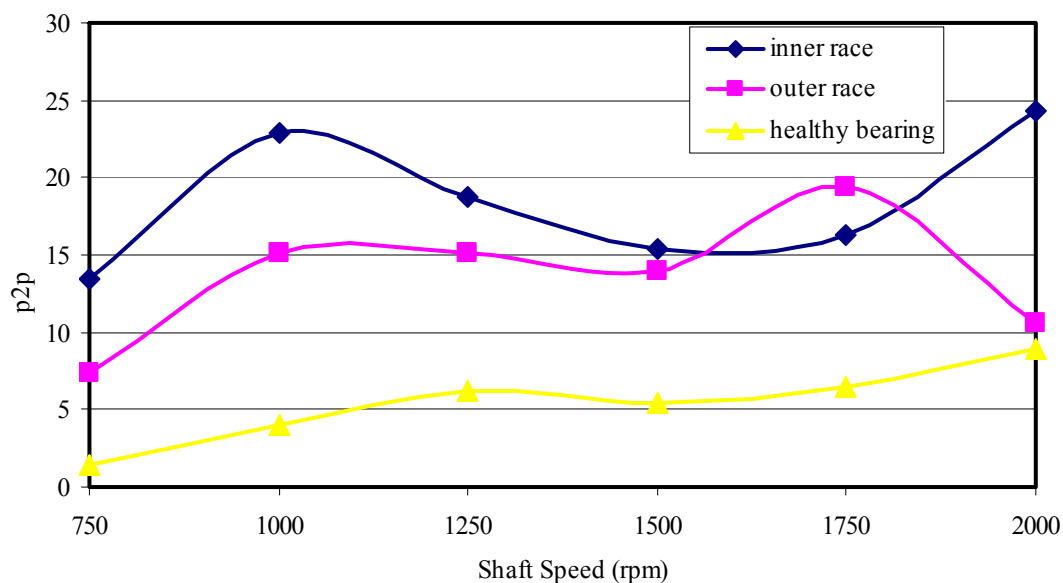
Figure 7.69 Peak to peak values of CLT's of acceleration signals under L0 load case for w=10.
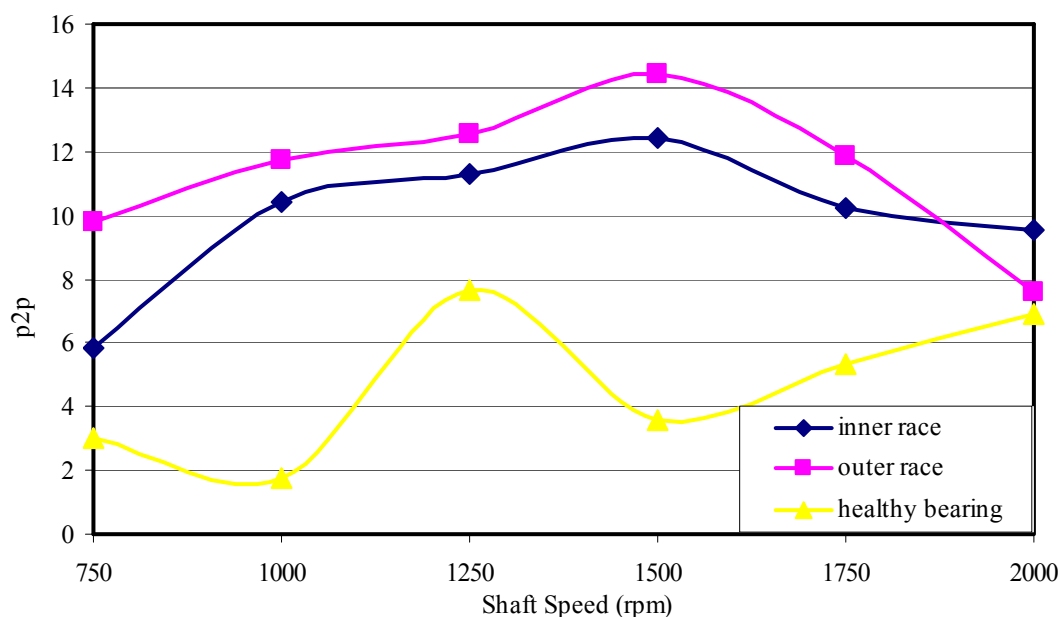
Figure 7.70 Peak to peak values of CLT's of acceleration signals under L1 load case for w=10.
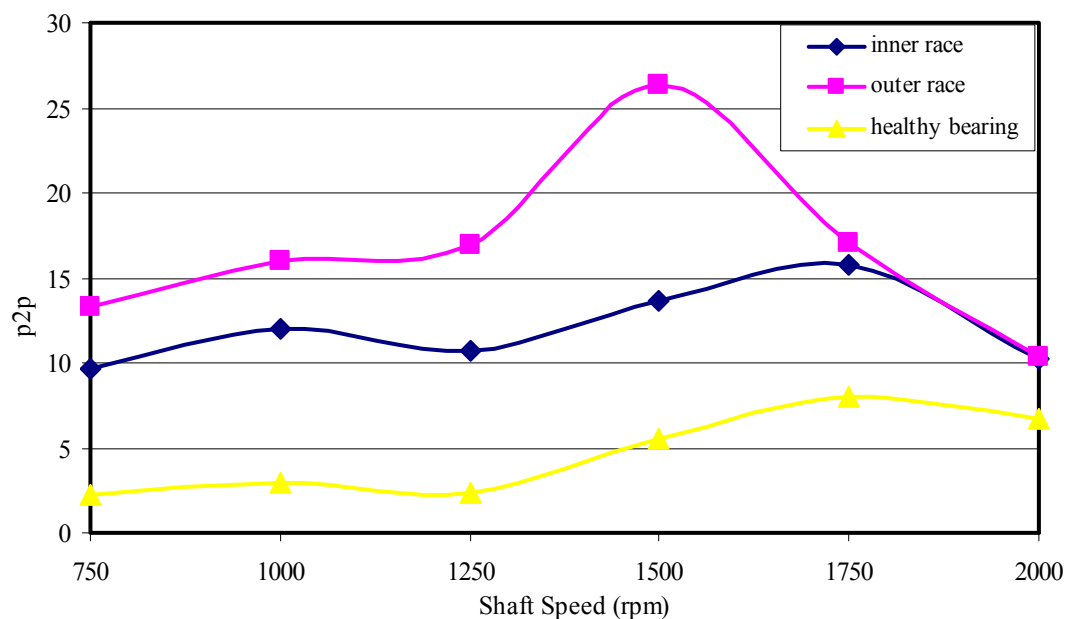
Figure 7.71 Peak to peak values of CLT's of acceleration signals under L2 load case for w=10.

7.2.2.8 Crest Factor (cf)

The crest factor values of the CLT signals are calculated for different shaft speeds and load cases. The crest factor values are given for healthy and faulty bearings for the window length w=10.

7.2.2.8.1 Crest factor values of CLT signals for w=10. The crest factor (cf) values of the curve length transforms of acceleration signals are given in Figures 7.72-7.74. As seen from the figures that the crest factor ratios between the faulty and healthy cases are high enough to use this parameter as a successful defect indicator. The inner race defects can be detected more easily for L0 load case. On the other hand, the outer race faults can be detected efficiently for L1 and L2 load cases. The efficiency of the crest factor on the defect detection depends on the shaft speed and the crest factor ratio between the faulty and healthy cases reduces as the window length increases.
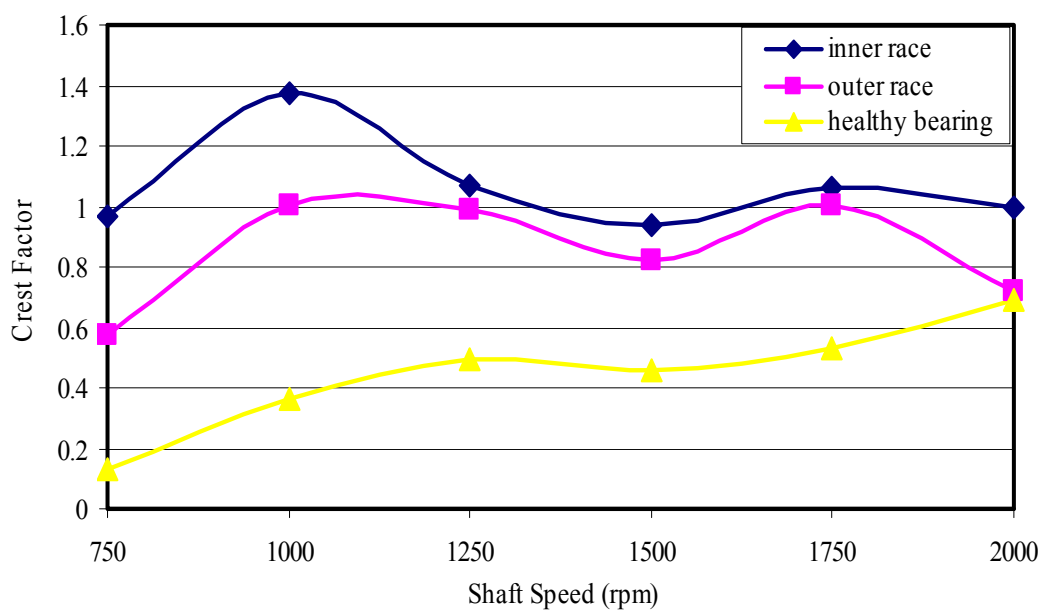
Figure 7.72 Crest factor values of CLT's of acceleration signals under L0 load case for w=10.
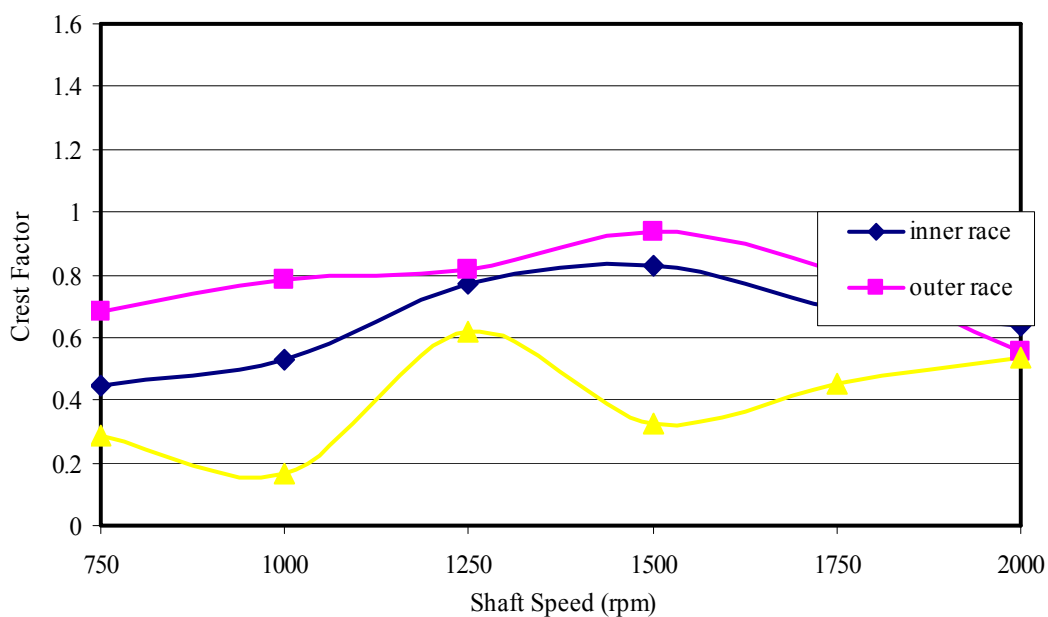
Figure 7.73 Crest factor values of CLT's of acceleration signals under L1 load case for w=10.
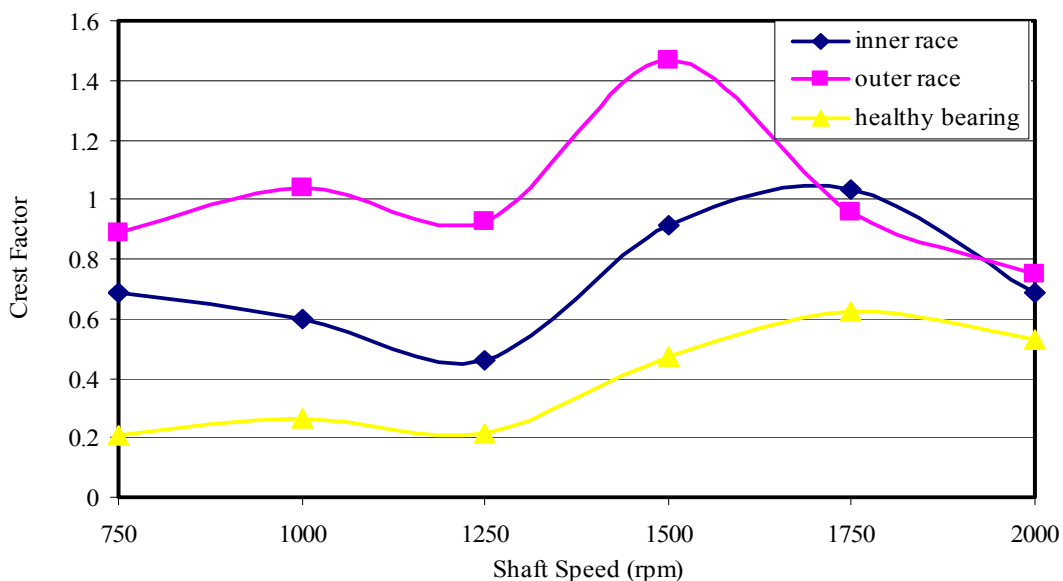
Figure 7.74 Crest factor values of CLT's of acceleration signals under L2 load case for w=10.

7.2.3 Statistical Moments of the CLT of Raw Acceleration Signals with dt

The statistical moments of the curve length transforms, which are calculated using the time increment dt in the formulation, are given in this section. The results for different statistical indices are given only for L1 load case and the window length w=10. Eight different indices for L1 load case are given in figures from 7.75 to 7.82.
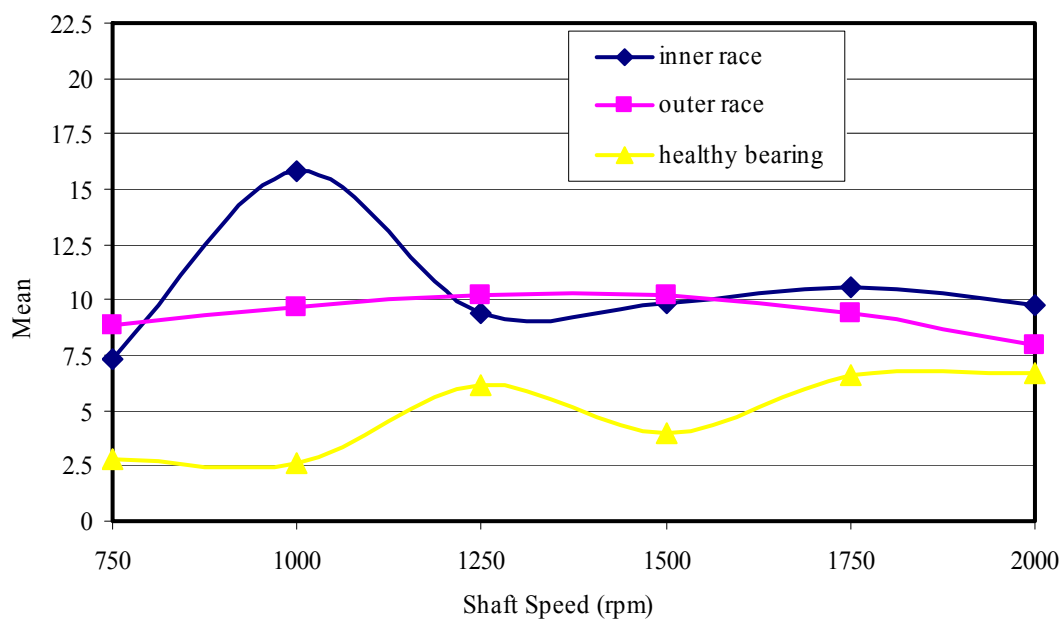
Figure 7.75 Mean values of CLT's of acceleration signals under L1 load case for w=10.
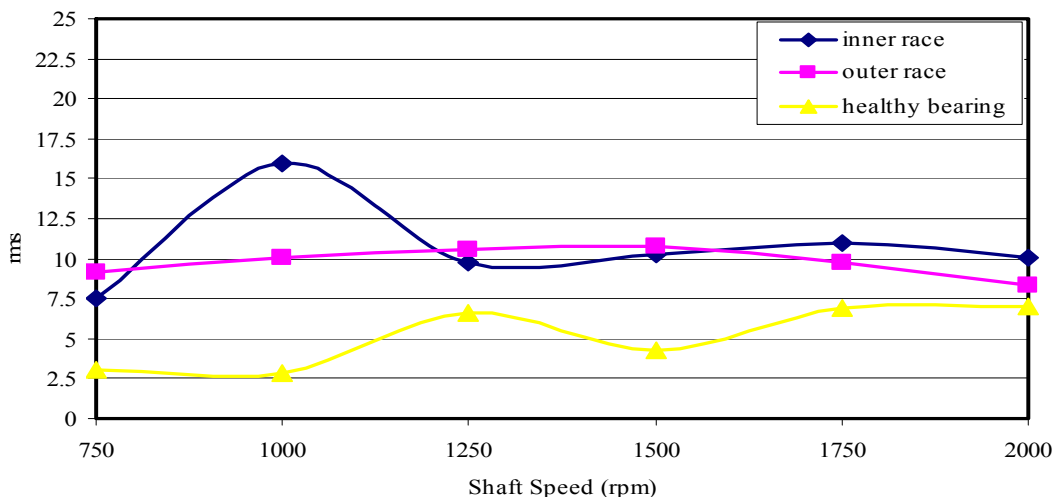
Figure 7.76 Rms values of CLT's of acceleration signals under L1 load case for w=10.
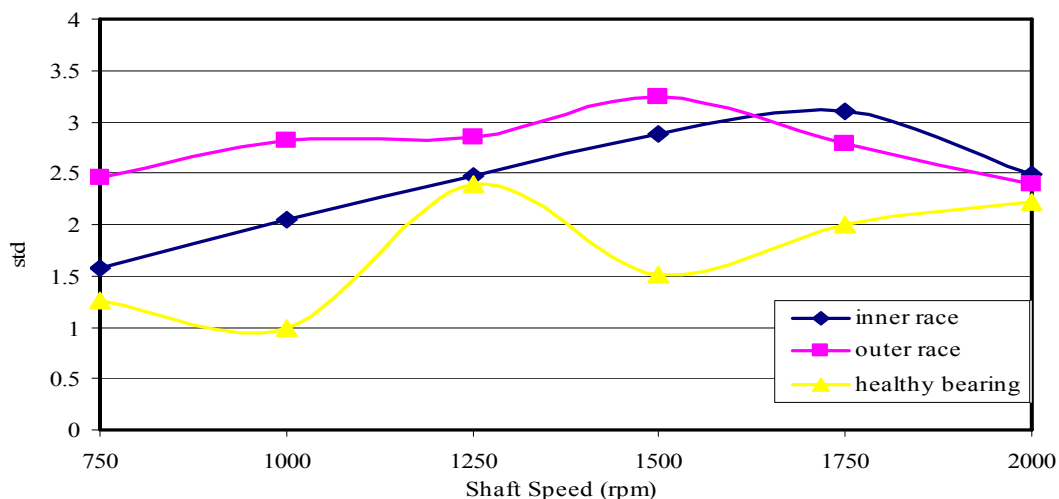
Figure 7.77 Standart devition values of CLT's of acceleration signals under L1 load case for w=10.
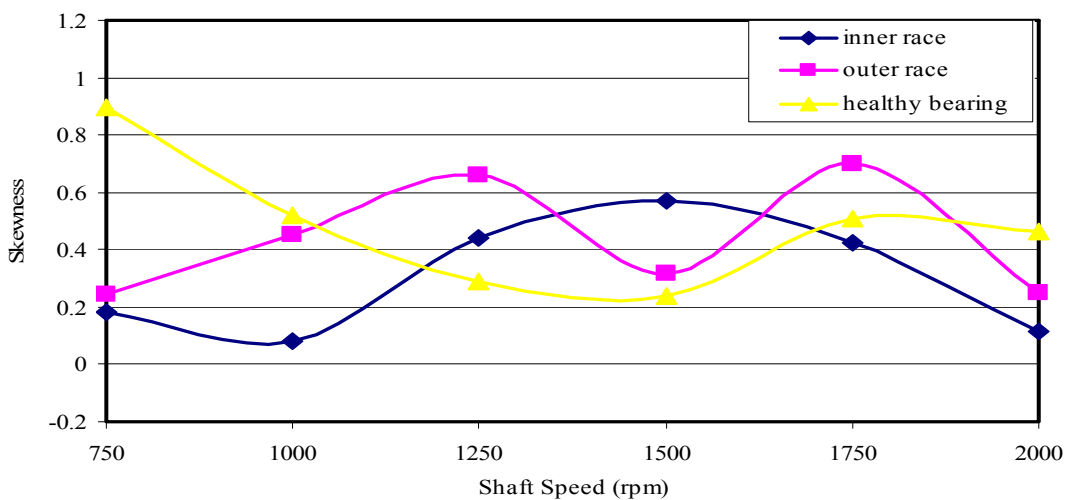
Figure 7.78 Skewness values of CLT's of acceleration signals under L1 load case for w=10.
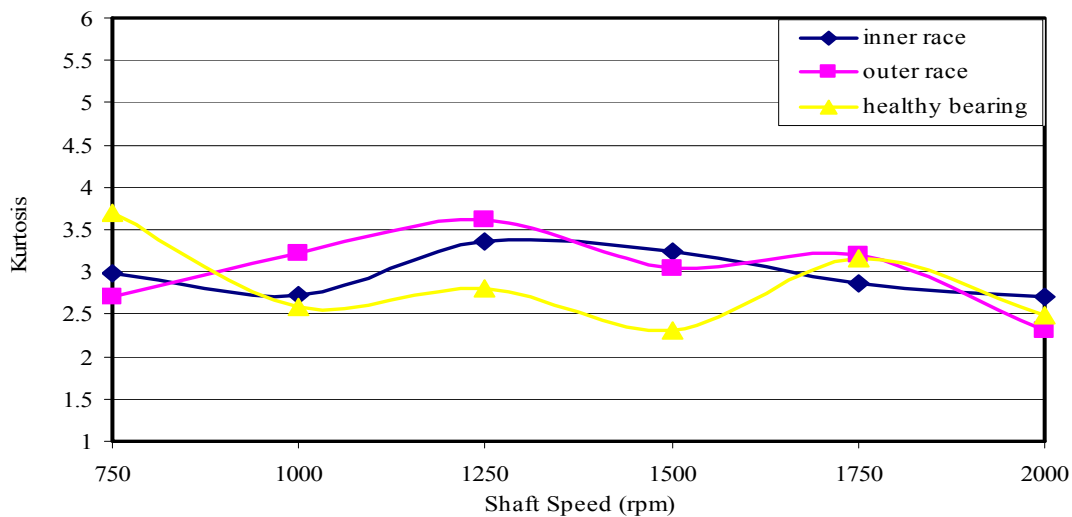
Figure 7.79 Kurtosis values of CLT's of acceleration signals under L1 load case for w=10.
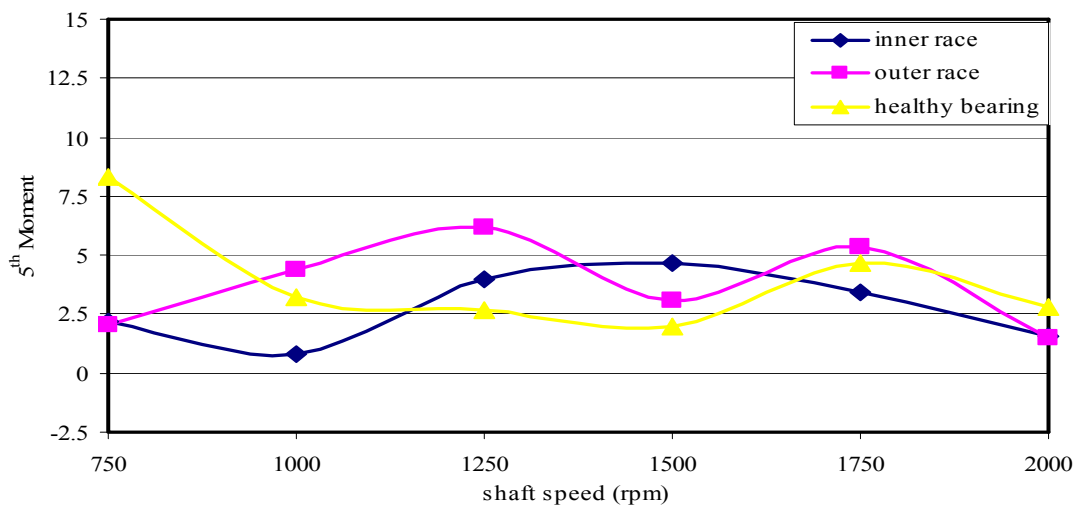
Figure 7.80 5th moment values of CLT's of acceleration signals under L1 load case for w=10.
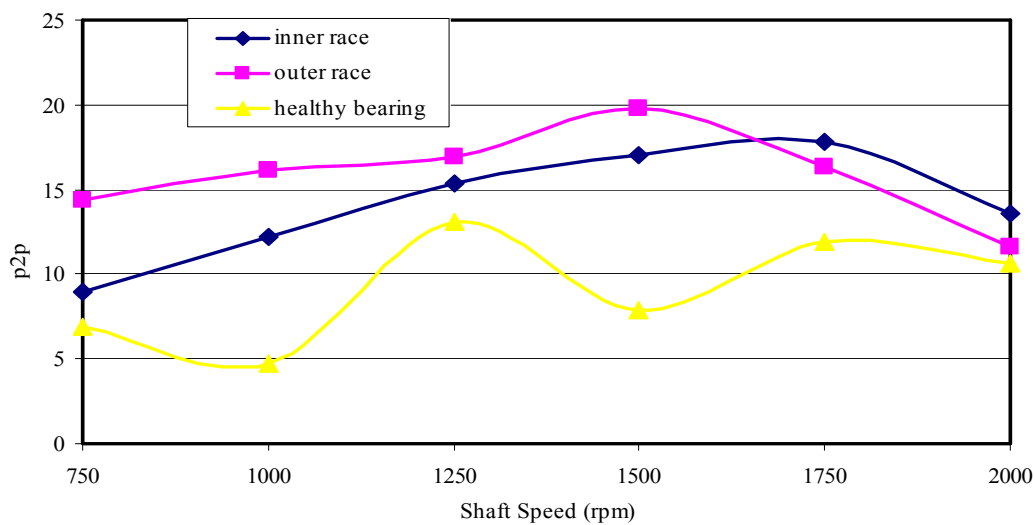
Figure 7.81 Peak to peak values of CLT's of acceleration signals under L1 load case for w=10.
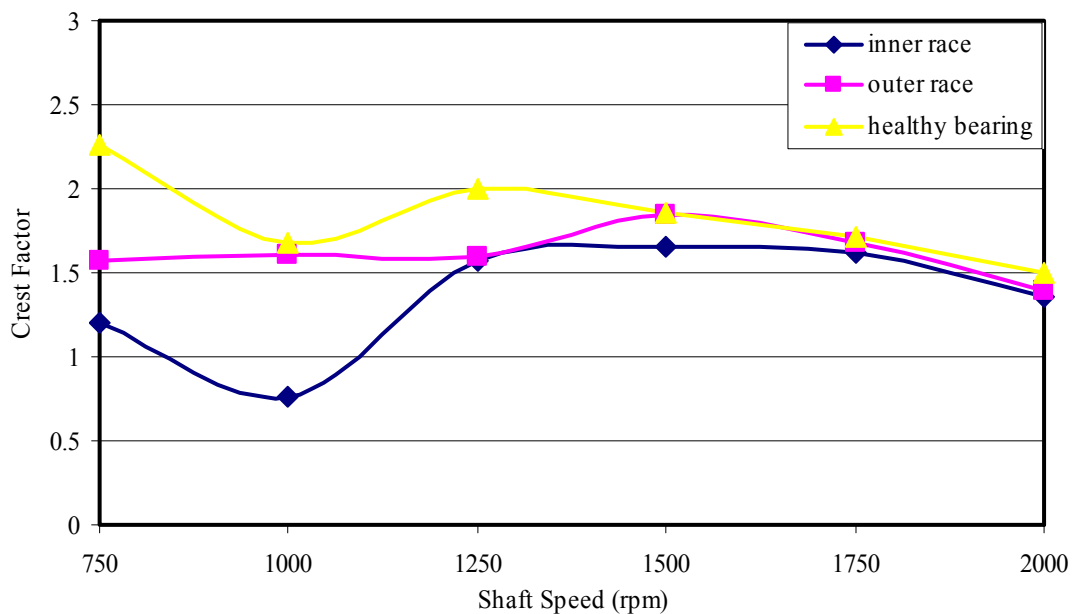
Figure 7.82 Crest factor values of CLT's of acceleration signals under L1 load case for w=10.

The ratio of the mean values for faulty and healthy cases given in Figure 7.75 are greater than the mean value ratios of CLT signals calculated for C=1. This means that the mean value parameter calculated by dt should be used as a defect indicator if the curve length transforms of acceleration signals are used for diagnostic purpose.

Figure 7.76 shows the rms values of the curve length transforms for healthy and faulty bearings calculated by using time increment dt. The ratios between the faulty and healthy cases obtained using dt are greater than those obtained with the transformation coefficient C. The rms parameter calculated with dt can be used as a good defect indicator.

The ratios of the statistical indices, standart deviation, skewness, kurtosis, fifth moment and peak to peak calculated using C are greater than the ratios obtained for dt. Besides, the crest factor ratios calculated using dt are greater than those obtained by using C and should be used for defect detection.

7.2.4 Statistical Moments of the CLT of Filtered Acceleration Signals with dt

The statistical moments of the curve length transforms, which are calculated using the time increment dt in the formulation, are given in this section. The curve length transform are calculated for filtered acceleration signals. The results for different statistical indices are given only for L1 load case and the window length w=20. Eight different indices for L1 load case are given in figures from 7.83 to 7.90. As seen from Figure 7.83, Figure 7.84 and 7.85 that the 7.89, filtering the acceleration signals makes some statistical indices useful for defet detection especially at high shaft speed region.

Figure 7.83 Mean values of CLT's of acceleration signals under L1 load case for w=20.

Figure 7.84 Rms values of CLT's of acceleration signals under L1 load case for w=20.

Figure 7.85 Standart deviation values of CLT's of acceleration signals under L1 load case for w=20.

Figure 7.86 Skewness values of CLT's of acceleration signals under L1 load case for w=20.

Figure 7.87 Mean values of CLT's of acceleration signals under L1 load case for w=20.
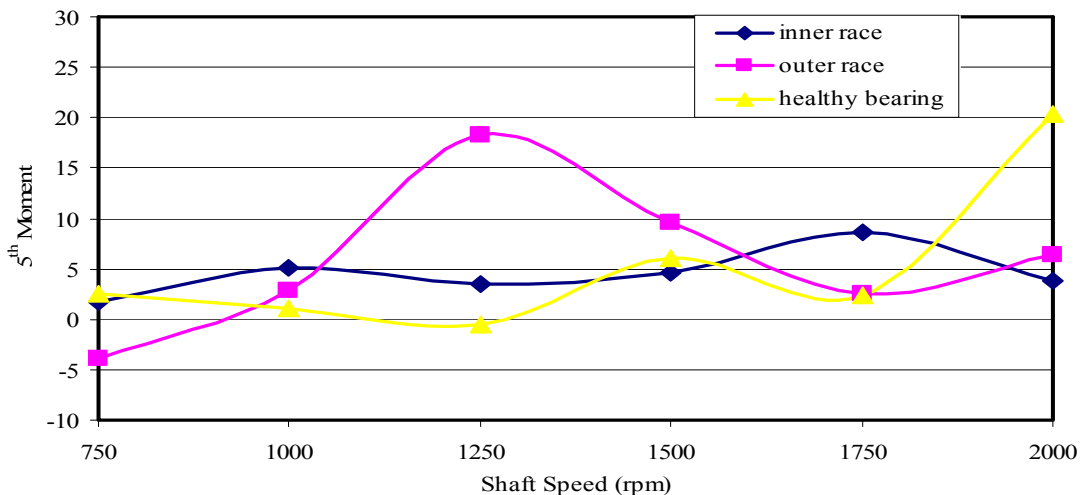
Figure 7.88 Fifth moment values of CLT's of acceleration signals under L1 load case for w=20.

Figure 7.89 Peak to peak values of CLT's of acceleration signals under L1 load case for w=20.

Figure 7.90 Crest factor values of CLT's of acceleration signals under L1 load case for w=20.

7.3 Comparing the Results

7.3.1 The Ratios of the Statistical Indices for Acceleration Signals and Their Curve Length Transforms

In this section, the ratios for three statistical indices, namely rms, kurtosis and peak to peak of the raw acceleration signals and their curve length transforms are given to show the effectiveness of the time domain parameters on the detection of local bearing defects. Figure 7.91 shows the rms ratios between the faulty and healthy cases for different shaft speeds. As seen from the figure that the rms ratio is a good defect indicator especially for the middle speed region. The rms ratio loses its detection capability when the shaft speed increases.
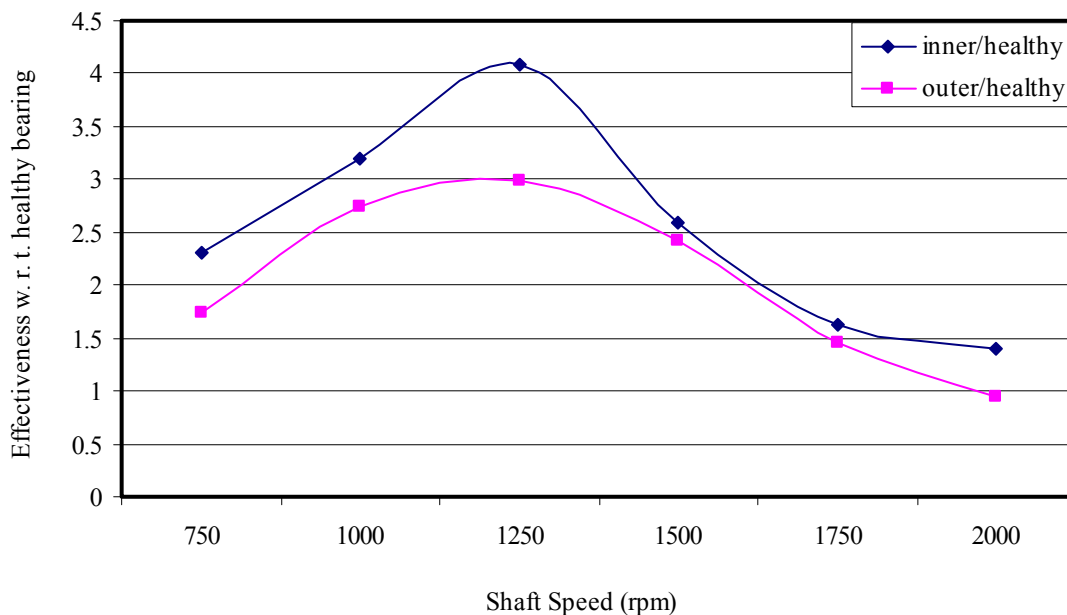
Figure 7.91 Rms ratios of raw acceleration signals under L0 load case.

Detection of the bearing faults by rms value is possible for L1 and L2 load cases at low shaft speeds as shown in Figure 7.92 and Figure 7.93.
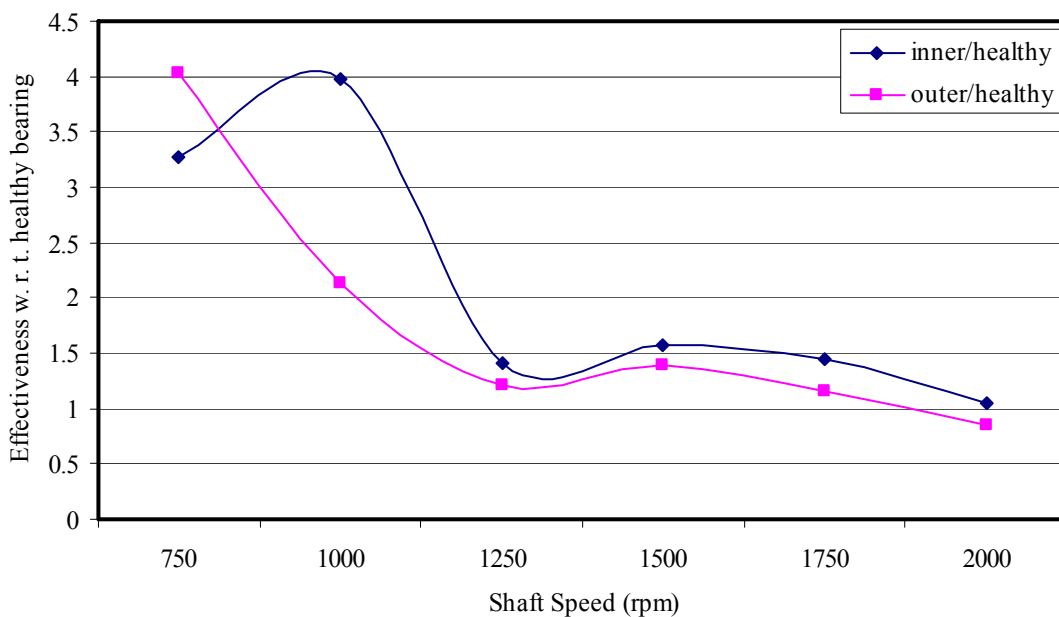
Figure 7.92 Rms ratios of raw acceleration signals under L1 load case.
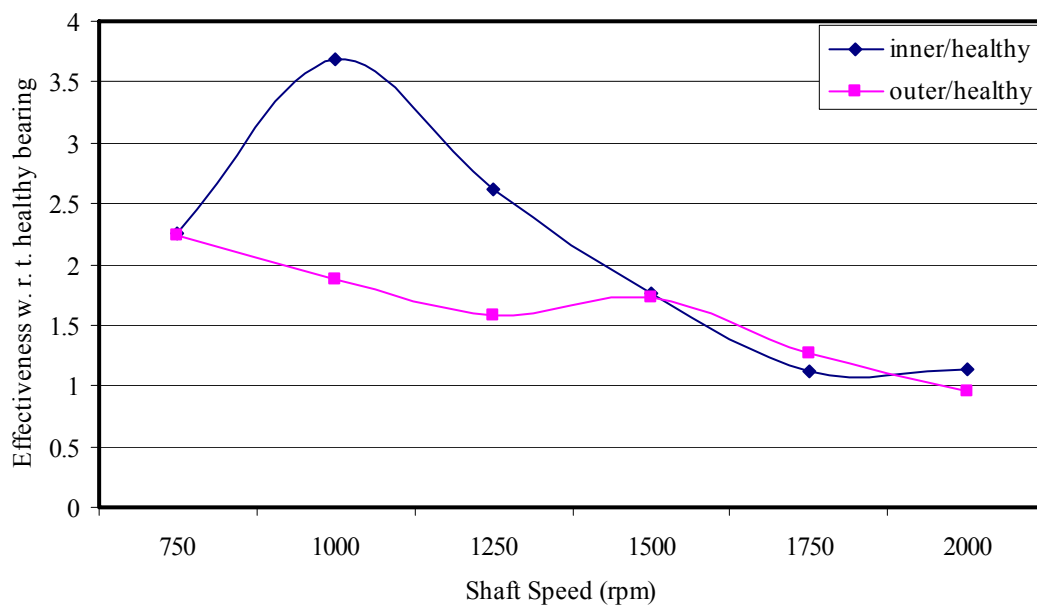
Figure 7.93 Rms ratios of raw acceleration signals under L2 load case.

Figure 7.94 shows the rms ratios calculated for the curve length transforms of the acceleration signals. It is seen from the figure that the rms parameter for CLT signals can be used as a defect indicator for a broad range of shaft speed. The performance of the rms value depends on the shaft speed. Figure 7.95 shows the rms ratios of the curve length transform signals calculated using dt. The rms values show that the

curve length transfom with dt gives higher rms ratios, which are useful for defect detection.
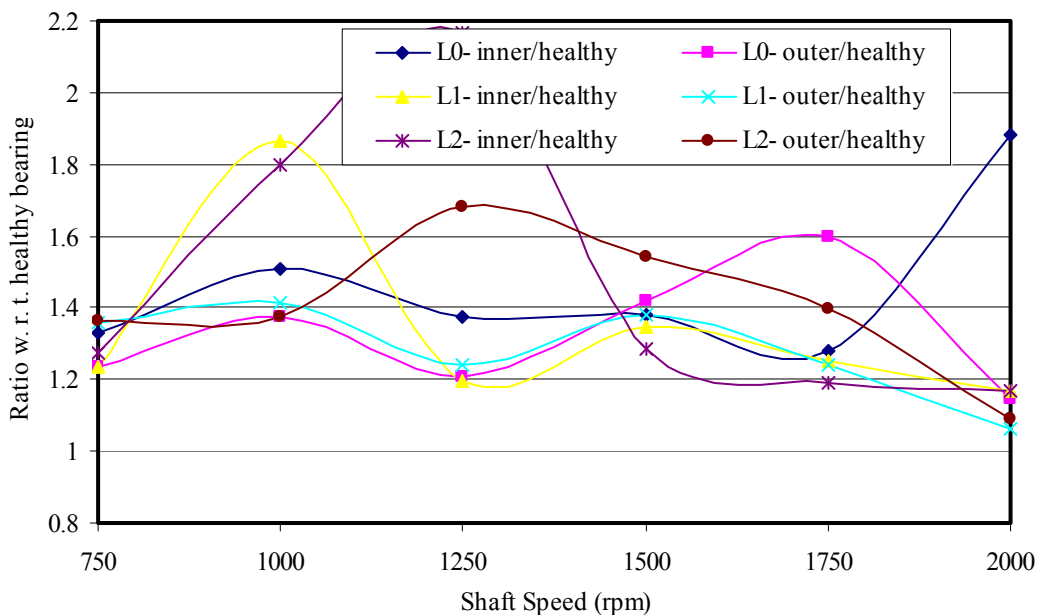
Figure 7.94 Ratios of the rms values of CLT signals with C=1, w=20.
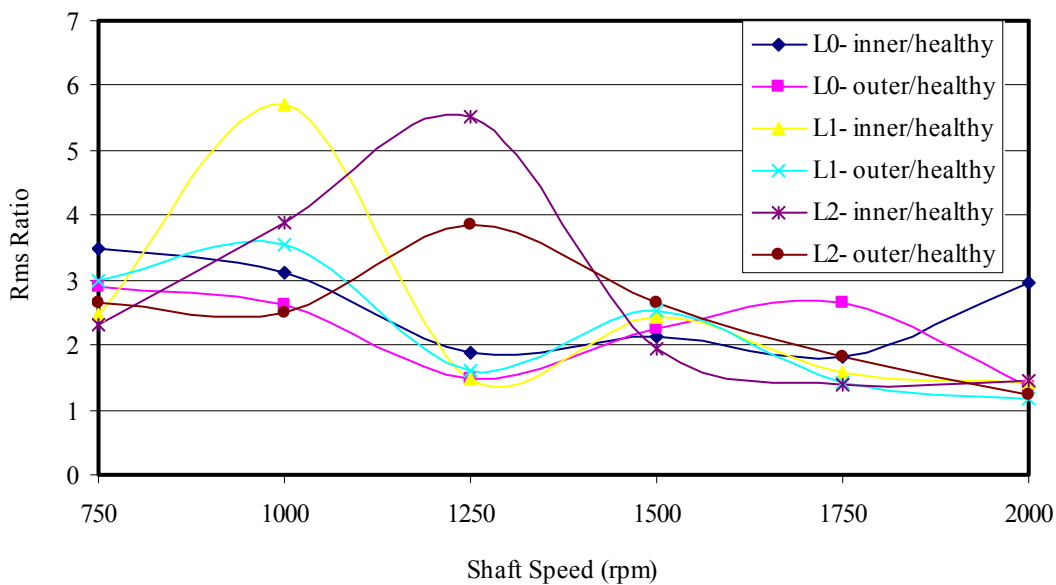
Figure 7.95 Ratios of the rms values of CLT signals with dt, w=20.

The kurtosis ratios between the faulty and healthy bearings are given for different shaft speeds and load cases in Figures 7.96-7.98 for raw acceleration signals. As mentioned before, the kurtosis parameter gives information about the existence of a defect at some specific shaft speeds. Generally, the kurtosis value is not a successful defect indicator.
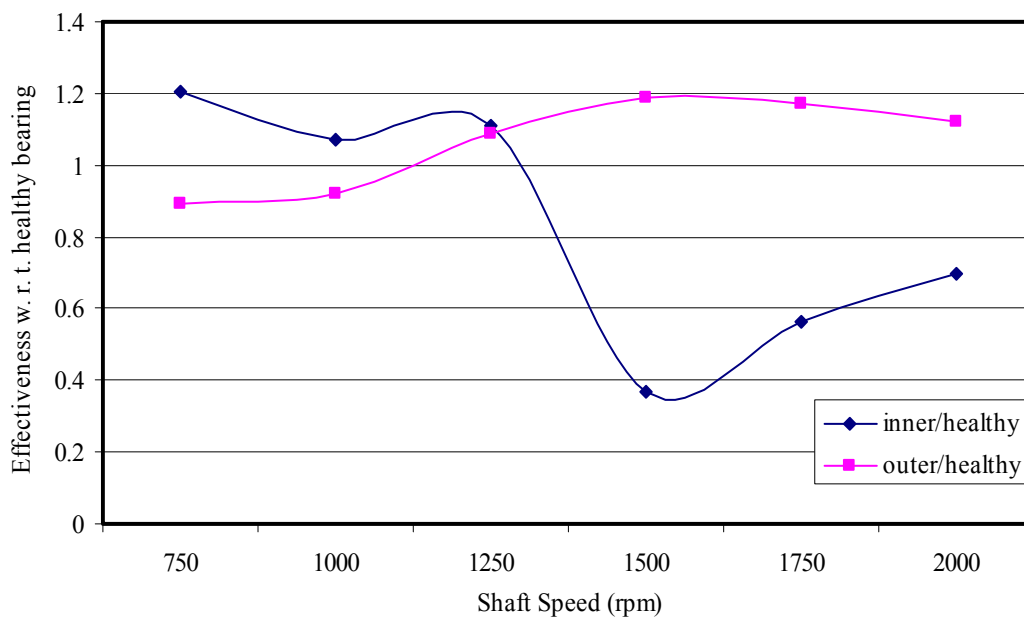
Figure 7.96 Kurtosis ratios of raw acceleration signals under L0 load case.
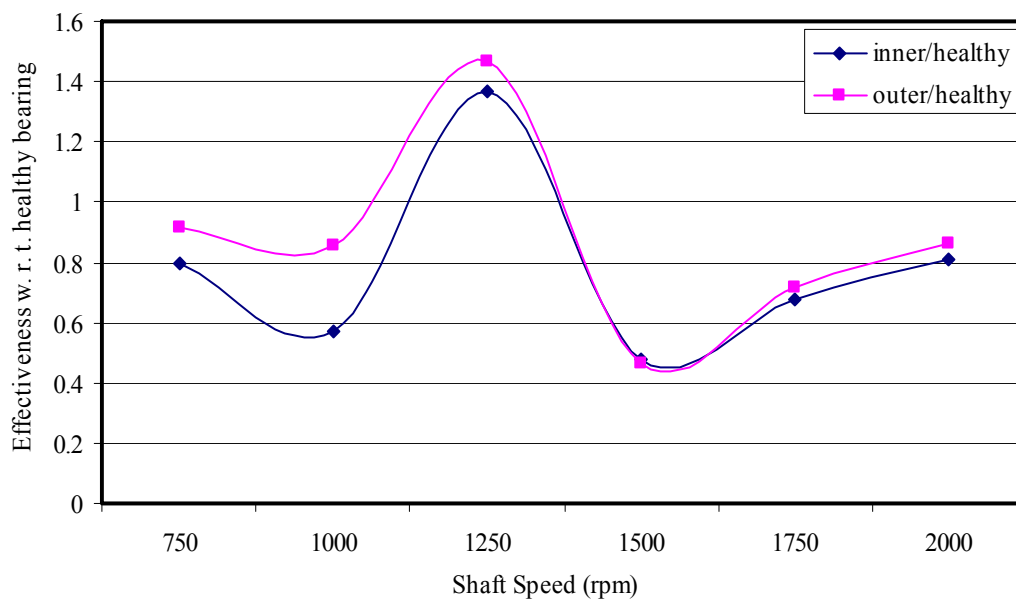
Figure 7.97 Kurtosis ratios of raw acceleration signals under L1 load case.
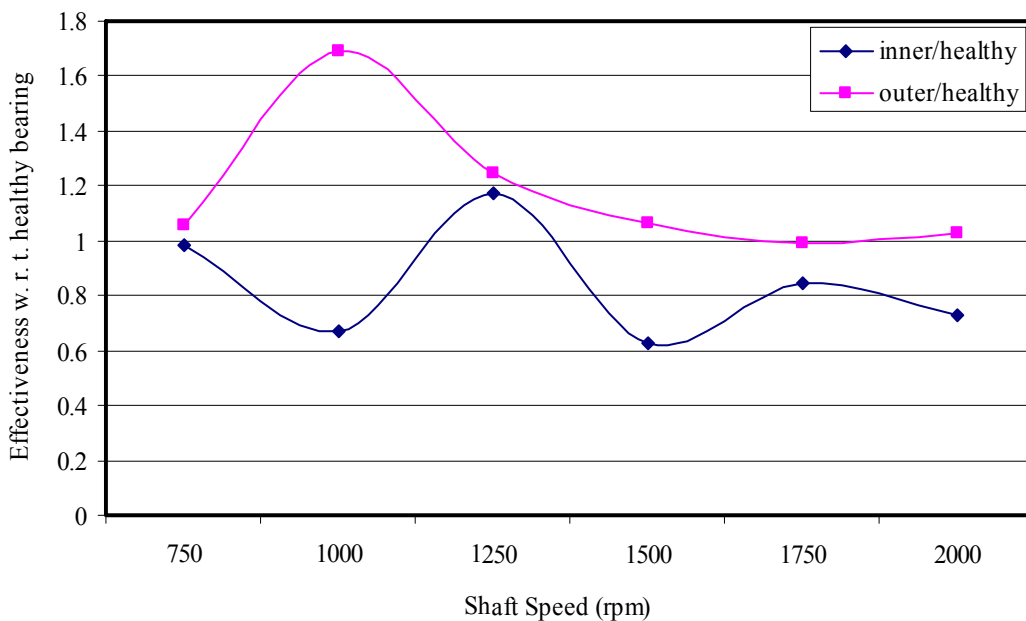
Figure 7.98 Kurtosis ratios of raw acceleration signals under L2 load case.
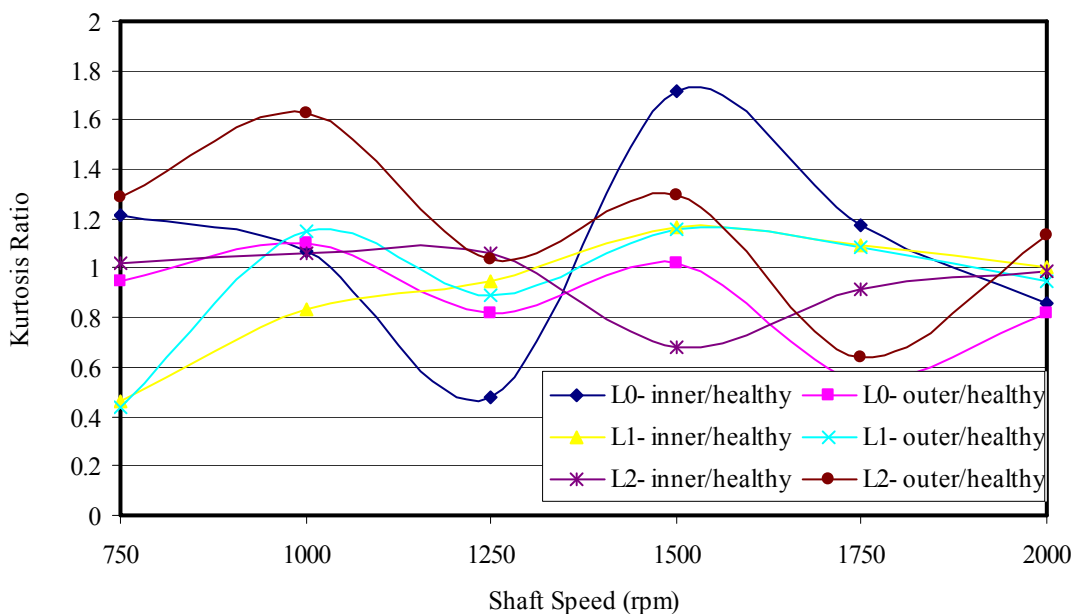
Figure 7.99 Ratios of the kurtosis values of CLT signals with C=1, w=20.

Figure 7.100 shows the kurtosis ratios of the CLT signals calculated using dt. As seen from the figure that, the kurtosis ratios are not high enough for all shaft speeds to make a descision about the condition of the bearing.
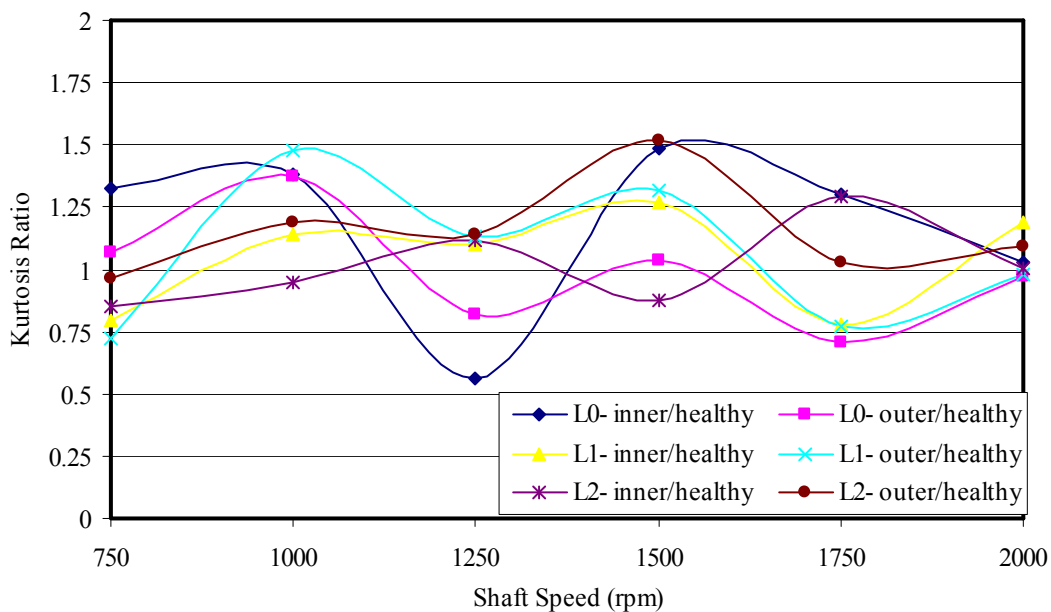
Figure 7.100 Ratios of the kurtosis values of CLT signals with dt, w=20.

Figures 7.101-7.103 show the peak to peak ratios of the raw acceleration signals for the faulty and healthy cases. As seen from the figure that the peak to peak ratios have a wavy nature and they are effective as a defect indicator especially at low speeds.
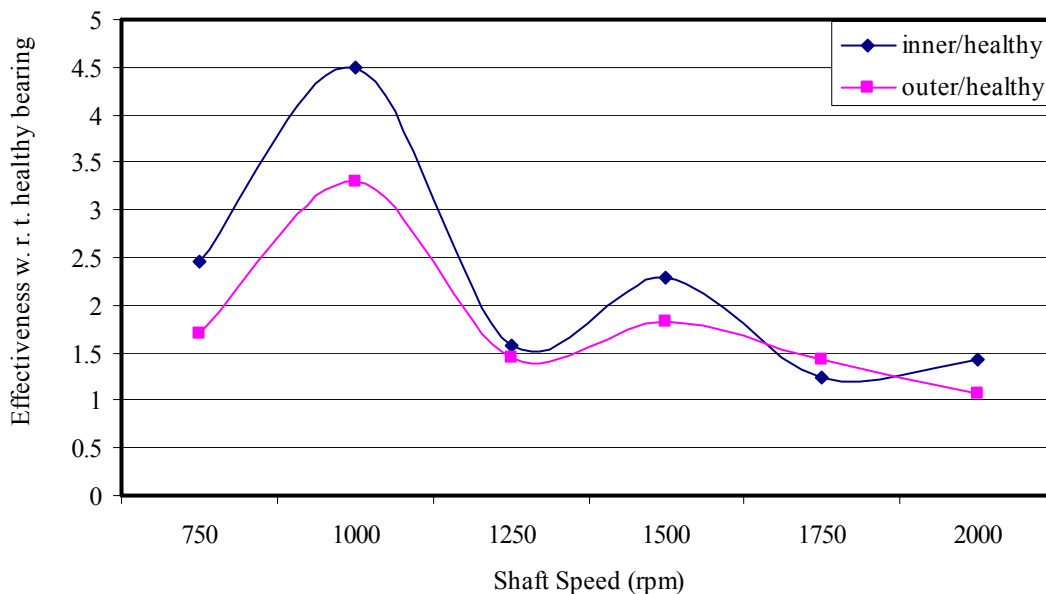
Figure 7.101 Peak to peak ratios of raw acceleration signals under L0 load case.
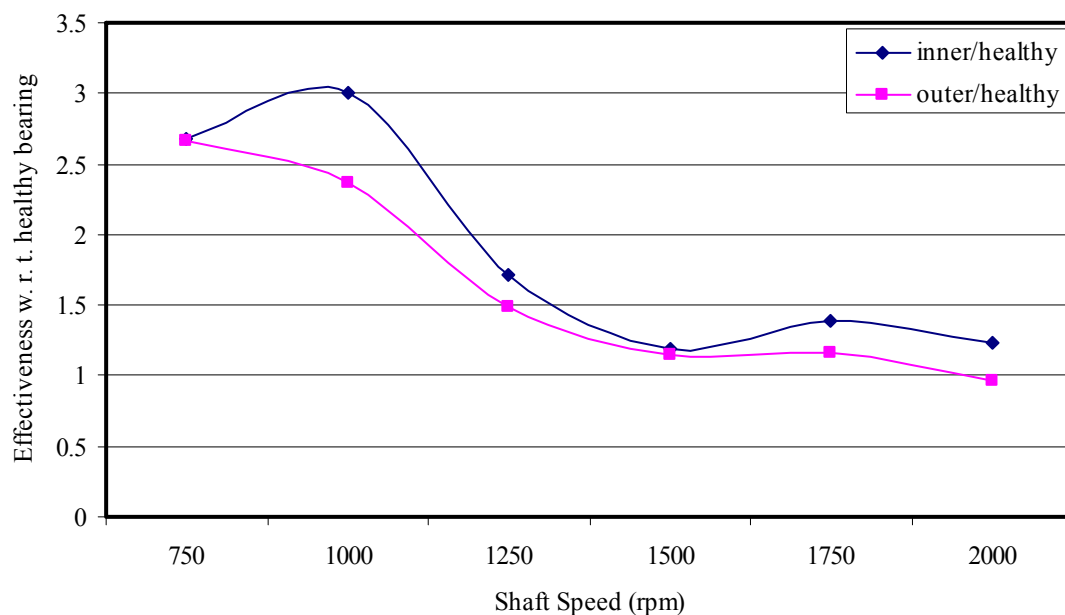
Figure 7.102 Peak to peak ratios of raw acceleration signals under L1 load case.
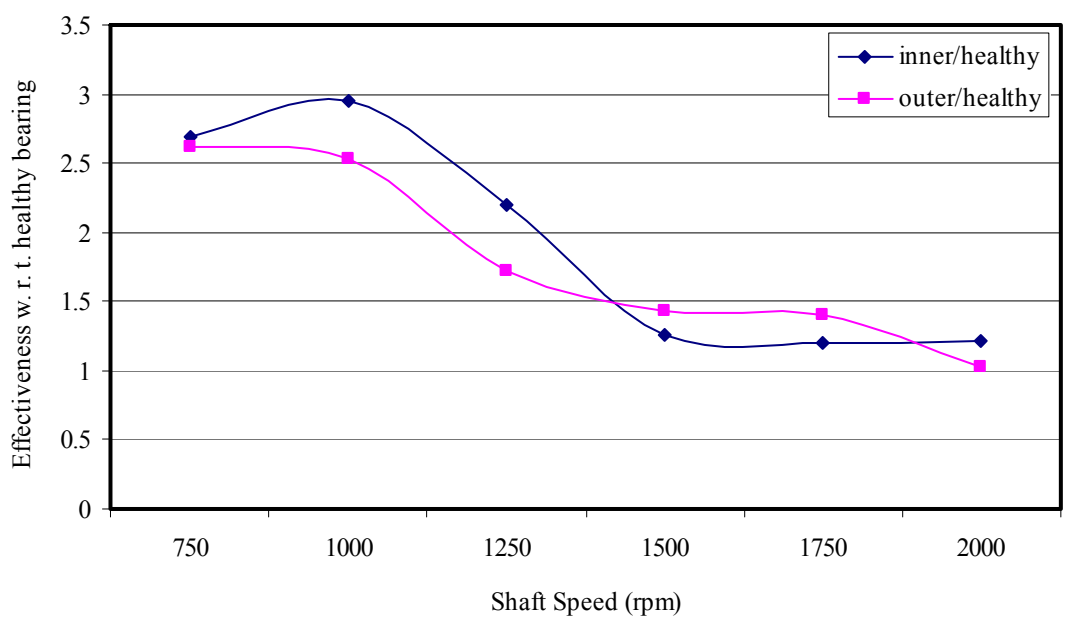
Figure 7.103 Peak to peak ratios of raw acceleration signals under L2 load case.

The peak to peak ratios for CLT signals calculated with C and dt are given in Figure 7.104 and 7.105, respectively. The window length in these figures is taken as 20.
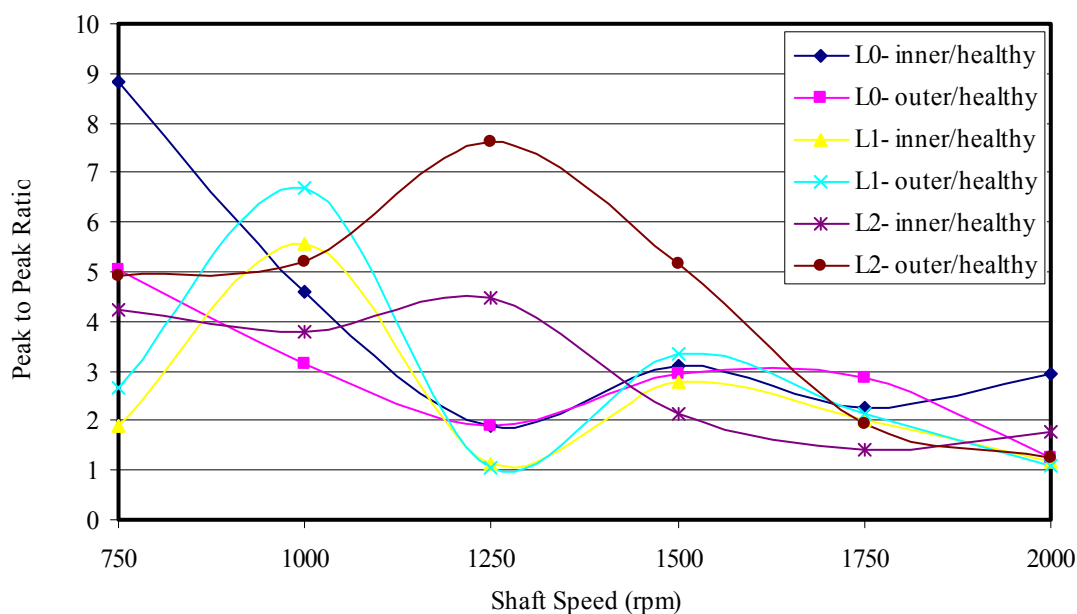
Figure 7.104 Ratios of the peak to peak values of CLT signals with C, w=20.
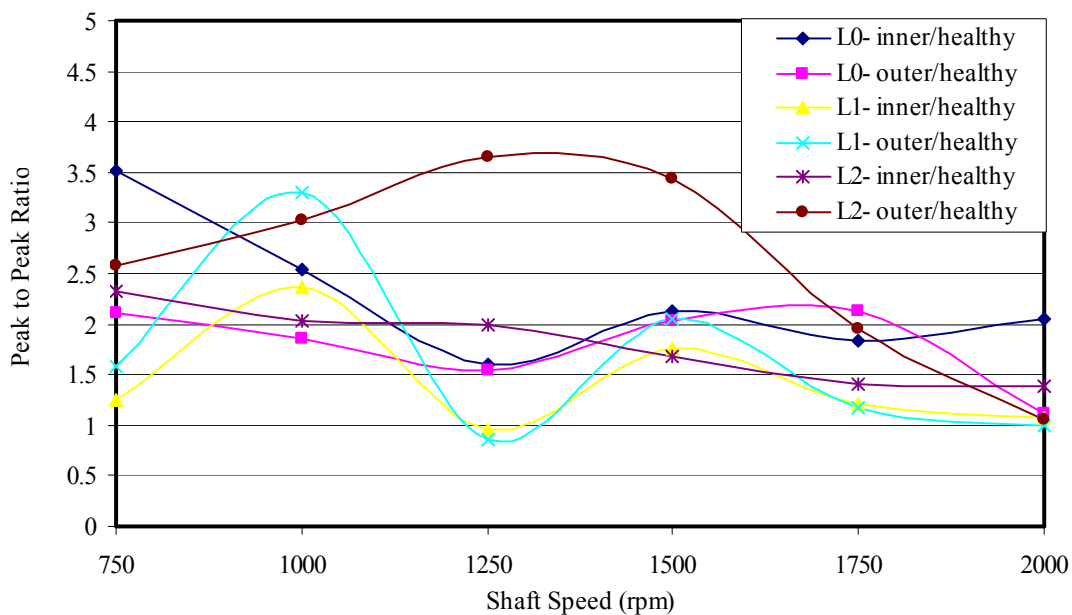
Figure 7.105 Ratios of the peak to peak values of CLT signals with dt, w=20.

The results given in Figure 7.104 show that, using CLT transform increases the peak to peak ratios between the faulty and healthy cases especially at some shaft speeds. This is a beneficial result of CLT for defect detection. But the same results are not obtained for the CLT transform calculated using the time increment dt as shown in Figure 7.105.

7.3.2 Effect of the Window Length on the Effectiveness of CLT

In this section, the three different moments of the curve length transforms of raw and filtered acceleration signal are given for different window lengths to show the effect of the window length on the statistical indices. The results are given for L0 and L1 load cases at 1000 rpm shaft speed. The curve length transforms are calculated using dt.
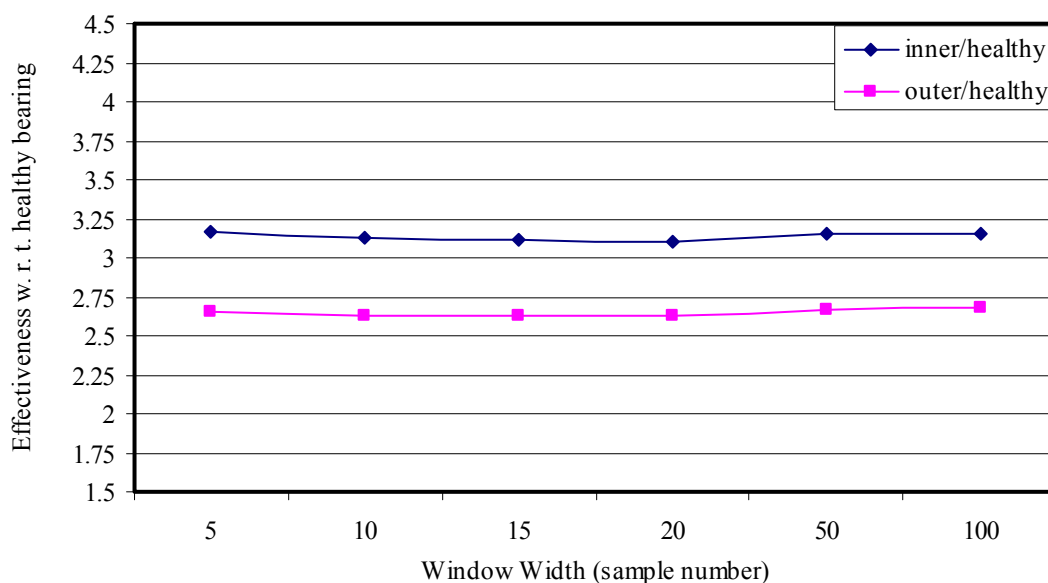
Figure 7.106 Rms ratios of the CLT signals versus window length for L0 load case at 1000 rpm.
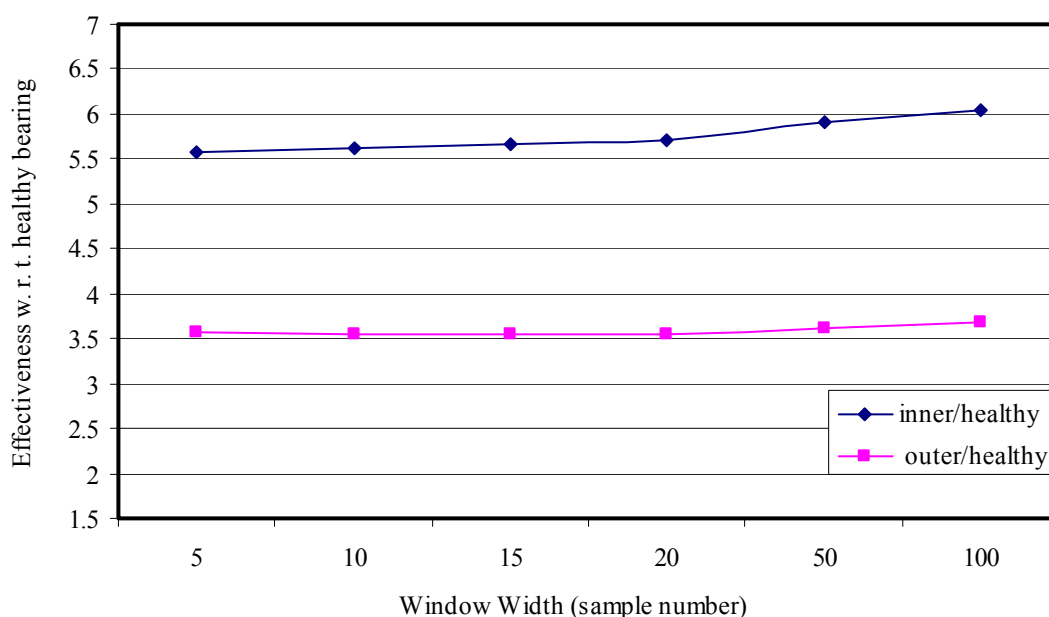
Figure 7.107 Rms ratios of the CLT signals versus window length for L1 load case at 1000 rpm.

The results given in Figure 7.106 show that, the rms ratios of CLT signals do not change with the increasing window length. The inner race faults can be defected easier than the outer race defects. On the other hand, the rms ratios tend to increase with increasing window length values as shown in Figure 7.107. The rms ratios of CLT signals are more efficient in detecting the defects for L1 load case.

Figure 7.108 and 7.109 show the kurtosis ratios of the CLT signals for L0 and L1 load cases, respectively.
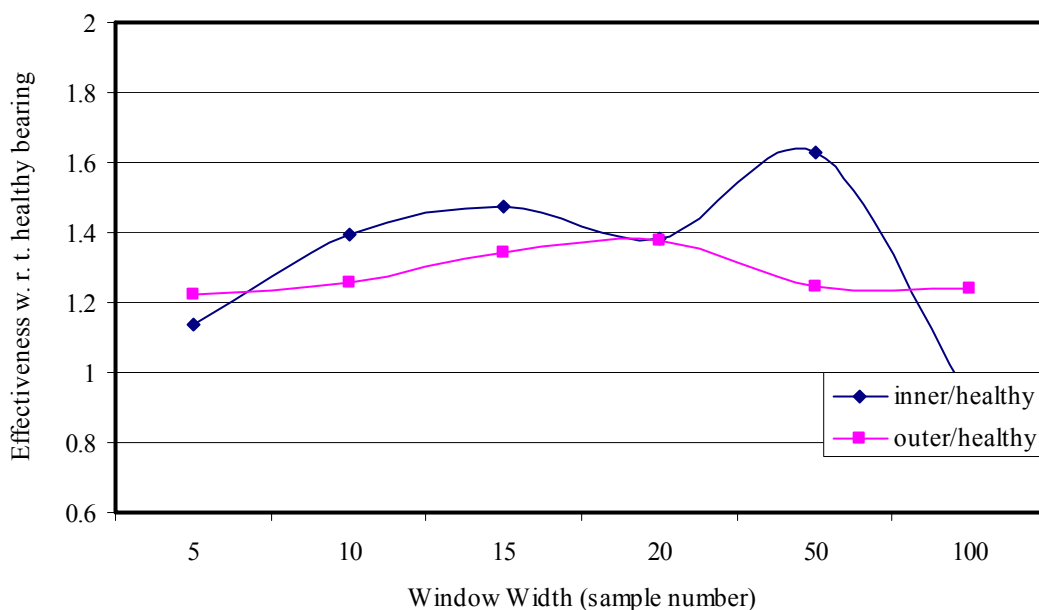
Figure 7.108 Kurtosis ratios of the CLT signals versus window length for L0 load case at 1000 rpm.
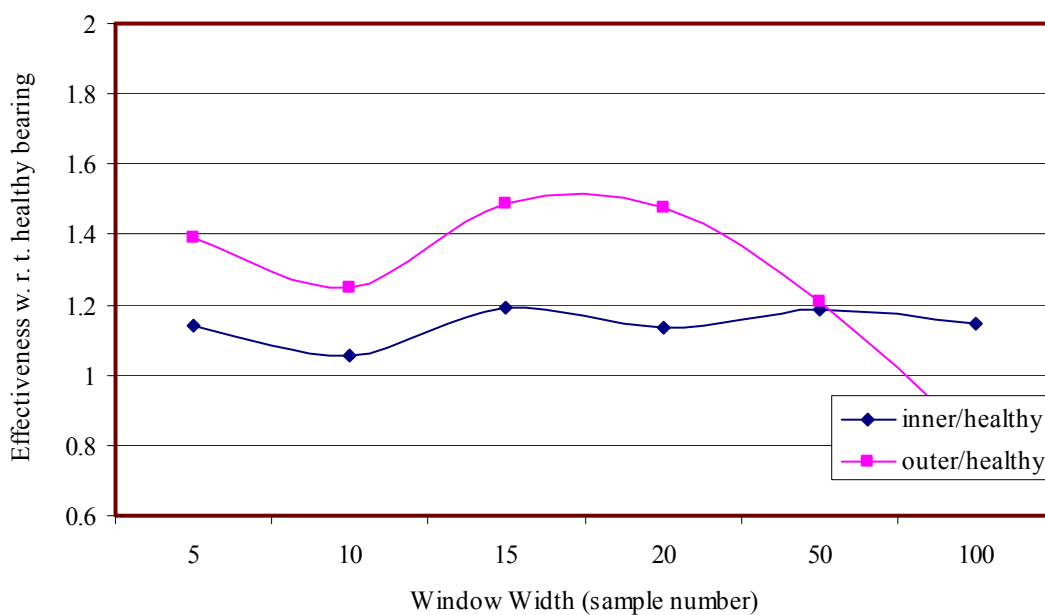
Figure 7.109 Kurtosis ratios of the CLT signals versus window length for L1 load case at 1000 rpm.

As seen from the kurtosis ratios given in Figure 7.108 and Figure 7.109, the CLT has a positive effect on the kurtosis parameter. The kurtosis ratio calculated for CLT signals may be helpful for defect detection. The length of the window has considerable effect on the kurtosis ratio.

The ratios of the peak to peak values versus window length are given in Figure 7.110 and Figure 7.111.
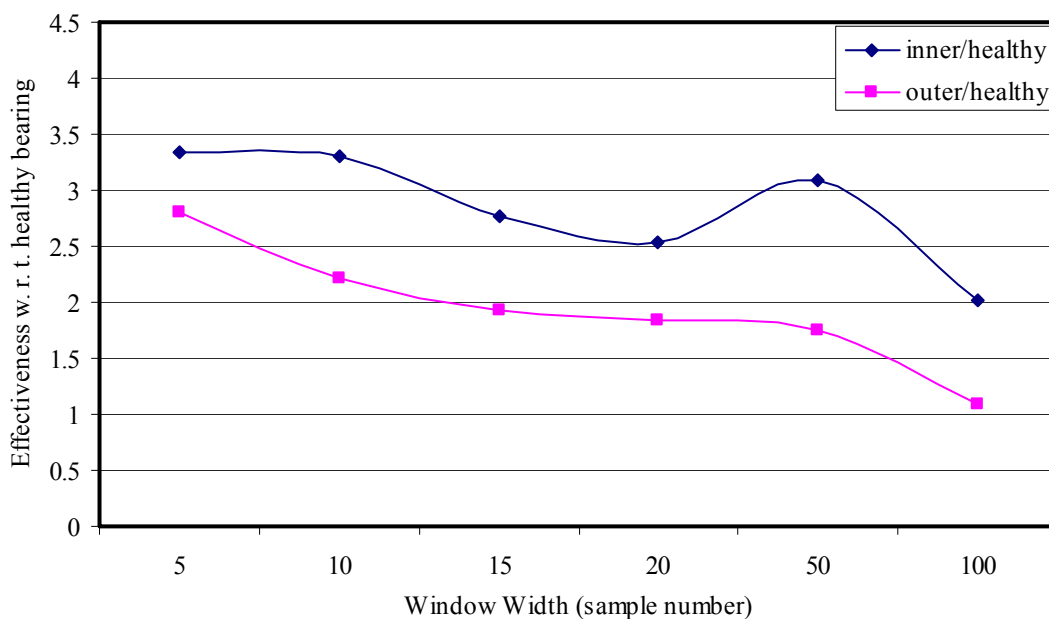
Figure 7.110 Kurtosis ratios of the CLT signals versus window length for L0 load case at 1000 rpm.
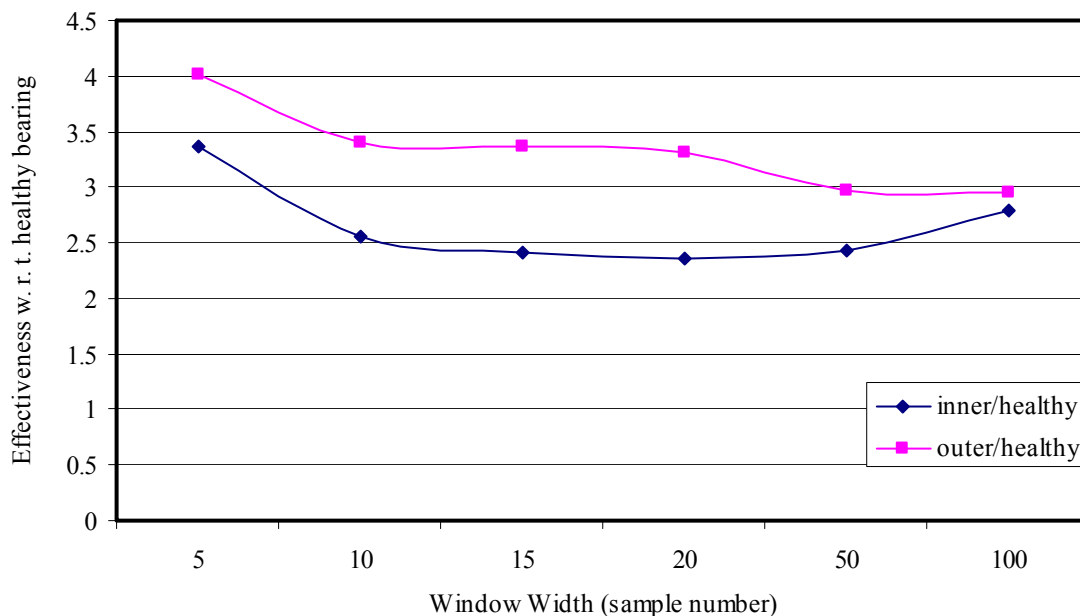
Figure 7.111 Kurtosis ratios of the CLT signals versus window length for L1 load case at 1000 rpm.

The peak to peak ratios derived from the CLT signals can be used for defect detection successfully. But the peak to peak ratios tend to reduce as the window length increases.

The ratios of the rms, kurtosis and peak to peak of the CLT signals calculated from the filtered acceleration signals are given in Figures 7.112-7.117. The rms ratios given in Figure 7.112 and Figure 7.113 are high enough to detect the inner or outer race defets for all window lengths.

Figure 7.112 Rms ratios of the CLT signals versus window length for L0 load case at 1000 rpm. (filtered acceleration signals)
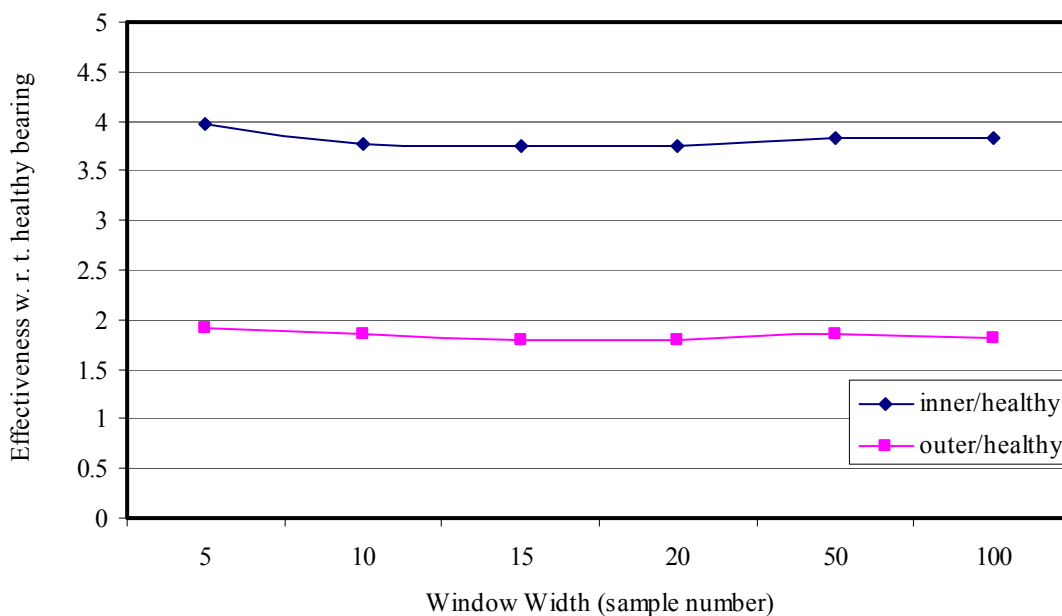
Figure 7.113 Rms ratios of the CLT signals versus window length for L1 load case at 1000 rpm. (filtered acceleration signals)

The kurtosis ratios for CLT signals are given in Figure 7.114 and Figure 7.115. The window length affects the kurtosis ratios as seen from the figures.
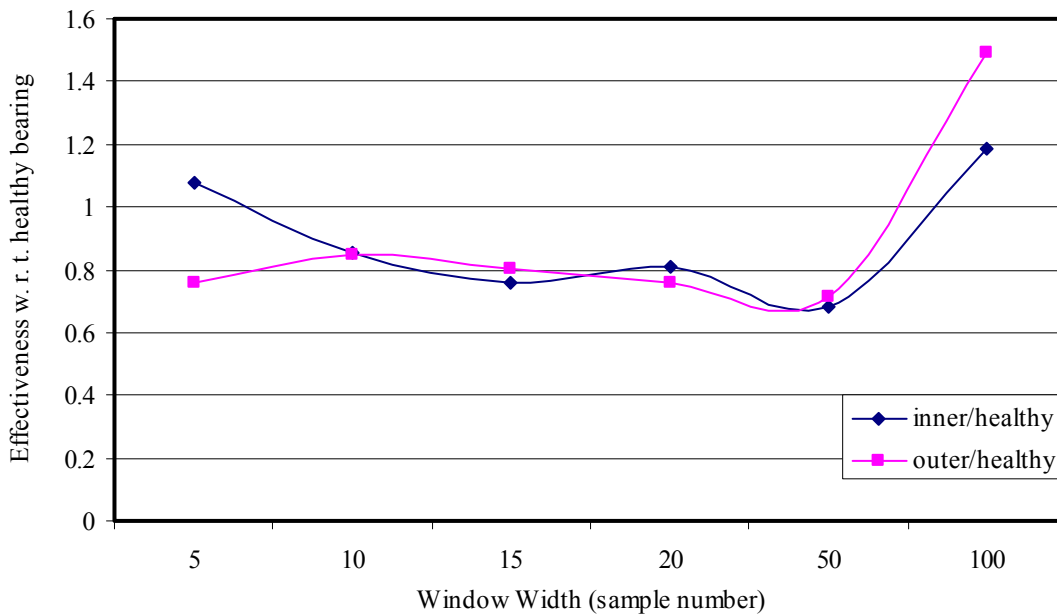
Figure 7.114 Kurtosis ratios of the CLT signals versus window length for L0 load case at 1000 rpm. (filtered acceleration signals)
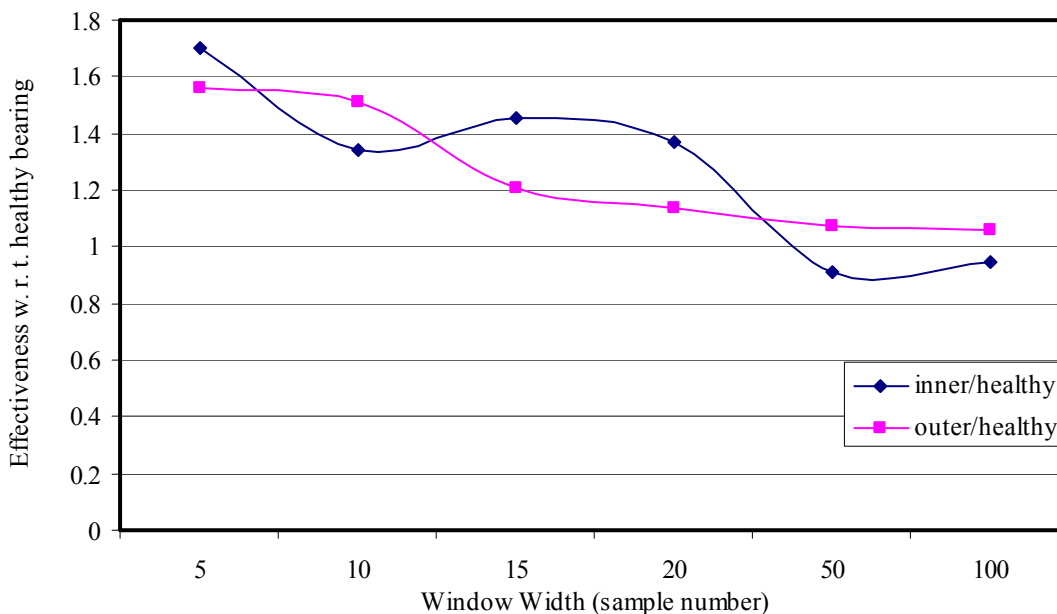
Figure 7.115 Kurtosis ratios of the CLT signals versus window length for L1 load case at 1000 rpm. (filtered acceleration signals)

The peak to peak ratios for CLT signals are given in Figure 7.116 and Figure 7.117. The window length affects the peak to peak ratios but this parameter can be used in detecting the inner or outer race defects for all window lengths.
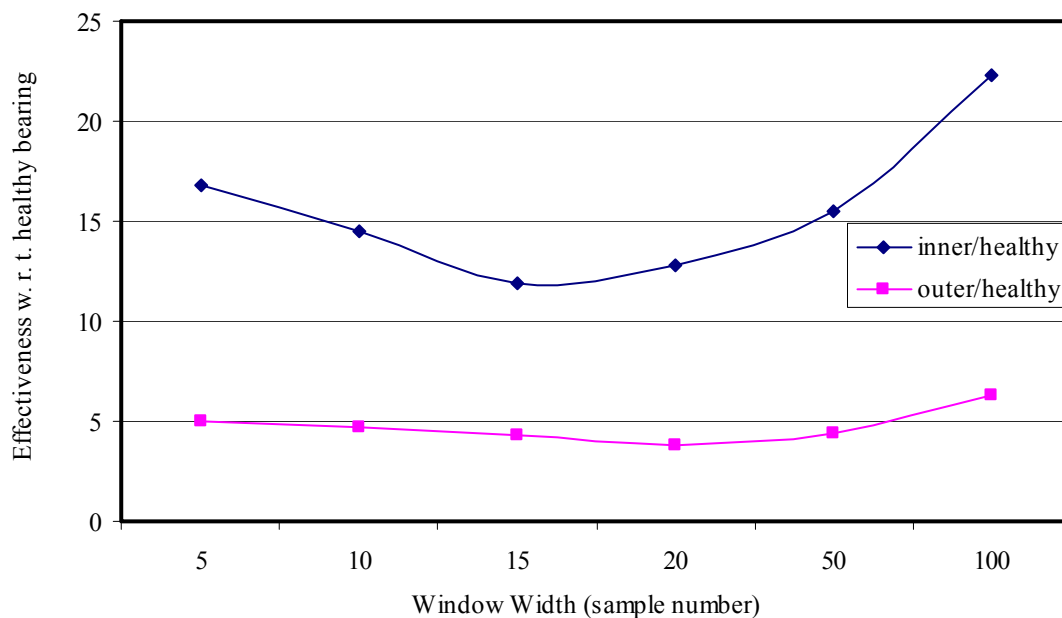
Figure 7.116 Peak to peak ratios of the CLT signals versus window length for L0 load case at 1000 rpm. (filtered acceleration signals)
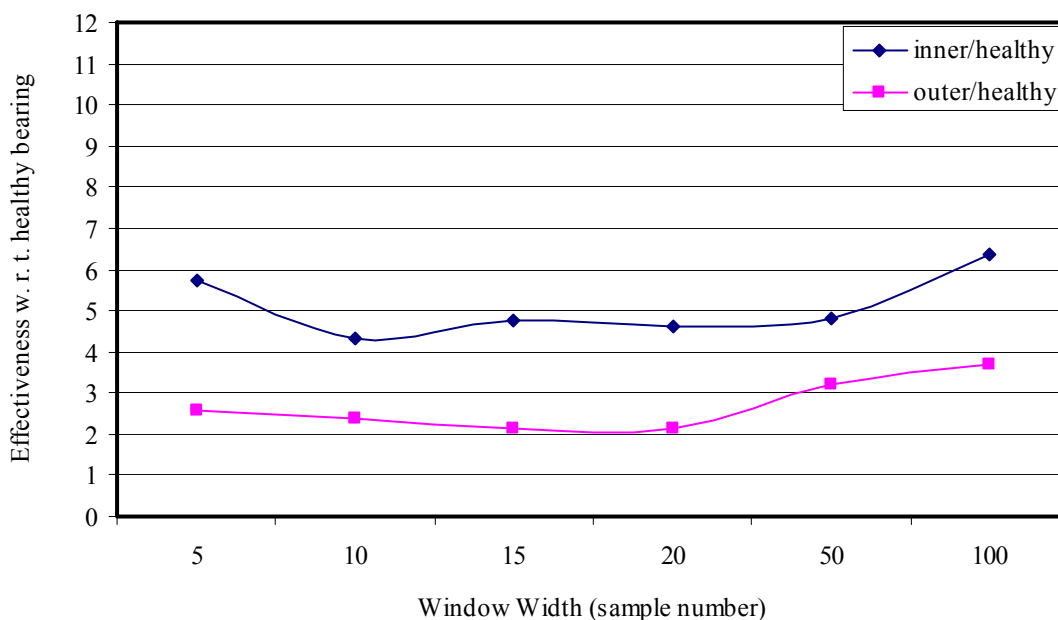
Figure 7.117 Peak to peak ratios of the CLT signals versus window length for L1 load case at 1000 rpm. (filtered acceleration signals)

CHAPTER EIGHT
CONCLUSIONS

The condition of the rolling element bearings having inner or outer race defect is monitored experimentally by vibration analysis. Vibration measurements are performed at different rotational speeds and different bearing loads. Two different masses are used to create the unbalanced load rotating with the shaft. The effectiveness of the time domain parameters on the fault diagnosis is investigated. Time domain parameters are applied to displacement, velocity and acceleration responses of the test rig for healthy and faulty cases. In the scope of this study, the curve length transform, which is a non linear time based transform, is applied to the vibration signals. The effectiveness of the curve length transform on the bearing defect detection is sought for different window lengths.

From the experimental results presented in this study, the fallowing points of discussion are summarized:

- The time domain parameters derived from the displacement responses are not suitable defect indicators.

- The velocity and acceleration responses of a structure including rolling element bearing can be used for defect detection with proper time domain parameters. But the usage of acceleration response gives better results.

- Filtering the acceleration signals around the bearing defect frequencies increases the defect detection capability of the time domain parameters.

- Filtering can help to see the bearing defect frequencies in the frequency spectrums of acceleration signals.

- Increasing the amplitude of the unbalanced load decreases the defect detection capability of the time domain parameters.

- Generally the time domain parameters are useful in defect detection at low rotational speeds.

- The amplitudes of the frequency spectrum at the shaft speed increases as the level of the unbalance increases.

- The natural modes of the bearing hausings are excited by the impact, which occurs between the rolling elements and defect.

- Generally the curve length transform gives better results for detecting the inner race defects.

- The mean and rms values of the curve length transformation calculated using dt should be preferred for defect detection. On the other hand, standart deviation and peak to peak values of the curve length transform calculated using C should be used while detecting the bearing defects.

- The window length used in the curve length transform doesn't affect rms values of the curve length transforms. The other time domain parameters are affected from the window length considerably.

- The curve length transforms of the filtered acceleration signals give high rms ratios between the faulty and healthy bearings.

- The level of the unbalance affects the performance of the curve length transform. The performance of the curve length transform is affected by the rotational speed.

- The curve length transform increase the effectiveness of the kurtosis as a defect indicator. The skewness and fifth moment parameters of the curve length transforms are not suitable defect indicators.

- The short time Fourier transform gives an idea about the existence of a defect in the bearing, but more powerful joint time frequency transform such as wavelet transform should be used to increase the resolution in both time and frequency domains.

REFERENCES

Afshari, N. (1998). *Model-based techniques for real-time fault detection of rolling element bearings.* (Phd. Thesis). Dept. of Systems, Control, and Industrial Engineering, Case Western University, USA.

Al- Ghamd, Abdullah M., & Mba, David. (2006). A comparative experimental study on the use of acoustic emission and vibration analysis for bearing defect identification and estimation of defect size. *Mechanical Systems and Signal Processing, 20,* <u>1537-1571.</u>

Al- Raheem, Khalid F., Roy, Asok., Ramachandran, K. P., Harrison, D. K., & Grainger, Steven. (2007). Rolling element bearing fault diagnosis using laplace-wavelet envelope power spectrum. *EURASIP Journal on Advances in Signal Processing,*Article ID 73629, 14 pages, doi:10.1155/2007/73629.

Choudhury, A., & Tandon, N. (2000). Application of acoustic emission technique for the detection of defects in rolling element bearings, *Tribology International, 33,* 39-45.

FAG Rolling Bearings. (1985). Rolling element damage. Schweinfurt: Georg Schäfer.

Friedman, Alan. (n.d.), *What Is The "Crest Factor" And Why Is It Used?*, DLI Engineering.

Heperkan, H., Kesgin, U. (Eds.). (2002). *Yazılım ve programlama uygulamalarıyla mühendisler için sayısal yöntemler.* İstanbul: Literatür Yayıncılık.

Khemili, Imed., Chouchane, Mnaouar. (2005). Detection of rolling element bearing defects by adaptive filtering. *European Journal of Mechanics A/Solids, 24,* 293-303.

Kıral, Z.(July 2002). *Simulation and analysis of vibration signals generated by rolling element bearings with defects.* (Phd. Thesis). Izmir: Dokuz Eylul University.

Kıral, Z., & Karagülle, H. (2006). Vibration analysis of rolling element bearings with various defects under the action of an unbalanced force, *Mechanical Systems and Signal Processing, 20,* 1967-1991.

Lebold, M., McClintic, K., Campbell, R., Byington, C.,& Maynard, K. (2000). Review of vibration analysis methods for gearbox diagnostics and prognostics. *Proceedings of the 54th Meeting of the Society for Machinery Failure Prevention Technology,* 623-634.

Lee, C. (2000). *Development of sampling equalization technique for fault detection of rolling element bearings running at variable speed.* (Phd. Thesis). The University of Alabama, USA.

Liu, B., Ling, S. F., Gribonval, R. (2002). Bearing failure detection using matching pursuit. *NDT & E International, 35,* 255- 262.

Mazanoğlu, K. (2004). *Roller Bearing Failure Detection Using Vibration Analysis.*(Master of Science Thesis). Izmir: Dokuz Eylul University.

Miettinen, J., & Leinonen, P. (1999). Monitoring of contaminants in a grease lubricated rolling bearing by acoustic emission in field environment. *Proceedings of the 2nd COST 516 Tribology Symposium.* 243-252.

Misiti, M., Misiti, Y., Oppenheim, Y., & Poggi, J. (1997). *Wavlet toolbox user's guide.* The MathWorks, Inc.

Neter, J., Wasserman, W., & Whitmore, G. A. (1988). *Applied statistics* (3th ed.). United States of America: Allyn & Bacon, Inc.

Normality, (n.d.). Retrieved March, 2008, from www.cfs.nrcan.gc.ca/subsite/wulder/normality

Orhan, S., Aktürk, N., & Çelik, V. (2006). Vibration monitoring for defect diagnosis of rolling element bearings as a predictive maintenance tool: Comprehensive case studies. *NDT & E International, 39,* 293-298.

ORS Rulman Kataloğu Teknik El Kitabı (1995). 158-159.

Sawalhi, N., & Randall, R. B. (2008 Part1). Simulating gear and bearing interactions in the presence of faults Part I. The combined gear bearing dynamic model and the simulation of localized bearing faults. *Mechanical System and Signal Processing, 22,* 1924-1951.

Sawalhi, N., & Randall, R. B. (2008 Part2). Simulating gear and bearing interactions in the presence of faults Part II. Simulation of the vibrations produced by extended bearing faults. *Mechanical System and Signal Processing, 22,* 1952-1966.

Sawalhi, N., Randall, R.B., & Endo, H. (2007). The enhancement of fault detection and diagnosis in rolling element bearings using minimum entropy deconvolution combined with spectral kurtosis. *Mechanical Systems and Signal Processing, 21,* 2616-2633.

Sendig911.(n.d.). Retrieved January, 2007, from http://www.sendig.com/old/E_E_911.html

SKF. (1996). SKF electronic handbook. Sweden:Leif Lewinscal.

Tandon, N., & Choudhury, A. (1999). A review of vibration and acoustic measurement methods for the detection of defects in rolling element bearings, *Tribology International, 32,* 469-480.

Tandon, N., Ramakrishna, K. M., & Yadava, G. S. (2007). Condition monitoring of electric motor ball bearings for the detection of grease contaminants. *Tribology International, 40,* 29–36.

Tandon, N., Yadava, G. S., & Ramakrishna, K. N. (2007). A comparison of some condition monitoring techniques for the detection of defect in induction motor ball bearings. *Mechanical Systems and Signal Processing, 21,* 244–256.

Vyas, Nalinaksh S., Satishkumar, D. (2001). Artificial neural network design for fault identification in a rotor-bearing system. *Mechanism and Machine Theory, 36,* 157-175.

APPENDICES

List of Tables

List of Figures